EPFL

Strategies for energy-efficient frontal polymerisation processing and microstructural evaluation of fibre reinforced composites

Jacobus Gerardus Rudolph STAAL

École
polytechnique
fédérale
de Lausanne

2023

Acknowledgements

This thesis concludes my PhD journey spanning the last four years that could best be described as intense, challenging at times but most of all as an invaluable and enjoyable experience. I would therefore like to thank prof. Véronique Michaud for giving me the chance to be a part of LPAC and for her unconditional support throughout the thesis. I admire her capability of multitasking and she was always able, and available, to give valuable suggestions for encountered problems. Dr. Baris Caglar is moreover greatly acknowledged for his guidance throughout the project and for always being available to discuss scientific results, while also regularly keeping an eye on the well-being outside of the lab.

The jury committee, consisting of dr. Christopher Plummer, prof. Fabien Sorin, prof. Vincent Sobotka and prof. Marco Sangermano, are thanked for their willingness to read and evaluate this thesis. Their feedback and questions have been valuable for completing this manuscript. Prof. Fabien Sorin is moreover thanked for taking part in the candidacy exam and the annual meetings throughout my PhD.

I would like to thank Raphaël Charvet for helping to materialise various moulds and measurement setups used in this thesis and for his help for the mechanical characterisation of fibre reinforced polymer samples. Gavin Waddell is acknowledged for showing me the practical insights on composite processing. Finally, Gary Perrenoud is greatly acknowledged for his invaluable help with the μCT imaging and analysis of UV-frozen flow fronts.

Over the past four years I was helped by a large number of students that were motivated to carry out their semester project or master thesis related to this thesis work. I would therefore like to thank Anup, Jiaying, Edgar, Sophie, Vincent, Sophie and Melissa for their efforts and their eagerness to learn. Edgar Smit and Mathieu Lefort are especially acknowledged for their excellent theses that formed the basis of some sections in this manuscript and it was a pleasure to work together with them during their master thesis projects.

A big thank you goes to many colleagues that were part of the LPAC in the past few years. The ever present vibrant and positive atmosphere in the lab made it an enjoyable place to work.

Acknowledgements

Jeroen

Abstract

Liquid composite moulding methods are widely applied for manufacturing of fibre reinforced polymer (FRP) composites and consist of two main stages: impregnation of fibrous reinforcements by a liquid monomer resin and curing of this resin. This thesis work proposes strategies towards the optimisation of both process stages. First, an UV-flow freezing method for the microstructural characterisation of dynamic infiltrating flows was optimised by fine-tuning of the resin formulation and experimental procedure. The method allowed for in-situ photopolymerisation of flow patterns characteristic of viscous-dominated, equilibrated and capillary-dominated regimes. X-ray micro-computed tomography analysis enabled high resolution volumetric imaging and quantification of the saturation levels of the characteristic flow patterns.

Frontal polymerisation offers unmatched reductions in energy demand and time for curing of FRPs. Current resin systems are incapable of overcoming the excessive heat uptake by fibrous reinforcements and are hence limited to fibre volume fractions (V_fs) well-below the desired minimum of 55%. Optimisation of the resin composition and mould configuration allowed for control of the governing heat balance while a defined processing window related this balance to the possibility of forming a self-sustaining polymerisation front. The maximum V_fs however remained limited by the heat loss to the fibres. Bridging of the V_f gap was achieved via a novel self-catalysed frontal polymerisation approach where a sacrificial resin channel in thermal contact with the FRP ensures enough pre-heating and catalyses the frontal polymerisation process. FRPs were produced with V_fs up to 62.2%, increasing the current maxima by 15-20%, at an energy demand reduced by over 99.5% compared to conventional oven-curing. Mechanical properties of the FRPs were comparable to those of traditional carbon FRPs while its glass transition temperature of 177.6±9.3°C was 18.5°C higher. To further evaluate process windows and the role of the mould, reinforcement and resin parameters, finite difference models were developed by the derivation of descriptive reaction-kinetics models that were calibrated and validated to experimental temperature recordings. The latter procedure allowed for accurate approximations of front velocities and temperature profiles and slightly overestimated peak temperatures. Application of the model to a series of case studies allowed for complementary insights on the role of the processing conditions and the occurrence of thermal instabilities. The combined strategies proposed in this work are believed to pave the way towards the energy-efficient production of FRPs by means of liquid composite moulding with an improved understanding on ongoing phenomena during resin infiltration.

Abstract

Keywords: Fibre reinforced polymers, Composite processing, Liquid composite moulding, Resin flow, UV-photopolymerisation, Out-of-Autoclave processing, Frontal polymerisation, Epoxide polymer, Reaction-kinetics modelling.

Résumé

Les méthodes de moulage des composites par voie liquide sont largement appliquées pour la fabrication de composites en polymère renforcés par des fibres (FRP). Elles consistent en deux étapes principales : l'imprégnation des renforts fibreux par une résine monomère liquide et le durcissement de cette résine. Ce travail de thèse propose des stratégies pour optimiser les deux étapes du processus. Tout d'abord, une méthode de figeage par UV de la résine en cours d'écoulement, pour la caractérisation microstructurale des flux d'infiltration dynamiques, a été optimisée en affinant la formulation de la résine et la procédure expérimentale. La méthode a permis la photopolymérisation in-situ de types d'écoulement caractéristiques en régime dominé par les forces visqueuses, ou capillaires, ou en équilibre. L'analyse par microtomographie aux rayons X a permis d'obtenir une imagerie volumétrique à haute résolution et de quantifier la distribution de saturation lors des schémas d'écoulement caractéristiques.

La polymérisation frontale offre des réductions inégalées de la demande en énergie et du temps de polymérisation des FRPs. Les systèmes de résine actuels sont incapables de surmonter l'absorption excessive de chaleur par les renforts fibreux et sont donc limités à des teneurs en fibres (V_fs) bien inférieures aux 55%, voire plus, souhaités. L'optimisation de la composition de la résine et de la configuration du moule a permis de contrôler l'équilibre thermique, tandis qu'une fenêtre de mise-en oeuvre a permis de relier cet équilibre à la possibilité de former un front de polymérisation auto-entretenu. Malgré cela, les teneurs maximales en fibres sont restées limitées par la perte de chaleur au niveau des fibres. L'écart V_f a été comblé grâce à une nouvelle approche de polymérisation frontale auto-catalysée dans laquelle un canal de résine sacrificiel en contact thermique avec le FRP assure un préchauffage suffisant et catalyse le processus de polymérisation frontale. Des FRP ont été produits avec des V_fs allant jusqu'à 62,2%, augmentant les maxima actuels de 15-20%, avec une demande d'énergie réduite de >99,5% par rapport à la polymérisation conventionnelle au four. Les propriétés mécaniques des FRPs étaient comparables à celles des FRPs traditionnels en carbone, tandis que leur température de transition vitreuse de 177,6±9,3°C était 18,5°C plus élevée que lors d'une cuisson thermique. Pour mieux évaluer les fenêtres de mise en oeuvre et le rôle des caractéristiques du moule, du renfort et de la résine, des modèles de différences finies ont été développés, incluant des modèles de cinétiques de réaction et données thermiques. Ils ont été calibrés et validés à l'aide de mesures expérimentales. Cette dernière procédure a permis d'obtenir des estimations précises des vitesses du front et des profils de température, tout en surestimant légèrement les températures maximales. L'application du modèle à une série d'études de cas a permis d'obtenir des informations complémentaires sur le rôle des conditions de mise en

Résumé

oeuvre et l'apparition d'instabilités thermiques. Les stratégies combinées proposées dans ce travail ouvrent des perspectives vers la production optimisée de FRPs en moulage par voie liquide grâce à une meilleure compréhension des phénomènes en cours pendant l'infiltration de la résine, et à la proposition d'un système de réticulation peu consommateur d'énergie.

Mots-clés : Polymères renforcés de fibres, mise en oeuvre des composites, moulage des composites par voie liquide, écoulement des résines, photopolymérisation UV, traitement hors autoclave, polymérisation frontale, polymère époxyde, modélisation de la cinétique de réaction.

Contents

Contents

Contents

List of Figures

List of Tables

Acronyms

μCT X-ray micro-computed tomography.

BADGE Bisphenol A diglycidyl ether.

C-C Carbon-carbon.

Ca Capillary number.

Ca* Modified capillary number.

Ca$_{opt}$ Optimum capillary number.

CMA-ES Covariance matrix adaptation evolution strategy.

DMA Dynamic mechanical analysis.

DSC Differential scanning calorimetry.

ECC 3,4-Epoxycyclohexylmethyl-3',4'-epoxycyclohexane carboxylate.

EDX Energy dispersive X-ray spectroscopy.

FROMP Frontal ring opening metathesis polymerisation.

FRP Fibre reinforced polymer.

FTIR Fourier-transform infrared spectroscopy.

FWHM Full width at half maximum.

HDMSi Hexadecyltrimethoxysilane.

I-Al Diaryliodonium tetrakis(perfluoro-tert-butyloxy)aluminate.

ILSS Interlaminar shear strength.

IOC-8 SbF$_6$ p-(Octyloxyphenyl)phenyliodonium hexafluorostibate.

ITX Isopropylthioxanthone.

LCM Liquid composite moulding.

LVR Linear viscoelastic regime.

MRI Magnetic resonance imaging.

MSE Mean squared error.

pDCPD Poly(dicyclopentadiene).

PI Photoinitiator.

PMI Polymethacrylimide.

PMMA Poly(methyl methacrylate).

PTFE Polytetrafluoroethylene.

R^2 Coefficient of determination.

RICFP Radical induced cationic frontal polymerisation.

RICP Radical induced cationic polymerisation.

RTM Resin transfer moulding.

SEM Scanning electron microscopy.

T$_g$ Glass transition temperature.

TMPDE Trimethylolpropane diallyl ether.

V$_f$ Fibre volume fraction.

VARI Vacuum Assisted Resin Infusion.

VLT Visible light transmission.

ZnI$_2$ Zinc iodide.

Symbols

A Arrhenius frequency factor [s^{-1}].

A_0 Absorbance in FTIR & UV-Vis spectroscopy [-].

A_w Areal weight of fibrous preform [g/m^2].

C_p Heat capacity [J/kg/K].

E_a Arrhenius activation energy [J/mol].

E_{eff} Effective activation energy [J/mol].

F_m Maximum force [N].

$G(\alpha)$ Polynomial function for describing cure kinetics [-].

H_r Enthalpy of polymerisation [J/g].

MSS Mean sum of squares [-].

N Number of fabric layers [-].

P Power density [W/m^3].

R Gas constant [J/mol/K].

S Saturation level [-].

T Temperature [K].

T^* Interface temperature [K].

T_0 Initial temperature [K].

T_p Peak temperature [K].

V_l Liquid volume fraction [-].

Δt Time step [s].

Δx Element width [m].

Symbols

Δy Element height [m].

α Conversion [-].

β Heating rate [°C/min].

β_z Zeldovich number [-].

ℓ Optical pathlength [cm].

η Viscosity [Pa·s].

$\frac{\partial \alpha}{\partial t}$ Conversion rate [s^{-1}].

κ Thermal conductivity [W/m/K].

ρ Density [kg/m^3].

σ_{lv} Liquid-vapour surface tension [N/m].

θ Static contact angle [°].

ε Molar attenuation coefficient [m^2/mol].

φ Ratio of power densities [-].

c Concentration [mol/L].

c_d Diffusion constant [-].

d_s Statistical rank difference of corresponding variables [-].

e Thermal effusivity [J/m^2/K/s$^{0.5}$].

$f(\alpha)$ Kinetics model [-].

h Sample thickness [m].

h_T Heat transfer coefficient [W/m^2/K].

k Temperature-dependent rate constant [-].

n Sample size of a dataset [-].

q_t Cumulative heat flow [J/g].

r Spearman's rank correlation coefficient [-].

v Velocity [m/s].

w Sample width [m].

1 Introduction

1.1 Motivation

Reinforcing a polymer material with a structural fibrous reinforcement results in a synergetic material that combines strong points of both components, while compensating the main limitations of the other material. Fibre reinforced polymer (FRP) composites are thus often selected for their excellent specific properties, e.g. stiffness-to-weight or strength-to-weight ratios, combined with good fatigue and corrosion resistances over their alternatives and have therefore benefited from a strong research focus over the last decades. Their use in industry for structural applications continuously increases since the 1970s [1, 2]. For example, modern aeroplanes now consist of up to 80% by volume of carbon FRPs [3] while composites are also applied in a wide range of other structural applications in the transport [4] and energy sectors [5], making up an estimated annual market volume of 12 megatons [1].

The quality of structural thermoset FRP parts and their resulting mechanical properties strongly depend on the ratio of relative content between the polymer and fibrous reinforcement, and on the quality of the manufacturing in terms of fibre/matrix adhesion, fibre alignment, and good impregnation, with optimum part qualities being attained when the FRP is free from any residual air pockets, commonly referred to as voids or pores [6], since the presence of voids is detrimental for the mechanical performance of the FRP, in particular in the direction transverse to the fibres [7, 8]. Processing of FRP, i.e. combining the polymer and fibrous reinforcement, exerts a major influence on the formation of voids and hence the resulting part quality [6]. Conventional manufacturing techniques employed by the composites industry can be divided into two main categories, namely 1. the consolidation of pre-impregnated fibrous preforms under high pressures and temperatures, e.g. in an autoclave, and 2. the impregnation of dry fibrous preforms by a monomer resin (or a low viscosity thermoplastic) followed by thermal curing or solidification.

Liquid composite moulding (LCM) is a class of FRP processing methods belonging to the second category that is known to yield structural FRPs with good part quality at an increased rate and cost-efficiency as compared to e.g. autoclave moulding. Infiltration by a monomer

resin under an applied pressure gradient imposes the need for sufficient rigidity of the dry fibrous preforms so as to avoid undesired distortions in the fibre alignment. This is achieved by the use of dual-scale fabric architectures where thousands of individual fibres are bundled into yarns, which are assembled in a, e.g. woven, braided or knitted, macrostructure. While these dual-scale fabric architectures bring the required stability for shape retention during processing, and are therefore without exception used in the context of LCM processing, their heterogeneous structure also introduces additional complexity in the flow behaviour of infiltrating resins [9] that narrows the window of processing conditions for production of void-free FRPs with optimum part quality [8–10].

The relationship between the processing conditions, the resulting flow behaviour and the final part quality in dual-scale fibrous architectures has been the topic of numerous studies over the last decades [9, 11]. Analysis of dynamic infiltrating flows is often based on macroscopic observations since accurate capture of the rapid ongoing phenomena imposes the need for characterisation methods possessing high time resolutions. Although these studies have improved the understanding on resin flow in LCM processing, the phenomena taking place on a microscopic scale, i.e. on the order of several μm, remain largely unexplored due to the absence of characterisation methods possessing the required spatial and time resolution at the same time. A system that would be able to polymerise very fast so as to freeze the flow at a desired time during the impregnation process followed by characterisation using high resolution methods would thus open the door to a better understanding of the flow phenomena and its development is therefore one of the objectives of the present work.

In addition, the thermal curing of infiltrated fibrous preforms is required to form the monomer resin into a polymer matrix and typically requires lengthy autoclave or oven-curing procedures, taking hours to days, at elevated temperatures and pressures, simultaneously requiring a significant energy demand and subsequent environmental cost to the process [12, 13]. For example, the production of a fuselage section of a Boeing 787 aeroplane is estimated to have an energy demand of 58 GJ [14], which is equivalent to the yearly energy consumption of three residents of Switzerland [15] or driving about 125,000 km in an electric car [16]. Extrapolated to its global volume, the thermal curing procedures bring a significant environmental impact to the FRP industry. Incentivised by the need to reduce this environmental impact, and hence to search for more efficient and sustainable FRP production methods, a variety of novel curing methods have been proposed that could each reduce the processing time or the required energy input [12, 13].

Frontal polymerisation has emerged as a particularly promising approach as it can allocate both these reductions, allowing for the productions of FRP parts in minutes with little external energy input [17, 18]. Governed by the released polymerisation enthalpy, frontal polymerisation systems can form an autocatalytically-induced front between hot (>200°C), formed polymer and cold monomer resin, after the local application of an initial external stimulus (e.g. heat or UV-irradiation). The front propagates autonomously through the impregnated fibrous preform until it is fully cured, as long as a threshold for activation of the autocatalytic

mechanism is exceeded [19]. An example of autonomous front propagation can be found by clicking Video 1. The requirement for overcoming a threshold activation energy imposes the need for precise control of the local heat balance between the resin reaction enthalpy, thermal diffusion and heat losses to the environment and fibrous reinforcements in order to successfully produce FRPs by means of frontal polymerisation. With the latter term becoming increasingly significant with increasing fibre volume content (V_f), a system-dependent maximum defines the V_f where the available activation energy falls below the threshold, resulting in premature quenching of the front [17, 19]. These maxima currently range, depending on the resin system, between 35-51% [20–22] which is below the V_fs typically applied in the FRP industry. Overcoming these limitations would pave the way for the adaptation of frontal polymerisation as a FRP manufacturing technique, offering fast and energy-efficient processing resulting in a minimal environment impact [20] and tooling costs [18] since no complex heating systems would be required. This has been a second objective of the present work.

1.2 Thesis outline

This thesis work aims to explore and validate strategies that can contribute to the development and optimisation of LCM processing methods. Two main research contributions are pursued that aim at 1. proposing strategies for improved analysis of dynamic flow behaviour during LCM impregnation and 2. developing methods to enable the frontal polymerisation-assisted processing of high-V_f FRPs. This leads to the following research questions that are addressed in the manuscript:

- **Can dynamic flow behaviour in dual-scale fibrous architectures be assessed on a microstructural level, thanks to fast-curing UV initiated resin systems that would allow to freeze the flow patterns without any major disturbances to the local microstructure?**

- **Which strategies can be employed to enable the production of high-V_f FRPs by means of impregnation and frontal polymerisation?**
  With the related questions:
    - What is the role of the governing heat balance during frontal polymerisation processing of FRPs?
    - Can an improved manufacturing route be proposed that increases the heat flux without the need for additional external heat?
    - Can these complex reaction kinetics and transient heat exchange mechanisms be modelled to propose processing windows?

To answer these questions appropriately, this thesis has been structured into the following chapters:

- **Chapter 2: State-of-the-Art**
  Comprises a review of the available literature in the context of LCM, analysis of dynamic flow behaviour and experimental and numerical studies on frontal polymerisation.

- **Chapter 3: Experimental**
  A description of the experimental methods employed throughout this thesis work in order to answer the research questions.

- **Chapter 4: Microstructural evaluation by in-situ UV-flow freezing**
  An optimised methodology for UV-flow freezing of flowing resin is presented and employed for a volumetric assessment of the characteristic flow patterns related to dynamic flow behaviour at different processing conditions.

- **Chapter 5: Frontal polymerisation-assisted processing of fibre reinforced polymers**
  An exploratory study on the role of the governing heat balance during the frontal polymerisation processing of FRP is presented. Methods to control the heat balance were identified and used to define the current limitations of the process, by acting on the mould material and resin composition.

- **Chapter 6: Self-catalysed frontal polymerisation processing**
  Based on the findings in Chapter 5, a novel method for the production of high-V_f FRPs is presented that allows to overcome the current limitations and reach the range of V_fs sought for by the FRP industry without requiring additional energy input.

- **Chapter 7: Modelling of Radical Induced Cationic Frontal Polymerisation**
  A numerical model describing the frontal polymerisation process used for experimental investigations is proposed and employed to gave a further insight in the observed phenomena.

- **Chapter 8: Conclusion & Outlook**
  Finally, the findings presented in this work are summarised and a perspective is placed on their potential for continued investigation.

2 State-of-the-Art

2.1 Liquid Composite Moulding

Liquid Composite Moulding is a class of FRP processing methods that are based on the impregnation of a liquid monomer resin into a dry fibrous preform, followed by a curing procedure to form a polymer matrix. Characterised by an advantageous trade-off between relatively fast processing and low tooling costs, e.g. compared to autoclave processing, with good resulting part qualities, LCM-based processing methods are widely applied in the thermoset composite industry. The family of LCM methods is typically differentiated by the mould types and/or the type of pressure application [23] with resin transfer moulding (RTM) and vacuum-assisted resin infusion (VARI) being the two most frequently employed methods [9]. RTM makes use of two solid mould halves during the infiltration of a pressurised resin system while the top mould of VARI is generally flexible with resin being infused by the application of a vacuum from an outlet. A typical process flow for RTM methods is shown in Figure 2.1. Fibrous reinforcements are first cut to the desired shapes, layed-up and aligned to achieve the desired fibre orientations. The stack of dried fabrics is then often compacted and preformed at elevated temperature to increase its shape retention for the subsequent processing steps. The preforms are placed in the RTM mould configuration followed by the infiltration of the liquid monomer resin under an applied pressure gradient. Once completely saturated, the mould is heated to cure the resin and an additional post-curing procedure is in some cases applied to ensure the maximum curing degree is reached as well as to anneal the part, after which the part can optionally be subjected to post-processing procedures, e.g. to enhance its surface quality.

The fabrics used in LCM processing are almost uniquely built-up of a dual-scale structure where bundles of fibres, having diameters in the order of 7-20 μm are assembled into a macroscopic, e.g. woven, knitted, braided or non-crimp, textile structure. While the use of these structures arises from the need for shape retention during the manipulation of dry fibrous preforms, the preforms used in LCM processes exhibit highly anisotropic, in general dual scale pore, networks that span from micron-scale pores within yarns, i.e. intra-yarn, up to millimetre-scale pores between yarns, i.e. inter-yarn [25].
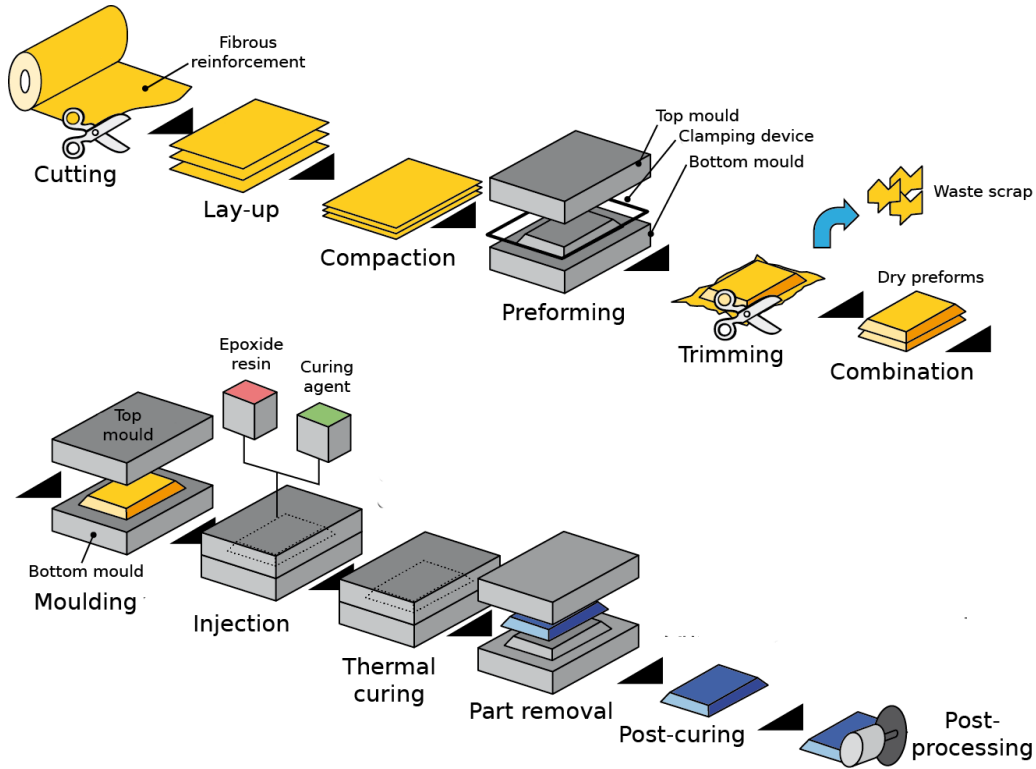
Figure 2.1: Schematic representation of resin transfer moulding (Adapted from: [24]).

2.2 Dual-scale flow behaviour

Flow through a dual-scale fibrous reinforcement can be considered as a flow through two superimposed porous media [6], each being governed by the dominance of different physical principles. The presence of closely spaced fibres make intra-tow channels particularly susceptible for capillary effects while their presence is less apparent in the inter-yarn channels where fibres are more sparsely spaced. The inverse on the other hand is true for the hydrodynamic forces imposed by the applied pressure on the monomer resin for its infiltration. The susceptibility differences for capillary and hydrodynamic pressures result in local permeability differences between intra- and inter-yarn channels [6, 8, 26], which can typically be observed by a bimodal distribution of flow velocities and preferential channel infiltration, i.e. dual-scale flow behaviour, if one of the forces is relatively dominant [6, 9, 27–30]. This is illustrated in Figure 2.2 where a flow regime dominated by capillary forces has a faster progression within yarns while flow propagates faster in the inter-yarn spaces when hydrodynamic forces are dominant, i.e. a viscous-dominated regime. It should be noted however that the differences in flow velocities result from the relative dominance of one of the governing forces as capillary and hydrodynamic pressures generally range between 1-100 kPa and 100-1000 kPa, respectively [9].

2.2.1 Void formation

The resulting 'fingering' in Figure 2.2 due to the relative differences in flow behaviour results in the formation of an unsaturated region where the preferential flow path, e.g. intra-tow for a capillary-dominated flow, is largely saturated while the remaining section, e.g. inter-tow for the exemplary capillary-dominated flow, remains largely unsaturated. In this situation, transverse liquid transfer from the preferential flow path into the delayed channel is reported [10, 31] to be dominant over longitudinal channel impregnation. This however generally also causes mechanical air entrapment in the channel, which is regarded as the main origin of void formation [7, 8, 28, 32]. The location and morphology of voids formed by mechanical air entrapment are directly dependent on the flow regime. Capillary-dominated flows typically result in the formation of voids in the inter-yarn regions, as demonstrated in Figure 2.2. The unconstrained nature of these voids makes their morphology generally spherical as this is energetically favourable due to the minimisation of surface tension [6, 8, 33]. It should be noted however that the equilibrium shape may not always be reached, resulting in voids with more irregular morphologies [6]. Viscous-dominated regimes on the other hand result in the formation of intra-yarn voids with elliptical shapes and higher aspect ratios due to the constraints imposed by the presence of surrounding fibres [6, 8, 33, 34]. The location of intra-yarn voids and the consequent adhesion to fibres due to surface tension [35] or geometrical constraints [10, 36] also limits the potential of void transport-induced removal [37]. Inter-yarn voids can typically migrate more easily through the fibrous preform and hence be removed [6].

Dual-scale flow behaviour can thus exert a significant influence on the void content and thereby the part quality of FRPs produced via LCM processing. In theory, mechanical air entrapment can be avoided when intra- and inter-yarn flows propagate at the same velocity, forming a so-called equilibrated flow front morphology [6]. In this favourable situation, voids would thus only be formed due to alternative mechanisms such as e.g. gas formation from curing reactions [32], curing shrinkage [38, 39] or nucleation of dissolved gasses in the resin when cooling down [7, 8, 40], resulting in a minimisation of the void content.

2.2.2 Capillary number

Quantitative descriptions of dual-scale flow behaviour are frequently made using the capillary number (Ca), which originates from soil science and describes the ratio of hydrodynamic and viscous forces as:

$$Ca = \frac{v\eta}{\sigma_{lv}} \tag{2.1}$$

where v denotes the fluid flow velocity, η the resin viscosity and σ_{lv} the liquid-vapour surface tension. Numerous reports [7, 28, 34, 35, 41, 42] have related the formation of an equilibrated front morphology or the minimisation of void content in a resulting composite to an optimum capillary number (Ca_{opt}). As demonstrated in Figure 2.2, capillary numbers lower than the
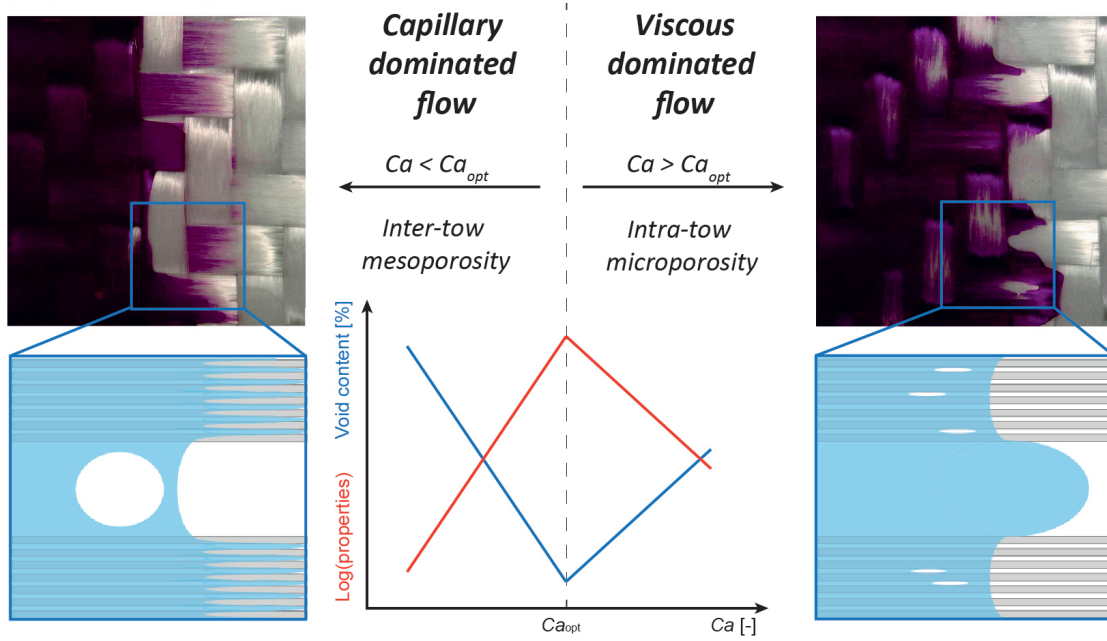
Figure 2.2: Demonstration of the influence of the capillary number on the void formation and final part properties during infiltration based on the fluid paths in a glass twill fabric under capillary- and viscous-dominated flow regimes.

optimum generally show capillary-dominated flow regimes with consequent inter-yarn void formation while viscous-dominated flow regimes and intra-yarn void formation are observed at higher values of the capillary number [43, 44]. Flow experiments are claimed to be the most suitable to study the impregnation of fibrous preforms and its relation to the capillary number since all governing parameters act simultaneously [42] while Ca_{opt} related to a minimisation of the resulting void content has also been characterised numerically [45]. In general, studies investigating the flow behaviour vary the infiltration velocity with the liquid viscosity and surface tension are kept constant [7, 27, 34, 44] while the role of these latter two parameters have only been investigated recently [46]. Despite extensive efforts, it has not been possible to-date to establish quantitative relations between the optimum capillary number and the processing conditions with the range of Ca_{opt} being known to differ for different resin-fibre systems. As reported by Michaud [9] and Park & Lee [35], typical values of Ca_{opt} range in the order of 10^{-3}, i.e. Caglar et al. [47] reported a value of $1.4 \cdot 10^{-3}$, Lebel et al. [48] a Ca_{opt} of $1.5 \cdot 10^{-3}$ and Lystrup et al. [49] $0.6 \cdot 10^{-3}$.

Several authors [27, 50, 51] reported similar observations using a non-dimensional modified capillary number, which is frequently used in the field of soil science, that includes the resin-fibre contact contact angle (θ):

$$Ca = \frac{v\eta}{\sigma_{lv}\cos(\theta)} \tag{2.2}$$

Use of the modified capillary number brings the advantage that matrix-fibre interactions are accounted for, although partially as it considers a static contact angle while dynamic contact angles in the presence of flowing liquids are known to significantly deviate from their static equilibrium [52–54]. This could explain the generally preferred use of Ca for the description of flow experiments. However, it should be noted that Ca_{opt} is merely an intrinsic property of the resin-fibre system and does not consider transient phenomena taking place, e.g. the spatiotemporal variation of pressure and the formation and transport of voids [38]. While several attempts have been made to account for these phenomena in a descriptive dimensionless number, e.g. the use of the so-called capillary ratio between capillary and injection pressures [55], the definition of a critical Ca for void mobilisation [48] or an analytical expression to predict void formation in woven fabrics by decoupling the flow in different domains [37], their use in studies on flow processing remains limited to-date and Ca has remained the main descriptor.

2.2.3 Description of unsaturated flow

Quantitative descriptions of the unsaturated region in a dual-scale flow are usually made via the local degree of saturation defining the fraction of the available pore space that is filled with resin and is defined as:

$$S = \frac{V_l}{1 - V_f} \tag{2.3}$$

where S is the saturation level, respectively, V_l the liquid volume fraction and V_f the fibre volume fraction in a representative volume element. The magnitude of the saturation level varies between 0 for an dry section and 1 when all the available pore space is impregnated. The evolution of the saturation level over the unsaturated flow region is used to both quantify the dual-scale flow behaviour, e.g. as reported by Nordlund & Michaud [29] for a range of viscous-dominated flow conditions, as well as to model them. The localised saturation is typically used in relation to the localised resin pressure and/or the permeability difference between saturated and unsaturated regions. An example of this relation was reported by Park & Lee [35] who demonstrated that, for a capillary-dominated flow regime, an incline of the resin pressure compared to the linear pressure drop over the fabric length would appear when the saturation drops below one, which corresponds to a decreased resin permeability due to reduced flow passages as the resin does not occupy the available pore space volume [35]. This gradual decrease continues up to an inflexion point where capillary pressures are more dominant and tow saturation is more prominent. Descriptions of saturation curves by semi-empirical models such as those proposed in soil-science by Van Genuchten [56] or Brooks & Corey [57] have been employed towards a further understanding on the role of capillary effects [11] as well as for quantification of e.g. local pressures and local permeabilities. The reader is referred to the recent thesis work of H.Teixidó [46] for a more in-depth discussion on models describing unsaturated flow. Accurate characterisation of saturation levels at a microscopic
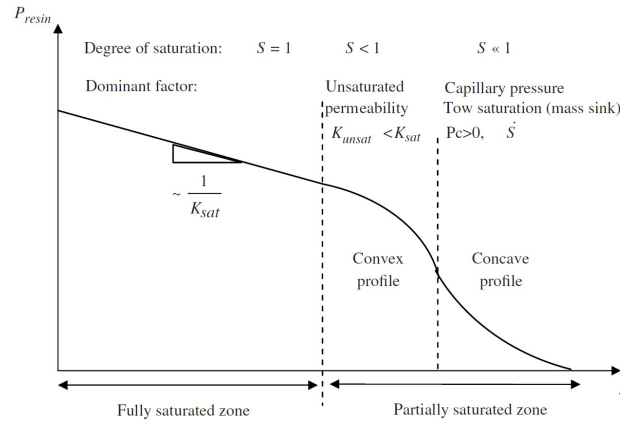
Figure 2.3: Relation between the localised resin pressure and saturation levels in a capillary-dominated flow regime (Source: [35]).

level is therefore required to derive improved descriptions and models for microstructural flow behaviour.

2.3 Microstructural evaluation methods

This section is an extract of the article 'Capillary Effects in Fiber Reinforced Polymer Composite Processing: A Review' by H. Teixidó[‡], J. Staal[‡], B. Caglar and V. Michaud published in 'Frontiers in Materials' 9, 1-24 (2022).

Based the aforementioned importance of understanding and controlling the dual-scale flow in LCM processing, a number of evaluation methods have been applied to analyse the on-going phenomena, ranging over a wide range of scales. Characterisation of dual-scale flow behaviour at a microstructural level is complicated by the rapid dynamic phenomena acting at a small scale combined with a potential opaque nature of many commercial available fibres in polymer composites, e.g. carbon or flax. A multitude of methods have been proposed to accurately image dual-scale flow, ranging from methods already widely established in other fields, e.g. Magnetic Resonance Imaging (MRI), to more exploratory techniques such as infrared thermography. With no universal agreement on the technique to visualise dual-scale flow behaviour, each specific method brings its own advantages and trade-offs between spatial resolution, recording speed and ease of implementation.

2.3.1 Post-mortem analysis

Post-mortem analysis on produced composite parts was one of the first and a facile methods to observe and quantify the role of capillary effects in FRP processing. These post-mortem methods almost uniquely quantify capillary effects via the void content present after final consolidation of the composite, while varying process parameters [28, 32, 34, 38, 58, 59] such

as the flow rate or the injection pressure and thereby the impregnation velocity. It should however be noted that in the latter case the velocity of the flow front, and hence the Ca, decreases with the impregnation length. The presence of an optimum Ca [28, 34, 58, 59], where minimum void content is present within the composite as illustrated in Figure 2.2, has been frequently reported using post-mortem analysis while Leclerc & Ruiz [34] observed similar trends when measuring the resulting tensile modulus and tensile strength. While bringing the advantage of being an easy method with relatively low equipment costs, post-mortem analysis of capillary effects could potentially lead to significant inaccuracies. These arise partially from the methods used for void content analysis such as, in order of increasing accuracy [60], Archimedes' principle [61], optical microscopy [32, 38, 61] and X-ray micro computed tomography (μCT) [62, 63], while the void content in a FRP part is also affected by phenomena occurring after passing of the flow front, e.g. void transport and dissolution into the resin [6, 35]. In spite of the strong assumption that the latter did not have a significant effect on the resulting void content in a chosen location, post-mortem analyses has been a useful tool for early assessments on the role of capillary effects in composite processing.

2.3.2 Optical characterisation

In-situ measurements of front progression and morphologies are an a priori more accurate to method to assess dual-scale flow behaviour, allowing for more direct observations of the ongoing phenomena compared to e.g. post-mortem analysis. Optical methods can record impregnating resins in fibrous preforms in a non-intrusive manner and at a high spatial and time resolution with simple equipment, making it an effective and low-cost method for flow characterisation [48]. Optical imaging is generally limited to translucent fabrics and relies on the matching of refractive indices to distinct phases [29, 48, 64], i.e. the refractive indices of epoxy/fibreglass can be very different from that of the air/fibreglass interface. The distinction between two interfaces can be further enhanced by colourants compatible with the test fluid [65, 66]. Recording a linear flow with a conventional camera and subsequent image analysis allowed Nordlund & Michaud [29] and Facciotto et al. [55] to estimate the width of the unsaturated region, which was subsequently modelled with finite difference [29] and finite element models [55]. Continuous imaging of these regions showed the progressive saturation of the preform, which was quantified from the pixel intensity in the successive pictures. Standard camera imaging however only captures the flow at the, generally glass, surfaces of the mould, which are known to be vulnerable to wall-effects, i.e. race-tracking between the preform and the mould halves, while effects of e.g. nesting are also not well captured [67, 68].

Visible Light Transmission VLT, illustrated in Figure 2.4a, has been proposed as an elegant method to overcome this limitation [64]. Placement of a diffuse light source below the transparent mould halves and of a camera above it makes the recorded light intensity an average over the preform thickness. Moreover, the signal is also significantly intensified. Lebel et al. [48, 51] employed VLT to characterise the relationship between processing conditions, i.e.
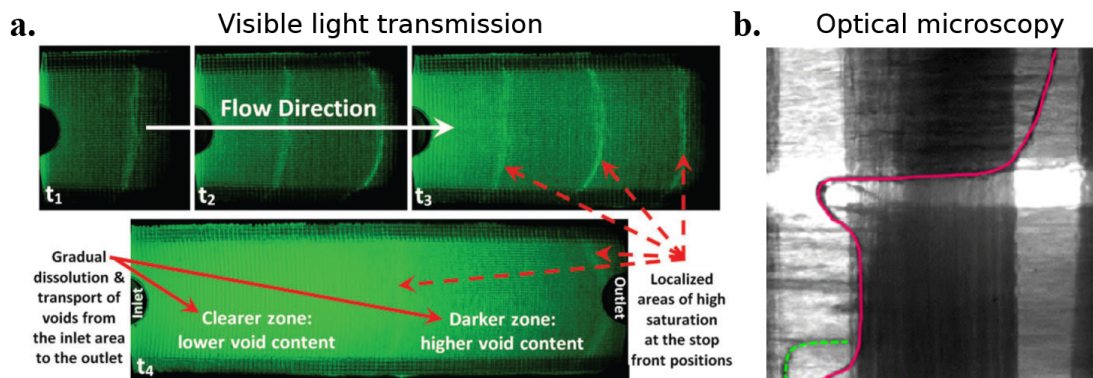
Figure 2.4: Demonstrations of optical methods for flow characterisation at different scales: a) Visible Light Transmission on centimetre-scale (Source: [51]) and b) optical microscopy imaging on micrometre-scale (Source: [69]).

via the Ca^*, and the saturation of a glass fibrous preform. The increased light intensity allowed them to accurately estimate the local void content after calibration with burnt-off composites after consolidation. Distinction of voids allowed them to estimate the optimum Ca^* as well as the onset of pressure-induced void mobility. Further contrast enhancement could be achieved by the addition of fluorophores into the probe liquid. This resulted in strong enhancement of the contrast, e.g. for the visualisation of intratow flow [42, 70], even enabling the use of optical methods for the characterisation of opaque carbon fibrous preforms [49]. The addition of dyes will however induce changes in resin properties, e.g. its wettability, and thereby may affect the apparent Ca or Ca^*, making the resulting observations not directly representative of pure resin systems.

Increases in spatial resolution on tow-scale could be achieved with the use of optical microscopy imaging. This increased resolution, however, comes at the cost of the overall field of view, making the method better suited for local detection of voids or microstructural dual-scale flow behaviour. Yoshihara et al. [69] investigated the role of capillary pressure, varied by the application of different fluorine coatings on the fibre surface, on the dual-scale flow behaviour in an optical microscopy setup. This allowed them to observe infusion of a woven fabric on a micron-scale, shown in Figure 2.4, which were coupled to numerical simulations. Zhao et al. [71] and Matsuzaki et al. [72] followed a similar approach in their studies on void formation and were able to accurately record capillary fingering and void formation upon the impregnation of a woven preform at a range of velocities falling the in the capillary-dominated regime. This allowed them to accurately capture the void formation and evaluation with the use of in-situ optical microscopy. However, flow analysis by means of optical microscopy can typically only be applied to single ply fibrous reinforcements if based on light diffusion and suffers from wall-effects in reflectance mode, while the upper limit of allowed infusion rates is defined by the maximum imaging rate of the microscope.

2.3.3   In-situ flow freezing

In-situ flow freezing was proposed as a novel method for the characterisation of dynamic flow behaviour in translucent fibrous reinforcements. Initially proposed by Caglar et al. [47], the method is based on the UV-photopolymerisation of infiltrating resins, transforming a dynamic situation into a static one and thereby overcoming any potential time constraints imposed by characterisation techniques. Caglar et al. [47] used a transparent poly(methyl methacrylate) (PMMA) mould configuration to in-situ polymerise infiltrating epoxide resins. Resin pressures were varied to produce capillary-dominated, equilibrated and viscous-dominated flow front morphologies in single-layer glass fibrous reinforcements, as shown in Figure 2.5. Optical imaging of the consolidated flow fronts in pristine fabrics and fabrics after application of an oxidative surface treatment allowed them to relate the processing conditions, i.e. Ca, to the apparent flow front morphology. Neitzel & Puch [73] followed up on this and used a similar methodology to assess void formation mechanisms in LCM processing. Using a semi-transparant glass mould and an acrylate-based UV-responsive system, they controlled the flow regimes in single-layer glass fibrous preforms by variation of the inlet pressure. Subsequent optical microscopy imaging on cross-sections of the cured flow front allowed them to assess the length of the unsaturated zone as a function of Ca^*.

These reports have partially demonstrated the potential of in-situ UV-flow freezing as a method for characterisation of dual-scale flow behaviour on a microstructural level. However, the use of a single fabric layer, potentially inducing the aforementioned wall-effects, in combination with a spatially-averaged [47] or discrete analysis strategy [73] may limit the observations that could be made. While the use in-situ flow freezing is partially hampered by the need for specially designed resin systems and rather thin (e.g. few layers) and transparent samples to avoid inhibiting the cure reaction that is highly dependent on UV-light, further optimisation of the methodology based on the work of Refs. [47, 73] could result in a promising strategy for the microanalysis of dynamic flow behaviour.

2.3.4   Integration of sensors

One of the proposed methods to track resin flow progression, and thereby progressive saturation and void formation, in LCM processing that is not limited to translucent fabrics is the inclusion in or in-between stacked preforms [74]. Methods using conductive sensors typically require a non-conductive fibrous preform to be placed in-between tow conductive parallel plates. Labat et al. [75] and later Gueroult et al. [26] infused a glass fibre preform with a conductive liquid and simultaneously recorded the voltage over the preform, which increased with increasing saturation levels. The first strong increase of the voltage was attributed to the passing of the unsaturated flow front followed by a period of void removal, while the final voltage was directly linked to the saturation and hence the void content in the part. The recorded void contents moreover followed the expected 'V-shaped' curve as a function of Ca^*. Carlone et al. [76, 77] employed a similar experimental methodology while recording the
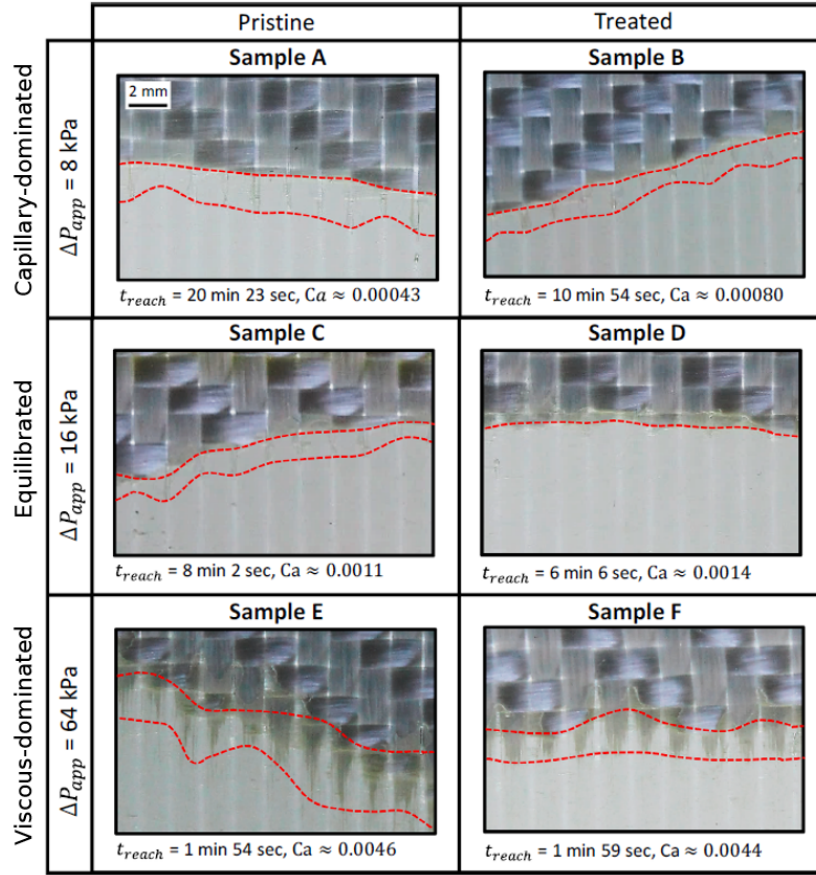
Figure 2.5: Optical imaging of front morphologies in capillary-dominated, equilibrated and viscous-dominated flow regimes after UV-photopolymerisation using pristine fabrics and fabrics subjected to an oxidative surface treatment (Source: [47]).

capacitance over the fabric preforms and correlated the observations to numerical models. This methodology also allowed for impregnation with less conductive resins. Similar saturation curves were obtained and verified in comparison with the void content in post-mortem optical microscopy images. They moreover compared the accuracy of progressive saturation tracking by dielectric with that recorded by pressure sensors, e.g. as proposed by Refs. [78, 79] and was found to be significantly higher. The requirement for a non-conductive fibrous preform limits the use of the methods developed by Refs. [26, 75–77]. Developments have been made to overcome this issue, e.g. by insulating the censor with a dielectric material and optimisation of the sensor characteristics [80, 81]. However, these types of sensors have not yet been employed to study unsaturated flow phenomena to-date. Alternatively, Villière et al. [82] proposed a method based on the saturation-dependence of the thermal behaviour of a resin-fibre system. Recording of heat fluxes induced by an electric heater was found to give an accurate representation of the local saturation, which were coupled with mathematical models to fit progressive saturation curves. Implementation of optical micro-flow sensors within tows on the other hand gives the possibility to record capillary pressures and intra-tow

saturation, as was demonstrated by He et al. [83] in their study on resin flow in prepreg process-ing. Although these sensors bring the potential for microstructural evaluation of dual-scale flow behaviour, their presence will inherently alter the resin flow, making it uncertain that a representative image could be obtained. The discrete nature of integrated sensors moreover limit the observations that can be made in a single impregnation. In combination with, in most configurations, a limited spatial resolution, the use of integrated sensors is generally regarded unfavourable for the analysis of dynamic flow behaviour.

2.3.5   Ultrasound imaging

Ultrasound imaging techniques on the other hand do not suffer form a discrete nature and are known for their high acquisition rates. Ultrasound techniques have therefore been used to track resin flow in fibrous preforms [84], in particular for through-thickness resin infusion [85–87]. Thomas et al. [86] tracked through-thickness resin flow via acoustic C-scan measurements giving a planar view of the sample. Ultrasound imaging moreover allowed for the successful characterisation of unsaturated permeability, given a microstructure-dependent minimum fibre content is present within the preform [87]. While this method gives an indication of the through-thickness saturation of the preform, its limited spatial resolution does not allow for the distinction of capillary effects such as dual-scale flow behaviour, localised saturation and void formation on a microstructural level.

2.3.6   Magnetic resonance imaging

Several works have utilised MRI as a tool to observe flow in porous media. While suffering from drawbacks such as large tooling costs and spatial resolutions that are limited to around 0.1 mm due to signal relaxation effects [88], MRI brings the advantage of an excellent material contrast between FRP constituents, i.e. fibres, polymer and voids, which could be further enhanced by the addition of contrasting agents or by specified measurement sequences [89]. MRI has therefore been applied for the characterisation of flow in porous media [90–92] with several studies specifically focusing on the visualisation of dual-scale flow behaviour. Leisen & Beckham [93] proposed a method of nuclear MRI and subsequent image analysis to quantify inter-yarn voids and their morphologies in saturated woven nylon fabrics, while Neacsu et al. [89] applied MRI to characterise capillary effects in glass fibre bundles. In the latter case they found fast MRI imaging able to track progressive transversal impregnation within bundles at different volume fractions and were able to use this data to backcalculate the driving capillary pressures. Endruweit et al. [88] carried out an extensive investigation regarding the use of MRI to in-situ image the impregnation of dual-scale textiles. Reconstructed 3D images had resolutions of 0.5 mm, visualising the mesostructure of fibrous preforms. An intermittent injection strategy was used to overcome time resolution limitations, which allowed for imaging of various flow regimes. Resulting images clearly visualised the progressing flow front and the formation of inter-yarn voids, while progressive progressive saturation was tracked by a gradual increase of the relative signal intensities. Observation of intra-tow flow and capillary

effects on a micron-scale are however beyond the physical capabilities of MRI techniques.

2.3.7 X-ray analysis

Intrinsic differences in X-ray absorption coefficients of composite constituents gave rise to a multitude of X-ray-based techniques that were applied to in-situ study the dynamic flow behaviour in LCM processing. Bréard et al. [94] continuously tracked through-thickness impregnation of a random mat stack using X-ray radiography. While the image resolution was insufficient to capture the fibrous preform, the fast imaging rates of X-ray radiography allowed for accurate tracking of the infiltrating fluids. Teixidó et al. [95] used an X-ray phase contrast method in-operando to assess the saturation of several types of fibrous preforms. Based on the material-sensitive phase modulation due to interference formed after passing X-rays through a grating, the material contrast, which can be a limiting factor for composites, is significantly enhanced [96]. Employing this method allowed for imaging of progressive saturation of 15×5 cm non-transparent fabrics over a range of capillary numbers and they were able to extract the thickness-averaged saturation curves from these images, with a time step below 10 seconds [97].

The use of μCT has allowed for the observation of dual-scale flow at an unprecedented resolution. Based on the reconstruction of three-dimensional images from a set of radial X-ray radiographs, X-ray μCT provides the ability to reconstruct through-thickness images of opaque materials [98]. Features down to sub-μm level can be reached, e.g. allowing for accurate imaging of carbon or glass FRPs, while image resolutions typically come at a cost of the volume that can be analysed and the measurement speed. 4D μCT (three-dimensional in space and time), e.g. to study the dual-scale flow behaviour, is moreover typically complicated by the possible occurrence of blurring effects, reducing the image resolution due to movement of the flow front [99]. To avoid this, the acquisition time should be short enough to limit the movement to less than one voxel per scan [99]. While some studies have thus aimed at indirect observations of dual-scale flow behaviour, e.g. by assessing thickness changes [100] or image-based computational fluid dynamics simulations [101], several investigations aimed at in-situ imaging of dual-scale flow behaviour through a fibrous preform. Vilà et al. [10] were the first to employ μCT to study the intra-tow infiltration of a glass fibre bundle in a μCT synchrotron beamline. Infusion was carried out under a capillary-dominated regime and was halted to image the flow front. Images were reconstructed from 900 radiographs taken over a period of 120 minutes with a voxel size of 2.5 μm^2. At a slightly reduced resolution, Larson et al. [102, 103] were able to drastically reduce the imaging time, i.e. to ~1.5 minutes, which allowed them to in-situ record the impregnation of an enclosed fibre bundle with capillary numbers up to 10^{-3}. Vilà et al. [10] and Larson et al. [102, 103] were both able to observe progressive saturation of the fibre bundle and were able to relate this to local capillary pressures and permeabilities, while the more homogeneous fibre distributions used by Larson et al. [102, 103] translated to more homogeneous distributions and magnitudes of capillary pressures. They were moreover able to gain an insight in the apparent dynamic contact angles and to relate this to fibre displacement.
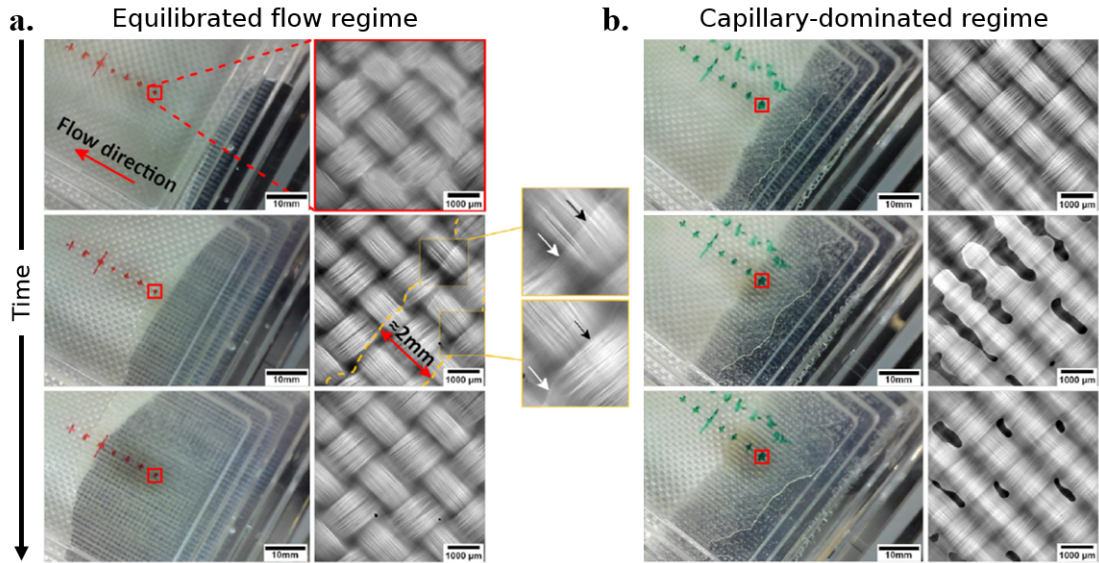
Figure 2.6: Progressive saturation recorded by synchrotron radiation radiation computed laminomography of a) equilibrated and b) capillary-dominated flow regimes. (Source: [99]).

Static contact angles after capillary wicking of a fibre bundle was studied in more detail by Castro et al. [104], who employed synchrotron-μCT to produce high-resolution images. Image analysis then allowed for an assessment of axial and transverse contact angles.

The resolution requirement to obtain an accurate representation of FRPs with a conventional μCT setup limits the sample size significantly. Castro et al. [99] overcame this limitation by making use of so-called synchrotron radiation computed laminography, where significant gains in field of view can be achieved by imaging planar samples at an angle ([105–107]. In combination with a fast acquisition rate, i.e. 1.8 minutes per tomogram, they were the first to in-situ image dual-scale flow behaviour in woven textiles with micron-scale resolution. Equilibrated flow regimes (Figure 2.6a) were imaged and, although slightly affected by blurring due to the movement of the flow front, the images clearly showed the microstructural evolution upon impregnation and the absence of void formation. Slower infusion rates in capillary-dominated regimes (Figure 2.6b) minimised the blurring effect, giving a highly detailed insight on progressive saturation and void formation upon impregnation. Moreover, they were able to segment and analyse both inter- and intra-yarn void distributions as well as gaining novel insights in the void formation mechanisms during LCM.

The spatial resolution of μCT for imaging of dual-scale flow behaviour on a microstructural level is thus unmatched compared to its alternatives. Overcoming its relatively low time resolution, which is regarded as the main limitation of μCT imaging, would make the preferred method for studying dynamic flow behaviour. By removing limitations on the time resolution or the range of flow regimes that can be assessed, UV-flow freezing, described in Section 2.3.3, has the potential to fill up this gap and complement μCT analysis.

2.4 Frontal polymerisation

2.4.1 The origins of frontal polymerisation

With the increasing incentive towards more sustainable processing of composites, frontal polymerisation has emerged as a promising out-of-autoclave method that delivers large reductions in environmental impact and processing time compared to traditional (thermal) consolidation methods [20], while often resulting in comparable or better polymer properties due to increased monomer conversions and/or cross-linking densities [20, 108, 109]. Frontal polymerisation is a self-sustaining reaction based on the localised reaction zone around a distinctly separated polymer-monomer resin interface [18]. Although other variants exist, e.g. isothermal frontal polymerisation that is governed by gradients in monomer concentration [19], thermal frontal polymerisation, driven by large thermal gradients present near the reaction zone, makes up the majority of the applications of frontal polymerisation as it offers significant advantages in polymerisation time, control and applicability [19]. It is therefore interchangeably referred to as frontal polymerisation and thermal frontal polymerisation in the continuation of this work. The existence of thermal frontal polymerisation in polymer systems was first reported in the early 1970s in the USSR, where Chechilo & Enikolopyan [110, 111] observed spontaneous polymerisation waves that formed in highly pressurised (>3500 atm) methyl methacrylate systems. Followed by two decades with limited progress, the research interest spiked in the late 1990s and early 2000s as the fundamental chemistry was developed for systems to undergo frontal polymerisation at ambient conditions while recent developments largely focus on its applications and engineering [18, 19]. A more detailed review on the historical origin of thermal frontal polymerisation is reported by Pojman [19].

2.4.2 The governing heat balance

The mechanism behind frontal polymerisation is governed by the heat released upon auto-catalytic polymerisation of a monomer system, hence forming a self-sustaining front that can propagate through the monomer resin (Video 1), if the exothermicity of the system is sufficient to overcome its own activation energy [17, 19]. The capability of a system to induce frontal polymerisation could therefore be directly linked to the local heat balance near the reaction zone. Assuming a situation where an enclosed domain is filled with a monomer resin formulation capable of undergoing frontal polymerisation and fibrous reinforcements, the local heat balance around a propagating front, schematically illustrated in Figure 2.7, is composed of four main terms:

1. **Polymerisation enthalpy**: Heat is solely generated by the exothermic polymerisation reaction and, by the use of highly reactive and exothermic resin systems, typically results in a localised temperature peak, often of >200°C, when rapidly transforming the monomer resin into a polymer.

2. **Thermal diffusion**: A significant heat flux imposed by the local thermal gradient be-

tween the hot, formed polymer and the cold monomer resin induces rapid heating of the neighbouring resin layer.

3. **Heat uptake by the mould**: Heat losses, e.g. to the mould environment, occur concurrent with the thermal diffusion. The importance of controlling the boundary conditions is discussed in Section 2.4.5.

4. **Heat losses to fibres**: The heat uptake by fibrous reinforcements increases with the filler content and therefore poses a significant complication for the production of high-V_f composite materials. The role of fillers is explained in more detailed in Section 2.4.6.

Initiation of a polymerisation front requires the local input of external energy, i.e. by UV-irradiation or the application of a heat source [19, 112], to activate the autocatalytic reaction mechanism. Propagating fronts are generally self-sustaining, and hence independent of the initial energy source, if the sufficient thermal energy is available to overcome the activation energy threshold for enabling the autocatalytic mechanism [17, 19]. However, fronts are known to quench if this condition is not met [18]. In reference to the local heat balance of Figure 2.7, it could thus be hypothesised that successful frontal polymerisation thus a minimum heat flux, dependent on the thermal gradient and thermal diffusivity around the front region, to rapidly induce autocatalytic polymerisation in an unpolymerised resin layer while concurrent heat losses would complicate the process.

Assuming an situation with a constant thickness, mould type and filler contents, a propagating front theoretically approaches a steady-state temperature that is directly related to the local heat balance. With the imposed heat flux, and hence the time required to provide sufficient energy to overcome the activation threshold, being directly dependent on the temperature gradient over the polymer-monomer resin interface, a correlation exists between the front temperature and propagation velocity [113]. The front temperature and velocity are therefore typically used to characterise propagating fronts [18]. Moreover, these direct relationships emphasise that control of the local heat balance is key in frontal polymerisation.

2.4.3 Frontal ring opening metathesis polymerisation

Frontal polymerisation has predominantly been reported in relation to free-radical polymerisation as it offers beneficial high reactivities and relatively moderate exothermicities, i.e. ~350 J/g [18, 114]. Frontal polymerisation in free-radical systems is driven by the Arrhenius-dependence of the reaction rates and requires a system to exhibit very high reaction rates at elevated temperatures and little or no reactivity at room temperature so as to allow for rapid heat release upon arrival of the front to overcome heat losses [19]. Although a multitude of free-radical-based systems capable of undergoing frontal polymerisation have been proposed [18, 19] since its discovery in the 1970s, Mariani et al. [115] were the first to report so-called frontal ring opening metathesis polymerisation (FROMP) that was later shown to be a well-performing and versatile system for the the production of polymer as well as

19
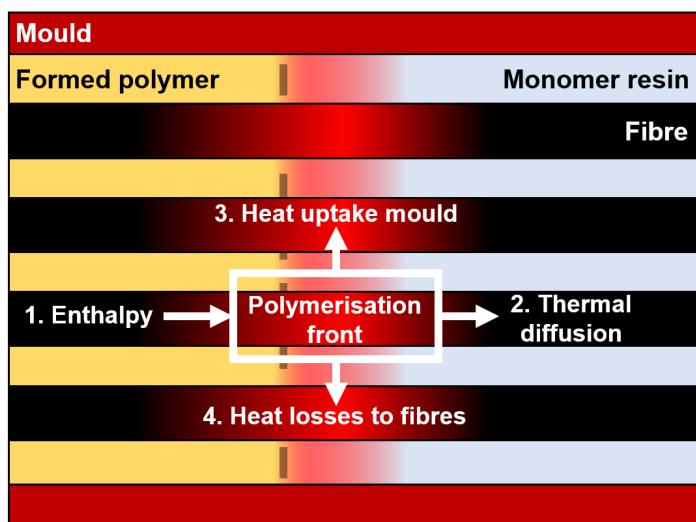
Figure 2.7: Schematic representation of local heat balance in frontal polymerisation being composed of 1. Generated enthalpy of polymerisation, 2. Thermal diffusion to boundary layer, 3. Heat uptake by the mould material and 4. Fibrous reinforcements.

FRPs [20, 21, 116]. FROMP systems are almost uniquely based on a (second generation) Grubbs' catalyst and dicyclopentadiene is mainly used as the primary monomer. Based on Ring Opening Metathesis Polymerisation [117, 118], FROMP requires the application of a thermal energy source while the exothermic heat originates from the opening of the dicyclopentadiene ring, forming a poly(dicyclopentadiene) (pDCPD) monomer.

The Arrhenius-dependence of FROMP, and other systems undergoing frontal free-radical polymerisation, brings complications in its processability since curing already proceeds at room temperature. Although taking place at a relatively low rate compared to the high-temperature frontal polymerisation, this precuring results in short pot lives that span in the order of minutes. The addition of phosphite inhibitors was shown by Robertson et al. [119] to significantly enhance the pot life, i.e. up to 30 hours, but comes at the cost of the frontal polymerisation performance since the frontal velocity was recorded to decrease with the inhibitor concentration. Further extension of the FROMP system to enable UV-initiation of fronts was proposed by the addition light-absorbing fillers [120] or dedicated photoactive compounds [121, 122] while the tuning of the mechanical properties was demonstrated by co-polymerisation [114, 123–125]. Moreover, recent reports [116, 124] have demonstrated the possibility to facilitate easy deconstruction, i.e. recycling, of polymers produced by FROMP.

Although highly system-dependent, FROMP systems are reported to propagate at velocities of ~0.5-1.4 mm/s with temperatures generally in order of 150°C [20, 114] and in some cases up to 215°C [18]. Robertson et al. [20] showed that tensile properties of FROMP-produced pDCPD polymer were comparable to those produced by an oven-curing procedure. Young's modulus of pDCPD is reported to be ~2 GPa for both processing strategies while the tensile strength was slightly lower when produced by FROMP. The same was true for the fracture toughness of ~3

MPa·m$^{1/2}$, which was found to be significantly higher than that of an oven-cured commercial epoxide-based resin system. Combined with an elevated glass transition temperature (T_g) of up to 172°C, the beneficial use of FROMP systems can be foreseen in wide range of applications as has been already demonstrated for e.g. additive manufacturing [126–128] or the production of functional materials [129–131]. Its applicability for the industrial production of FRPs could be limited by the inherent short pot lives.

2.4.4 Frontal polymerisation of epoxide systems

Epoxide systems have been widely applied for the production of thermoset FRPs due to their good mechanical properties over other thermoset polymers while the advantages of undergoing a cationic reaction pathway, not being inhibited by the presence of oxygen and able to undergo dark-curing [132] in contrast to free-radical polymerisations, have simultaneously led to intensive investigations on cationic UV-photopolymerisation. Epoxide systems moreover offer the advantage of a low curing shrinkage [133, 134], which is reported to be in the order of 2-6% and can be further reduced by optimisation of the monomer composition [135], that can limit the formation of residual stresses [136] and enhance the retention of the polymer geometry or morphology.

To overcome the inherent thickness limitations of the cationic UV-photopolymerisation due to the attenuation of UV-light [137, 138], investigations of inducing frontal polymerisation in systems undergoing cationic photopolymerisation commenced in the early 2000s with a specific focus on its initiation by UV-light. Crivello et al. [139] first observed frontal polymerisation in a cationic system composed of oxetane and oxirane monomers and reported reaction fronts with temperatures up to 169-232°C in the presence of a diaryliodonium salt cationic initiator after UV-irradiation of the sample surface, followed by thermal initiation by a heating wire. In subsequent reports [140, 141] they were moreover able to relate the front characteristics to the reactivity of the used monomer. Investigations were however limited to low molecular weight monomers possessing high mobilities and reactivities while systems only depending on onium salts were assumed to be incapable of inducing frontal polymerisation in the more bulky monomer systems that are typically used in the thermoset FRP industry.

2.4.4.1 Radical induced cationic frontal polymerisation

To overcome this limitation, Mariani et al. [142] were the first to demonstrate so-called radical induced cationic frontal polymerisation (RICFP). This reaction pathway was inspired by radical induced cationic polymerisation (RICP) [143] where the presence of a free-radical (photo-)initiating compound in combination with a cationic initiator can strongly enhance the reaction kinetics during cationic photopolymerisation. This mechanism can be transformed into an autocatalytic reaction, i.e. RICFP, in the presence of a free-radical initiator that can be thermally activated at temperatures below that of the cationic initiator and given that the system reactivity and heat release are sufficient to maintain the local temperature above the
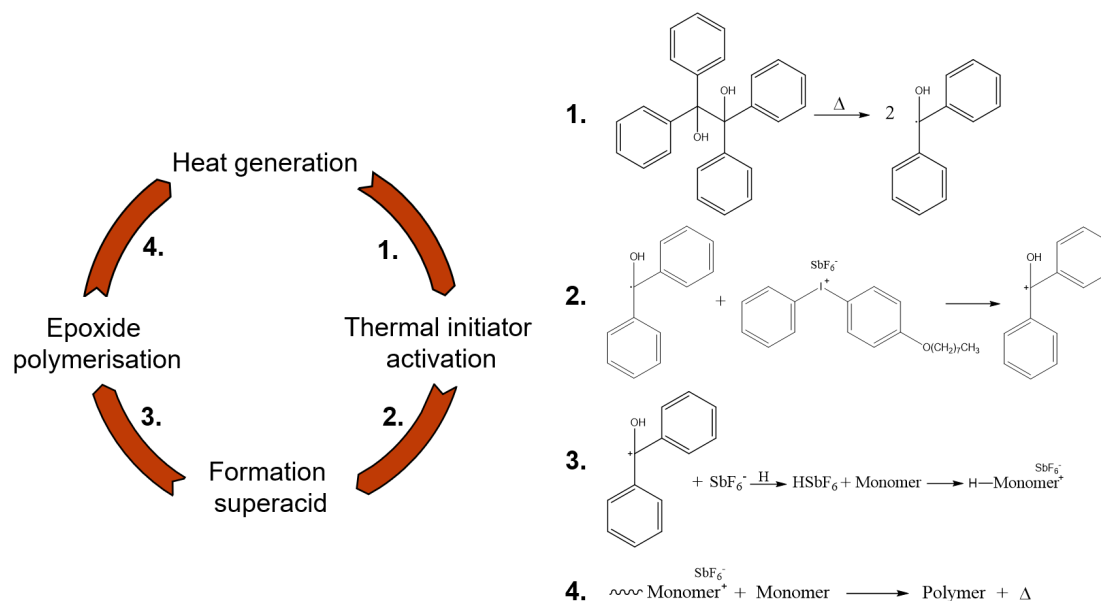
Figure 2.8: Schematic overview of the autocatalytic RICFP process. The key steps in this process are: 1. Thermal activation of the thermal initiator, 2. Formation of a carbocation by interaction between the thermal initiator-derivative and the photoinitiator, 3. Initiation of epoxide polymerisation by a superacid resulting from the formed carbocation and 4. Exothermic polymerisation of epoxide monomer.

dissociation temperature [142]. Figure 2.8 shows a schematic yet simplified representation of the autocatalytic RICFP following the pathways reported by Refs. [142, 144–146]. High local temperature would first induce the thermal dissociation of the free-radical initiator; the dissociated derivatives, containing a radical active centre, can subsequently be oxidised to a carbocation by interaction with a cationic initiator. The formed carbocation then forms a superacid [146] by extracting a proton from the monomer or solvent that can commence the polymerisation of epoxide monomers. The consequent highly exothermic ring opening polymerisation provides thermal energy to the system, allowing for further dissociation if the aforementioned activation energy is overcome, hence making it autocatalytic.

The RICFP mechanism brings several advantages compared to FROMP, which are largely due to its dual-initiator configuration. First of all, the system is responsive to both thermal and UV-triggers with equal efficiency for initiation of the autocatalytic mechanism [108]. The application of a thermal source would allow for direct dissociation of the free-radical initiator, which is therefore referred to as thermal initiator in the continuation of this work. Cationic initiators used for RICFP are generally also photoresponsive [147] and could hence initiate polymerisation upon UV-irradiation, as will be further elaborated upon in Section 2.4.4.2. RICFP systems are moreover typically independent of Arrhenius kinetics as their initiation threshold is solely dependent on the thermal dissociation of the thermal initiator, resulting in excellent pot lives of over one month while being kept at 50°C [108].
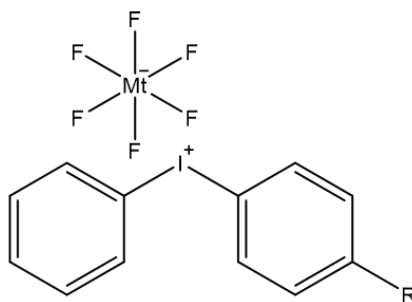
Figure 2.9: Chemical structure of a diaryliodonium salt cationic photoinitiator.

2.4.4.2 Tuning of the UV-response

With its origin in the field of UV-photopolymerisation, reports on RICFP have to-date mainly focused on UV-irradiation to initiate frontal polymerisation. Onium salts [148, 149] make up the majority of cationic initiators in both fields [147] and are made up of an organic cation and an inorganic anion, which each govern specific properties of the initiator [134, 150]. The cation determines the light absorbance characteristics such as the photosensitivity and quantum yield while also partially determining the thermal stability of the compound [147]. The anion on the other hand predominantly determines the polymerisation rate and degree [148, 150] as it mainly influences the reactivity and the strength of the formed superacid and reactivity of the onium salt. Pioneered by Crivello et al. [151], diaryliodonium salts have been a widely used class of photoinitiators for UV-photopolymerisation because of their good thermal stability, tuneable reactivity and optical transparency of the resulting polymer [147]. The general chemical structure of diaryliodonium salts is shown in Figure 2.9 with the R-group representing long alkyl chains that can reduce the toxicity and increase the solubility of the photoinitiator [152]. Commonly used anions are, in order of increasing reactivity, $BF_4^- < PF_6^- < AsF_6^- < SbF_6^-$, which are all capable of forming superacids. Tetrakis(perfluoro-tert-butyloxy)aluminate (I-Al) has moreover been identified by Klikovits et al. [153] as a promising anion with resulting reactivities that outperform photoinitiators based on the common anions while Taschner et al. [154] identified several other potentially promising anions that further increase the photoinitiator reactivity.

As illustrated by the reaction pathway in Figure 2.10, absorbance of UV-light by the diaryliodonium salt results in the excitation and subsequent cleavage of the cation to finally form a strong acid that promotes the cationic polymerisation of an epoxide monomer resin [144]. Efficient UV-initiation requires the absorbance spectrum of the photoinitiator to match that of the incoming UV-light. Typical absorbance spectra of diaryliodonium salts are in the range of 220-350 nm [134], depending on the chemical structure of the cation. Photosensitisation is regarded as an efficient strategy to expand the absorbance spectrum of an UV-photopolymerisable resin formulation, in specific cases even up to the visible spectrum [147]. Photosensitisers exist in a wide range, undergoing different sensitisation mechanisms and with varying compatibilities with onium salt types, as extensively reviewed by Malik et al. [147].

$$\text{Ar}_2\text{I}^+ \text{X}^- \quad \xrightarrow{h\nu} \quad \left[\text{Ar}_2\text{I}^+ \text{X}^-\right]^{\ddagger} \quad \longrightarrow \quad \left\{ \begin{array}{l} \text{Ar}\dot{\text{I}}^+ \text{X}^- + \ \dot{\text{Ar}} \\ \text{ArI} + \ \dot{\text{Ar}}^+ \text{X}^- \end{array} \right\} \quad \longrightarrow \quad \text{HX}$$

$$\text{HX} + \text{M} \quad \longrightarrow \quad \text{H-M}^+\text{X}^- \quad \xrightarrow{\text{M}} \quad \text{H-(M)}_n\text{M}^+\text{X}^- + \underset{\text{(heat)}}{\triangle}$$
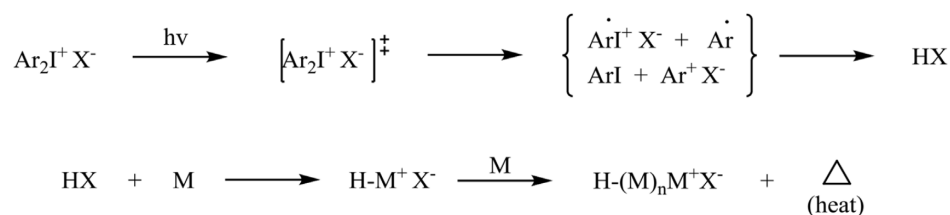
Figure 2.10: Chemical pathway for UV-initiation of epoxide polymerisation by a diaryliodonium salt (Source: [144]).

Isopropylthioxanthone (ITX) was identified as a compatible photosensitiser for indirect photolysis of diaryliodonium salts via electron transfer from the triplet state of ITX to the iodonium salt [155]. Caglar et al. [47] employed ITX to expand the wavelength spectrum to above 400 nm to allow UV-photopolymerisation through PMMA while Klikovits et al. [153] reported that a small amount of ITX was sufficient to induce UV-photopolymerisation in a system consisting of their novel I-Al photoinitiator and bisphenol A diglycidyl ether (BADGE). Bomze et al. [108] studied the use of ITX to tune the UV-response of a BADGE-based RICFP system and reported that concentrations below 0.2% allowed for improved UV-initiation capabilities while increased concentrations were found to induce shielding. The presence of ITX at these concentrations was found to not affect the front characteristics during RICFP propagation.

2.4.4.3   Tuning of the autocatalytic front propagation

Once the activation threshold is overcome, the autocatalytic RICFP mechanism (Figure 2.8) is enabled, resulting in a self-sustaining polymerisation front that is maintained providing that sufficient energy is available to overcome the activation energy threshold [17, 19]. As previously explained in Section 2.4.4.1, the autocatalytic phase is an interplay between a cationic photoinitiator, a free-radical thermal initiator and an epoxide monomer and hence each of these components has a specific influence on the resulting front characteristics.

In addition to its largely determining role on the UV-response of a RICFP resin, an increased reactivity, i.e. strength of the formed superacid, of the photoinitiating compound is reported to enhance the reaction rate during the frontal propagation phase while the redox potential should be sufficient to induce the formation of a carbocation out of the free-radical thermal initiator [147]. Diaryliodonium hexafluoroantimonate photoinitiators, and in particular p-(octyloxyphenyl)phenyl iodononium hexafluorostibate (IOC-8 SbF$_6$) [108, 144, 146, 156–158] are reported to be sufficiently reactive and possess the required redox potential to induce self-sustaining frontal polymerisation. Increasingly reactive photoinitiator compounds were found beneficial for the front characteristics during RICFP processing. Knaack et al. [145] compared the front velocity and temperatures of resin systems containing IOC-8 SbF$_6$ or I-Al as photoinitiators. At a concentration of 1 mol%, the system containing I-Al exhibited front velocities that were increased by 250% compared to those of IOC-8 SbF$_6$-containing systems while the minimum layer thickness that could be successfully cured reduced by a factor four.

Gachet et al. [159] studied a range of novel sulfonium-based initiators capable of undergoing RICFP and reported front velocities and temperatures up to 2.2 mm/s and 270°C, which exceeded those reported by Knaack et al. [145]. Taschner et al. [154, 160] identified promising photoinitiators for RICFP ranging from a wide range of initiator classes. The developed bismuthonium-based initiator showed strong improvements in storage capability compared to IOC-8 SbF$_6$, although this came with a reduction in front characteristics. Iodonium borate initiators showed comparable front characteristics and resulting curing degrees as systems containing I-Al while tuning of the anion had a direct influence on the colour and transparency of the formed polymer. Despite promising results, novel photoinitiators with increased reactivities are to-date still finding their way into the field due to limited commercial availability with IOC-8 SbF$_6$ remaining the more conventional choice of cationic photoinitiator.

The thermal initiating compound plays a crucial role in RICFP since its reactivity affects both the reaction rates of a given RICFP resin system as well as the onset temperature for activation of the autocatalytic mechanism [145]. Peroxides are known to be efficient free-radical generators, e.g. for initiation of free-radical polymerisation, and dibenzoyl peroxide was therefore first proposed as thermal initiator for RICFP [142] while Groce et al. [158] used an 1,1-iso(tert-butylperoxy)-3,3,5-trimethylcyclohexane peroxide initiator, more commonly known under its commercial name Luperox 231, to induce RICFP in vinyl ether resins. Bomze et al. [146] investigated the structure-property relations of various thermal initiator types. They explored a range of peroxide initiators and found that the majority was insufficiently reactive to induce RICFP in a BADGE resin while others showed bubble formation that was partially attributed to decarboxylation of the formed radical species. Carbon-carbon (C-C) labile compounds were found highly beneficial for RICFP due to their high reactivity combined with an excellent stability, which was hypothesised to be due to the possibility for formed radicals to recombine if not reacted [146, 161], and the absence of gaseous byproducts. The reactivity of the thermally induced radicals was found dependent on the sidegroups of the C-C labile compounds and the presence of an oxygen atom was needed to produce sufficiently reactive radicals to sustain RICFP. 1,1,2,2-Tetraphenyl-1,2-ethanediol (benzopinacol) was identified as the most promising free-radical thermal initiator and was used in the majority of following studies on RICFP systems [108, 144, 145, 156, 157, 162].

Alternatively, the use of boron trifluoride amine complex thermal initiators has been proposed by Scognamillo et al. [163, 164] and Zhou et al. [165], as it could successfully induce a frontal polymerisation wave while front propagation properties were controlled by its concentration. The presence of an amine initiator, a Brønsted base, inhibits its compatibility with onium salts as it would directly scavenge formed protons and hence this is incompatible with RICFP and unable to initiate frontal polymerisation by UV-irradiation. Zhou et al. [165] overcame this latter limitation by using two separate solutions. Initiation by UV-light would first take place in the photoactive solution containing a iodonium salt after which the front propagates to the second resin solution containing the amine complex thermal initiator. Although this novel approach of combining two separate systems for frontal polymerisation could offer benefits for localised tuning of the front characteristics, it would introduce complications

in the context of FRP processing and alternative (thermal) initiator configurations are thus preferred.

In an addition to being a largely determining factor for the resulting polymer properties, the monomer composition has been used to control the front propagation of a RICFP system. Most reports on RICFP have based their resin formulations on BADGE [22, 108, 145, 146, 156] or 3,4-epoxycyclohexylmethyl-3',4'-epoxycyclohexane carboxylate (ECC) [142, 159, 165, 166] since these monomers are frequently applied in industrial applications due to their good mechanical properties while few reports [144, 157] were able to successfully induce RICFP in commercial epoxide resins. The increased reactivity and exothermicity, reported up to 650 J/g [159], of ECC monomer allows for front formation with less reactive initiators [146]. Demonstrations of RICFP in ECC-based resins have resulted in front velocities ranging from 0.3-4.4 mm/s combined with exceptionally high front temperatures of up to 300°C [142, 146, 159]. Insufficient control of these front temperatures was however found to result in undesired foaming [146, 166] that degrades the resulting polymer quality [167]. The lower reactivity of BADGE systems reduces its front characteristics. Bomze et al. [146] reported a ten-fold decrease of the front velocity compared to an ECC based formulation with similar initiator concentrations. Increased velocities of up to ~0.7-1.7 mm/s were reported when using the more reactive I-Al cationic initiator at different concentrations [22, 145, 156]. Front temperatures remained below 210°C [145].

The addition of diluents has been envisaged to alter the reaction rates and thereby the front characteristics of the system. Dung Tran et al. [22] and Knaack et al. [145] assessed the influence of adding 20 mol% of various diluents on the front characteristics of a BADGE resin system. They observed that lower molecular weight additives simultaneously reduced the resin viscosity and also accelerated the polymerisation kinetics, resulting in a strong increase of the cure characteristics, e.g. the front velocity, minimum layer thickness and the polymerisation enthalpy, although coming at the cost of a reduced T_g. (3-Ethyloxetan-3-yl)methanol was proposed as the preferred diluent leading to a strong increase in cure characteristics and a nearly complete curing degree, while limiting the T_g decrease by ~10-15°C. Malik et al. [162] reported on the use of ECC as a diluent for two types of BADGE-based resin formulations and observed that the improved processability due to decreased viscosity came at the cost of the resulting monomer conversion and T_g. Liu et al. [167] reported severe degradation of the formed polymer when using ethylene glycol diglycidyl ether as an additive for the RICFP of BADGE, which emphasises the need for thermal control when increasing the reactivity of the system.

The concentration of reactive species has been a proven way to control the frontal polymerisation behaviour of RICFP systems, i.e. by adjusting the heat generation of the local heat balance. Mariani et al. [142] and Knaack et al. [145] observed that a minimum initiator concentration is required to successfully induce frontal polymerisation. Front velocities are reported to increase with both increasing photo- [142, 145, 158] and thermal initiator contents [108, 142]. Significant differences exist however between the observed trends. For example, Mariani et

al. [142] observed that an increased diaryliodonium salt concentration first increased the front velocity of an ECC resin followed by the formation of a plateau while Groce et al. [158] reported continuous increases for both the front velocities and temperatures of a vinyl ether system undergoing RICFP. Knaack et al. [145] on the other hand observed a minor inflexion in the front velocity exhibited by their system composed of BADGE, I-Al and benzopinacol with front temperatures reaching a plateau. Although a better agreement was found for the role of the thermal initiating compound [108, 158], the compared behaviour suggests that the relationship between the initiator concentration and the resulting front characteristics are highly dependent on the resin system that is used.

The use of RICFP is reported to be beneficial for the resulting polymer properties, compared to e.g. oven-curing. Bomze et al. [108] compared BADGE polymer produced by RICFP with anhydride-cured BADGE noted that both the tensile properties, i.e. Young's modulus, tensile strength and failure strain, and the T_g was increased from 154°C to 168°C. This difference is likely explained by the absence of a cross-linking agent that is incorporated into the network, e.g. inducing similar changes as the aforementioned low molecular weight cross-linking agents. A microstructural study carried out by Švajdlenková et al. [168] moreover revealed that the bulk density of RICFP-produced polymer was slightly higher than that produced with a curing agent. The combination of beneficial resulting properties and an excellent storage stability combined with fast propagation rates and a tunable resin reactivity thus underlines the potential of RICFP as a promising strategy for the production of epoxide polymer and composites, further discussed in Section 2.4.6.1, although increased control of the heat generation is required to avoid potential degradation of the resulting polymer.

2.4.5   Boundary conditions in frontal polymerisation

Controlling the boundary conditions, and hence the term accounting for heat losses to the environment in Figure 2.7, to shift the heat balance in frontal polymerisation has been merely investigated to-date. Knaack et al. [145] were able to define a minimum layer thickness of a RICFP resin where frontal polymerisation could be successfully sustained and observed that this limit could be reduced by increasing the resin reactivity, i.e. heat output rates. The existence of a minimum layer thickness could be understood as a direct relation between the boundary heat losses to the surface-to-volume ratio of a resin system. Datta et al. [169] observed a similar relationship and observed that a decreasing thickness results in reduced front characteristics. Tiani et al. [170] and Gao et al. [171] observed a thickness limitation in their numerical studies on free-radical frontal polymerisation and were able to relate the capability of a system to sustain a front and the formation of oscillating instabilities, as is further discussed in Section 2.4.7.

The importance of the surface-to-volume ratio of a propagating front could be explained by the heat losses mainly acting at the sample-mould boundary, as was confirmed investigation of Goli et al. [172]. They moreover suggested that the use of an insulating mould configuration

is beneficial for the front characteristics, which was in line with the observations of Gao et al. [171]. Naseri & Yourdkhani. [173] compared three increasingly insulating mould types for the production of pDCPD-based carbon FRPs and recorded increased front temperatures at the interface of highly insulating foam and insulating glass mould configurations that exceeded those recorded in a thermally conductive aluminium mould by ~50-100°C. Moreover, the degree of cure was found to follow the same trend although differences were in the order of the statistical uncertainty. Centellas et al. [21] however reported front velocities in a pDCPD-based carbon FRPs with two converging fronts to be higher when conductive boundary conditions (i.e. a preheated aluminium plate placed in thermal contact with a vacuum bag in a VARI setup) were imposed. Increased front temperatures were recorded when insulating boundary conditions (i.e. replacing the aluminium plate by an insulating tool) were used, resulting in a reduced energy consumption. The increased front temperatures however also resulted in limited thickness control at the location where fronts merged, that was subsequently prone to fracture. While these studies indicate a crucial role of boundary effects in frontal polymerisation-assisted FRP, the exact role of boundary heat losses during front propagation remains poorly understood and no optimised systems have been proposed to-date.

2.4.6 Frontal polymerisation of composites

2.4.6.1 Self-sustaining frontal polymerisation

The addition of fillers to a frontal polymerisation system could induce complications due to the significant heat uptake by reinforcements, i.e. acting as an additional heat loss term in the local heat balance, combined with a reduced resin volume and hence a reduced overall heat output. The limitations introduced by fillers are particularly apparent when fronts are initiated by UV-irradiation since the often opaque nature of conventional reinforcements leads to extensive attenuation, therefore strongly reducing the light penetration depth, in some cases only allowing for thermal initiation of frontal polymerisation [108]. Translucent fillers, e.g. glass, are slightly less affected by this phenomenon since light is scattered from the filler particle surface [146] and, despite a strong increase of the required initiation time [156], UV-activated RICFP was demonstrated in the presence of SiO_2 [156] and ZrO_2 particles [145].

The nature of the filler material strongly influences frontal polymerisation. The high thermal conductivity of conductive fillers made out of e.g. carbon [175, 176] or metal [177, 178] is generally beneficial for front progression by transporting heat from the front towards the neighbouring monomer region [175]. Numerical work presented in Refs. [174, 176, 177] suggested however that this was only true for low V_fs, e.g. below 20% for carbon FRPs, as illustrated in Figure 2.11, after which the heat uptake by the fillers becomes dominant, slowing down front propagation. Insulating fillers are reported [108, 145, 156] to generally reduce the front velocity, which was also observed numerically for glass FRPs. Dung Tran et al. [22] carried out an experimental study on the role of a wide range of fillers in a BADGE/I-Al/benzopinacol system capable of RICFP. In contrast to the other studies, they did not observe the expected
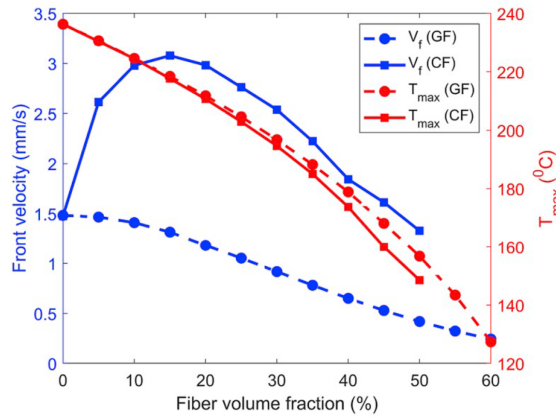
Figure 2.11: Numerical estimations of front velocities and temperatures in carbon and glass FRPs as a function of the V_f (Source: [174]).
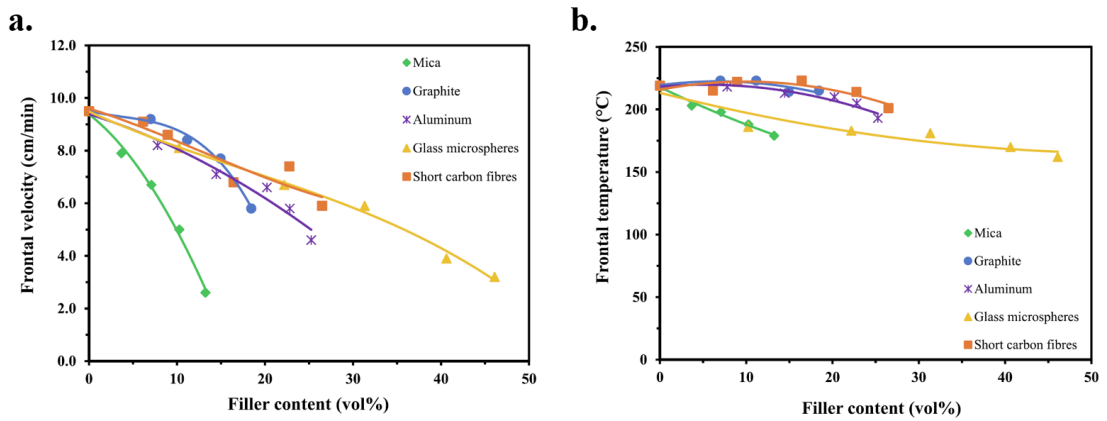
Figure 2.12: Front characteristics with of an RICFP resin with different fillers added at a range of concentrations: a) front velocity and b) front temperature (Source: [22]).

trends since front velocities in Figure 2.12a decreased with increasing V_f independent of the thermal nature of the filler while the front temperature in Figure 2.12b showed an initial slight increase up to ~15% V_f for the conductive fillers followed by the expected gradual decrease. A significant difference of ~20% in the maximum V_f that could be successfully polymerised was observed between systems filled with glass microparticles and those filled with conductive fillers, which was attributed to its beneficial insulating nature combined with differences in particle morphology.

The maximum V_f that could successfully sustain a front is a central consideration in the reports on frontal polymerisation-assisted FRP processing, which has received a significant research interest over the last years. Robertson et al. [179] were the first to demonstrate the possibility of producing FRPs using a FROMP resin system and reported a maximum V_f of 51% while tensile properties were comparable to those produced by oven-curing of the FROMP resin and a commercial resin system with a >99% reduction in energy consumption and

environmental input. Centellas et al. [21] were able to slightly increase the maximum V_f to 52.0% and simultaneously reported increased curing degrees, i.e. 88.2% compared to 80.5% by Robertson et al. [180].

While the first studies mainly assessed the compatibility of RICFP systems with different fibre types [144, 157, 181], later developments have shown the potential of RICFP as a technique to produce FRPs. Using the aforementioned resin system, Dung Tran et al. [22] were able to produce woven carbon FRPs with V_fs of about 35% and recorded tensile properties to be similar to those produced by with anhydride-cured BADGE resin while also resulting in increased curing degrees. Gachet et al. [159] used their novel sulfonium-based initiator system and an ECC monomer resin and were able to induce fronts in carbon FRPs with V_fs of around 40% with exceptionally high front velocities of over 2.15 mm/s although being recorded in through-thickness direction.

2.4.6.2 Frontal polymerisation driven by external heat input

Although showing promising initial results, the maximum V_f of FRPs that could be produced by self-sustaining polymerisation fronts remains below the industrially relevant range of V_fs, i.e. >55%. Shifting the heat balance by the addition of an external energy input has been employed in several studies towards further increasing the V_f limit. Resistive heater mats placed in thermal contact with the uncured carbon FRP [20] were shown to be beneficial to induce frontal polymerisation in through-thickness direction with front temperatures increased by ~20-30°C. This method was later employed by Lloyd et al. [116] and Parikh et al. [182] to increase the maximum V_f that could be successfully polymerised by a FROMP system to 64.8%. Fronts were reported to initiate autonomously at a preheating temperature of 70°C which resulted in a temperature increase of ~50°C combined with a curing degree of 80% at an energy input of 9 kJ for a 12×10 cm FRP [182]. Increased curing degrees, i.e. 89%, and T_gs, by ~65°C, were reported when the part was heated to 200°C after ignition of the front, i.e. simulating a post-curing procedure, while increasing the required energy input to 48 kJ [182]. The latter strategy is similar to the method proposed by Malik et al. [183] who prepared 55% V_f carbon FRPs using a RICFP resin system by heating the mould configuration to 150°C for 30 minutes. Although no reports on the energy consumption were made, the applied curing time was over five times that reported by Parikh et al. [182] and the proposed process was therefore likely more energy consuming.

Naseri & Yourdkhani proposed an elegant way to shift the local heat balance in a pDCPD resin system by the integration of a nanostructured heater, i.e. a layer of bucky paper, at the top surface of a carbon FRP. As illustrated in Figure 2.13, the application of an electrical current and subsequent resistive heating by the integrated heater increased the local temperature until a front was initiated in through-thickness direction. Although the V_f of the resulting FRPs has not been reported, this strategy appeared to be beneficial as nearly complete monomer conversion was achieved for the 10×10 cm carbon FRPs after curing for one minute and at a total energy demand of 4.49 kJ. Moreover, the heating temperature of the nanostructured
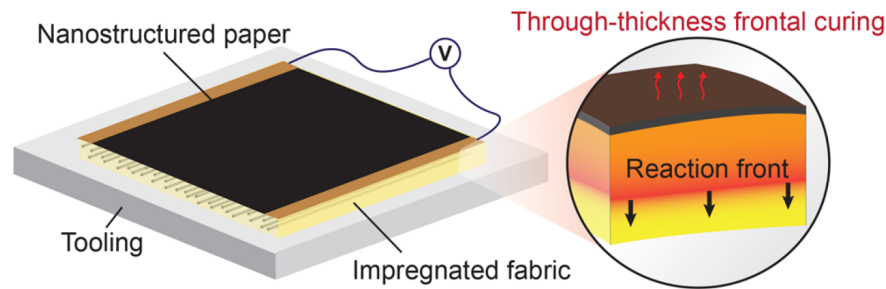
Figure 2.13: Schematic representation of through-thickness frontal polymerisation of FRPs induced by integrated nanoheaters (Source: [173]).

heaters could be tuned via the applied voltage while their presence was suggested to have a further use for e.g. de-icing during the use-phase of the FRP. Their implementation in carbon FRPs however requires an adjacent insulating, e.g. glass fabric, layer which hence significantly limits the design freedom for the resulting composites. Although having shown a promising potential to overcome the current limitations of frontal polymerisation-assisted FRP processing, all the described solutions require a continuous heat input that could be expected to scale with the part size, thus reducing the advantage of frontal polymerisation as a versatile, low-energy FRP processing method.

2.4.7 Instabilities in frontal polymerisation

Travelling frontal polymerisation waves are prone to a variety of instabilities, e.g. hot spots, spin-modes or fingering [168, 184–187], that induce deviations from the steady-state front characteristics [19]. The occurrence of a certain type of instability is highly related to the geometrical configuration of a frontal polymerisation system as well as its propagation direction. For example, ascending fronts in a vertically aligned domain are reported to be vulnerable for buoyancy-driven convection, where heated monomer resin from near the front region rises and is replaced by colder monomer resin, resulting in a continuous circular resin flow as the front propagates [188]. On the contrary, descending fronts in the same vertical domain, i.e. coincident with gravity, could show convective instabilities if the resulting polymer is in a liquid state, making the more dense, formed polymer sink ahead of the front due to so-called Rayleigh-Taylor effects [18, 189].

Fronts propagating in-plane are reported to show periodically oscillating front temperatures, illustrated in Figure 2.14, as a result of thermal instabilities induced by the boundary conditions of a frontal polymerisation system [170, 177, 190, 191]. Goli et al. [191], Gao et al. [171] and Tiani et al. [170] observed this behaviour in thin resin layers in an enclosed mould configuration while Lloyd et al. [190] and Kumar et al. [192] employed it to produce patterned polymer samples. The appearance of these oscillations was related to a situation where the exothermic heat release rate is comparable to the thermal dissipation rate [171, 190]. Gao et al. [171] hypothesised that this cyclic behaviour was a result of rapid dissipation of the
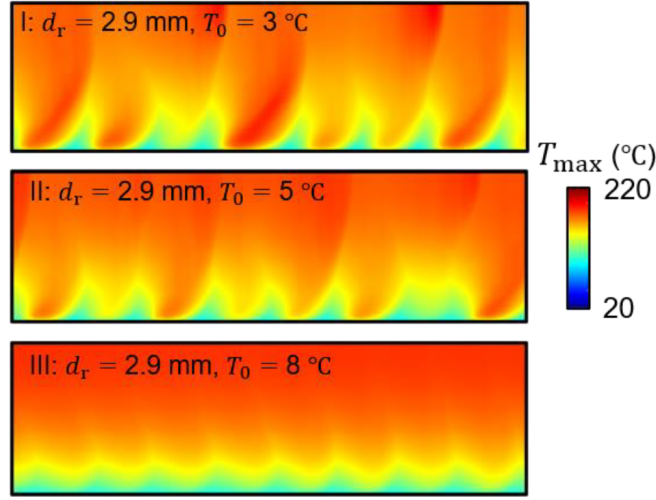
Figure 2.14: Exemplary temperature fields demonstrating oscillatory thermal instabilities generated with different initial temperatures (Source: [171]).

reaction heat to the mould environment that is insufficient for stable continuation of the front. The resulting drop in front temperature would then suppress both the chemical reaction and thermal transport, after which the system slowly recovered after the delayed enabling of the autocatalytic mechanism. Repeating of this cycle would then result in the observed oscillations. This was in line with the reasoning of Tiani et al. [170] who related the formation of spatial oscillations to the temporal variation of thermal diffusion at the boundary resin-mould interface and observed the period behaviour occurring at a specified range of Biot numbers.

The Zeldovich number (β_z), initially proposed to describe the bifurcation behaviour of flame propagation in gas-phase reactions [18], has been used to describe the occurrence of thermal instabilities in frontal polymerisation as [19, 191]:

$$\beta_z = \frac{T_m - T_0}{T_m} \frac{E_{eff}}{RT_m} \tag{2.4}$$

where T_m and T_0 denote the front and initial temperatures, respectively, and E_{eff} the effective activation energy of the autocatalytic mechanism. A critical Zeldovich number ($\beta_{z,c}$) exists above which periodic oscillations of the front temperature are observed [184, 193]. Masere et al. [194] reported a $\beta_{z,c}$ of 8.4 for a methyl methacrylic acid system while Goli et al. [191] found a $\beta_{z,c}$ of 11.37 for their FROMP-pDCPD system. It could thus be expected from Equation 2.4 that the onset of thermal instabilities could be delayed by either decreasing the initial temperature, increasing the front temperature or increasing the activation energy.

Lloyd et al. [190] however reported the incompatibility of the Zeldovich number for more complex reaction pathways and instead found a good descriptor in the ratio of reaction (P_R) and diffusion (P_D) defined as [171]:

$$\varphi = \frac{P_R}{P_D} \quad \text{with} \quad P_R = \rho_r H_r A \exp\left(-\frac{E_a}{R\overline{T}}\right), P_D = \kappa_r \frac{\overline{T}}{L_\theta^2} \tag{2.5}$$

with ρ_r the resin density, H_r the polymerisation enthalpy, A the Arrhenius frequency factor, E_a the activation energy and $\overline{T}) = 0.5(T_0 + \overline{T_f})$ the average between initial and front temperatures. Following this descriptor, stable fronts would be characterised by a $\varphi \gg 1$ while fronts would attenuate if $\varphi \ll 1$. Intermediate φ of ~1 were found to produce the described oscillating thermal behaviour [171, 190]. The exact range on which this behaviour could be observed is likely dependent on the resin system since Lloyd et al. [190] observed undulations at φ values as low as 0.4-0.5.

2.5   Frontal polymerisation modelling

The highly complex and fast reaction kinetics of frontal polymerisation complicate the experimental observations that can be made. For that reason, the development of complementary numerical models has both been found beneficial for understanding the ongoing phenomena and will be essential for the effective process design during the industrial implementation of frontal polymerisation-assisted FRP processing.

2.5.1   Reaction-kinetics modelling

Models describing polymerisation kinetics can be roughly divided into two main classes, namely mechanistic and phenomenological models. While mechanistic models bring the advantage of capturing all the individual reaction steps, they often bring complications for the derivation and application of the models [195], especially for fast and rapid reaction mechanisms such as RICFP. Phenomenological models on the other hand allow for a description of the ongoing kinetics by a single equation and are therefore more practical for engineering purposes [196] but require experimental characterisation at each variation of the resin system while in some situation [197], e.g. diffusion-controlled effects after vitrification [195], they are unable to accurately capture ongoing phenomena [197]. Phenomenological models are therefore often applied to describe complex polymerisation kinetics so as to overcome potential complications in the derivation and application of mechanistic models [195]. Coupled with the heat equation with an additional heat generation term, thermal-kinetic models for systems without fillers have their general form as the following set of partial differential equations:

$$\begin{cases} \kappa \nabla T + \rho H_r \dfrac{\partial \alpha}{\partial t} = \rho C_p \dfrac{\partial T}{\partial t} & \text{(2.6a)} \\[2mm] \dfrac{\partial \alpha}{\partial t} = k(T) f(\alpha) & \text{(2.6b)} \end{cases}$$

where Equation 2.6a is the modified heat equation with κ denoting the thermal conductivity, T the temperature, ρ the density, H_r the polymerisation enthalpy, $\frac{\partial \alpha}{\partial t}$ the conversion rate and C_p the heat capacity. Equation 2.6b describes the reaction-kinetics model with $k(T)$ denoting the temperature-dependent rate constant and $f(\alpha)$ the kinetics model. The rate constant in Equation 2.6b is mostly assumed to follow Arrhenius behaviour and is hence defined as:

$$k(T) = A \exp\left(\frac{-E_a}{RT} \right) \tag{2.7}$$

with A referring to the Arrhenius frequency factor, E_a the activation energy, R the gas constant and T the temperature. The phenomenological nature of the kinetics model results in a variety of descriptions that could be applied. Table 2.1 lists a number of models frequently applied in

Table 2.1: Overview of kinetics models used in relation to epoxide or frontal polymerisation.

Type	$f(\alpha)$
nth order [175, 208, 209]	$(1-\alpha)^n$
Prout-Tompkins	$(1-\alpha)^n \alpha^m$
nth order-Prout-Tompkins [210, 211]	$(1-\alpha)^n(1+k_{cat}\alpha)$
Prout-Tompkins with diffusion term [20, 212]	$(1-\alpha)^n \alpha^m \frac{1}{1+\exp[c_d(\alpha-\alpha_c)]}$

relation to modelling of the curing kinetics of epoxide polymerisation or frontal polymerisation. Model parameters are typically derived using differential scanning calorimetry (DSC) and a number of model-free kinetic methods are well-established for estimation of the parameters of Equation 2.7, e.g. the Flynn-Wall-Ozawa method [198] described in ASTM standard E698. Derivation of the remaining parameters related to the kinetics model is traditionally done using isothermal DSC analysis, e.g. via the Kissinger method [199, 200]. This is however complicated for fast curing resin systems where the reaction time is in the order of the inherent time lag for heating the sample at the start of the measurement, potentially omitting a significant part of the ongoing cure reaction [201–203]. Alternatively, several studies have fitted kinetic models on dynamic DSC measurements, i.e. where a constant heating rate is imposed [201, 203–206], resulting in accurate model predictions although complications occur when vitrification is observed [201, 205, 207].

More accurate descriptions for resin systems that show vitrification were demonstrated by Bernath et al. [201], who compared the Kamal-Malkin model [213] with the Grindling model [214] for the description of fast curing epoxide resins. The Kamal-Malkin model is defined as:

$$\frac{d\alpha}{dt} = \left(k_1 + k_2\alpha^m\right)(1-\alpha)^n \tag{2.8}$$

with k_1 and k_2 referring to Arrhenius reaction rate coefficients, m and n the reaction orders. The Grindling model accounts for the occurrence of vitrification by proposed a method based on a combination of a nth order model with a Prout-Tompkins model, while the effects of vitrification are included by the introduction of a kinetics-controlled reaction rate coefficient k_{eff}:

$$\frac{d\alpha}{dt} = k_1(1-\alpha)^{n1} + k_{eff}\alpha^m(1-\alpha)^{n2} \quad \text{with} \quad \frac{1}{k_{eff}} = \frac{1}{k_2} + \frac{1}{k_{2,diff}} \tag{2.9}$$

where k is the reaction rate coefficient and n and m the reaction orders. Equation 2.9 could thus be understood as a combination between two independent reaction mechanisms, i.e. denoted with subscripts 1 and 2, with the effective reaction rate constant allowing for the kinetic model to switch between a chemical-controlled and diffusion controlled state by defining different analytical expressions for $k_{2,diff}$ as a temperature-dependent function

related to the T_g and the imposed shift (ΔT_g) by overcoming the T_g, i.e. the T_g when full conversion is reached, i.e.:

$$
K_{2,diff} =
\begin{cases}
K_{2,diff}^{T=T_g} \exp\left(T_g^2 \dfrac{c_1}{c_2} \left(\dfrac{1}{T} - \dfrac{1}{T_g} \right) \right) & T < T_g & \text{(2.10a)} \\[3ex]
K_{2,diff}^{T=T_g} \exp\left(\dfrac{c_1 \left(T - T_g \right)}{c_2 + T - T_g} \right) & T_g \le T \le (T_g + \Delta T_g) & \text{(2.10b)} \\[3ex]
K_{2,diff}^{T=T_g + \Delta T_g} \exp\left(\dfrac{c_1 c_2 \left(T_g + \Delta T_g \right)^2}{\left(c_2 + \Delta T_g \right)^2} \left(\dfrac{1}{T} - \dfrac{1}{T_g + \Delta T_g} \right) \right) & T > (T_g + \Delta T_g) & \text{(2.10c)}
\end{cases}
$$

The definitions for the diffusion-controlled rate-constant in Equations 2.10a-2.10c thus describe the different stages, i.e. becoming increasingly dominant as the temperature approaches the T_g (Equation 2.10a), a transition stage (Equation 2.10b) and a fully diffusion controlled stage (Equation 2.10c). The inclusion of diffusion-controlled kinetics and differentiation between the different stages was found highly beneficial for the model accuracy describing the curing behaviour of an epoxide system, resulting in better fitting over the complete range of curing degrees while the more conventional Kamal-Malkin reaction-kinetics model (Equation 2.8) overestimated the curing reaction, especially at higher conversions [201]. The use of the Grindling model however significantly increases the number of parameters that should be fitted on experimental data, i.e. 11 instead of e.g. 6 for a Kamal-Malkin model, imposing the need for complex optimisation algorithms.

Bailleul models [215] make up a second class of phenomenological models that are frequently applied for the modelling of cure-kinetics in epoxide systems. Contrary to the imposed kinetics models listed in Table 2.1, Bailleul models describe the kinetics part of Equation 2.7 by a polynomial function ($G(\alpha)$) while defining the rate constant coefficient in relation to a randomly chosen reference temperature (T_{ref}), as:

$$
\frac{d\alpha}{dt} = k(T)G(\alpha) \quad \text{with} \quad k(T) = A \exp\left(-E_a \left(\frac{T_{ref}}{T} - 1 \right) \right), \quad G(\alpha) = \sum_{i=0}^{m} G_i \alpha^i \tag{2.11}
$$

where G_i refers to the polynomial coefficients. The principal Bailleul model does not include for the effect of vitrification on the curing rates. Ruiz & Trochu [216] proposed an extension of the model to include these effects by the addition of the term:

$$
K(T, \alpha) = (\alpha_{max}(T) - \alpha)^{n(T)} \tag{2.12}
$$

with α_{max} denoting the maximum curing degree for isothermal curing and n a temperature-dependent power exponent. Using the additional term, Ruiz et al. [216] observed that the

Bailleul model showed a significantly improved model accuracy compared to e.g. a Prout-Tompkins model (Table 2.1). Keller et al. [203] moreover demonstrated a good model accuracy when describing a fast curing epoxide resins, using a fourth-order polynomial divided by a second-order polynomial for $G(\alpha)$ and a linear dependence for $n(T)$.

2.5.2 Modelling of frontal polymerisation

2.5.2.1 Early mathematical descriptions

First attempts on modelling frontal polymerisation took place in the late 1990s on systems undergoing free-radical polymerisation. Goldfeder et al. [185] was the first to model frontal polymerisation in a steady-state situation by proposing a mechanistic model describing the individual reaction rates, i.e. initiation, propagation and extinction of free-radical polymerisation, while a similar approach was later used in e.g. Refs. [217, 218]. They proposed an analytical expression for the front temperature of a system without fillers by adiabatic self-heating, i.e. all the polymerisation enthalpy is used for heating the resin system, which was redefined by Ref. [19] as:

$$T_p = T_0 + \frac{H_r}{\rho C_p}(1 - \alpha_0)$$
(2.13)

where T_p denotes the front temperature, T_0 the initial temperature, H_r, ρ and C_p the resin enthalpy, density and heat capacity respectively, while α_0 refers to the initial curing degree. The competition between the released heat and thermal diffusion introduced increased complexities in the development of models describing the front velocity of propagating fronts, resulting in the following model describing the front velocity (v):

$$v^2 = \frac{\kappa R T_p}{2 E_{a,d}(T_p - T_0)} k_d^0 e - \frac{E_{a,d}}{R T_p}$$
(2.14)

where κ denotes the thermal conductivity of the resin, $E_{a,d}$ the activation energy for the dissociation constant, k_d^0 the reaction rate constant for initiator decomposition and e the Euler's constant. This model gave good approximations of the experimentally recorded front velocity of steadily propagating fronts when used in its analytical form while typically resulting in an overestimation of ~20% when solved numerically. Volpert and coworkers moreover developed a multitude of alternative mathematical expressions for capturing the highly non-linear behaviour of propagating fronts during both thermal and isothermal frontal polymerisation [219]. Tiani et al. [170] recently proposed a similar mechanistic model. Although they were able to describe frontal polymerisation in one- and two-dimensions, there model is yet to be validated experimentally. The derivation of mechanistic models is however reported [219] to be only possible for systems undergoing free-radical polymerisation to-date due to the relatively limited complexity in polymerisation kinetics of these systems, i.e. as opposed FROMP or

RICFP.

2.5.2.2 Finite element modelling of frontal ring opening metathesis polymerisation

Models describing FROMP developed by the researchers at the University of Illinois make up the vast majority of recent modelling efforts. The very fast and complex polymerisation kinetics of FROMP systems impose the need for phenomenological reaction-kinetics models to describe their curing behaviour. Goli et al. [211] were the first to model FROMP-curing of pDCPD using a nth order Prout-Tompkins model. Subsequent reports however, starting from the work of Robertson et al. [20], uniquely used a Prout-Tompkins kinetics model with a diffusion term [212] (listed in Table 2.1).

Finite element methods were used by both Goli et al. [211] and Robertson et al. [20], as well as in all subsequent reports [21, 131, 171, 172, 176–178, 191, 220], to solve the partial differential equations of Equation 2.6a. This allowed for modelling of both transient, e.g. the formation of a front upon initiation, and steady-state front behaviour. Domains were limited to one- and two-dimensions since the large thermal gradients over the front region, i.e. of ~100-200°C following Section 2.4, impose the need for highly refined meshes. Mesh sizes typically ranged in the order of 10^{-6}-10^{-5} metres [172, 178, 220] combined with an average time step of 0.01 seconds [172, 176, 178]. The use of adaptive meshing algorithms, integrated in the Multiphysics Object-Oriented Simulation Environment (MOOSE) [221], was found to strongly reduce the computational cost and hence the computation time. Wang [220] simulated FROMP with a conventional finite element method package, i.e. ABAQUS, by developing custom subroutines and was able to simulate domains of 2.6×2.6 mm, using a mesh size of 0.02 mm, in 1.5 hours. Domains used for FROMP simulations in MOOSE were significantly larger, reaching up to centimetre scale [211]. To further reduce the computational cost, Refs. [174, 222, 223] proposed analytical expressions describing the front characteristics, although these are limited to steady-state approximations in an adiabatic domain.

Front initiation was in all cases simulated by thermal initiation, i.e. increasing the temperature at one of the domain boundaries, for a set time. Trigger temperatures were generally in the order of ~200°C [176] and trigger times ranged from 1-7 seconds [20, 176]. A number of works reported on the simulation of FROMP to produce FRPs [20, 21, 176]. To do this, the parameters of Equation 2.6a, i.e. H_r, ρ, C_p and κ, were adapted by a homogenisation between resin and fibrous reinforcements using the rule of mixtures:

$$\overline{H_r} = (1 - V_f)H_r \tag{2.15}$$

$$\overline{\rho} = V_f \rho_f + (1 - V_f)\rho_r \tag{2.16}$$

$$\overline{C_p} = V_f C_{p,f} + (1 - V_f) C_{p,r} \tag{2.17}$$

$$\overline{\kappa} = V_f \kappa_f + (1 - V_f) \kappa_r \tag{2.18}$$

with subscripts f and r referring to the fibre and resin phases. The majority of studies did not make a distinction between thermal conductivity in in-plane and through-thickness directions [20, 21, 177], which are inherent to FRPs due to the non-isotropic fibre orientations [224]. Goli et al. [176] are the only ones to use separate expressions for the directionality of the thermal conductivity of a FRP system for simulating frontal polymerisation at a yarn-scale by employing the extended Rayleigh model [225]. Substituting Equations 2.15-2.18 into Equation 2.6a yields a generalised thermal-kinetic model for FRPs under the assumption of homogenisation of the domain:

$$\begin{cases} \overline{\kappa} \nabla T + \overline{\rho} \overline{H_r} \dfrac{\partial \alpha}{\partial t} = \overline{\rho} \, \overline{C_p} \dfrac{\partial T}{\partial t} \\ \dfrac{\partial \alpha}{\partial t} = k(T) f(\alpha) \end{cases} \tag{2.19}$$

Gao et al. [177] assessed the validity of the homogenisation assumption on a FROMP system with metal strips placed at varying spacings. The recorded front velocities at a spacing of 0.2 mm were found identical to those calculated for a homogenised domain while increased spacings gradually deviated from the homogenised predictions. Given that fibre diameters are typically well-below 0.2 mm, the validity of a homogenised approach for simulating FRPs could be hypothesised. It should however be noted that inter-yarn spacings could approach 0.2 mm that, with no reports on the role of the fibre properties on the validity of the homogenisation approach, an influence of the fibre microstructure may be present that would be ignored when homogenising the domain.

Numerical estimations are often validated experimentally by comparing the front characteristics, i.e. maximum front temperature and front velocity. Robertson et al. [20] reported a minor overestimation of front temperature (7°C, 3.2%) and an underestimation of the front velocity (0.4 cm/min, 6.3%). Goli et al. [176] made a similar observation with numerical predictions on the front temperature and velocity closely corresponding to the experimental data over at V_fs ranging between 0-50%. One-dimensional simulations, considering adiabatic conditions, on the other hand were reported to strongly overestimate the front temperature, i.e. by ~20°C, while giving comparable front velocities. Several authors [20, 131, 175, 177, 178] moreover validated the numerical models by comparison of the simulated morphologies of propagating fronts by those recorded optically. For example, Robertson et al. [20] compared the morphologies in a pure pDCPD system, shown in Figure 2.15a, and in the presence of a carbon fibre yarn guiding the front (Figure 2.15b) and concluded both cases to be sufficiently
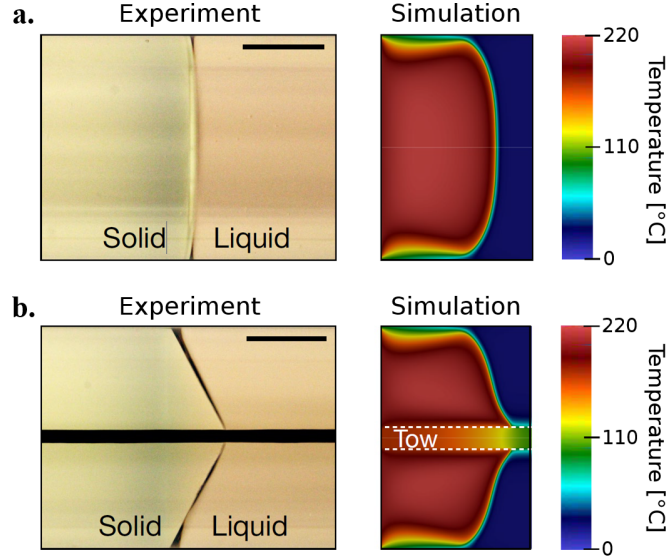
Figure 2.15: Validation of numerical models by comparing experimental and numerical front morphologies of a) pure pDCPD system and b) a pDCPD in the presence of a carbon fibre yarn (Source: [20]).

similar to validate the numerical work. Comparisons of the temperature profiles near the front regions are however yet to be made and would further increase the confidence in the developed models.

2.5.2.3   Modelling of epoxide frontal polymerisation

Frulloni et al. [226] are to-date the only ones to model the frontal polymerisation of epoxide systems. Based on a resin system composed of BADGE and a diethylenetriamine thermal initiator, i.e. incapable of undergoing RICFP, they used a modified Kamal-Malkin model to describe the ongoing reaction kinetics:

$$\frac{d\alpha}{dt} = \left(k_1 + k_2\alpha^m\right)\left(\alpha_{max} - \alpha\right)^n \tag{2.20}$$

with k_1 and k_2 referring to Arrhenius reaction rate coefficients, m and n the reaction orders and α_{max} the maximum attainable conversion at different isothermal DSC temperatures. Parameters were fitted on isothermal DSC measurements, which was possible due to the relatively low reaction rates of the system, i.e. compared to FROMP or RICFP systems, and hence avoiding the inaccuracies due to thermal lagging described in Section 2.5.1.

Implementation of Equation 2.20, substituted into Equation 2.6a, into an cylindrical finite difference domain allowed for estimation of the front behaviour. Although the front temperatures were overestimated by ~20°C in an adiabatic one-dimensional domain, solving the

model in a two-dimensional domain showed the expected approximation of a steady-state temperature as well as the influence of the boundary effects on the front characteristics. The work by Frulloni et al. [226] therefore paves a way towards the numerical implementation of RICFP, although the strongly increased reaction rates are expected to introduce additional model complexities, i.e. similar to the numerical work on FROMP.
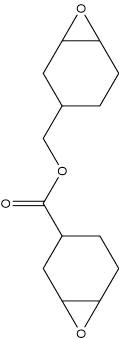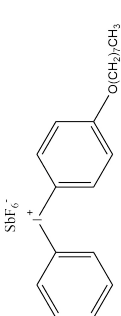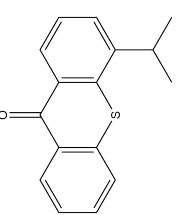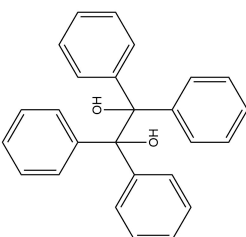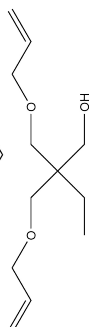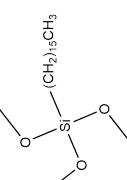
3 Experimental

3.1 Resin preparation

Resins were based on 3,4-epoxycyclohexylmethyl-3',4'-epoxycyclohexane carboxylate (ECC) monomer with a molecular weight of 252.31 g/mol that was acquired from commercial providers IGM (OC1005, the Netherlands), Daicel (Celloxide 2021P, Japan) and Lambson (UViscure S105, United Kingdom) over the course of this thesis work. No significant differences in the photopolymerisation behaviour or resulting polymer properties were observed between the commercial resin formulations. p-(octyloxyphenyl)phenyliodonium hexafluoroantimonate (IOC-8 SbF_6, ABCR, Germany), isopropylthioxanthone (ITX, Genocure ITX, Rahn, Switzerland) and benzopinacol (Thermo Fisher Scientific, Belgium) were respectively used as cationic photoinitiator, photosensitiser and free-radical thermal initiating compound. An overview of the molecular structures of the monomer and initiating compounds is shown in Table 3.1. Properties of UV-flow freezing resins were varied by the addition of a diluent based on trimethylolpropane diallyl ether (TMPDE, TMPDE90, Perstorp, Sweden) and a hexadecyltrimethoxysilane surfactant (HDMSi, Sigma Aldrich, Germany).

Resin preparation commenced with the drying of commercial ECC resins under vacuum to remove possible humidity as well as low-boiling-point additives. The thermal initiator and photosensitiser were dissolved by overnight stirring at high shear rate, after which the photoinitiator and possible additives were added and left to dissolve for a minimum of 3-4 hours at high shear rate. Resins were degassed under vacuum for a minimum of 30 minutes prior to the start of the experiment.

Table 3.1: Molecular structures of resin compounds.

Abbreviation	Chemical name	Molecular weight	Structure
ECC	3,4-Epoxycyclohexylmethyl-3′,4′-epoxycyclohexane carboxylate	252.31 g/mol	
IOC-8 SbF$_6$	p-(Octyloxyphenyl)phenyl iodonium hexafluorostibate	645.08 g/mol	
ITX	Isopropylthioxanthone	254.35 g/mol	
Benzopinacol	1,1,2,2-Tetraphenyl-1,2-ethandiol	366.45 g/mol	
TMPDE	Trimethylolpropane diallylether	214.30 g/mol	
HDMSi	Hexadecyltrimethoxysilane	346.60 g/mol	

Transmittance of commercial and in-house produced PMMA
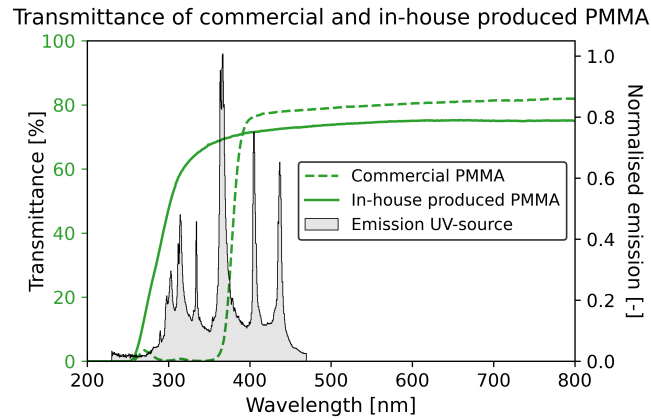
Figure 3.1: UV-Vis transmittance spectra of commercial and in-house produced PMMA compared to the emission spectra of the used UV-source.

3.2 UV-flow freezing

3.2.1 Experimental procedure

Moulds for UV-flow freezing experiments were composed of in-house produced PMMA plates. This was done as to improve its transmittance of UV-light since commercial PMMA, used by Caglar et al. [47], was found to have a lower transmittance limit of about 370 nm, as shown in Figure 3.1, and hence absorbed a significant part of the spectrum emitted by the UV-source. In-house produced PMMA on the other hand the has a lower usable limit of ~270 nm that captures nearly the complete emission spectrum. The difference between commercial and in-house produced PMMA is mainly attributed to the absence of UV-absorbing additives in the latter one. The absence of these additives increased the brittleness of the PMMA while a lower surface quality resulted in a slight decrease of the transmittance of in-house produced PMMA compared to that of commercial PMMA. These disadvantages were however outweighed by the beneficial enhanced transmittance in the UV-spectrum and flow freezing moulds were composed of in-house produced PMMA mould halves. To produce the PMMA mould halves, PMMA pellets (Plexiglas, Evonik, Germany) were dried under vacuum at 60°C for 24 hours after which they were poured in a ~12×280×280 mm steel mould cavity. 1.5 mm thick aluminium plates were placed above and below the pellets to enhance the surface quality of the resulting PMMA plates. The steel mould was, after closure, placed in a laboratory press (PEI 150P) where it was subjected to a cycle consisting of 1. a temperature ramp from room temperature to 180°C at a rate of 20°C/min with an applied pressure of 0.13 bar, 2. an isothermal period at 180°C and 0.13 bar for 30 minutes, 3. compression at 3.2 bar and 180°C for 30 minutes and finally 4. a cooling ramp of 0.1°C/min while maintaining the compaction pressure. Plates were subsequently cut to 200x100 mm mould halves and manually polished to improve their surface quality.

The transparent mould was, as schematically illustrated in Figure 3.2a assembled by two
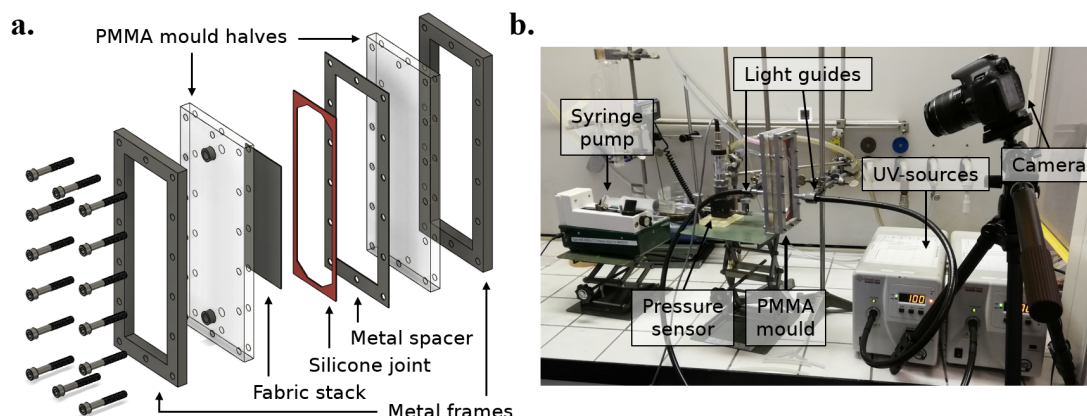
Figure 3.2: Experimental configuration for UV-flow freezing experiments: a) schematic representation of the PMMA mould and b) experimental setup for impregnation and UV-photopolymerisation.

metallic frames surrounding the PMMA plates while the mould cavity was defined by a 1 mm thick aluminium spacer and an in-house produced silicone rubber, made of Neukasil RTV17 and Neukasil Crosslinker C5 (both Altropol, Germany). UV-flow freezing analysis was carried out on 2x2 twill weave glass fibrous preforms (Suter Kunststoffe, Switzerland) with an areal weight of 390 g/m^2, an ends/picks count of 6/6.7 cm^{-1} and a linear density of 340 and 272 tex in warp and weft, respectively. The fabric was manually cut to strips of 100x50 mm and three layers were stacked in the mould cavity, corresponding to an estimated V_f of 45%, before assembling and closing the mould. Inlet and outlet tubes were located at both ends of the mould cavity.

The experimental configuration for infiltration and UV-flow freezing is shown in Figure 3.2b. Sample production commenced with the manual resin infusion of the empty section of the cavity near the inlet, followed by resin impregnation at varying constant flow rates using a Razel Scientific Instruments R-100e syringe pump. The inlet pressure and resin temperature were recorded by a pressure sensor (Keller Series 35XHTT) place in-series between the syringe pump and the inlet. Impregnation was recorded by a camera (Canon EOS 700D) placed perpendicular to the mould surface and resin infusion was stopped when flow fronts reached about two-thirds of the fabric length after which the inlet tube was disconnected to release the resin pressure. UV-irradiation was started directly after the disconnection of the inlet tube. Two EXFO Omnicure high-pressure mercury UV-sources, i.e. one mounted with a S2000 standard light and one with a S2001 surface light source, were placed at opposing sides of the mould. The intensity of the UV-sources, recorded over a spectrum of 250-410 nm using a Control-cure Silverline UV radiometer, was adapted by the intensity setting and distance to the PMMA surface, i.e. as shown in Figure 3.3. It was aimed to maximise the UV-intensity, covering the full fabric width, while avoiding thermal fracture of the PMMA mould halves. UV-irradiation was maintained for 240 seconds after which the UV-sources were relocated to polymerise the remaining sections of the impregnated fabric stack. Fabrics were removed
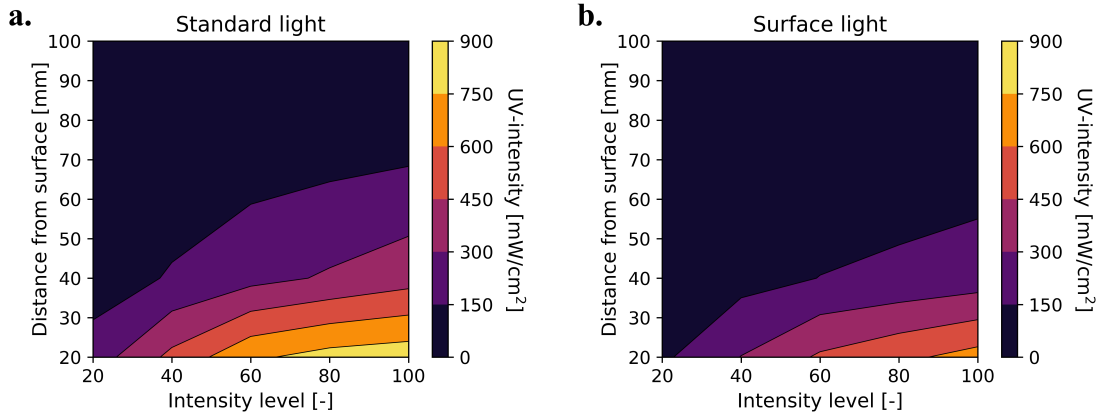
Figure 3.3: UV-intensity of a) EXFO Omnicure S2000 standard light source and b) EXFO Omnicure S2001 surface light source as a function of the set intensity level and the distance from the mould surface.

from the mould and placed in an oven at 120°C a minimum of one hour to ensure complete curing of the sample.

3.2.2 Rheological analysis

The rheological behaviour of resins used for UV-flow freezing experiments was characterised using a TA instruments AR2000ex rheometer. Flow conditions during impregnation were simulated in a Peltier couette setup in continuous shear mode. Temperature ramps ranged between 15-30°C at a rate of 0.1°C/min while shear rates were kept constant at 10 s^{-1}. The viscosity-temperature behaviour was fitted with an Arrhenius law [66, 227]:

$$\eta(T) = A \cdot \exp\left(\frac{E_a}{RT}\right) \tag{3.1}$$

where η is the dynamic resin viscosity, A the pre-exponential factor, E_a the activation energy, R the molar gas constant and T the resin temperature. Only the data recorded between 20-30°C was considered for the fitting procedure to avoid an influence of thermal lagging, i.e. the delayed overcoming of thermal inertia of the measurement setup, as shown in Figure 3.4. Resulting fits showed good correlation with the experimental data and were used to estimate the resin viscosity in UV-flow freezing experiments based on the recorded resin temperature.

The photocuring behaviour of the developed resins was assessed using a photorheology configuration consisting of an in-house produced PMMA transparent bottom plate with a diameter of 20 mm connected to an UV-source and a 20 mm diameter metallic top plate. UV-intensities were recorded by placing a radiometer at the PMMA surface and were verified before every measurement. Measurements were carried out in oscillation mode with an oscillation frequency of 1 Hz, a gap of 200 μm and an oscillation strain of 1%. An calibration
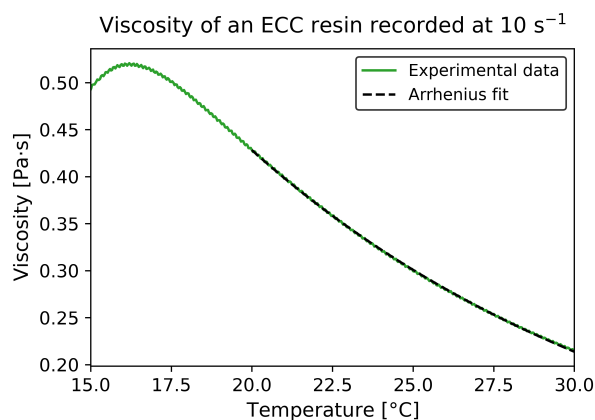
Figure 3.4: Exemplary temperature-dependent viscosity characterisation fitted with an Arrhenius relation (Equation 3.1).
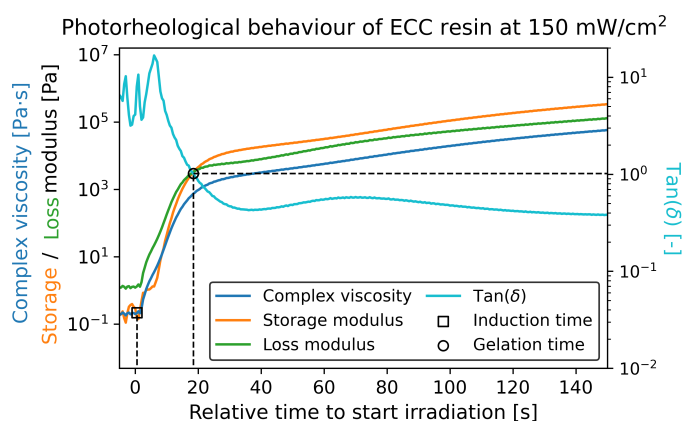
Figure 3.5: Exemplary photorheology data recorded for an ECC-based resin using an UV-intensity of 150 mW/cm^2. Induction and gelation times were used as main descriptors for photorheological analysis.

procedure was prepared to confirm that the measurement was carried out in the the linear viscoelastic regime (LVR), where samples were irradiated for 30 seconds at low ($\sim$25 mW/cm^2) UV-intensity followed by a variation of the oscillation sweep from 0.001-100%. This cycle was repeated for eight times to characterise the LVR over a large range of viscosities and hence to support the confidence in the experimental findings.

Photorheology procedures were carried out over a period of 1000 seconds. UV-irradiation was started after 20 seconds of measurement time and was maintained during the complete measurement procedure. The recorded data was corrected for the delay of irradiation and was, as demonstrated in Figure 3.5, assessed by two main descriptors: the induction and gelation time. The induction time was defined as the time between the start of irradiation and the onset of the viscosity increase, defined as the time it overcomes the variability (i.e. the average complex viscosity before irradiation plus its standard deviation) before irradiation. A

spline interpolation of the experimentally recorded viscosity data was used to for improve the accuracy of the induction time estimation. The gelation time was defined as the time where the phase angle between the viscous and elastic moduli, i.e. $\tan(\delta)$, equalled one.

3.2.3 Surface tension

The surface tension of resin formulations were characterised via the pendant drop method at ambient temperatures using a Krüss DSA30 drop shape analyser. This method can determine the surface tension based on the shape and volume of a droplet when it is in equilibrium with gravity. Resulting surface tension values were averaged over a minimum of three recordings and were assumed to be constant over the considered temperature ranges for in-situ flow freezing experiments.

3.2.4 Post-curing analysis

Post-curing strategies were developed by means of differential scanning calorimetry (DSC) using a TA Instruments DSC Q100. Aluminium hermetic pans were filled with ~2-3 mg of resin and an empty pan was used as reference. Dynamic heat flow measurements consisted of a temperature ramp from -20-270°C at a rate of 5°C/min. Polymerisation enthalpies were determined by integration of the heat flow signal after baseline correction. Quasi-isothermal procedures consisted of an initial temperature ramp from -20-120°C at 5°C/min after which the sample was kept at 120°C for one hour to simulate post-curing in an oven.

3.2.5 UV-vis spectrophotometry

UV-absorbance/transmittance of different constituents was characterised by UV-vis spectrophotometry (Varian Cary 50 Bio) recording over a spectrum of 250-800 nm at an interval of 1 nm. The transmittance of PMMA mould halves was assessed on ~12×50×50 mm pieces after polishing of its surfaces. The absorbance of the resin constituents, dissolved in dichloromethane at a concentration of 0.05 mM, was recorded using a 10 mm quartz cuvette over a similar wavelength spectrum.

3.2.6 Flow front analysis

Frozen flow front morphologies were characterised by μCT using a RX Solutions Ultratom at the EPFL PIXE platform. Post-cured samples were manually cut to strips of ~15 mm in width after which a contrasting agent was deposited near the front region to enhance the contrast at the interface between polymer and air and hence allow for identification of the flow front. This contrasting agent was, following Sket et al. [228], composed of 60 g of zinc iodide (ZnI_2), 10 mL of ethanol, 10 mL of water and 10 mL of surfactant (Kodak Photo-flo 200, USA). The contrasting agent was pipetted onto the sample strips and was left to partially dry overnight,

followed by a second deposition before placing the sample into the μCT setup. Acquisitions were made with a voltage of 60 kV and an X-ray current of 85 μA. The voxel size was fixed to 3.5 μm^3 while the sample volume was adapted based on the length of the unsaturated flow front region. The saturated and unsaturated regions μCT images were manually segmented using Avizo software (Thermo Fisher Scientific). The segmented volume was subsequently voxelised and analysed by an in-house developed Python script. Saturation curves were calculated for each slice in front direction as:

$$S = 1 - \frac{n_{vxl}}{n_{vxl,tot}} \tag{3.2}$$

where S denotes the saturation level, n_{vxl} the number of voxels in a slice identified as unsaturated and $n_{vxl,tot}$ the total number of voxels in a slice. Saturation levels for individual fabric layers were calculated by dividing the sample thickness into three horizontal sections.

3.3 Frontal polymerisation-assisted production of fibre reinforced polymers

3.3.1 Experimental configurations for frontal polymerisation processing

3.3.1.1 Varying resin composition

Variations of the heat generation term of the local heat balance were introduced by changing the initiator concentrations of the resins. Photo- and thermal initiator concentrations were varied over a range of 0.5-1.5 w% and 0.22-4.25 w%, respectively, while the concentration of photosensitiser ITX was varied between 0-0.32 w%. The resins with varying initiator and photosensitiser contents were characterised in composite systems containing about 12% V_f extracted carbon fibre tows. The low V_f ensured frontal polymerisation to take place in all studied resin mixtures while simultaneously capturing the influence of the highly conductive carbon fibres. Experiments were carried out in an in-house produced silicone elastomer mould with a 45×12×7 mm cavity volume that was filled with resin and carbon fibre yarns and was subsequently closed with a second mould half. A schematic representation of the experimental setup can be found in Figure 3.6. Fronts were initiated by the insertion of a soldering pin, preheated at 250°C, at one extreme of the mould while temperatures were recorded by three integrated K-type thermocouples placed at respectively 20, 30 and 40 mm from the initiation point.

3.3.1.2 Mould variation

The role of the mould design was investigated on neat resin systems to avoid the interference of thermal transport induced by the presence of (carbon) fibre reinforcements, while initiator concentrations were reduced to avoid degradation of the formed polymer. For this investigation, the thermal initiator and photosensitiser concentrations were kept constant at 1 and 0.05% by weight, respectively, while the photoinitiator concentration was varied between 0.15-0.75 w%. An interchangeable mould with a 90×35×5 mm mould cavity, defined by a silicone elastomer joint and steel spacer, was filled with resin and enclosed by mould
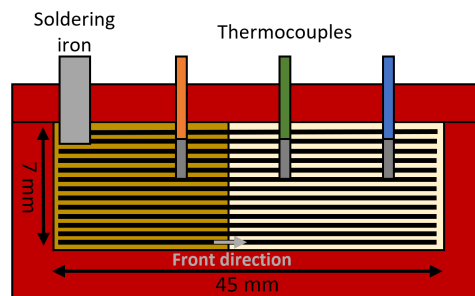
Figure 3.6: Overview of the experimental configuration for characterisation of the role of the heat flow by variation of the resin composition.

Table 3.2: Thermal properties of used mould materials.

Material	Thermal conductivity [W/m/K]	Specific heat [kJ/kg/K]	Density [kg/m^3]	Thermal effusivity [kJ/m^2/K/s$^{0.5}$]
Mould steel	32.0*	0.46*	7850*	339.9
Silicone elastomer	0.27*	0.50*	1450	14.0
PVC foam core	0.029	1.39*	60	1.56
Polymer	0.17	1.20*	1165	15.4

*Material properties were not provided by the supplier and are approximated from general material databases.
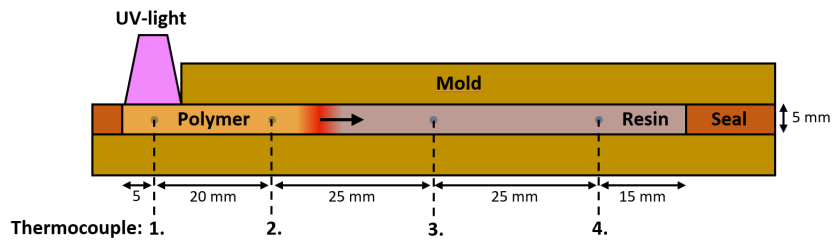
Figure 3.7: Schematic representation (longitudinal cut) of the mould configuration used for the production of neat polymer.

halves made of either conductive mould steel, insulating silicon elastomer or highly-insulating Teflon-covered PVC-foam. A schematic representation of the experimental setup can be found in Figure 3.7 while an overview of the thermal properties of the considered mould materials is presented in Table 3.2.

Fronts were initiated by UV-irradiation through a 10 mm opening in the upper mould half until front formation was observed. UV-intensities were kept low, i.e. in the order of 125 mW/cm^2, to avoid an initial overshoot of the front temperature. Thermocouples were integrated at 5, 25, 50 and 75 mm from the initiation point.

3.3.1.3   Vacuum-assisted hand layup

A vacuum-assisted hand layup methodology was used to study the role of thermal management on the frontal polymerisation processing of carbon FRPs. This processing strategy was expected to be beneficial for frontal polymerisation due to the increased insulating properties of an air interface over e.g. a RTM configuration composed of two solid mould halves. 2×2 twill weave carbon fibrous preforms (Suter Kunststoffe, Switzerland) with an areal weight of 285 g/m^2, an ends/picks count of 3.5/3.5 cm^{-1} and 6K fibres per yarn was manually cut in strips of ~80×60 mm. Photo- and thermal initiator contents of the resin were varied while keeping a ratio by weight of about 3:4 to limit the degrees of freedom in the assessment while the photoinitiator concentration was generally kept low, i.e. <1%, as was the case in Section 3.3.1.2. A mould configuration for vacuum-assisted hand layup consisted, as schematically shown in Figure 3.8, of a Teflon-covered PVC foam core bottom plate and a silicone elastomer joint
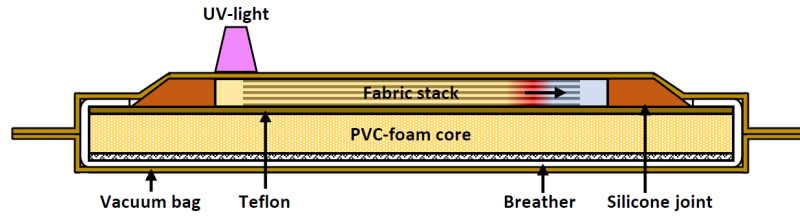
Figure 3.8: Schematic representation of the mould configuration used for vacuum-assisted hand layup processing.

to define a 5 mm cavity. Resin impregnated fibrous preform layers were alternately placed in the cavity, followed by manual compaction of the fabric stack. The completed layup was subsequently enveloped with a high-temperature vacuum bag (Diatex Polyimide HM 25 μm, France) and the internal pressure was regulated to 500 mbar for a period of 30 minutes or until a uniform thickness was reached. Fronts were initiated by high intensity (>500 mW/cm^2) UV-irradiation in one of the resin-rich corners of the mould and the front was left to propagate autonomously. Stalled or quenched fronts were attempted to be re-initiated by UV-irradiation near the front region inside the impregnated fabric stack. The number of fabric layers was varied between 12 and 14 and the final V$_f$ was determined using the following relation:

$$V_f = \frac{NA_w}{\rho h} \tag{3.3}$$

where N is the number of fabric layers, A_w the fabric areal weight, ρ the density of carbon fibres, taken as 1.8 g/cm^3, and h the sample thickness. Thicknesses were averaged over five positions for cured samples while assumed to equal the cavity height if no front was formed.

3.3.1.4 Self-catalysed frontal polymerisation

FRP production by the newly proposed self-catalysed frontal polymerisation methodology was carried out in a Teflon-covered Rohacell IG-F 110 polymethacrylimide (PMI) foam core (Evonik, Germany) mould. Mould cavities were defined by in-house produced frames of various heights and a silicon joint was placed inside the cavity to avoid leakage of resin. Carbon and glass twill fibrous preforms, as described in Sections 3.3.1.3 and 3.2.1 respectively, were cut to strips of 100×50 mm were cut and stacked in the mould cavity. A gore-tex flap was placed over the last 20 mm as a resin barrier while the remaining section of the fabric stack was covered with an aluminium foil layer upon which a 0.5 mm thick perforated carbon FRP separator was placed. 1.5 mm thick aluminium strips were placed at the edges of the carbon FRP separator to define a resin channel with a controlled height. This resin channel was filled with strips of 150 g/m^2 polyester breather fabric (Suter Kunststoffe, Switzerland) or left empty. A schematics representation of the mould configuration is shown in Figure 3.9

The fabric stack and resin channel were simultaneously impregnated under a constant flow
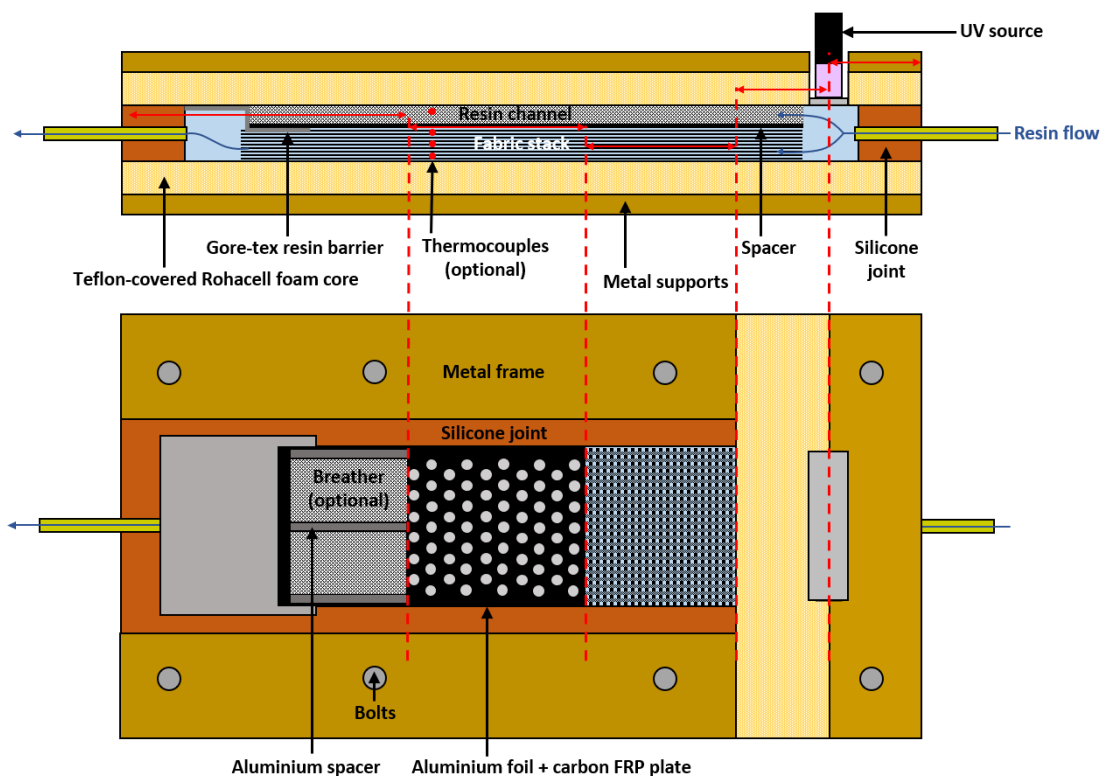
Figure 3.9: Schematic representation of the mould configuration for self-catalysed frontal polymerisation with a longitudinal and planar section on the top and bottom, respectively.

rate of 30 mL/hr using a Razel Scientific Instruments R-100e syringe pump. Frontal polymerisation was initiated by high intensity (>850 mW/cm^2) UV-irradiation by an EXFO Omnicure S2000 standard UV-source through an opening in the mould half covered with a layer of high-temperature 25 μm Diatex Polyimide HM vacuum bag. Produced composites were left to cool for a minimum of 10-15 minutes after completion of the frontal polymerisation process while remaining enclosed in the mould cavity. Fibre volume fractions were determined via the sample thickness and Equation 3.3, assuming a bulk density of 2.6 g/cm^3 for glass FRPs. Investigations on FRP production in the absence of a resin channel were produced in a similar mould configuration and with an identical procedure for impregnation and initiation.

3.3.2 Heat flow analysis

The heat output of resins presented in Section 3.3.1.1 was determined using quasi-isothermal DSC measurements. Samples of 2-3 mg freshly mixed resin were weighed in aluminium hermetic pans and measurement procedures consisted of an initial heating phase from -20-105°C at a rate of 5°/min, followed by an isothermal phase of 30 minutes. Maximum heat outputs corresponded to the recorded peak maxima after baseline correction, as illustrated in Figure 3.10.
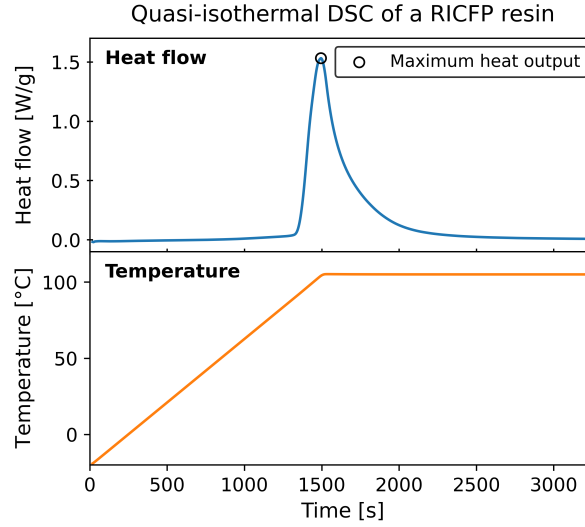
Figure 3.10: Exemplary quasi-isothermal DSC curve after baseline correction for the characterisation of the heat output of RICFP resins. The encircled point corresponds to the maximum heat output.

Spearman's rank correlation coefficients of the resulting distributions were determined using the following relation:

$$r = 1 - 6 \sum \frac{d^2}{n\left(n^2 - 1\right)} \tag{3.4}$$

where r is the Spearman's rank correlation coefficient, d_s the difference in statistical rank of corresponding variables and n the number of variables.

3.3.3 Thermal analysis of frontal polymerisation

Thermal analysis of propagating polymerisation fronts was applied in several instances in this thesis work. Recordings were made by in-house produced 0.1 mm diameter K-type thermocouples connected to a National Instruments DAQ device that was coupled to an in-house developed LabView procedure. Data was acquired at an acquisition rate of 100 Hz to accurately capture the large temperature gradients experienced in frontal polymerisation.

3.3.3.1 Derivation of front velocities

Front velocities were derived for neat-polymer samples, using a configuration as presented in Section 3.3.1.2, and composite samples as presented in Section 3.3.1.1. Integrated thermocouples in the mould allowed for the recording of temperature profiles upon frontal polymerisation, as demonstrated in Figure 3.11a. Front velocities were subsequently derived by linear
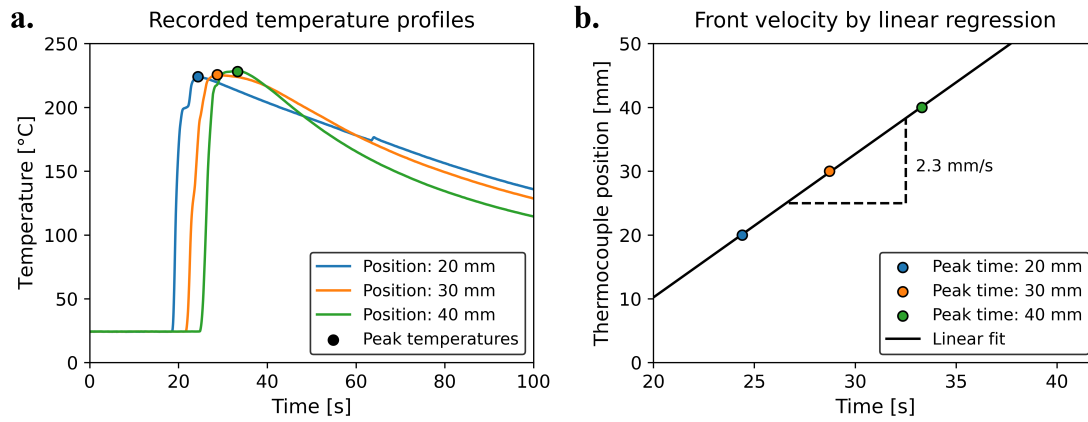
Figure 3.11: Exemplary overview of the experimental procedure for characterisation of the front velocity. a) recorded temperature profiles for a 12% V_f composite system, and b) linear regression of peak instants, corresponding to the maxima of the thermocouple recordings in a), to derive the front velocity.

regression of the peak times of the corresponding temperature profiles, i.e. Figure 3.11b.

3.3.3.2 Temperature profiles in self-catalysed frontal polymerisation

Preheating and front temperatures in self-catalysed frontal polymerisation processing were characterised for both carbon and glass preforms of about 50-53% V_f, in 5.3- and 9-mm mould cavities. Temperature profiles were recorded by four thermocouples that were embedded at the bottom, centre and top of the fabric stack, as well as on top of the breather fabric filling of the resin channel, at about 65 mm of the fabric length in front direction. Recordings were started simultaneously with the start of UV-irradiation. Peak temperatures were defined as the maximum recorded temperature while preheat temperatures were taken as the temperature 10 seconds before the appearance of the peak.

3.3.3.3 Resin channel fillers in self-catalysed frontal polymerisation

The influence of fillers in the resin channel of a self catalysed frontal polymerisation was assessed using FRPs composed of 18 layers of carbon twill weave fabric and a mould cavity height of 7.3 mm, corresponding a V_f of ~56%. Resin channels were either filled with a strip of breather fabric or left empty. In the latter case, 2×2×1.5 mm alumina cubes were placed at the front and end of the resin channel to avoid buckling of the separator. Two series of three thermocouples were placed at the top, centre and bottom of the fabric stack, i.e. above layers 17, 9 and 1, respectively. The separation distance was measured optically when placing the thermocouples and equalled ~0.8 cm. Preheating and front temperatures were recorded as described in Section 3.3.3.2. Delay times were defined as the time between the initial increase of the thermocouple, corresponding to the passing of the front in the resin channel, and the

recorded peak temperature at that thermocouple position.

3.3.4   Interface temperatures

Interface temperatures between the polymer and mould in a configuration described in Section 3.3.1.2 were, under the assumption of perfect thermal contact, calculated as the weighted mean based on the relative thermal effusivities between the polymer and mould material:

$$T^* = \frac{e_p T_p + e_m T_m}{e_p e_m} \tag{3.5}$$

where T^* represents the interface temperature, e the thermal diffusivity and subscripts p and m denote the polymer and mould sections, respectively. Temperatures in the bulk polymer (T_p) were taken as the peak temperatures of the thermocouple recordings in the bulk material while the temperature in the bulk of the mould (T_m) was assumed to be 25°C. The thermal effusivity of a given material was calculated from the square root of its thermal conductivity by its volumetric heat capacity and are listed in Table 3.2.

3.3.5   Monomer conversion

The curing degree of formed polymer was assessed by Fourier-transform infrared spectroscopy (FTIR). Strips of about 4 mm were cut transversely to the front direction and subsequently ground to a powder. FTIR signals were recorded over a range of 650-4000 cm^{-1} at an interval of 4 cm^{-1} and spectra were averaged over 64 scans. Conversions were calculated from the deconvoluted 789 cm^{-1} oxirane absorbance peak height relative to the 1724 cm^{-1} -C=O peak after baseline correction, with uncured resin used as reference material, i.e.:

$$A_0 = 1 - \frac{\left(A_{0,789} / A_{0,1724}\right)_P}{\left(A_{0,789} / A_{0,1724}\right)_R} \tag{3.6}$$

where A_0 represents the absorbance and subscripts P and R refer to the formed polymer and uncured resin, respectively. FTIR analysis was limited to pure polymer samples since the presence of fibres was expected to result in significant attenuation of the FTIR signal while also bringing complications in the sample preparation.

3.3.6   Localised initiator deposition

Solutions for localised initiator deposition were prepared by the dissolution of IOC-8 SbF$_6$ photoinitiator in acetone. Fibrous preforms were cut to layers of 80×60 mm and sizings were burnt-off at 450°C in a Nabertherm B400 furnace for 2.5 hours. The initiator solution was

sprayed onto fabrics, which were placed onto a metallic grid after cooling down, and were subsequently dried in a 85°C oven for two hours ensure complete evaporation of the solvent. Composites were produced following the procedure described in Section 3.3.1.3.

The photoinitiator efficacy after the deposition process was validated by the dissolution of 300 mg IOC-8 SbF_6 in 10 mL of acetone. The solution was heated at 85°C until the acetone was completely evaporated. A resin containing 0.75 w% photoinitiator, 0.05 w% photosensitiser and 1% thermal initiator was then prepared following the procedure described in Section 3.1 and analysed by dynamic DSC, described in Section 3.3.2. The resin was moreover used to produce carbon FRPs and compared to FRPs produced with pristine IOC-8 SbF_6.

Calibration of the spraying method, i.e. the amount and concentration of photoinitiator required to deposit a set content onto the fibre surface, was done by assessing the deposited photoinitiator content as a function of the sprayed quantity and the photoinitiator concentration in the spray. Fabrics were weighed after spraying to determine the deposited spray quantity. The deposited photoinitiator was extracted after evaporation of the solvent using a Soxhlet extraction. Five fabrics with an expected deposited photoinitator quantity of 4.3 mg were placed in a cellulose Soxhlet thimble that was placed in a 100 mL Soxhlet extractor connected to a 500 mL round-bottomed flask filled with 200 mL acetone and a Friedrichs condenser. The flask was placed in a silicon oil bath set to 95°C to created 4-6 refluxes per hour for approximately 24 hours. 30 grams of the resulting solution was heated to 85°C until reduced to 3 grams as to concentrate the solution by 10 times. The photoinitiator concentration was estimated by UV-Vis spectroscopy, following a procedure described in Section 3.2.5, and the Beer-Lambert law:

$$A_0 = \varepsilon \times c \times \ell \tag{3.7}$$

where A_0 denotes the absorbance, ε the molar attenuation coefficient, c the photoinitiator concentration and ℓ the optical path length. The molar attenuation coefficient of IOC-8 SbF_6 was determined using a calibration series of five solutions with concentrations ranging from 2.30-7.35 w%.

Fibre morphologies and surface compositions were analysed by a combination of scanning electron microscopy and energy dispersive X-ray spectroscopy (SEM-EDX, Zeiss GeminiSEM 300). Measurements were made on a pristine fabric and fabrics with 14.5 mg and 4.3 mg of photoinitiator deposited per 80×60 patch. Single yarns were removed from each fabric, cut to a length of ~1 cm and fixed on a sample holder with carbon tape. EDX measurements were carried out at a working distance of 8.5 mm and an acceleration voltage of 8.5 kV.

3.3.7   Analysis of chemical and mechanical properties of composites

A comparative assessment on the mechanical and chemical properties was made for FRPs produced by self-catalysed frontal polymerisation and oven-cured FRPs. Self-catalysed frontal polymerisation FRPs were produced following the procedure described in Section 3.3.1.4, using a 7.3 mm mould cavity and 18 layers of carbon twill fabric, corresponding to a V_f of 55-60% depending on the sample thickness. The energy consumption during UV-irradiation was recorded by a Voltcraft SEM6000 device placed in series with the UV-source.

Oven-cured reference samples were produced with three different resins, i.e. the RICFP resin system described in Section 3.1, Sicomin SR8100 & Sicomin 8822 hardener (Sicomin, France) and Araldite LY 8615US & Aradur 8615 hardener (Huntsman, Switzerland). Reference samples were prepared similar to Section 3.3.1.4 in the absence of a resin channel, using 18 layers of carbon twill fabric in a mould composed of steel mould halves with a cavity height of 5.3 mm. Impregnation of the fabrics was carried out at a rate of 30 mL/hr. Oven-cured RICFP samples were placed in an oven preheated to 150°C after the impregnation was completed while the temperature at the centre of the stack was recorded via an integrated thermocouple. The mould was removed after 25 minutes and left to cool at room temperature. Sicomin and Araldite samples were cured following their respective prescribed procedures, i.e. Sicomin samples were post-cured for 8 hours at 80°C after an initial 24 hours at room temperature while Araldite samples were cured for 24, 2 and 3 hours at respectively 40, 120 and 180°C. The energy demand of the oven-curing procedures was recorded by placement of the Voltcraft SEM6000 device in series with the oven.

T_gs were characterised by Dynamic Mechanical Analysis (DMA, TA Instruments DMA Q800) in three point bending mode with an oscillation strain and frequency set to 0.1% and 1 Hz, respectively. Samples were cut in strips of 55×10×5.3 mm parallel to the front direction and a minimum of three measurements were made per sample type. Measurements consisted of two subsequent heating cycles from 15-250°C and 15-300°C at a rate of 3°C/min. The T_g of
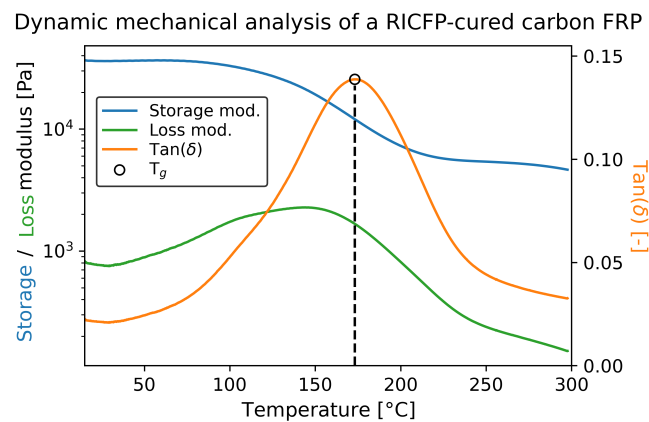
Figure 3.12: Exemplary dynamic mechanical analysis curves to determine the T_g of a carbon FRP produced by self-catalysed frontal polymerisation.

each cycle was determined from the maximum of the tan(δ) curve, representing the phase angle between storage and loss moduli as is illustrated in Figure 3.12.

Interlaminar shear strength of composite samples was characterised following ASTM standard D2344 using a universal tensile machine (UTM) Series LFM-125 kN (Walter & Bai, Switzerland) with a 10 kN load cell. Samples of 32×10.5×5.3 mm were placed on a three-point bending setup with 3 mm diameter supports and a 6 mm diameter loading nose. The span was set to 20 mm and a testing speed of 1 mm/min was used. The interlaminar shear strength was calculated from the maximum applied force (F_m) via the relation:

$$ILSS = 0.75 \frac{F_m}{w \cdot h} \tag{3.8}$$

where w and h represent the sample width and thicknesses, respectively. A minimum of four tests were carried out per sample and all samples failed in shear.

Young's moduli of the produced FRP samples were evaluated by measuring the ultrasonic resonance frequency by a Grindosonic Mk5 (Lemmens NV, Belgium) device. Rectangular samples with dimensions similar to those used in DMA measurements were used and Young's modulus was calculated following ASTM standard E1876.

3.4   Modelling of RICFP

3.4.1   Kinetic model fitting

Kinetic models of resin systems, prepared as described in Section 3.1, were derived for two resin systems. A resin composition for composite production, similar to the one used in Section 6, was composed of 0.75 w% IOC-8 SbF$_6$ photoinitiator, 0.05 w% ITX photosensitiser and 2.13 w% benzopinacol thermal initiator and is referred to as composite RICFP resin. The production of pure polymer on the other hand was simulated with concentrations of 0.3 w%, 0.05 w% and 0.8 w% of photoinitiator, photosensitiser and thermal initiator, respectively. This resin formulation is referred to as reduced RICFP resin in the continuation of this work. The enthalpy and conversion rates were determined by dynamic DSC analysis with measurement procedures similar to those described for dynamic analysis in Section 3.2.4 with heating rates (β) varied between 5-25°C/min following ASTM standard E698. A minimum of two repeats were made per heating rate. Resulting heat flows were corrected by a fitted third order polynomial baseline to elucidate the heat output by the resin from the heat losses to heat the sample, as well as to correct for potential artefacts due to weight difference between aluminium hermetic pans. The effective conversion of the sample was calculated from the cumulative heat output and the overall integrated resin enthalpy under the assumption that the maximum attainable conversion was achieved at the end of the measurement:

$$\alpha = \frac{q_t(T)}{H_r} \tag{3.9}$$

where α denotes the effective conversion, q_t the cumulative heat flow at temperature T and H_r the polymerisation enthalpy calculated as the integrated heat flow over the complete measurement range. A demonstration of the derived conversion from a dynamic DSC measurement is shown in Figure 3.13.
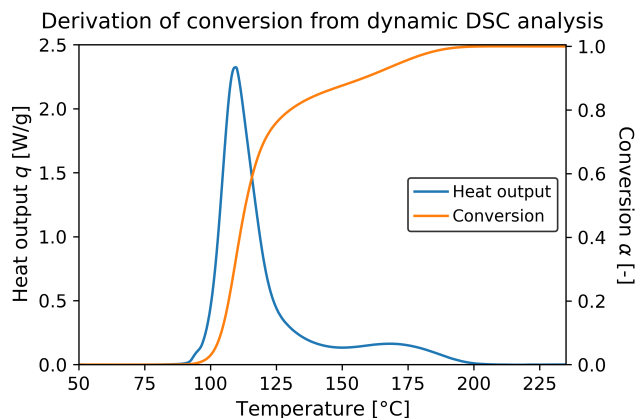
Figure 3.13: Exemplary dynamic DSC measurement and derivation of the effective conversion.

DSC analysis of RICFP resins consistently showed two peaks in the heat output and were therefore deconvoluted by a model similar to the Grindling model (Equation 2.9), assuming a two-stage process with two distinct terms in the reaction-kinetics model:

$$\frac{d\alpha}{dt} = k_1(T)f_1(\alpha) + k_2(T)f_2(\alpha) \tag{3.10}$$

where subscripts 1 and 2 denote the first and second apparent heat flow peaks as indicated in Figure 3.13. The reaction rate constants of Equation 2.6b were described by an Arrhenius function, i.e. Equation 2.7. The activation energy was derived using the Flynn-Wall-Ozawa method as described in ASTM standard E698. Following this method, the activation energy was calculated from the slope of the linear regression between the inverted peak temperatures (T_p), i.e. the temperature corresponding to the respective maximum heat outputs, recorded in DSC analysis, and the logarithmic heating rate ($\log(\beta)$).

The kinetics parts of Equation 3.10 was modelled by a model-free kinetics approach. After an initial assessment, a combination of an autocatalytic model with diffusion term for the initial autocatalytic curing, i.e. following Robertson et al. [20], and a nth order model for the second exothermic peak were considered to describe the autocatalytic RICFP process. Both models are listed in Table 2.1. The inclusion of a detailed model accounting for diffusion-controlled polymerisation into Equation 3.10 was considered out of scope for the current exploratory work. The combination of the diffusion term in the Prout-Tompkins model found to be a good representation for the averaged vitrification effects. This yields the following expression that was used to describe the cure kinetics of the RICFP system:

$$\frac{\partial\alpha}{\partial t} = A_1\exp\left(-\frac{E_{a,1}}{RT}\right)(1-\alpha)^{n_1}\alpha^m\frac{1}{1+\exp\left[c_d\left(\alpha-\alpha_c\right)\right]} + A_2\exp\left(-\frac{E_{a,2}}{RT}\right)(1-\alpha)^{n_2} \tag{3.11}$$

where A denotes the Arrhenius frequency factor, E_a the activation energy, n and m reaction orders and c_d and α_c diffusion constants.

The remaining seven parameters of Equation 3.11, i.e. A_1, n_1, m_1, c_d, α_c, A_2 and n_2, were simultaneously fitted to the complete set of dynamic DSC recordings. A Covariance Matrix Adaptation Evolution Strategy (CMA-ES), following the work of Bernath et al. [201], was employed for this complex fitting procedure. CMA-ES is a stochastic method for the optimisation of highly non-linear functions [230] as demonstrated in Figure 3.14. The cost-function was defined as the mean sum of squares (*MSS*) between the fitted conversion rates and their corresponding experimental values derived by DSC analysis:

$$MSS = \frac{1}{n}\sum_{i=1}^{n}\left[\left.\frac{d\alpha_i}{dt}\right|_{exp} - \left.\frac{d\alpha_i}{dt}\right|_{pred}\right]^2 \tag{3.12}$$
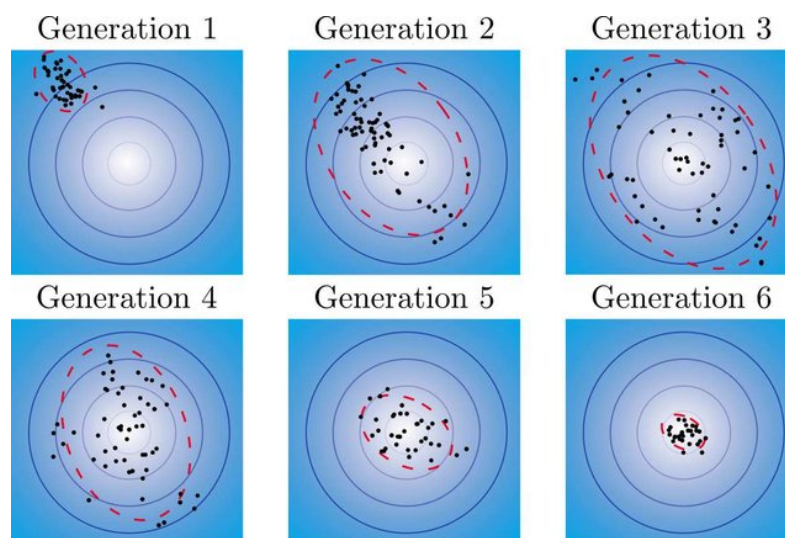
Figure 3.14: Schematic representation of the CMA-ES optimisation procedure (Source: [229]).

Table 3.3: Overview of densities and temperature-dependent heat capacities for RICFP resin, carbon & glass fibre and PMI foam derived by DSC analysis.

Material	Density [g/cm^3]	Thermal conductivity [W/m/K]
RICFP system	1.05	0.17
Carbon fibre	1.8	10.45
Glass fibre	2.6	1.3
PMI foam	0.11	0.029

where n is the sample size and subscripts exp and $pred$ refer to the experimental and fitted conversion rates, respectively.

3.4.1.1 Derivation of model parameters

Solving Equation 2.6a required the derivation of the heat capacity, density and thermal conductivity of the components making up the experimental configuration. Heat capacities of ECC monomer resin and polymer, carbon fibrous reinforcement and PMI foam were determined by modulated DSC over a range of 15-250°C at a rate of 5°C/min and a modulation rate of 1°C/min. Formed polymer, carbon fibre and PMI foam were ground to a powder before placement in aluminium hermetic capsules. Sample weights were ~7-8 mg while the temperature-dependence of the resulting heat capacities was described by linear regression. The temperature-dependent heat capacity of glass fibre was derived from generic material databases.

Densities of all components were provided by the supplier. The thermal conductivity of the

RICFP system was taken as 0.17 W/m/K [231], under the assumption of similar thermal conductivities between the monomer resin and the formed polymer, while the thermal conductivity of PMI foam was estimated to be 0.029 W/m/K. The anisotropic thermal conductivity of woven preforms was taken as the mean of the in-plane (κ_{ip}) and through-thickness component (κ_{tt}):

$$\kappa_c = 0.5 \cdot \left(\kappa_{ip} + \kappa_{tt}\right) \tag{3.13}$$

In-plane thermal conductivity was calculated by a rule of mixtures, i.e. Equation 2.18 while the thermal conductivity in through-thickness direction was calculated by the semi-empirical Clayton model [232] at the same V_f:

$$k_{c,tt} = \frac{k_m}{4} \left[\sqrt{\left(1 - V_f\right)^2 \left(\frac{k_{f,t}}{k_m} - 1\right)^2 + \frac{4 k_{f,t}}{k_m}} - \left(1 - V_f\right) \left(\frac{k_{f,t}}{k_m} - 1\right) \right]^2 \tag{3.14}$$

where κ denotes the thermal conductivity with subscripts c, f and m referring to the composite, fibre and matrix. Subscripts tt and t refer to the respective through-thickness and transverse directions and V_f to the fibre volume fraction. The axial thermal conductivities of carbon and glass fibre were assumed, based on generic material databases and Refs. [20, 176, 220], to be 10.45 and 1.3 W/m/K, respectively, and an orthotropic ratio of 5 was assumed for the transverse direction. Using the described relations, in-plane and through-thickness conductivities of carbon FRPs were estimated to be 1.54 and 0.38 W/m/K respectively at a V_f of 40%. Predicted thermal conductivities of 2.54 and 0.68 W/m/K at 60% V_f were in line with experimentally reported values [224]. In a similar way, the thermal conductivity of glass FRP systems was determined to be 0.42 W/m/K in in-plane and 0.20 in through-thickness direction, also assuming a V_f of 40 %. Equation 3.13 then yields an estimated thermal conductivity of carbon and glass FRPs of 1.61 and 0.31, respectively, at a V_f of 40%.

3.4.2 Numerical implementation

The RICFP process was modelled using a finite difference method that was implemented in Python. Simulations were generally carried out in a two-dimensional domain while one-dimensional simulations were, because of their computational efficiency, used for initial approximations or fitting procedures. The heat equation, i.e. Equation 2.6a, was discretised using an explicit Euler forward difference method in time and a central difference space in space, i.e.:

$$f'(x) = \frac{f(x+h) - f(x)}{h} \quad \text{and} \quad f''(x) = \frac{f(x-h) - 2f(x) + f(x+h)}{h^2} \tag{3.15}$$

which, considering element dimensions Δx & Δy and timestep Δt for an element i, j at time

t, allows for discretisation of the temperature gradients in x- and y-direction as well as the transient temperature change as:

$$\frac{\partial^2 T}{\partial x^2} = \frac{T_{i-1,j}^t - 2T_{i,j}^t + T_{i+1,j}^t}{(\Delta x)^2} \quad , \quad \frac{\partial^2 T}{\partial y^2} = \frac{T_{i,j-1}^t - 2T_{i,j}^t + T_{i,j+1}^t}{(\Delta y)^2} \quad , \quad \frac{\partial T}{\partial t} = \frac{T_{i,j}^{t+1} - T_{i,j}^t}{\Delta t} \quad (3.16)$$

Substitution of these terms into Equation 2.6a and subsequent rearrangement then allows for an explicit description for calculation of the temperature evolution in a two-dimensional domain that was solved at time *t*:

$$T_{i,j}^{t+1} = T_{i,j}^t + \frac{\Delta t}{\rho C_p}\left[\frac{\kappa_c}{(\Delta x)^2}\left(T_{i-1,j}^t - 2T_{i,j}^t + T_{i+1,j}^t\right) + \frac{\kappa_c}{(\Delta y)^2}\left(T_{i,j-1}^t - 2T_{i,j}^t + T_{i,j+1}^t\right)\right]$$
$$+ \frac{(1-V_f)H_r\Delta t}{C_p}\frac{\partial \alpha}{\partial t} \quad (3.17)$$

where $T_{i,j}^t$ denotes the temperature of element at location i, j at time t and Δx and Δy the element height and width, respectively. The discretisation is moreover schematically illustrated in Figure 3.15. The material constants were adapted to the corresponding domain, i.e. for the composite domain ρ and C_p were taken as the respective density and heat capacity of the RICFP system, determined from Table 3.3 and a rule of mixtures as function of the V_f (Equations 2.16 & 2.17) while κ_c denotes the thermal conductivity (Equation 3.13) of the same system and H_r the resin enthalpy corrected for the V_f (Equation 2.15). The mould domain was simulated using the corresponding material parameters listed in Table 3.3 with an assumed isotropic thermal conductivity while the heat generation term was omitted due to the absence of exothermic components. One-dimensional models were discretised considering the described composite domain with j set uniformly to one while omitting the term dependent on Δy.

The curing degree of the resin system of Equation 3.11 was also discretised using an explicit forward Euler scheme in time, yielding:

$$\alpha_{i,j}^{t+1} = \alpha_{i,j}^t + A_1 \exp\left(-\frac{E_{a,1}}{RT}\right)(1-\alpha_{i,j}^t)^{n_1}\left(\alpha_{i,j}^t\right)^m \frac{1}{1+\exp\left[c_d\left(\alpha_{i,j}^t - \alpha_c\right)\right]}$$
$$+ A_2\exp\left(-\frac{E_{a,2}}{RT}\right)(1-\alpha_{i,j}^t)^{n_2} \quad (3.18)$$
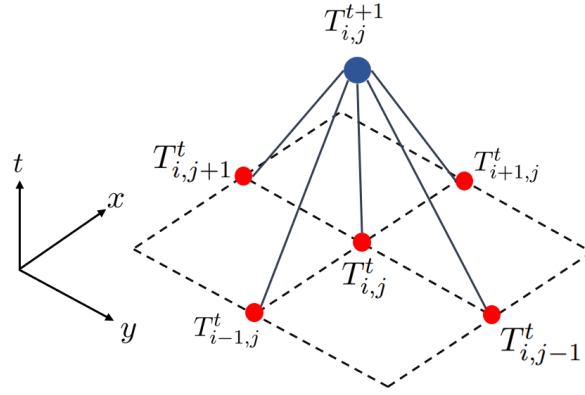
Figure 3.15: Schematic illustration of two-dimensional discretisation for solving the Equation 3.17.

3.4.3   Domain & boundary conditions

Two-dimensional simulations were performed on a domain, schematically presented in Figure 3.16, that was composed of a horizontal 25×5.3 mm region comprising the RICFP composite system that was vertically enclosed by domains representing the mould material with a length of 25 mm and a height generally taken as 15 mm. Perfect thermal contact was assumed between the composite system and the mould and a symmetry condition was applied over the centreline of the domain to reduce computational cost. A convective boundary condition was set at the extremes of the domain as:

$$\kappa \frac{\partial T}{\partial x}\bigg|_{bc} = h_T(T|_{bc} - T_\infty) \quad \text{and} \quad \kappa \frac{\partial T}{\partial y}\bigg|_{bc} = h_T(T|_{bc} - T_\infty) \tag{3.19}$$

where κ denotes the thermal conductivity of the material at the domain boundary, $T|_{bc}$ the temperature at the boundary, T_∞ the temperature of the environment away from the boundary, set to 25°C and h_T the heat transfer coefficient, which was fixed to 15 W/m^2/K based on Refs. [172, 233]. In a discretised form, i.e. after substitution of Equation 3.15, the temperatures of boundary elements were computed at each timestep, for example for an element at the horizontal boundary, as:

$$T_{x,j}^t = \frac{T_{x-1,j}^t + \frac{T_\infty h_T \Delta x}{\kappa}}{1 + \frac{h_T \Delta x}{\kappa}} \tag{3.20}$$
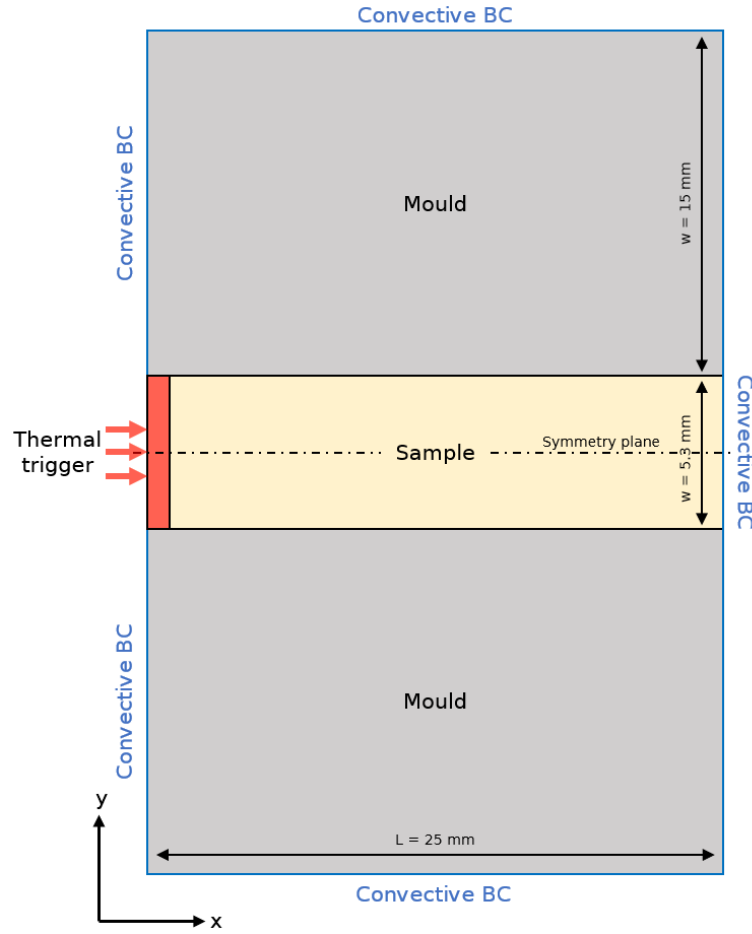
Figure 3.16: Schematic illustration of the two-dimensional modelling domain. Acronym 'BC' denotes the boundary condition.

3.4.4   Meshing & Numerical stability

Domains were meshed with square elements of which the element size was varied between cases so as to optimise the concurrent resulting model accuracy and computational cost. Mesh sizes and timesteps were varied to identify the numerical stability regions. These were related to the Von Neumann stability criterion, which defines a stable window when applied to linear partial differential equations [234]. When applied to the classical heat equation, i.e Equation 2.6a without the heat generation term, the Von Neumann stability criterion yields:

$$\frac{\kappa}{\rho C_p} \frac{\Delta t}{(\Delta x)^2} \leq \frac{1}{2} \quad \rightarrow \quad \Delta t \leq \frac{(\Delta x)^2}{2} \frac{\rho C_p}{\kappa} \tag{3.21}$$

which defines an upper bound for the timestep Δt that is quadratically related to the element size Δx.
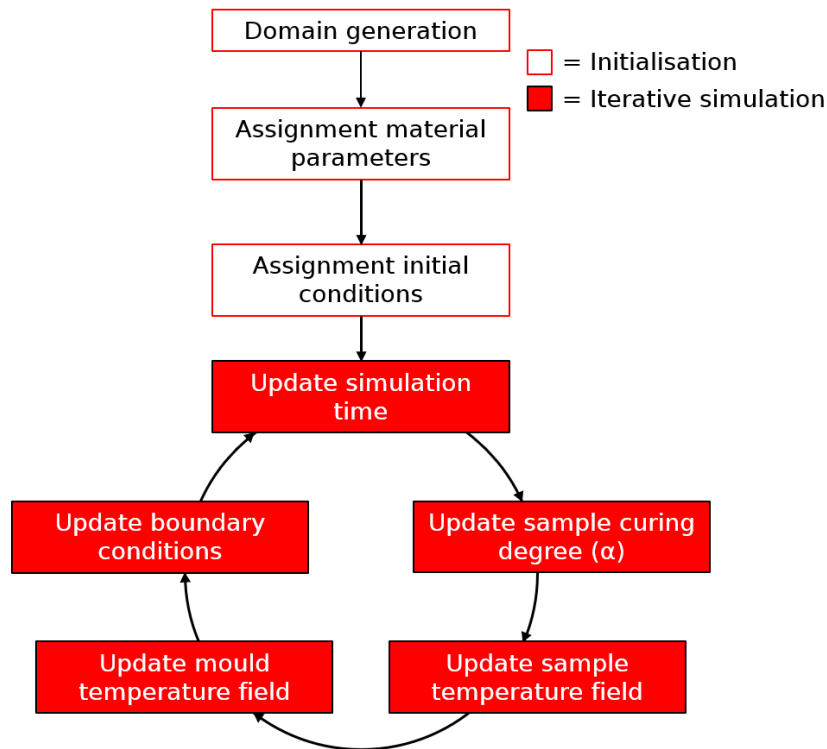
Figure 3.17: Schematic illustration of the solving procedure used for finite difference modelling of RICFP.

3.4.5 Solving procedure

The finite difference models were solved as schematically illustrated in Figure 3.17. Calculations commenced with the initialisation of the sample and mould domains and assignment of the respective material properties and initial conditions, i.e. initial temperature and curing degree. The model was then iteratively solved for each timestep in the set simulation time. Each iteration started by updating the curing degree of the sample domain using Equation 3.18. The updated conversions were subsequently used to determine the temperature fields of the sample domain via Equation 3.17, followed by calculation of temperature fields of the mould domains and updating of the boundary temperatures.

3.4.6 Experimental validation & fitting

Numerical results were validated using an experimental configuration as described in Section 3.3.1.4 with a mould cavity height of 5.3 mm and in the absence of a resin channel. Experiments were carried out using the resin systems described in Section 3.4.1, i.e. a pure polymer, using the reduced RICFP resin system, and carbon and glass FRPs composite systems. The V_f of FRPs were varied based on the number of resin layers and were kept around 35-40%. Four thermocouples were integrated in the centre of the mould cavity at different positions along

the front direction. Spacings were kept around ~20 mm and exact locations were determined by optical analysis of an image taken after placing the thermocouples. Temperature profiles were recorded and used to determined the front temperatures and front velocities as described in Section 3.3.3.

Numerical models were fitted to the experimental data to improve their accuracy. Averaged temperature profiles were used to reduce the influence of the experimental variability inherent to RICFP, in particular in the presence of fibrous reinforcements. The fitting procedure was carried out as a grid search using a one-dimensional domain to reduce the computational cost. Numerical optimisation focused on the fitting of the thermal conductivity and resin enthalpy for both the reduced and composite RICFP resin systems since these parameters were prone to the largest experimental uncertainty. Optimum parameters were initially selected to approximate the front temperature and velocity with a set accuracy, as is further discussed in Section 7.4. A final selection was then made based on the similarity of the temperature profile with the averaged experimental temperature profiles. This comparison was made considering the temperature profiles up to 150°C to elucidate the phase largely dependent on thermal diffusion from the phase of rapid autocatalytic heat release since the latter is already considered as it strongly influences the peak temperature. The fitting accuracy was quantified by the mean squared error (MSE) of the experimental and numerical temperature profiles:

$$MSE = \frac{1}{n} \sum_{i=1}^{n} \left[\left. T_i \right|_{exp} - \left. T_i \right|_{pred} \right]^2 \tag{3.22}$$

with subscripts exp and $pred$ denoting the experimental data and numerical predictions. The accuracy of the optimised parametric combinations was subsequently confirmed by their implementation on a two-dimensional domain.

4 Microstructural evaluation by in-situ UV-flow freezing

In-situ UV-photopolymerisation is, as highlighted in Section 2.3, considered a promising strategy for microstructural evaluation of infiltrating resin flows in LCM as it has the potential to overcome the time constraints of high spatial resolution characterisation methods. Based on the methodology proposed by Caglar et al. [47], this chapter presents the further development of the in-situ UV-flow freezing methodology to ensure the accuracy of the captured microstructural representations of dynamic flows in fibrous preforms. The undertaken steps consist of 1. the development of a fast-curing resin formulation, 2. optimisation of the methodology and 3. assessment of microstructures by μCT. This chapter focuses on the use of epoxide systems as these were believed to be the most accurate representation of commercially used resin systems while variations of the resin composition are proposed for facile variation of the capillary number.

4.1 Resin development

4.1.1 Photocuring epoxide resin

Adaptation of the resin composition and its resulting UV-photopolymerisation characteristics can be regarded as the basis for the in-situ flow freezing methodology. To generate accurate representations, resins were optimised to display rapid conversions from a liquid state, i.e. with viscosities in the order of conventional commercial resin systems, to a set polymer that retains its position and morphology despite potential backpressure exerted by the uncured resin in the fabric stack. The flow freezing behaviour of resins was simulated by photorheology measurements as described in detail in Section 3.2.2. Experiments aimed to be carried out in the linear viscoelastic region (LVR) to minimise potential experimental errors induced by the set measurement parameters and hence to increase the confidence in the observed trends. However, since the LVR behaviour is typically in competition with the measurement accuracy due to torque levels that approach the machine limit, which, combined with the large range of viscosities encountered during photocuring, limit the operation window that can be chosen. Figure 4.1 shows that measurements at low viscosity require a minimum oscillation strain
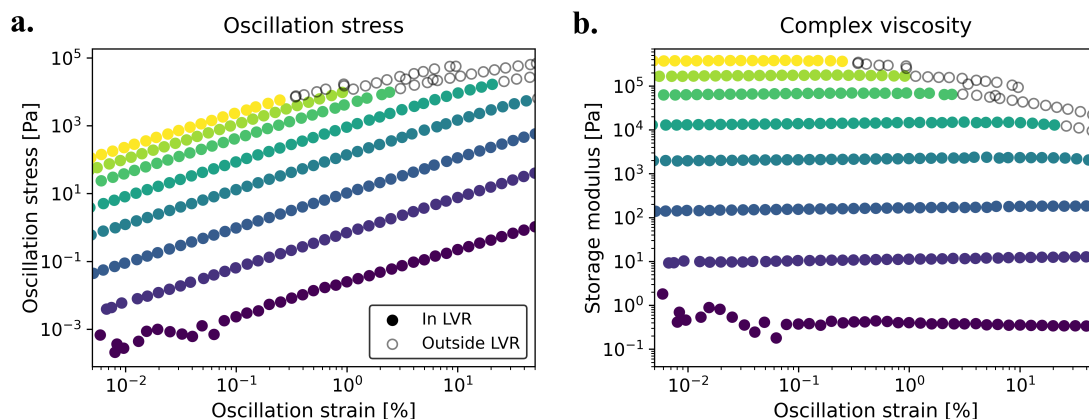
Figure 4.1: Definition of a processing window in the linear viscoelastic region for rheological assessment of an epoxide resin at different curing degrees as a function of a) the oscillation stress and b) the complex viscosity.

to overcome the torque limit and thereby avoid scattering of the recorded oscillation stress (Figure 4.1a) being translated to e.g. the complex viscosity (Figure 4.1b). Too high oscillation strains on the other hand resulted, predominantly at high curing degrees, in an inflexion of the oscillation stress and a sudden drop of the complex viscosity. An oscillation strain of 1% presented a good compromise, allowing for stable recordings at low viscosity while recordings remained in the LVR up to complex viscosities of $\sim 10^5$ Pa·s.

Fast UV-photopolymerisation requires the rapid generation of active centres upon the absorbance of UV-light, which is directly dependent on the reactivity of the photoactive compound in a resin system. IOC-8 SbF$_6$ was selected as photoinitiator, e.g. over 4-isobutylphenyl-4'-methylphenyliodonium hexafluorophosphate used by Caglar et al. [47], since the rate of polymerisation in epoxide systems is reported [147, 149] to scale with the photoinitiator reactivity. Increasing photoinitiator concentrations were found to result in slight increases of the induction time, i.e. the time between the start of irradiation and the onset of the initial viscosity increase, as shown in Figure 4.2a. Concentrations of 2 & 4 w% moreover showed increased scattering. While the absolute differences remain close to the measurement, the trend observed in Figure 4.2a was attributed to increased shielding by the photoactive compound [149], and hence delayed transmission rates of UV-light. The gelation time in Figure 4.2b on the other hand was found to decrease with increasing photoinitiator concentrations which is likely explained by the increased number of active centres that could be simultaneously formed with an increased photoinitiator content, resulting in higher polymerisation rates and hence reduced gelation times. A photoinitiator concentration of 1 w% was found to be the optimum as it allowed for both low induction and low gelation times.

Further enhancement of the UV-absorbance characteristics was achieved the use of a photosensitising compound. While the selected compound is identical to the one proposed by Caglar et al. [47], its molar ratio compared to the photoinitiating compound was found to
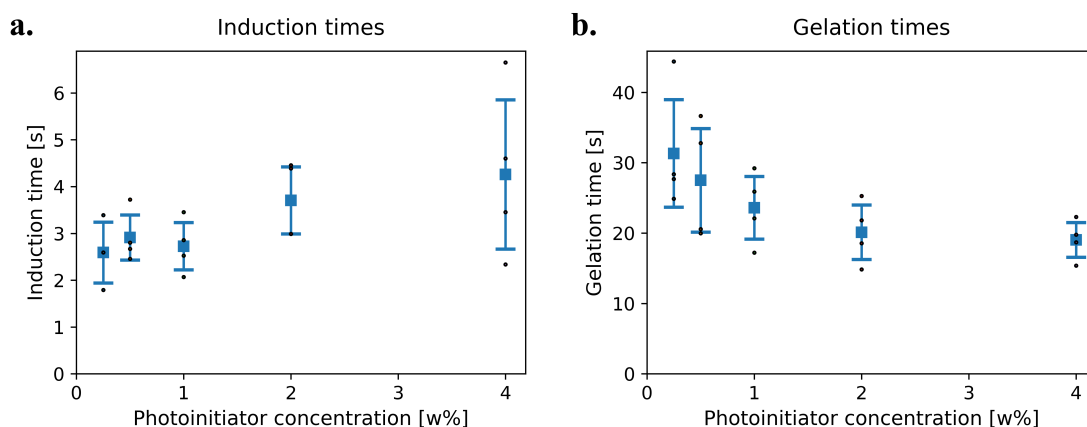
Figure 4.2: Photorheological assessment on the a) induction and b) gelation times with varying photoinitiator content.
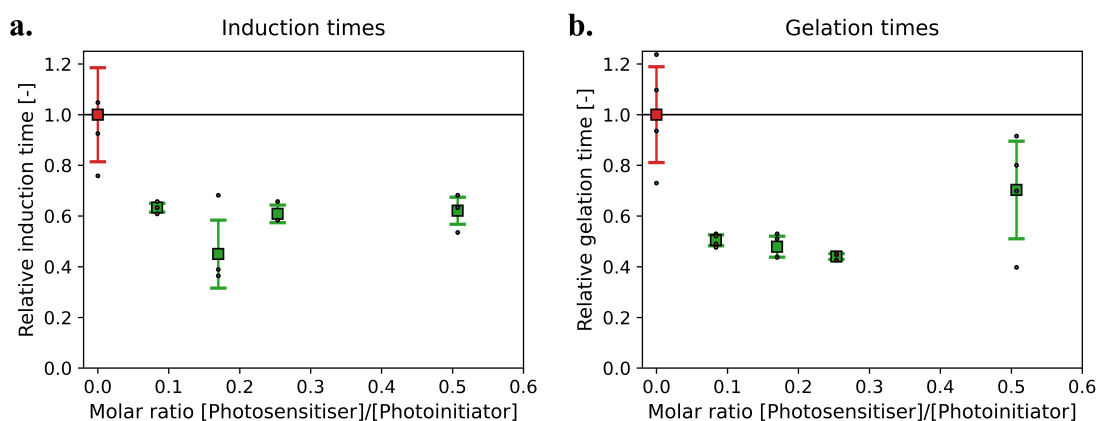
Figure 4.3: Photorheological assessment on the a) induction and b) gelation times with varying molar ratios of photoinitiating and photosensitising compounds.

be of significant influence on the photo-curing kinetics. Figure 4.3 shows that the addition of an ITX photosensitiser resulted in a strong decrease of both the induction and gelation times (Figure 4.3a and Figure 4.3b, respectively) due to the improved overlap between the resin absorbance spectrum and the emission of the used UV-sources, which is confirmed by UV-vis spectroscopy in Figure 4.4. Molar ratios between 0.2-0.3 were found the optimum and resulted in reductions in induction and gelation time of up to 56.0 and 55.0%, respectively. Increased molar ratios resulted in scattering of the gelation times, which was attributed to the aforementioned shielding effects.

Photopolymerisation in the case of composite materials is typically complicated by the extensive attenuation and scattering of the filler material. The in-situ flow freezing methodology was expected to suffer from similar limitations and it was found unlikely that the maximum attainable conversion would be achieved in the presence of (glass) fibrous reinforcement with
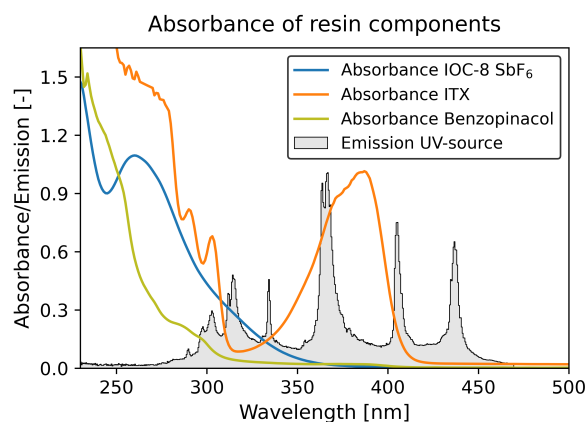
Figure 4.4: Absorbance of the different components of the developed UV-photopolymerisation resin. Resin constituents were recorded after dissolution in dichloromethane at a concentration of 0.05 mM.

elevated (e.g. >35%) V_fs. A postcuring procedure was therefore established to ensure complete solidification of the flow front, allowing for post-processing and μCT analysis without introducing distortions in the front morphology. DSC analysis in Figure 4.5a showed that a resin consisting of ECC monomer, a photoinitiator and photosensitiser underwent thermal curing at temperatures above ~135°C and maximum heat outputs were recorded at 143°C. The addition of benzopinacol as a free-radical (thermal) initiator, i.e. inducing RICP [143], significantly lowered the temperature required for thermal curing. A benzopinacol concentration of 0.5 w% was found the optimum as allowed for formation of polymer with high curing degrees, based on the total enthalpy of 552.7 J/g, at limited temperatures of 100-120°C while being sufficiently low to avoid the onset of frontal polymerisation. Simulation of the foreseen oven curing procedure at 120°C by a quasi-isothermal DSC procedure shown in Figure 4.5 confirms the benefit of the introduced RICP mechanism for postcuring, showing a large heat output when reaching the isothermal temperature while being significantly lower when no free-radical thermal initiating compound was added. An assessment of the absorbance spectra in Figure 4.4 moreover showed that the absorbance spectra of benzopinacol only slightly overlapped with the emission spectrum of the UV-source and hence is believed to be of negligible influence on the UV-photopolymerisation behaviour of the developed resin composition.

An optimised resin composition was therefore concluded to be composed of 1 w% IOC-8 SbF$_6$ photoinitiator, 0.1 w% ITX photosensitiser and 0.5 w% benzopinacol thermal initiator. This fast-curing resin system has the potential to achieve gelation within 13 seconds at UV-intensities >200 mW/cm^2 while viscosities of 10 Pa·s were typically attained within 10 seconds. Figure 4.6 shows that the photocuring behaviour of the developed resin is highly dependent on the incoming light intensity and a significant decrease was observed at low UV-intensities, i.e. <100 mW/cm^2. The latter might be significant due to the attenuation and scattering induced by the presence of glass fibres in UV-flow freezing experiments, especially within the yarns
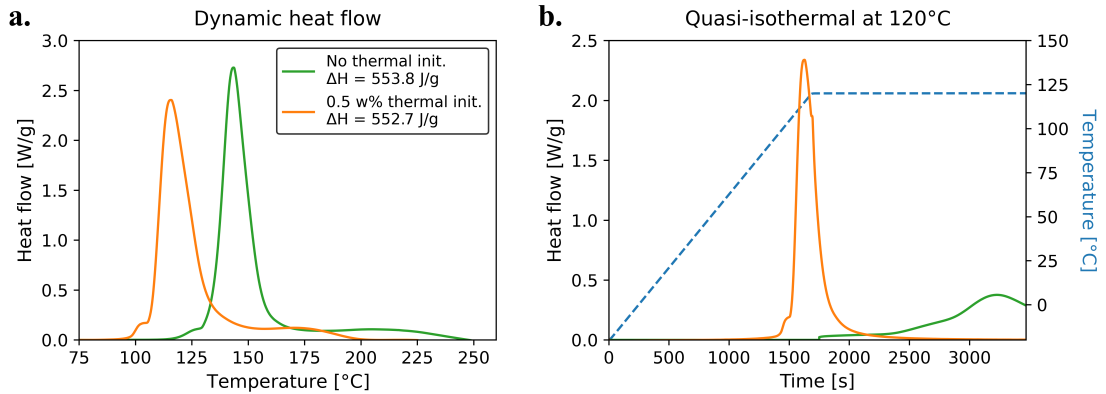
Figure 4.5: Analysis of postcuring of resins with and without thermal initiating compound: a) dynamic heat flow measurements and b) simulation of oven curing by a quasi-isothermal measurement at 120°C.
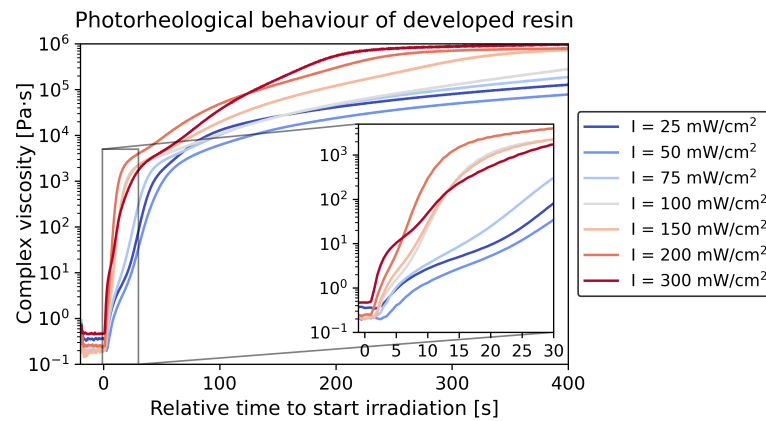
Figure 4.6: Photorheological behaviour of the standard resin with varying UV-irradiation intensities.

where the density of fibres is the highest, and it supports the need of a dedicated postcuring process. While curing rates and their dependence on the UV-intensity could likely be improved by e.g. the use of more reactive acrylate systems, at the cost of increased dissimilarity with commercial (epoxide) resin formulations, the curing rates of the current system were expected to be sufficient to obtain an accurate representation of the flow front morphology at yarn-scale. Further expansion of the methodology to allow for the assessment of intra-yarn morphologies and e.g. contact angles, are believed to require both increased curing rates as well as an assessment of the shrinkage upon polymerisation.

4.1.2 Additives for variations of the capillary number

As discussed in Section 2.2.2, the capillary number (Ca) is known to play an important role in determining the flow behaviour in LCM processing. A complete and predictive understanding
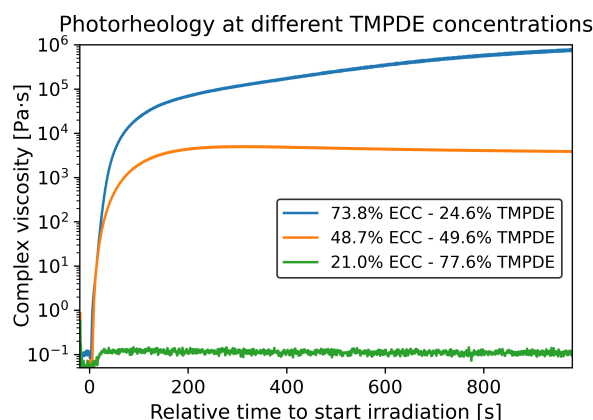
Figure 4.7: Photorheological behaviour of epoxide resins with different TMPDE contents.

of the optimum Ca, corresponding to a balanced flow morphology with minimum porosity [11], has however not been achieved to-date. While contributing to the understanding of the relation between Ca and the flow morphology for a given resin-system and set processing conditions is considered out of scope for the current thesis work, suitable additives were identified that allow for straightforward variation of the Ca using the in-situ UV-flow freezing methodology.

Trimethylolpropane diallyl ether (TMPDE) was identified as a suitable diluent for the resin system described in Section 4.1.1, i.e. to induce variations in the resin viscosity. Due to the absence of epoxide functional groups, TMPDE was mainly believed to act as a charge transfer agent, contributing to the rate of polymerisation without being incorporated in the polymer network. The latter however decreases the maximum attainable viscosity upon polymerisation with an increasing TMPDE content, as was confirmed by photorheological analysis presented in Figure 4.7. TMPDE contents up to ~25 w% were found to both enhance the rate of viscosity increase as well as the final viscosity. Further increase of the TMPDE concentration on the other hand were found to increasingly impede the formation of a solid polymer, with resulting viscosities remaining well-below 1 Pa·s at an ECC/TMPDE ratio of 20/80% by weight. The TMPDE content was therefore kept below 20 w% to ensure that the resulting polymer be sufficiently solidified to avoid any undesired distortions of the flow front morphology during its post-processing and analysis.

Variations of the liquid-vapour surface tension were induced by the addition of small quantities of hexadecyltrimethoxysilane (HDMSi). The addition of 5% HDMSi was sufficient to reduce the surface tension of the ECC resin described in Section 4.1.1 by over 10 mN/m. As illustrated in Figure 4.8, variations of the surface tension in a combined system are largely governed by HDMSi content while the TMPDE concentration is most influential for the resin viscosity.

The resin viscosity is known to be highly temperature-dependent, as illustrated Figure 4.9, resulting in a decrease in viscosity up to ~30-40% when increasing the temperature from 20 to
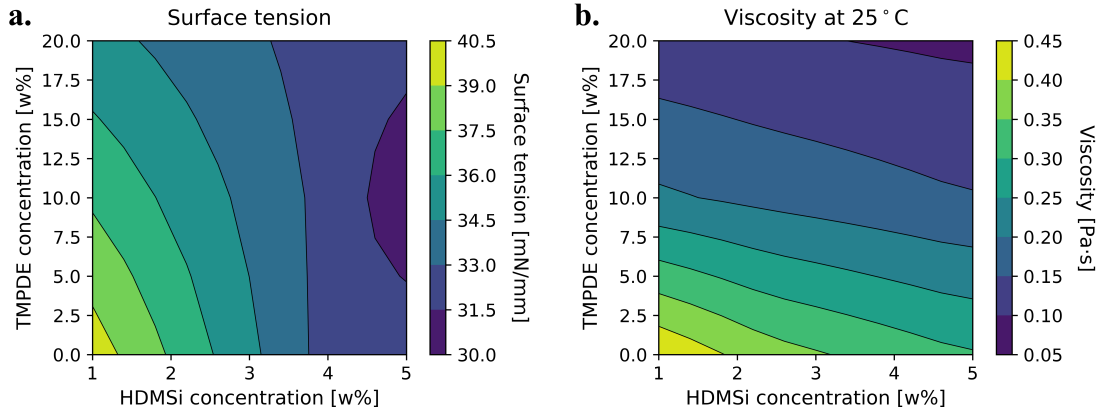
Figure 4.8: Influence of additives TMPDE and HDMSi on a) the surface tension and b) the viscosity of an epoxide resin system.
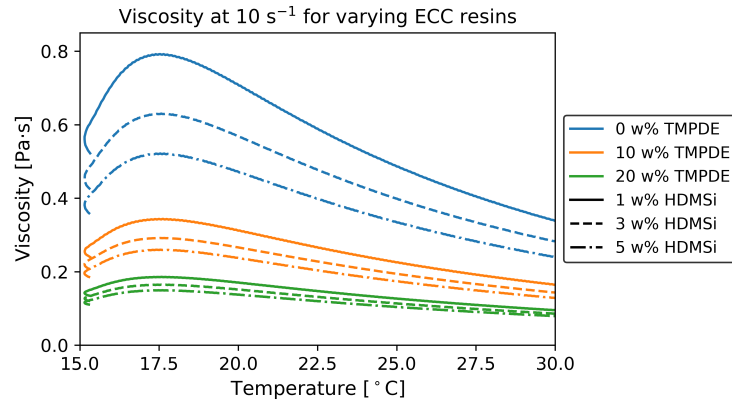
Figure 4.9: Viscosity-temperature relation of the considered resin formulations.

30°C. Not accounting for the temperature dependence of the resin viscosity would, following Equation 2.1, result in a similar error in the capillary number. Accurate definitions of the capillary number could be made based on the fitting of the viscosity curves of Figure 4.9 by Equation 3.1. The resulting Arrhenius parameters are listed in 4.1. The combination of Figure 4.8 and 4.1 can be regarded as an instrument for fine tuning of the resin properties which could be further employed to induce variations in the Ca.

4.2 Method optimisation

In addition to the curing characteristics of the resin, optimisation of the overall methodology for in-situ flow freezing was required to ensure that accurate representations of the dynamic flow front morphologies were obtained. Several adaptations in the methodology were made compared to the one proposed by Caglar et al. [47]. The number of fabric layers was increased to reduce the relative influence of the wall-effects discussed in Section 2.3.2. Infiltration under

Table 4.1: Fitted Arrhenius parameters to describe the temperature dependence of resins with additives.

	Concentration			
ECC [w%]	TMPDE [w%]	HDMSi [w%]	Frequency factor [s^{-1}]	Activation energy [kJ/mol]
100	0.0	0.0	$3.05 \cdot 10^{-10}$	-51.34
99.0	0.0	1.0	$1.12 \cdot 10^{-10}$	-55.01
97.0	0.0	3.0	$2.81 \cdot 10^{-10}$	-52.24
95.0	0.0	5.0	$4.84 \cdot 10^{-10}$	-50.46
89.0	10.0	1.0	$9.53 \cdot 10^{-10}$	-47.80
87.0	10.0	3.0	$1.57 \cdot 10^{-9}$	-46.19
85.0	10.0	5.0	$1.74 \cdot 10^{-9}$	-45.66
79.0	20.0	1.0	$3.23 \cdot 10^{-9}$	-43.35
77.0	20.0	3.0	$4.44 \cdot 10^{-9}$	-42.28
75.0	20.0	5.0	$6.33 \cdot 10^{-9}$	-41.19

a constant imposed flow rate was believed to be beneficial over the impregnation under a constant applied pressure since the latter would result in a decrease of the flow velocity, and hence Ca, with the infiltration length. The observed flow front morphology may in this case not directly correspond to the given Ca due to difficulties at estimating the flow velocity at the instant of UV-flow freezing. Moreover, a delay might be present for the front to adapt to its desired morphology and hence the captured morphology might not directly represent the steady-state situation at a certain Ca. These phenomena would be avoided if resins propagate through the preform at a constant velocity, which is was achieved by the application of a constant flow rate.

Maintaining a constant infusion rate requires the inlet resin pressure, imposed by the syringe pump, to be gradually increased with increasing impregnation length. Consequently, resins were subjected to a significant pressure gradient when reaching the desired ~two-thirds of the fabric length where flow freezing takes place. Figure 4.10a shows that the resin pressure at the inlet was in the order of 0.3-0.7 bar for a typical range of infusion rates. Inlet pressure only slowly recovered after switching off the syringe pump. An investigation on the influence of these retaining hydrodynamic pressures using a non-curing resin showed that the pressurised resins induced significant movements of the flow front of up to 7.6 and 18.3 mm in two minutes for flow rates of 30 and 110 mL/hr, respectively, as illustrated in Figure 4.10c. The front progression moreover induced changes in the flow front morphology, partially equilibrating the typical dual-scale morphology.

The undesired flow front progression was minimised by removal of the inlet tube, which allowed for backwards flow of the resin in the inlet system and resin pool and thereby for rapid relaxation of the resin pressures as shown in Figure 4.10b. Removal of the hydrodynamic forces acting on the resin made that fronts only propagated by capillary forces (Figure 4.10c),

limiting the propagation to a few millimetres. The capillary-driven flow nevertheless induced changes of the flow front morphology, which, amplified by the woven architecture of the fibrous preform, resulted in a more blurred appearance of the front. The limited movement of the flow front was believed to be sufficiently reduced to obtain a representative image of the dynamic flow front after UV-flow freezing and were in the same order as front movement rec-
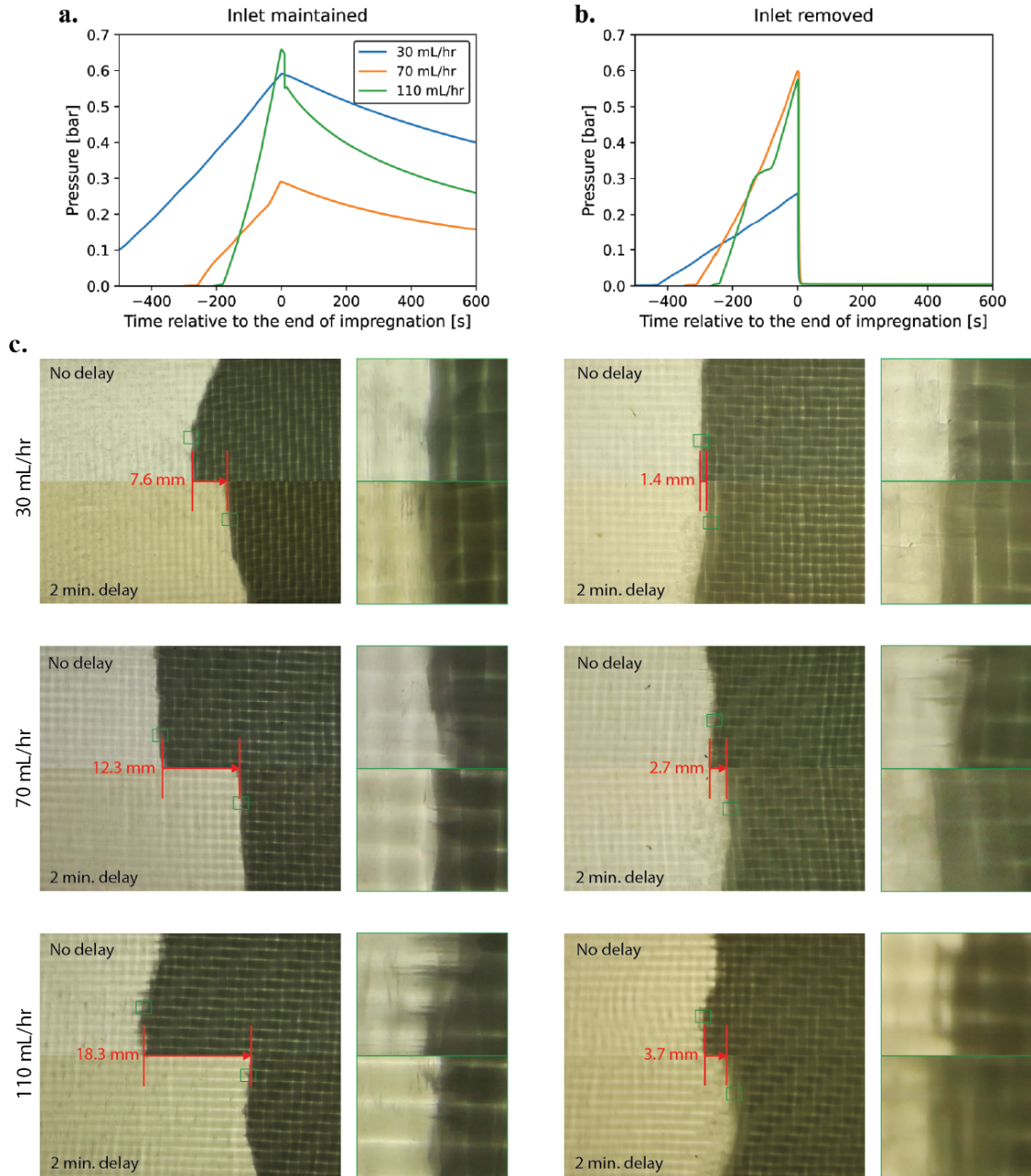
Figure 4.10: Influence of the resin pressure on the front movement after the stopping impregnation: pressure profiles when inlet tubes are a) maintained or b) released and c) optical analysis of front movement and flow front morphology.

Table 4.2: Overview of the experimental conditions used for UV-flow freezing experiments at different flow regimes.

Flow regime	Viscous-dominated	Equilibrated	Capillary-dominated
IOC-8 SbF$_6$ [w%]	0.99	0.99	0.99
ITX [w%]	0.05	0.05	0.05
Benzopinacol [w%]	0.50	0.50	0.50
Temperature [°C]	19.40	21.36	19.29
Viscosity [Pa·s]	0.448	0.366	0.451
Surface tension [mN/m]	48.24	48.24	48.24
Flow rate [mL/hr]	42.85	11.65	3.69
Flow velocity [mm/s]	0.534	0.145	0.460
Capillary number [-]	0.00496	0.00117	0.00043

orded by Caglar et al. [47] after UV-flow freezing. The observed transient changes of the flow front morphology emphasises the need for fast UV-photopolymerisation and hence the efforts for tuning of the resin system presented in Section 4.1 and the optimisation of the mould configuration.

4.3 Assessment of saturation at microstructural scale

The optimised methodology was subsequently applied to produce flow front morphologies at varying flow conditions as reported by Caglar et al. [47], i.e. viscous-dominated flow regime at Ca ≈ 0.00496, an equilibrated regime of Ca ≈ 0.00117 and a capillary-dominated flow at Ca ≈ 0.00043. The experimental conditions corresponding to these flow regimes are listed in Table 4.2. Optical assessment of the flow front morphologies in Figure 4.11 did not show any apparent differences between the dynamic infiltrating fronts and those after UV-photopolymerisation, suggesting that the curing degree was sufficient to largely avoid undesired distortions of the flow front as previously discussed in Section 4.2. The same held for the post-curing procedure which showed a similar front morphology despite having been subjected to elevated temperatures. Further validation on a microstructural level is however desired, i.e. to confirm the hypothesised negligible influence of thermal effects, due to heating during UV-photopolymerisation, and curing shrinkage.

The various flow front morphologies,illustrated in Figure 4.11 showed several differences with those observed at similar values of the capillary number by Caglar et al. [47] in Figure 2.5. These differences are most apparent for the viscous flow regime, where the unsaturated flow length reported by Caglar et al. [47] appeared to be longer, i.e. ~2 yarn widths, than that in Figure 4.11, only spanning ~1 yarn width. The origin of these difference is attributed to the difference in resin infiltration conditions, as discussed in Section 4.2. Apparent differences in the optical recordings may have also resulted from the optical scattering by the increased number of fabric layers that was used in this work, reducing the visibility of the front morphology during

through-thickness optical imaging.

A volumetric assessment of the flow front morphologies by μCT enabled the visualisation and identification of the unsaturated flow behaviour at micron-scale for all of the considered flow regimes, presented in Figure 4.12. The three-dimensional representations already indicate differences between the different flow regimes, where the unsaturated region recorded in an equilibrated flow regime (Figure 4.12b) appeared to more smoothened compared to the viscous- and capillary-dominated regimes that showed more sharp features resulting from preceding flow.
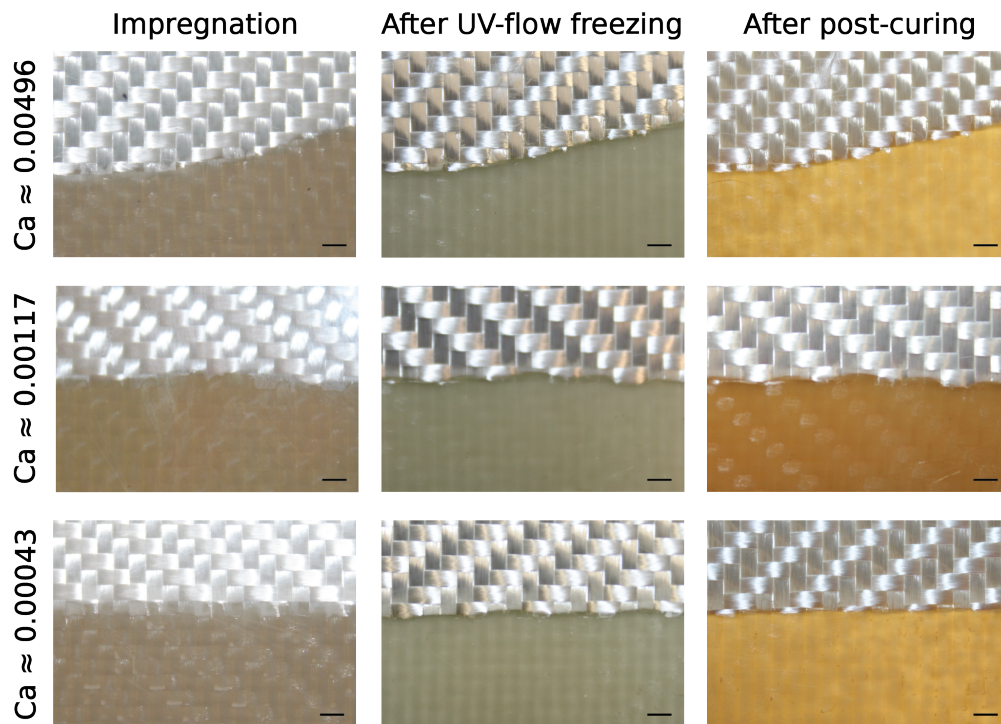
Figure 4.11: Optical imaging of flow front morphologies related to varying capillary numbers. Front morphologies were recorded during resin infiltration, after UV-flow freezing and after post-curing.

A representative image from this volume in Figure 4.13 shows that the used resolution of 3.5 μm in combination with the used contrasting agent resulted in a clear separation between saturated and unsaturated regions. Inter-yarn voids could be observed within the saturated region if sufficiently large in size while the resolution and contrast between the polymer and air phases was insufficient to identify intra-yarn voids. The use of automated segmentation methods was complicated by the presence of a number of artefacts. Residual air pockets in the unsaturated region, i.e. not filled with contrasting agent, appeared as voids in this region while identification of the front was in some cases complicated by the limited contrast of the front in regions with a high fibre density, e.g. within transverse yarns as illustrated in Figure 4.13. Finally, blurring effects of fibres spanning several voxels complicated their distinction

a. Viscous-dominated – Ca ≈ 0.00496   **b.**   Equilibrated – Ca ≈ 0.00117

c. Capillary-dominated – Ca ≈ 0.00043
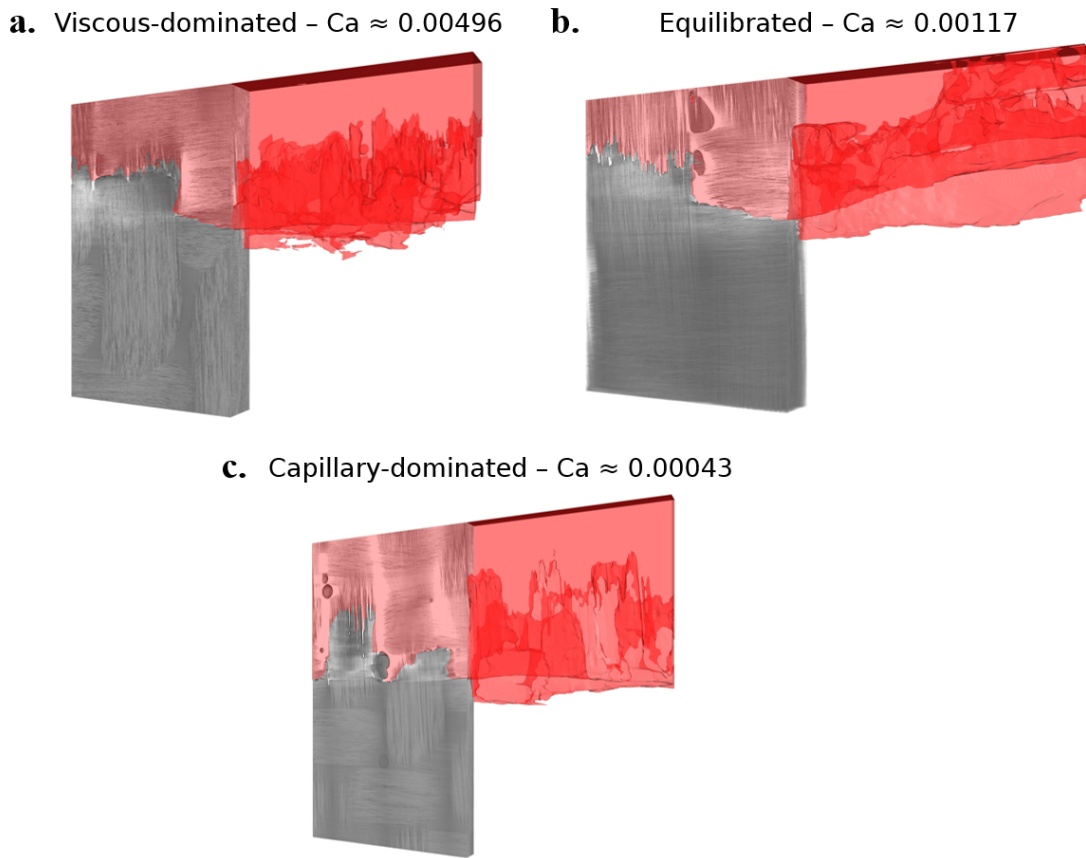
Figure 4.12: Three-dimensional representation of UV-frozen flow fronts recorded at different flow regimes: a) viscous-dominated with a Ca ≈ 0.00496, b) equilibrated with a Ca ≈ 0.00117 and c) capillary-dominated with a Ca ≈ 0.00043.

from regions near the flow front with reduced concentrations of contrasting agent. While overcoming these artefacts by e.g. optimisation of the μCT procedure, the application of the contrasting agent and the use of advanced segmentation techniques unlock the potential of an improved and unbiased characterisation of UV-frozen flow front morphologies, the employed manual segmentation strategy enabled the characterisation of unsaturated flow behaviour at a microstructural level.

The saturation curves derived from the recorded μCT volumes in Figure 4.14 indicated expected differences between the different flow regimes. The saturation curves were largely similar between fabric layers for all of the assessed flow regimes. The centre layer showed in some cases slightly delayed saturation, which was attributed to a combination of the different flow behaviour due to the aforementioned wall-effects in combination with a reduced capillary-induced flow by delayed UV-photopolymerisation at lower UV-intensities. This shift was however believed to be of negligible influence since the recorded saturation curves were similar to those as the outer fabric layers.
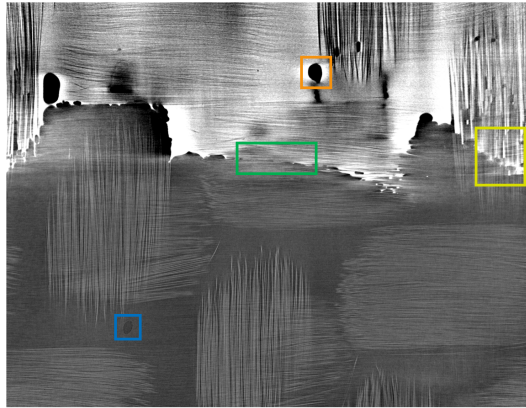
Figure 4.13: Representative slice of a μCT image indicating the recorded artefacts: blue) an inter-yarn void, orange) air pocket in a region with deposited contrasting agent, green) polymer-air interface in a transverse yarn and olive) blurring effects.

The viscous-dominated flow regime of Figure 4.14a, was found to have a linearly decreasing saturation level over the flow front region that corresponded to preceding inter-yarn flow. Flow front morphologies corresponding to a Ca of 0.00117 shown in Figure 4.14b showed some nonlinearities over the recorded saturation curves, which was believed to be a result of the woven fabric architecture, e.g. the presence of transverse yarns that locally acted as a barrier for the infiltrating resin. The increased appearance of nonlinearities in a (semi-)equilibrated flow regime compared to viscous- and capillary-dominated (Figure 4.14c) flow regimes would be explained by the absence of a preferential flow path where the flow would theoretically alter locally between an inter-yarn region to an intra-yarn region. The appearance of a barrier such as the presence of a transverse yarn would require the flow to make an additional alteration, potentially leading to a delay in the flow path.

Although not visible on the optical images presented in Figure 4.11, a flow regime highly dominated by capillary forces was identified at a capillary number of 0.00043. The saturation curve for this flow regime in Figure 4.14c showed a bisegmented trend where the initial steep decrease was believed to correspond to the inter-yarn flow while the following gradual decrease was attributed to extensive capillary wicking. It should be noticed that the relative ratio of these two phenomena is affected by the incapability to distinguish fibres from the intra-yarn flow at the current μCT resolution and the inflexion point should in reality be present at a lower saturation level. The combined use of the developed UV-flow freezing methodology and μCT was thus found able to visualise capillary wicking in LCM processing that can only be matched by the use of synchrotron-μCT as demonstrated by e.g. Castro et al. [99]. The flow rates used for producing the flow fronts shown in Figure 4.14 however all exceed the limit observed by Castro et al. [99] above which blurring of the μCT recordings would occur, which further confirms the benefit of the presented methodology.
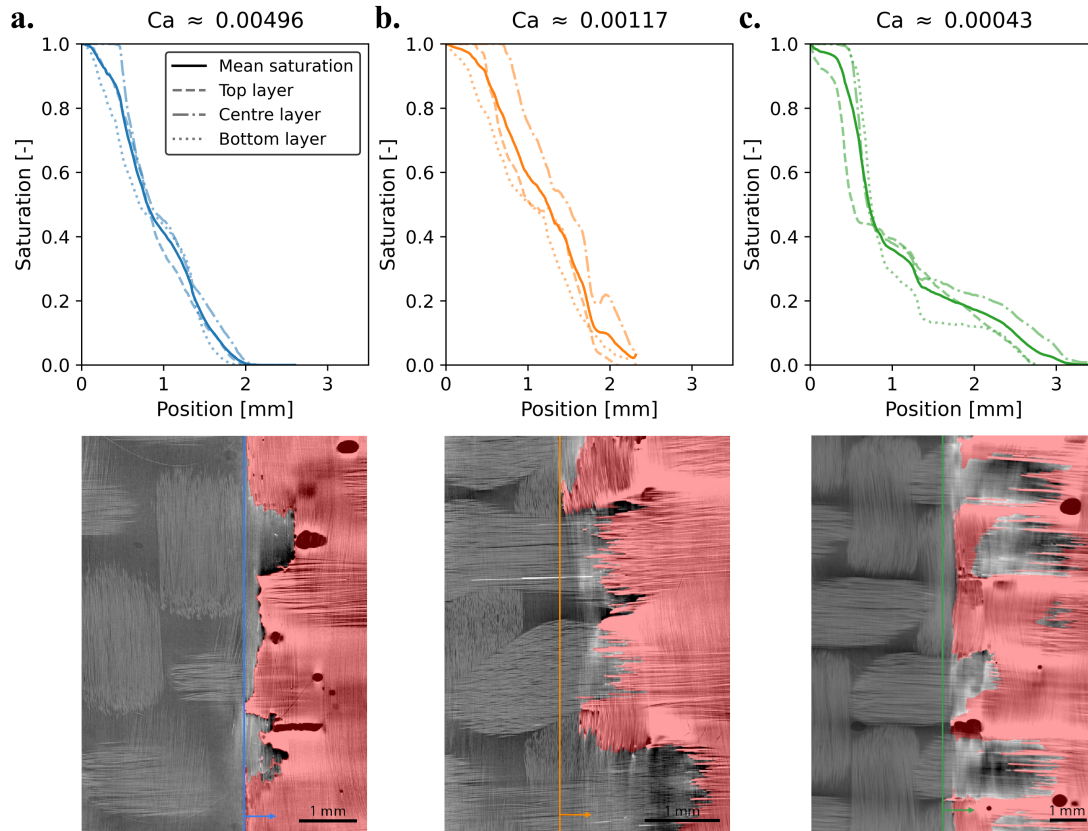
Figure 4.14: Saturation curves derived by μCT analysis of flow front morphologies at a) viscous-dominated, b) equilibrated and c) capillary dominated flow regimes. Bottom row: representative slices of μCT images with the unsaturated region marked in red and a vertical line indicating the start of this region, corresponding to a position of 0 mm.

4.4 Conclusion

A combination of UV-flow freezing and μCT was foreseen as a promising strategy to enable the microstructural evaluation at a wide range of dynamic flow conditions in LCM processing. Based on the methodology presented by Caglar et al. [47], an optimised resin formulation was proposed. The induction time of viscosity increase, corresponding to the onset of curing, and gelation time of UV-photopolymerisable resins were strongly decreased by tuning of the photoinitiator and photosensitiser concentrations while the addition of a free-radical thermal initiator was found beneficial for thermal post-curing of the UV-frozen flow fronts. Additives were identified to allow for facile variation of the viscosity and surface tension and hence the governing parameters of the capillary number. Optimisation of the experimental configuration by the use of in-house produced PMMA mould halves, to maximise the UV-transmittance, impregnation under a constant flow rate and the rapid relaxation of the resin pressure upon the start of UV-flow freezing, to minimise undesired distortions of the flow front morphology, contributed to accuracy of the resulting representation of dynamic flow behaviour. μCT

analysis of flow front morphologies produced at viscous-dominated, equilibrated and capillary-dominated flow regimes allowed for a volumetric assessment and the derivation of saturation curves. Strong capillary wicking could be observed at low values of the capillary number while the variability in the evolution of saturation correlated to features in the fabric architecture. These observations confirmed the potential of UV-flow freezing as a tool for microstructural evaluation of dynamic flow behaviour bringing additional benefits such as a low cost and its ease of implementation, e.g. compared to synchrotron-μCT.

Further assessment on the obtained representations of dynamic flow behaviour, e.g. by making a direct comparison between UV-flow freezing and dynamic (slow-)flow experiments, would validate the accuracy of the developed methodology and define the range of spatial resolutions that could be reached. Development of the methodology to observed intra-yarn flow, e.g. to characterise dynamic contact angles, would further require estimations of the curing shrinkage. The UV-flow freezing methodology is envisioned to contribute to the understanding on the role of the capillary number, with use of the aforementioned additives, in LCM as well as to study the role of the fibrous preform by variation of the fabric architecture and types. Extension of the methodology to allow for characterisation of opaque fabric architectures was initially foreseen by the use of frontal polymerisation for flow freezing. This was however hampered by the limited UV-initiation efficiency, impeding the initiation of frontal polymerisation in the presence of high V_fs, and the large thermal expansion upon front propagation, distorting the flow front morphologies, of current resin formulations. Overcoming these limitations by the development of novel, dedicated resin formulations is foreseen to further increase the potential of the UV-flow freezing methodology.

5 Frontal polymerisation-assisted processing of fibre reinforced polymers

*This chapter is an extract from the article 'Thermal management in radical induced cationic frontal polymerisation for optimised processing of composites' by J. Staal, E. Smit, B. Caglar and V. Michaud, published in 'Composites Science & Technology' **237**, 110009 (2023).*

Following Section 2.4, Radical Induced Cationic Frontal Polymerisation (RICFP) is considered a promising low energy method for processing of fibre reinforced polymers (FRPs). Efforts to-date are however limited by the heat uptake of fibre contents, impeding the production of FRPs with fibre volume fractions (V_fs) typically sought for in industry. In this chapter we explore various strategies to optimise the local heat balance in order to overcome the current limitations and pave the way for its adaptation to an industrial processing method for high-V_f structural FRPs. The heat generation term is varied by tuning of the initiator concentrations while the role of boundary heat losses is assessed by varying the mould material. The role of the local heat balance is moreover elucidated by the definition of a processing window as function of the heat generation, i.e. initiator concentration, and the heat losses, i.e. V_f. Finally, a proof-of-concept of local initiator deposition for further fine tuning of the thermal management is proposed.

5.1 Controlling the heat output via the resin composition

Optimised RICFP resins for FRP production were expected to mainly benefit from high heat release rates over large polymerisation enthalpies since the influence of concurrent thermal diffusion would be expected to increase with decreasing heating rates, potentially limiting the front temperatures and complicating local activation of the autocatalytic RICFP mechanism. Figures 5.1a-c show that increases in the photo- and thermal initiator concentrations directly correlated with increased heat outputs, resulting from the increased number of simultaneously growing polymer chains present upon initiation. The increased reactivity of the system moreover resulted in increased front velocities, i.e. Figures 5.1d-f, which is in line with observations made by Refs. [108, 142, 158]. Spearman's rank correlation coefficients listed in Table 5.1 confirmed that all these trends were significant. Variation of the photosensitiser
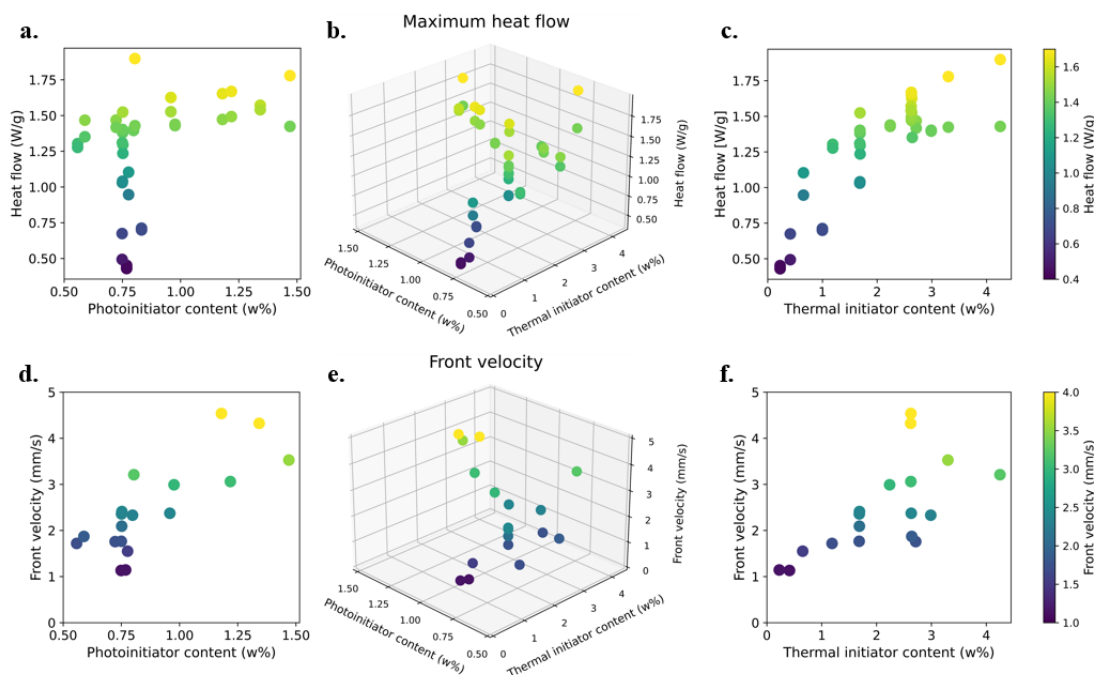
Figure 5.1: Heat output of neat RICFP resin recorded in quasi-isothermal DSC measurements with varying concentrations of a) photoinitiator, b) both initiators and c) thermal initiator. Front velocities, recorded by integrated thermocouples, with varying concentrations of d) photoinitiator, e) both initiators and f) thermal initiator.

concentration on the other hand, shown in Figure 5.2, did not impose an apparent trend for both the maximum heat output and the resulting front velocity, despite the Spearman's rank correlation coefficient being significant for the former. This significance was attributed to a limitation of the considered experimental set while the distributions in Figure 5.2a clearly show the resulting heat outputs to be scattering around a centreline.

The similarity between the trends observed in Figures 5.1a-c and 5.1d-f confirms the hypothesised relationship between the two characterised parameters, i.e. an increased resin exothermicity can enhance the propagation speed of a travelling front as it allows for faster overcoming of the required activation energy for localised activation of the autocatalytic reaction mechanism. The thermal initiator concentration appeared to have the largest influence on the maximum heat output, as is supported by the Spearman's rank correlation coefficients listed in Table 5.1, showing a strong initial increase and subsequently levelled of above 3 w%. The front velocity in Figure 5.1d-f however showed more linear trends as a function of the initiator concentration. The difference in trends observed for the maximum heat outputs and front velocities can be largely explained by the thermal degradation and foaming due to excessive heat generation [146, 167] at higher initiator concentrations. This foaming acts as an intrinsic cooling mechanism, lowering the front temperature and hence the front velocity. Since this phenomenon increases with the resin exothermicity, i.e. initiator content, its signifi-

Figure 5.2: Photosensitiser concentration dependence of: a) heat output recorded in DSC measurements and b) front velocities recorded by integrated thermocouples.

Table 5.1: Spearman's rank correlation coefficients on the composition dependence of heat outputs and front velocities.

Resin component	Heat flow [W/g]		Front velocity [mm/s]	
	Coeff.	p < 0.05	Coeff.	p < 0.05
Photoinitiator	0.529	$4.6 \cdot 10^{-4}$	0.643	0.018
Thermal initiator	0.759	$1.4 \cdot 10^{-8}$	0.846	$2.7 \cdot 10^{-4}$
Photosensitiser	-0.418	$7.3 \cdot 10^{-3}$	-0.258	0.394

cance is more visible at the highest concentrations, hence inducing a flattening of the curves in Figure 5.1d-f compared to those in Figure 5.1a-c. While the onset of thermal degradation at higher initiator contents could be avoided by increasing the V_f, i.e. increasing the heat loss term, the results in Figure 5.1d-f show the limitation of assessing the role of resin components by its resulting front characteristics. The proposed DSC procedure does not suffer from this behaviour and is therefore considered as the preferred method to characterise the heat output of RICFP resin. The trends observed in Figure 6 are different compared from those reported for an ECC resin by Mariani et al. [142]. This difference is believed to result from the use of different initiator types exhibiting different reactivities. The relationship between the heat output of RICFP resins and its initiator concentrations is thus expected to be highly dependent on the resin composition.

5.2   Estimation of heat losses to the mould

Variation of the mould material and thereby the magnitude of heat losses to the environment was found to have only a limited influence on the front characteristics of a neat RICFP system. The recorded front temperatures, shown in Figure 5.3a and Table 5.2, showed a ranking between the conductive steel, insulating silicone elastomer and highly insulating Teflon-
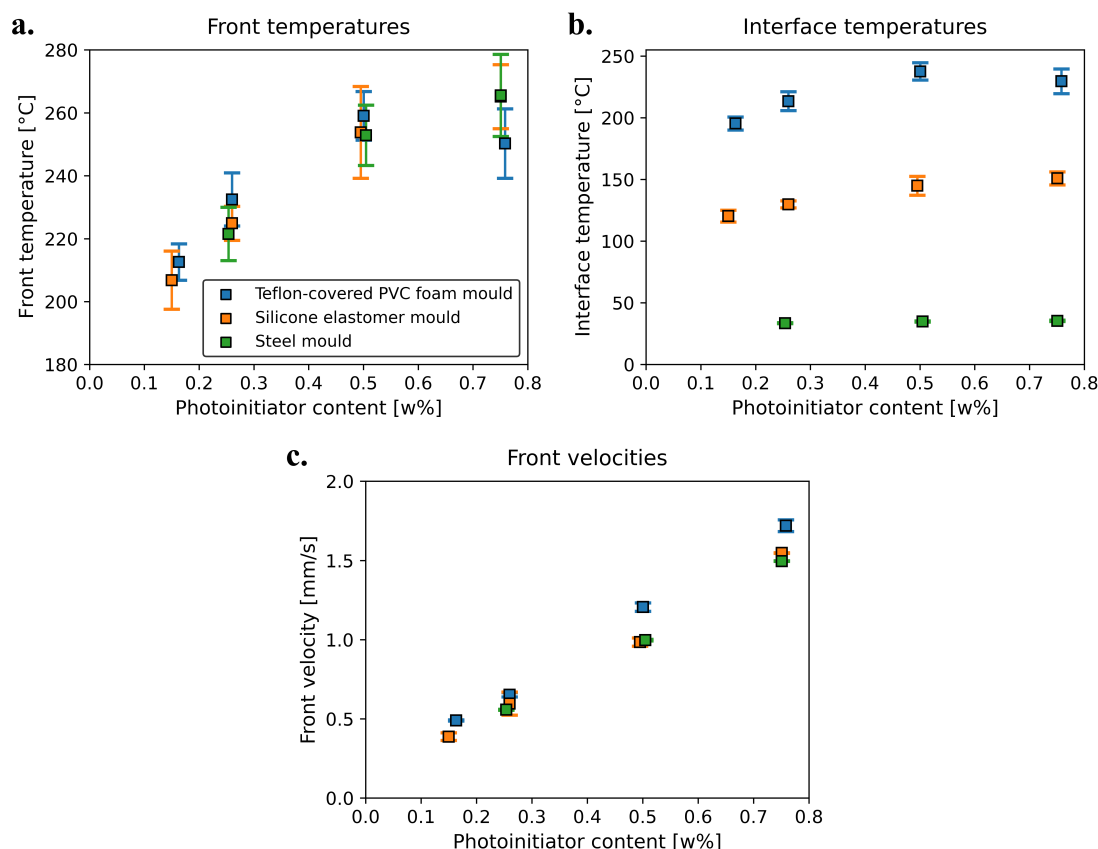
Figure 5.3: Comparative overview of front characteristics in neat resin systems with varying resin compositions using different mould types: a) Front temperatures, b) Front velocities, c) Predicted interface temperatures.

covered PVC foam core mould configurations, which was however not significant. The absence of statistical difference between the mould configurations was attributed to the location of the temperature measurement within the sample, while heat loss effects to the mould are reported [172] to mainly act at the sample boundary. This is confirmed by the calculated interface temperatures in Figure 5.3b and Table 5.2, predicting significant differences of over 80°C between the Teflon-covered PVC foam and silicone elastomer configurations. The predicted temperature of ~33-35°C for metal moulds was insufficient to polymerise the resin close to the interface and a layer of ~0.5 mm typically remained uncured.

The combined results of Figures 5.3a & 5.3b thus suggest that the choice of mould material and its consequent extensive thermal losses can potentially induce strong thermal gradients over the mould cavity. This prevented the formation of a front at a photoinitiator content of 0.15 w% in a conductive steel mould configuration. Front temperatures at a concentration of 0.75 w% deviated from the apparent linear trends due to the onset of polymer degradation, with foaming of the polymer acting as an intrinsic cooling mechanism. Although this allows for an indication of the maximum front temperatures that could be reached with the current

Table 5.2: Comparative overview of front characteristics and resulting monomer conversion of neat polymer samples. Acronyms PI and FWHM denote the photoinitiator and full with at half maximum, respectively.

PI content [w%]	Front temp. [°C]	Interface temp. [°C]	Front velocity [mm/s]	FWHM [s]	Conversion [-]
		Mould steel			
0.15	-	-	-	-	-
0.25	221.5±8.5	33.5±0.4	0.56±0.00	38.9±2.1	0.54±0.08
0.50	252.9±9.6	34.9±0.4	1.00±0.01	35.2±1.4	0.77±0.00
0.75	265.5±13.0	35.4±0.6	1.50±0.00	34.7±2.2	0.96±0.03
		Silicone elastomer			
0.15	206.8±9.3	120.4±4.9	0.39±0.02	113.4±12.3	0.61±0.01
0.25	224.9±5.4	129.8±2.8	0.60±0.07	75.4±7.9	0.67±0.04
0.50	253.8±14.6	144.9±7.6	0.99±0.03	83.4±5.6	0.77±0.01
0.75	265.2±10.2	150.9±5.3	1.55±0.00	81.3±12.8	0.93±0.00
		Teflon-covered PVC foam core			
0.15	212.6±5.3	195.4±5.3	0.49±0.00	470.0±13.1	0.65±0.05
0.25	232.5±7.7	213.5±7.7	0.65±0.01	294.5±15.5	0.68±0.02
0.50	259.0±7.0	237.6±7.0	1.21±0.03	289.7±22.6	0.85±0.02
0.75	250.2±11.1	229.6±10.0	1.72±0.04	172.4±14.9	0.80±0.08

system without degradation of the polymer taking place, the extensive heat uptake by high contents of fibrous reinforcement typically prevents these temperatures to be reached.

The front velocities in Figure 5.3c and Table 5.2 showed similar trends between the conductive steel and insulating silicone elastomer mould, while they were significantly higher in the Teflon-covered PVC foam core configuration. These trends slightly deviate from those shown in Figure 5.3a and give rise to the suggestion that the front velocity depends on the average temperature over (most of) the sample cross-section, i.e. partially capturing the influence of the acting thermal gradients. A relation between the ranking of front velocities in Figure 5.3c and the thermal properties of the mould material could moreover be hypothesised. Table 3.2 shows that the thermal effusivity, representing the ability of a material to exchange thermal energy with its surroundings, of steel is about 20-25 times that of both ECC polymer and silicone elastomer, while the estimated thermal effusivity of a Teflon-covered PVC foam core is about a factor ten lower than that of the latter two materials. The results in Figure 5.3c suggest that increased front velocities could be achieved when the thermal effusivity of the mould material is significantly lower than that of the RICFP polymer while front velocities are relatively constant when the thermal effusivity of the mould is comparable or higher.

Assessment of the resulting monomer conversion in Figure 5.4a and Table 5.2 showed a similar general trend where, for photoinitiator concentrations up to 0.5 w%, neat-polymer
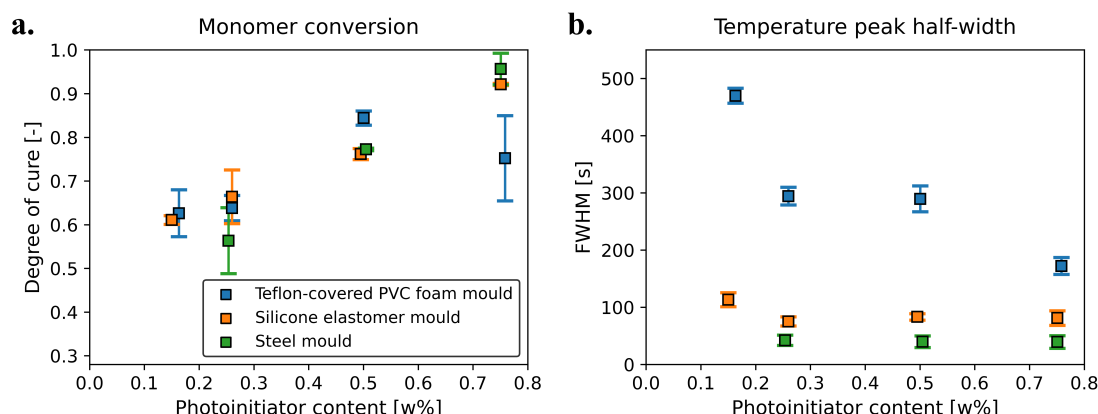
Figure 5.4: Resulting distributions of a) curing degree and b) rate of temperature decrease defined by the full-width at half maximum of neat polymer systems with varying initiator contents in different mould configurations.

samples produced in a Teflon-covered PVC foam configuration had higher conversions than those produced in a silicon elastomer mould. Sample conversions of polymer produced in a steel mould configuration were significantly lower at a concentration of 0.25 w% while being comparable to those produced in a silicone elastomer mould at 0.5 w%. It should be noted however that, since only the solid fraction of the sample could be measured (i.e. after removal of the previously discussed uncured sections at the sample top and bottom), the actual conversion over the sample cross-section is expected to be well-below the reported values. The inversed trend between the considered mould configurations at a photoinitiator concentration of 0.75 w% is explained by the severe degradation of the polymer, in particular when produced in the insulating mould configurations, causing interference in the FTIR spectra.

The monomer conversion of RICFP-produced in Figure 5.4a ranged on average between 0.6-0.85. This is lower than reported for BADGE systems by e.g. Dung Tran et al. [22], which is mainly attributed to the highly cross-linked network and limited monomer mobility of ECC polymer. Significant improvements are foreseen by the addition of low molecular weight monomers, e.g. 1,6-hexanediol diglycidyl ether [22], that possess higher mobilities. The curing degree nevertheless showed larger differences between mould configurations as would initially be expected from the front characteristics, i.e. Figure 5.3. While this is partially explained by the strong temperature gradients present over the sample cross-section, as concluded from the differences in interface temperatures shown in Figure 5.3b, the mould configuration was found of significant influence on the cooling phase. As illustrated in Figure 5.5, the insulating nature of a silicon elastomer mould and a Teflon-covered PVC foam core mould resulted in the polymer samples being subjected to elevated temperatures after passing of the front for a significantly longer period of time as compared to a conductive steel mould configuration. The full width at half maximum (FWHM), i.e. the total time a sample remains above half the peak temperature as illustrated in Figure 5.5, in Figure 5.3 and Table 5.2 demonstrate that

Figure 5.5: Influence of the mould configuration on the cooling rate after frontal polymerisation demonstrated by temperature profiles recorded by single thermocouples of a RICFP resin with 0.25% photoinitiator in different mould types.

the cooling stage in a Teflon-covered PVC foam core is significantly longer compared to the other mould configurations. This extended period is believed to act as a post-curing period, increasing the monomer conversion after passing of the front.

5.3 RICFP-assisted processing of fibre reinforced polymers

The use of a highly insulating Teflon-covered PVC foam core setup was concluded beneficial to the RICFP process and was subsequently used for the production of carbon FRPs. Given a system consisting of a resin with a set initiator concentration and a set carbon fibre V_f, three different scenarios could unfold upon initiation: 1. A self-sustaining front formed and propagated through the fabric stack, 2. The front had to be supported by UV-irradiation or 3. No front could be formed. Figure 5.6 shows that these scenarios took place in distinct zones and hence could be used as a process window. A few outliers can be detected in Figure 5.6, which are likely a result of difficulties in the thickness control in the vacuum-assisted hand layup setup, inducing local variations in V_f that potentially result in locally increased heat losses and quenching of the propagating front. Further optimisation of the experimental methodology is expected to overcome this. Using the improved mould design in combination with a tuned resin composition, it was possible to induce self-sustaining fronts with V_fs up to 45.8%, exceeding previously published maxima for systems cured by RICFP [22, 159]. Supported fronts could moreover successfully cure FRPs with V_fs up to ~50%.

The importance of controlling the local heat balance can moreover be understood from the defined process window. For example, a horizontal movement, where the V_f increases with a constant initiator content, would be expected to gradually reduce the available activation energy for enabling of the autocatalytic mechanism until it falls below its threshold [17, 19], which inhibits autonomous front propagation. Introduction of extra energy by means of

Processing window vacuum-assisted hand layup
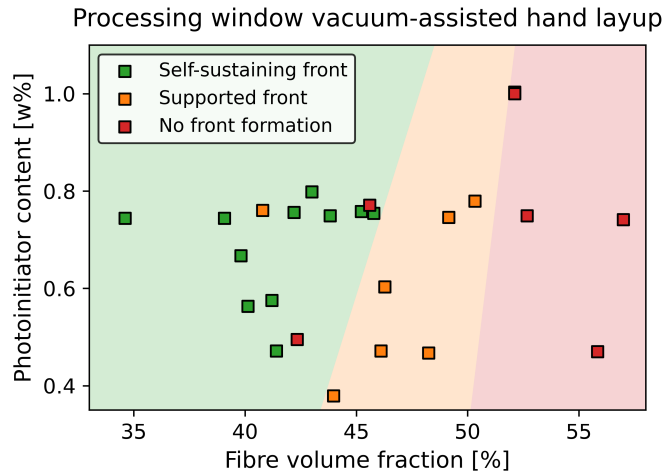
Figure 5.6: Relationship between the possibility to form a self-sustaining or supported front as a function of the fibre volume fraction and photoinitiator content in a PVC foam mould. Photo- to thermal initiator ratios generally equalled 3:4 by weight.

UV-irradiation would induce an upwards shift in the local heat balance and hence overcome the activation energy threshold, allowing for the presence of slightly higher V_fs until it falls below the threshold again. This latter V_f defines the maximum V_f that could be achieved with a certain experimental configuration. The limiting V_fs for the formation of self-sustaining and supported fronts could moreover be adapted with the initiator content, e.g. an increased initiator concentration and hence heat release rate could compensate the heat losses as a result of increased V_fs. While the process will be dependent on the combination of specific resin systems and experimental configurations, its definition could be further employed to optimise RICFP-processing of FRPs, contributing to the application of frontal polymerisation to an industrial composite processing technique.

5.4 Tuning of the local heat balance by initiator deposition

This section is based on the supervised master thesis work of E. Smit.

The results described in Section 5.3 emphasise the need for control of the local heat balance as a function of the fibre content. While this could be achieved via the resin composition in simple geometries with a constant V_f, a method for localised adjustment of the heat balance was foreseen to be beneficial for optimised processing of more complex configurations containing variations of the V_f over the part volume. Localised initiator deposition was identified as a potential strategy for tuning of the local heat balance, where the additional initiator deposited onto the fibre surface in high-V_f regions can increase the heat generation rate in that region, allowing for self-sustaining frontal polymerisation to be maintained. The methodology was initially developed for the deposition of IOC-8 SbF_6 photoinitiator since its high atomic weight constituents allowed for easier characterisation of fibre surfaces after deposition, e.g. by EDX.

Heat output of resin with recovered photoinitiator

Figure 5.7: Comparison of the heat output, recorded by dynamic DSC, between resins containing pristine and recovered photoinitiator.

Dissolution of IOC-8 SbF_6 was possible in acetone and ethanol while complete dissolution was not achieved in water or isopropanol. Acetone was therefore chosen as the preferred solvent to avoid potential negative effects induced by the presence of trace ethanol [235]. Its increased volatility is moreover reported [236] to have a less pronounced effect on the resulting mechanical properties of the polymer as compared to ethanol. Evaporation of the spraying solution resulted in the initial formation of a gel-like substance that only returned to a powder-like state after being kept under vacuum at 85°C for 2-3 days. The heat output of resins prepared with the recovered photoinitiator was similar to that of resins containing pristine photoinitiator as shown in Figure 5.7, indicating that the dissolution, and hence the spraying process, did not degrade the photoactive compound. Dissolution and evaporation in acetone did however make the recovered photoinitiator significantly more difficult to dissolve in epoxide resin, taking over 40 hours while pristine photoinitiator was typically dissolved in 2-4 hours. Although the origin of this difference is not completely understood, it might be a result of the more complicated evaporation of solvated acetone molecules.

Spraying of an acetone-based solution onto fibrous preforms was found to modify the fibre sizing, resulting in a significant stiffening of the fabrics that prevented nesting and compaction that is necessary to reach the desired V_fs > 30%. Fabrics were therefore desized to assess the potential of the proposed methodology. The absence of a dedicated sizing would however come at the cost of reduced fibre-matrix interfacial properties that would also be expected to reduce the overall mechanical properties of the FRP [237] and a compatible sizing should thus be developed for future application of the method. About 0.023 g/cm^2 of spraying solution was found necessary to saturate a desized fabric layer and its photoinitiator concentration was calculated from the total fabric surface present in the mould cavity, i.e. the surface area and the total number of layers, and was typically in the range of ~4-15 mg/layer. This corresponds to an photoinitiator concentrations in the spray solution of 3.6-13.6 mg/g acetone while actual concentrations at the moment of deposition were typically higher due to the evaporation of acetone. The latter was confirmed by UV-vis spectroscopy of the solution obtained after
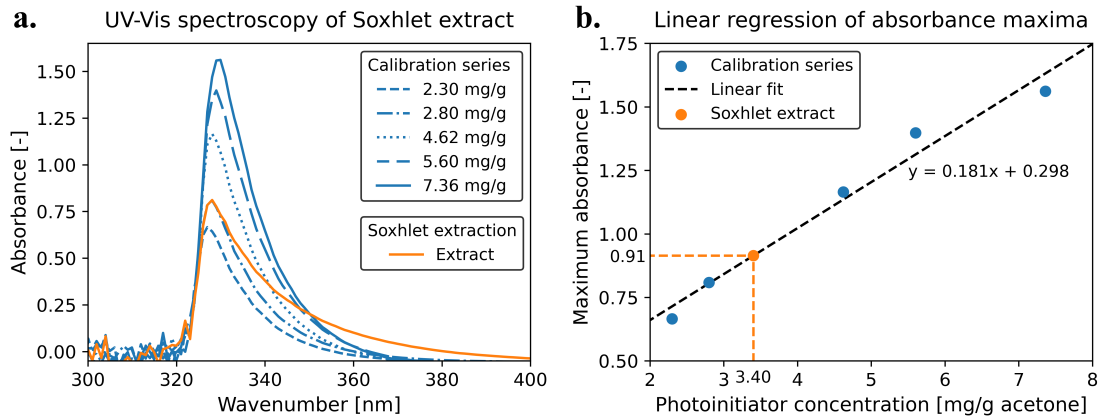
Figure 5.8: Estimation of the photoinitiator concentration in the Soxhlet extract: a) comparison of UV-Vis absorbance spectrum with calibration series and b) linear regression of the absorbance maxima to determine the photoinitiator concentration.

Soxhlet extraction shown in Figure 5.8. Linear regression of the absorbance maxima shown in Figure 5.8b indicated that the concentration of the Soxhlet solution was approximately 3.4 mg/g acetone, corresponding to an initial spray solution of 10.9 mg/g, which was significantly higher than the aimed concentration of 4.3 mg/g. Figure 5.8b moreover allowed for estimation of the molar attenuation coefficient of IOC-8 SbF$_6$, which equalled 0.181 $(mg/g)^{-1}$ or 2799 L/mol/cm.

SEM-EDX analysis of the deposited fibre surfaces in Figure 5.9 showed a fluorine signal that was distributed homogeneously over the sample surface. The absence of this signal for pristine fabrics, as listed for the elemental analysis in Table 5.3, confirmed that the fluorine signal corresponds to the presence of the photoinitiator, from which it thus can be concluded that the deposition procedure allows for a homogeneously distributed initiator content. Although the low contents, and hence low signal intensities, did not allow for quantitative estimations of the photoinitiator concentration on the fibre surface, the results in Table 5.3 suggest that the deposited concentration can be increased by increasing the concentration in the spray solution.

Validation of the developed local deposition methodology was done via the production of FRPs. The maximum V_fs that can be produced with a set initiator composition has been illustrated in Figure 5.6 and the effectiveness of the methodology would be confirmed if increased V_fs, e.g. in the regions requiring a supported front, could be polymerised autonomously after initiator deposition. Initial trials were made for resin systems containing 0.47 w% and 0.6 w% photoinitiator and 0.13 w% and 0.2 w% were deposited, respectively. The V_fs were tuned to, according to Figure 5.6, allow for successful front formation at the combined initiator concentration while the initiator concentration of the resin only would be insufficient. The additional deposited initiator content was however insufficient to induce frontal polymerisation in the presence of the increased V_fs, not even when the deposited initiator concentration was
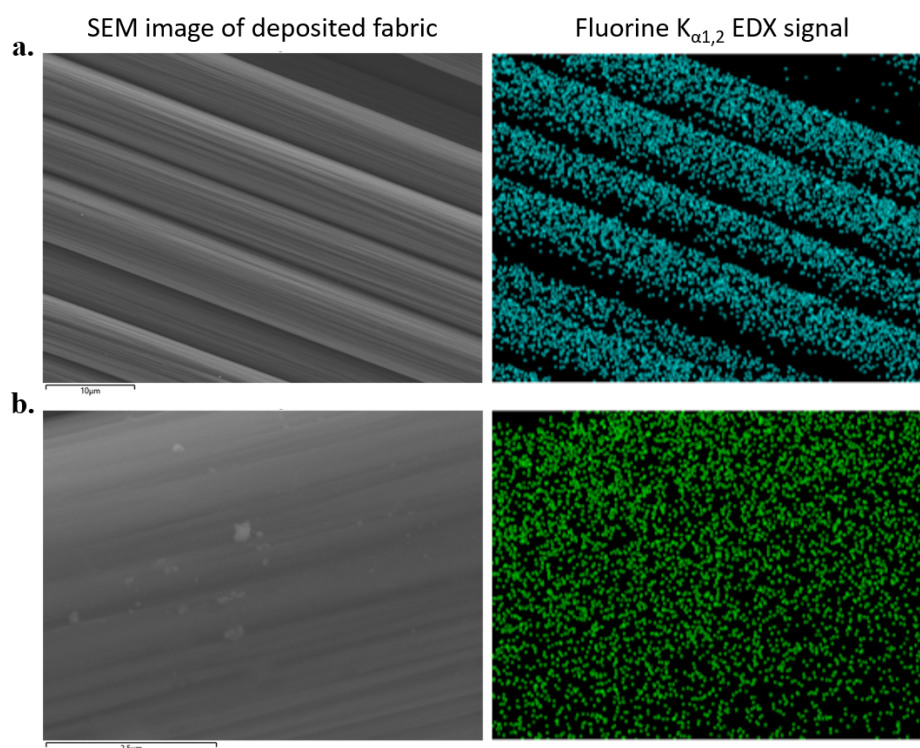
Figure 5.9: Combined SEM-EDX analysis of fibre surfaces after deposition of a) 14.5 mg/layer and b) magnified image after deposition of 4.3 mg/layer.

strongly increased, i.e. from 0.2 w% to 0.6 w%. Several explanations could be hypothesised for the absence of an improvement after deposition of the initiator. First of all, the recovered initiator was described to take significantly longer to disperse in the resin formulation and the layup time may thus be insufficient for the resin to incorporate the initiator near the fibre surface. Insufficient adhesion onto the fibre surface on the other hand might have displaced the initiator during the sample production, e.g. to the more resin-rich sections, and hence undoing the foreseen benefit of localised initiator deposition. Finally, assuming a good dispersion of the deposited initiator, the diffusion length of the initiator might be insufficient to contribute to the bulk polymerisation. Although the latter would hamper the use of localised initiator deposition for controlling the governing heat balance, the method may bring additional benefits for intra-tow curing, i.e. where fibres are closely spaced, which is to be assessed in future work. While the results presented in this section provide a robust strategy for the deposition of reactive compounds onto the fabric surface, further investigations are required to both validate and optimise the hypothesised methodology.

5.5   Conclusion

This chapter aimed to derive an improved understanding of the governing thermal phenomena during RICFP and to employ them for optimised processing of FRPs. Variation of the initiator

Table 5.3: Elemental analysis by EDX of deposited and pristine fibre surfaces.

Element	Reference [w%]	14.5 mg/layer deposited [w%]	4.3 mg/layer deposited [w%]
C	89.5±0.7	85.5±0.7	90.1
O	8.0±2.0	6.3±0.2	4.4
N	2.1±1.4	4.1±0.5	3.5
Si	0.3±0.1	0.4±0.1	0.1
I	-	2.0±0.5	0.8
Sb	-	1.5±0.4	0.9
F	-	0.3±0.1	0.2

concentration was confirmed as an effective strategy to control the heat generation term while variation of both the photo- and thermal content played a significant role. A newly proposed quasi-isothermal DSC characterisation method was found to beneficial over the conventional characterisation strategy e.g. via the front characteristics. The mould configuration had a strong influence on the both the front characteristics and the resulting curing degrees due to the formation of large temperature gradients over the sample thickness. Reduced heat losses by the use of highly insulating mould constituents was found to enhance the front polymerisation performance of a neat-polymer system, which could be translated to an upwards shift of the heat balance in FRP systems. Using the improved mould configuration and tuned resin composition, it was possible to produce FRPs with V_fs of 45.8%, exceeding previously reported maxima for RICFP systems, and reaching meaningful values of fibre content for structural composites, although still with a margin for improvement. A process window was moreover defined that related the possibility to form a self-sustaining or supported front in the proposed experimental procedure as a function of the V_f and initiator content. An initiator deposition method was proposed to locally tune the heat balance although validation of the proof-of-concept is desired in future work. The combined presented results emphasise the need and promise of controlling the local heat balance in frontal polymerisation-assisted FRP processing.

6 Self-catalysed frontal polymerisation processing

Although a careful control of the heat balance enables to reach the maximum potential of a frontal polymerisation resin system, the maximum attainable V_f with this system remains below the desired range of >55% with no additional heat input. Alternative strategies are therefore requested to bridge this gap and, as outlined in Section 2.4.6, several researchers proposed to use external heaters such as a heated plate or resistive heaters, which inherently increases the energy demand. From another perspective, knowledge of composite manufacturing methods may provide an alternative approach: resin channels are frequently introduced in conventional LCM processing methods to improve the impregnation kinetics of fibrous preforms. While these high-permeability channels could be created inside fabric stacks [238], flow kinetics are typically controlled by spacers [239] or by grooved or porous layers that are placed on top of the fabric stacks. Optimised placement of these structures [240–242] strongly reduces the impregnation time while they can be removed after the curing process and hence do not affect the resulting FRP properties. Inspired by this practice, a novel self-catalysed frontal polymerisation processing method is presented in this chapter that exploits the high exothermicity of RICFP resins in sacrificial resin channels for providing the additional energy needed to reduce the activation energy threshold for self-sustaining frontal polymerisation, i.e. avoiding the need of a (dis)continuous external energy input. A detailed description of the self-catalysed frontal polymerisation method is presented followed by its experimental validation. Geometrical and compositional variations are explored, followed by a comparison of the resulting FRP properties with conventional oven-cured FRPs.

6.1 Process configuration optimisation

Using an optimised ECC monomer-based resin formulation in combination with a vacuum-assisted hand layup methodology, it was concluded in Section 5 that the maximum allowed V_f present in the FRP that can be successfully polymerised equalled 45.8%. This maximum V_f was found to slightly decrease, i.e. to 41.8%, when produced in a RTM configuration consisting of two Teflon-covered foam core mould halves. This minor decrease is attributed to the increased heat uptake by the rigid mould halve compared to the more insulting vacuum
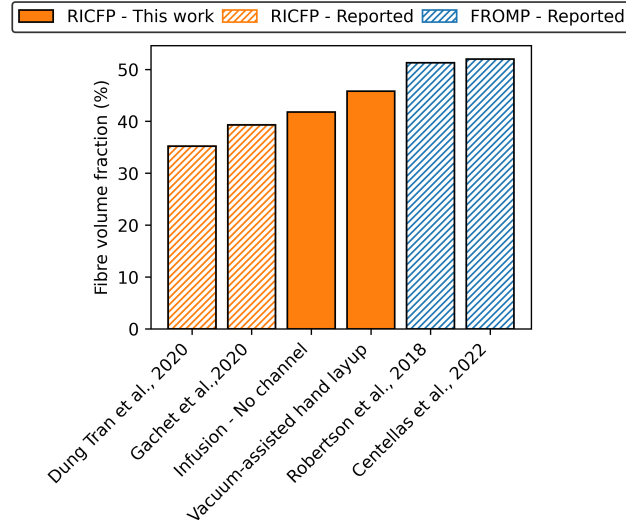
Figure 6.1: Comparative overview of maximum fibre volume contents reported for frontal polymerisation processing of FRPs without continuous energy input.

bag/air interface. Figure 6.1 nevertheless shows that this maximum V_f remains higher than other reported maxima for RICFP systems while being significantly lower than those reported for FROMP systems, both of which are nevertheless below the industrially relevant range for structural applications (>55% V_f). To improve on this, a novel self-catalysed frontal polymerisation process was developed where a sacrificial resin channel is placed on top of the fabric stack and separated by a separator. This process configuration, schematically shown in Figure 6.2, can strongly enhance the front characteristics of a given resin-fibre system without the need for any (dis)continuous energy input.

Similar to most conventional FRP manufacturing processes, the self-catalysed frontal polymerisation processing method comprises an impregnation and a curing phase. Impregnation of the fabric stack and the sacrificial resin channel is carried out simultaneously. The large permeability difference between these sections requires the integration of a resin barrier in the resin channel to avoid the resin race-tracking through this section, leaving the fabric stack unsaturated. Once the fibres are completely saturated, a front is initiated in a resin-rich section of the mould, i.e. as shown in Figure 6.2a, by localised UV-irradiation, i.e. similar as was done for vacuum-assisted hand layup processing described in Section 5, followed by auto-catalytic propagation until the fabric/channel section is reached. The absence of fillers, and hence the increased thermal equilibrium, makes the front propagate faster through the resin channel. Frontal polymerisation in the fabric stack on the other hand is delayed, as shown in Figure 6.2b, since the heat uptake by the fibres is such that the activation energy threshold can initially not be exceeded. The increased temperature upon frontal polymerisation of the resin channel induces heat transfer, resulting in rapid preheating of the top section of the fabric stack, i.e. to 50-100°C within several seconds. The thermal energy of this preheating contributes to the available activation energy and hence lowers the energy that should be

a. UV-initiation phase

b. Front propagation phase
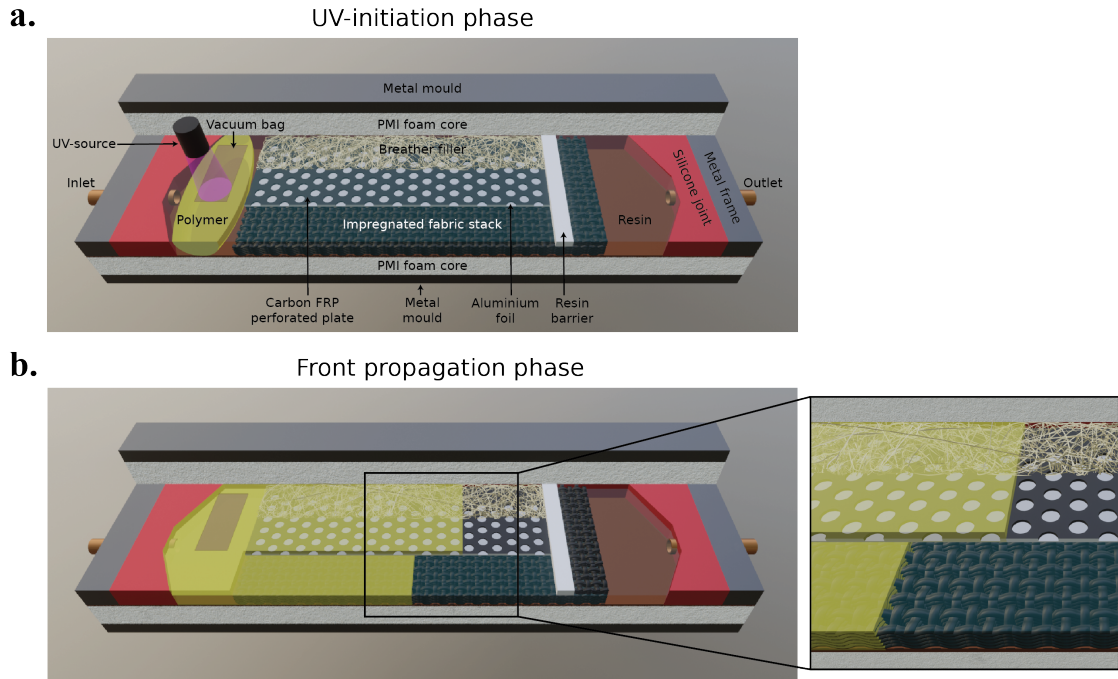
Figure 6.2: Schematic representation of the self-catalysed frontal polymerisation processing method: a) initiation phase and b) propagation phase.

supplied by the propagating front. A secondary front propagates through the fabric stack once the temperature within the fabric stack is sufficiently high to sustain frontal polymerisation, allowing for successful frontal polymerisation of FRPs with significantly increased V_fs. This configuration moreover brings the advantage that an external energy input is only required during the initiation stage, i.e. to form a polymerisation front. The heat transfer between the channel and the fabric stack needs to be tuned to achieve an optimal processing strategy. This was largely achieved via the separator, which ideally possesses a high thermal conductivity in through-thickness direction, i.e. from the resin channel to the fabric stack, and a low conductivity in the in-plane direction to avoid excessive spreading of the front. Moreover, the separator must be sufficiently stiff to avoid bending by the compacted fabric stacks and to maintain a constant channel geometry, resulting in maximum sample flatness. The combination of a perforated carbon FRP plate and an aluminium foil layer was chosen as the preferred combination to fulfil these requirements over e.g. metallic or polytetrafluoroethylene (PTFE) separators.

An optical image of a carbon FRP sample produced with this optimised configuration, after removal of the sacrificial resin layer, is shown in Figure 6.3a. The resulting FRPs did not show any major apparent differences compared to those produced by e.g. conventional frontal polymerisation or oven-curing. The resin-rich regions near the initiation zone and the outlet showed severe degradation due to the absence of fibrous reinforcements, and hence their consequent heat losses, in these regions. The FRP sections did however not show increased

a.

b.
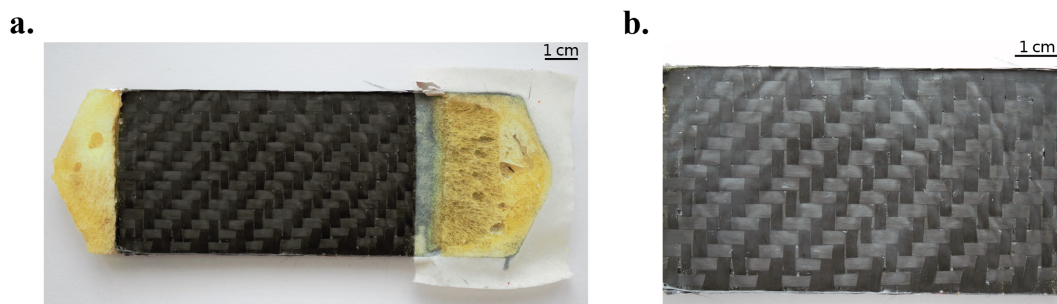
Figure 6.3: Optical imaging of a) a carbon FRP produced by self-catalysed frontal polymerisation after removal of the sacrificial resin channel and b) magnified view of its top surface.

void contents as compared to conventional curing strategies, from which the absence of bubble formation or foaming during the frontal polymerisation process was concluded.

The stiffness of the carbon FRP plate used as separator between the fabric stack and the sacrificial resin channel allowed for a uniform sample thickness over the sample length although the inherent variation in compaction and nesting of the fabric stack in some cases induced minor bending or deformation of the separator that are retained in the FRP part. Wrinkling of the aluminium foil layer upon mould closure occasionally resulted in the formation of a pattern onto the FRP top surface, as illustrated in Figure 6.3b. Further optimisation of the resin channel configuration is foreseen to minimise the formation of these process-related artefacts.

6.2 Temperature profiles in self-catalysed frontal polymerisation processing

Recorded temperature profiles in Figure 6.4 provide a more detailed view of the ongoing phenomena during self-catalysed RICFP processing. With V_fs of ~50-55% and in the absence of a resin channel, fronts could not sustain in either the thermally conductive carbon or insulating glass fabric stacks since the available RICFP resin could not provide sufficient energy to overcome the heat losses to the fibres and surroundings. The introduction of a sacrificial resin channel led to the successful formation of a front, as evidenced by the recorded temperature peaks in Figure 6.4. Upon frontal polymerisation of the resin channel, the temperature close to the channel, i.e. top of the fabric stack, rapidly increased to ~85°C after which it reached a plateau after 10-15 seconds. This was followed by a gradual temperature increase throughout the fabric stack until the overall temperature was sufficiently high to allow for the passing of the secondary front through the fabric stack. Frontal polymerisation of the fabric stack rapidly increased the temperature, with peaks above 200°C, at all the through-thickness positions after which cooling took place slowly to maintain the heat and thereby maximise the resulting curing degree of the FRP.
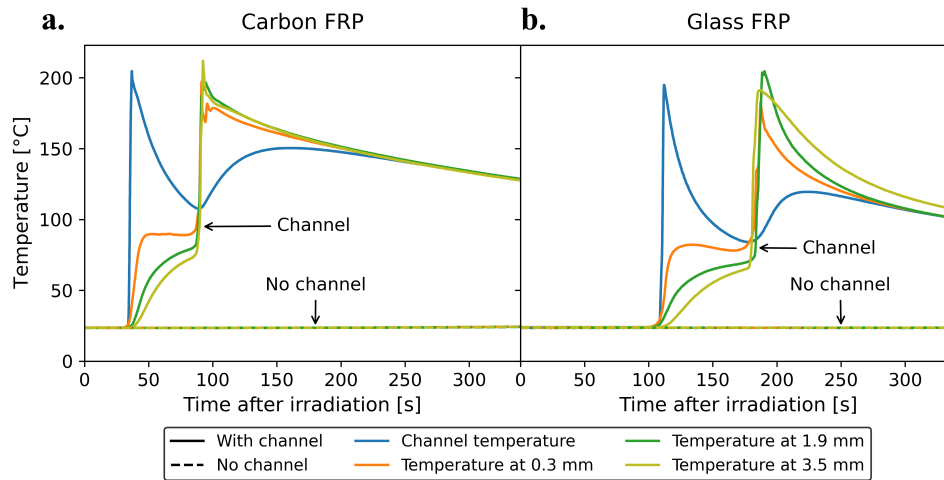
Figure 6.4: Exemplary temperature profiles recorded for a) carbon FRPs and b) glass FRPs during RICFP processing with and without the presence of a sacrificial resin channel. Positions are defined as the vertical distance from the resin channel/separator.

Minor differences in front characteristics were induced between carbon (Figure 6.4a) and glass (Figure 6.4b) FRPs, which are related to the differences in their intrinsic thermal properties. The lower thermal conductivity of glass fibres resulted in reduced preheating rates throughout the fabric stack. The final preheating temperatures were nevertheless comparable to those recorded for carbon FRPs, indicating that the delay in preheating was compensated by a reduced velocity of the secondary front, which is typically observed in the presence of low thermal conductivity fillers [175–177]. The system is therefore suggested to possess the capability to self-adapt based on its constituents, as long as sufficient energy is provided to overcome the activation energy threshold.

An evaluation on the influence of the fabric stack thickness, while maintaining the same resin channel geometry, was carried out to further assess the potential of producing thicker FRPs and hence widening the potential range of applications of the self-catalysed RICFP processing method. Figure 6.5 shows the recorded preheating and front temperatures for both considered fabric types in a 5.3 mm cavity and a 9 mm cavity, while the combined data can be found in Table 6.1. With a constant resin channel thickness, these cavity heights resulted in FRP thicknesses of about 3.8 and 7.3 mm for the respective 5.3 and 9 mm cavities. The preheating temperatures near the resin channel were similar for both cavity heights since these were mainly determined by the front temperatures inside the resin channel, having a similar geometry in all the considered cases. Front temperatures in this section were, especially for the glass FRPs, generally slightly lower than those recorded deeper into the fabric stack. Supported by DSC measurements shown in Appendix A.1.1, this was attributed to initial curing of the resin during the delay period between the frontal polymerisation of the resin channel and the arrival of the secondary front, despite the preheating temperatures being below the estimated onset of autocatalytic mechanism (also Appendix A.1.1). This precuring reduced the available
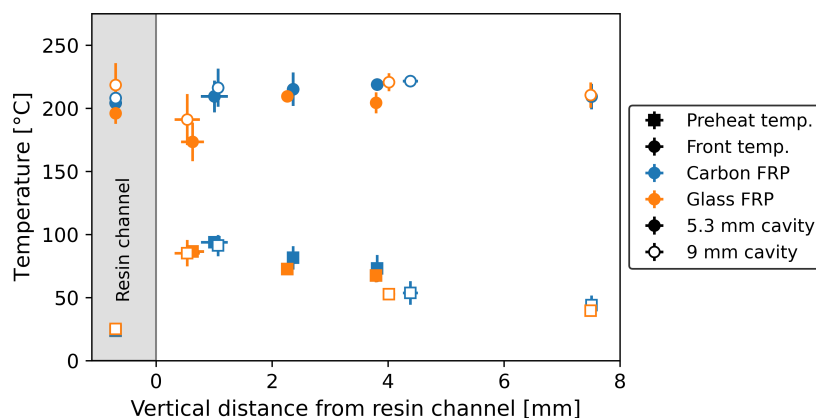
Figure 6.5: Average recorded preheating and front temperatures in carbon and glass FRPs at different positions of 5.3 mm and 9 mm mould cavities.

epoxide groups and thereby the polymerisation enthalpy that can be released upon passing of the front, resulting in a lower front temperature. However, the extent of precuring was maintained sufficiently low to allow successful frontal polymerisation was observed in all configurations, while the limited decrease of the front temperature was not expected to result in differences in the curing degree as it was followed by a lengthy cooling procedure.

The fabric stack height mainly influenced the preheating temperatures in the lower parts of the mould cavity. Preheating temperatures were more uniform in a 5.3 mm cavity with preheating temperatures varying ~10°C between the top, middle and bottom thermocouple positions for both considered fabric types. The middle position in a 9 mm cavity showed preheating temperatures of ~53°C that corresponded to a decrease of about 20°C compared to those recorded at a similar distance from the resin channel, i.e. the lower thermocouple, in a 5.3 mm cavity. This is explained by the increased heat sink and diffusion effect due to presence of more fibres and more resin due to the increased cavity height. Since roughly the same amount of thermal energy is provided by the resin channel, the average preheating temperature would be expected to be lower, i.e. 40-45°C for the lowest thermocouple position in a 9 mm cavity. However, these preheating temperatures sufficiently lowered the required activation energy to surpass the threshold and hence promoted the formation of a front. Further optimisation of the channel geometry, e.g. the channel height, is moreover expected to allow for increased control of the preheating temperatures. Resulting front temperatures were comparable for both cavity heights since preheating temperatures were low enough to avoid extensive precuring to take place.

6.3   Control of polymerisation front morphologies by channel fillers

The presence of fillers in the resin channel was found to significantly influence the front characteristics of the secondary front. To illustrate this dependence and its potential to control

Table 6.1: Overview of recorded preheat and front temperatures at different vertical positions in experimental configurations with varying fabric type and mould cavity height.

	Carbon fabric			Glass fabric	
Height [mm]	**Preheat temp. [°C]**	**Front temp. [°C]**	**Height [mm]**	**Preheat temp. [°C]**	**Front temp. [°C]**
		5.3 mm cavity			
Channel	23.7±0.2	204.2±2.6	Channel	23.9±0.5	196.2±8.3
2.20±0.23	93.9±4.0	209.5±12.5	1.83±0.20	86.6±3.4	173.5±15.3
3.56±0.05	81.6±9.3	215.2±13.6	3.46±0.05	72.8±4.0	209.5±3.7
5.01±0.01	73.2±10.7	218.9±12.5	4.99±0.01	67.6±5.3	204.5±8.3
		9 mm cavity			
Channel	24.0±1.0	208.2±8.4	Channel	25.3±1.4	218.7±17.2
2.27±0.02	91.3±8.4	216.4±15.1	1.74±0.22	85.3±10.1	191.2±20.2
5.58±0.13	53.8±9.4	221.7±4.2	5.21±0.11	52.9±4.4	220.8±7.2
8.71±0.00	44.1±7.6	209.4±10.1	8.69±0.01	39.6±3.9	210.6±10.1

the self-catalysed frontal polymerisation process, carbon FRPs of ~55% V_f were produced using either resin channels filled with breather material, i.e. a non-woven material frequently used for guiding air flow in FRP production, or unfilled resin channels. Filling the resin channel with a strip of breather fabric corresponded to a V_f of ~7.5% which was believed to be, in line with the use of insulating fillers [175–177], sufficient to reduce the front velocity inside the resin channel. Propagation of the channel and secondary fronts typically resulted in smooth temperature profiles, e.g. similar to Figure 6.4a, when a breather strip was placed inside the resin channel. Preheating temperatures in a 7.3 mm cavity shown in Figure 6.6a ranged from 89.9±4.2°C close to the resin channel to 64.9±4.4°C and 48.9±3.9°C in the middle and bottom of the fabric stack, respectively. The delay between the passing of both fronts was on average 46.4±5.8 seconds, as displayed in Figure 6.4b.

The use of an unfilled resin channel was expected to increase the available energy for heat transfer and hence increase the preheating temperatures and front characteristics of the secondary front. The delay time in this configuration (Figure 6.6b) was with 94.7±6.6 seconds nearly double that of when a breather strip was placed in the resin channel, which was likely due to the expected increased difference in front velocities between the channel and secondary fronts. Figure 6.6a however shows that this extended delay time only slightly increased the preheating temperatures in the bottom and middle thermocouples to respectively 58.0±6.0°C and 66.3±7.4°C while the preheating temperature closest to the resin channel was even lower, i.e. 81.7±5.4°C as compared to when a filled resin channel was used.

Experimental configurations using an unfilled resin channel moreover showed significant inconsistencies in the peak times and temperature profiles (see Appendix A.1.2). The peak times, i.e. corresponding to the arrival of the front at the thermocouple position, were used
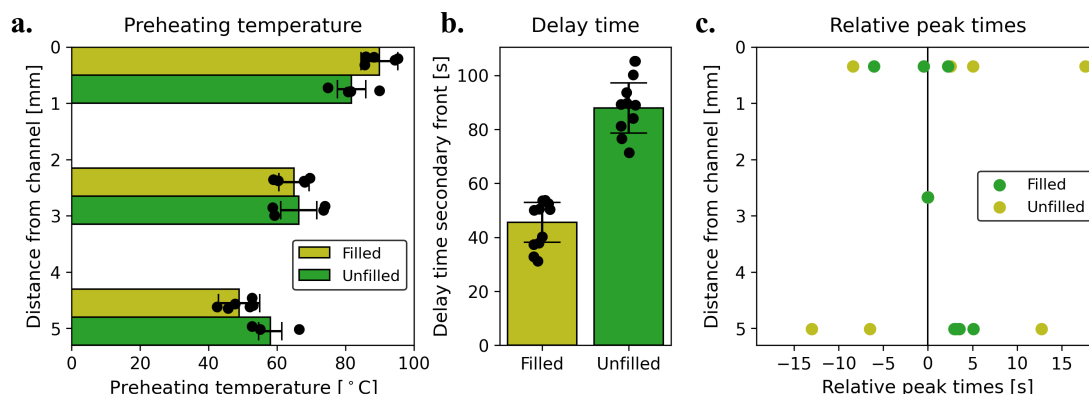
Figure 6.6: Comparison between filled and unfilled resin channel configurations: a) preheating temperatures at different vertical positions in fabric stack, b) mean delay times between the fronts in the resin channel and the secondary fronts recorded at two-thirds of the fabric length, c) peak times at different vertical positions in the fabric stack relative to the middle thermocouple positions.
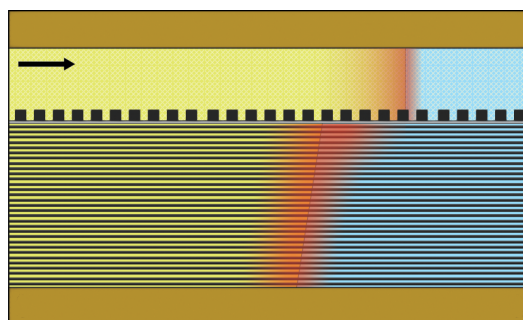
Figure 6.7: Schematic representation of the expected front morphology in self-catalysed frontal polymerisation process with a filled resin channel. The arrow denotes the direction of front propagation.

to obtain a further indication of the front morphology. Represented by the relative peak time compared to the middle thermocouple position, Figure 6.6c shows that there was no apparent trend in the peak times for a system with an unfilled resin channel, suggesting that no consistent front morphology was present. An explanation for this could be hypothesised from the more uniform preheat temperatures in combination with increased precuring due to the larger delay times, resulting in the formation of a discontinuous front that propagates when enough activation energy is present locally. Configurations where the resin channel was filled with breather fabric on the other hand showed good correlation on the relative peak times between samples in Figure 6.6c. The short delay between the top and middle thermocouple positions combined with the slight lag of the lower thermocouple suggests a hypothetical front morphology as shown in Figure 6.7. Although further investigation is required to find an optimum solution, the observations presented in this section highlight the potential of controlling the self-catalysed frontal polymerisation process by the addition

of fillers in the resin channel. An optimum solution is expected to balance the heat flow, inducing the formation of a consistent front morphology while also ensuring a sufficiently high compressive strength to resist against bending induced by the compressed high-V_f fabric stacks.

6.4 Comparison between self-catalysed and oven-cured FRPs

The chemical, i.e. T_g, and mechanical properties, i.e. ILSS and Young's modulus, of FRPs produced by the proposed self-catalysed frontal polymerisation methodology, reported in Figure 6.8 and Table 6.2, were found to be comparable to its oven-cure alternatives. The self-catalysed frontal polymerisation processing method required only a fraction of the energy demand for front initiation by UV-irradiation, as compared to the energy consumption recorded during the lengthy oven-curing procedures prescribed to produce FRP parts with commercial Sicomin and Araldite resins, requiring respective external energy inputs of 1.994±0.000 and 7.142±0.047 kWh as shown in Figure 6.8a. Replacement of these resins by a RICFP resin allowed for the formation of a front after an initial preheating period, shown in Appendix A.1.3, strongly reducing the required curing time and hence the energy demand, which is in line with Ref. [183]. Integration of a sacrificial resin channel however allowed for the production of FRPs with an average V_f of 59.1±2.0%, and individual V_fs reaching up to 62.2%, while bringing a further reduction of the required energy input, solely resulting from UV-irradiation, of 99.5%. Moreover, since energy input was only required to initiate the frontal polymerisation process, and is hence independent of the part size, this difference is expected to increase when larger samples are produced.

T_gs of FRPs produced by the self-catalysed frontal polymerisation process were significantly higher than that of oven-cured RICFP FRPs, as reported in Figure 6.8b and Table 6.2. The T_gs of oven-cured RICFP FRPs moreover increased significantly compared to the other sample types after being subjected to a second DMA cycle. This suggests that the maximum attainable monomer conversion was not achieved after the oven-curing cycle which is likely a result of the fast temperature decrease in the presence of a metal mould [243] (see Appendix A.4) and hence the absence of an intrinsic post-treatment upon passing of the front. The insulating nature of the foam-core mould allowed self-catalysed frontal polymerisation-produced FRPs to nearly reach their maximum attainable conversion without a postcuring treatment, i.e. only minor increases in T_g were observed upon a second DMA cycle, which was also the case for oven-cured FRPs produced with commercial resin formulations. Self-catalysed RICFP FRPs however showed increased scattering in the T_g values compared to the reference samples. This is largely believed to result from the inherent variation in compaction and nesting of the fabric stack that ultimately induces small changes in the in the channel geometry. These variations in channel thickness, and hence available heat transfer to the fabric stack, could induce (localised) differences in preheating and front temperatures, resulting in different degrees of cross-linking within the FRP part. These deformations moreover introduced small thickness variations, e.g. the pattern formation described in Section 6.1, in the self-catalysed
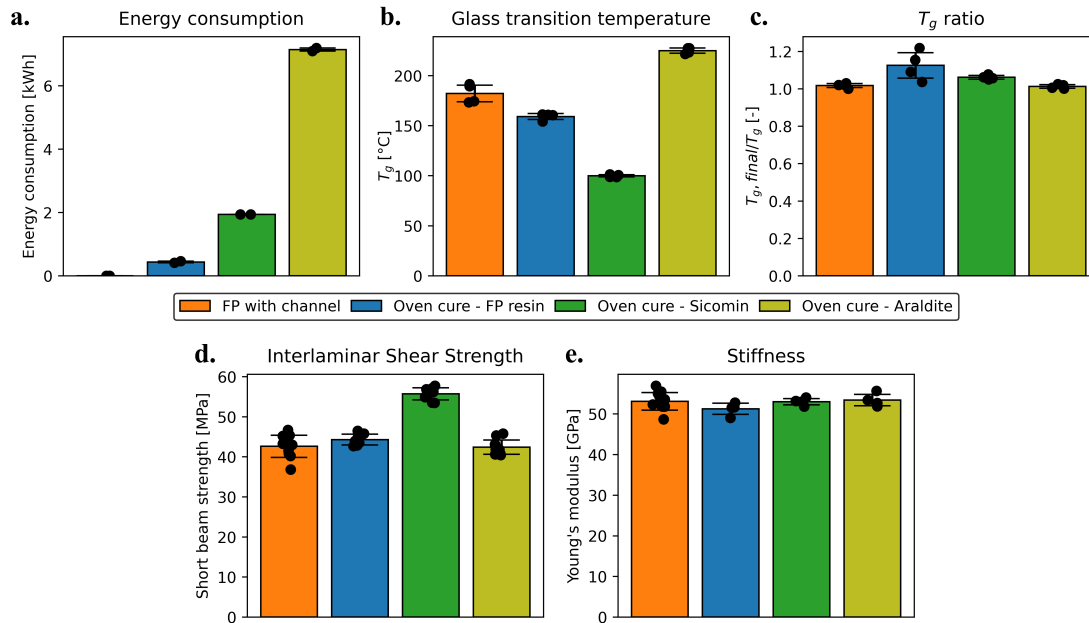
Figure 6.8: Comparative overview between self-catalysed RICFP FRPs, oven-cured RICFP FRPs and oven-cured commercial Sicomin and Araldite FRPs: a) energy consumption, b) glass transition temperature, c) ratio of T_gs between subsequent DMA cycles, d) interlaminar shear strength and e) stiffness.

FRP samples, potentially inducing an experimental inaccuracy in the DMA recordings. Further optimisation of the resin channel geometry is expected to overcome these deviations, allowing to optimally benefit from the presence of a sacrificial resin channel in RICFP FRP processing.

Evaluation of the mechanical properties by assessment of the ILSS in Figure 6.8d and Young's moduli in Figure 6.8e, while also listed in Table 6.2, showed similar behaviour for self-catalysed and oven-cured RICFP FRPs, as well as the oven-cured Araldite FRPs. While showing increased scattering due to the aforementioned geometrical deviations in the resin channel, the resulting properties suggest that the newly proposed self-catalysed frontal polymerisation processing

Table 6.2: Comparative overview of energy cost and resulting chemical and mechanical properties between FRPs produced with a sacrificial resin channel and oven cured FRPs. Acronym E denotes Young's modulus.

Sample type	V_f [-]	Energy cost [kWh]	T_g [°C]	T_g ratio [-]	ILSS [MPa]	E [GPa]
Self-cat. RICFP	59.1±2.0	0.002±0.001	177.6±9.3	1.02±0.02	42.3±2.6	53.1±2.2
Oven - RICFP	56.5±0.5	0.434±0.026	159.1±2.9	1.13±0.07	43.8±1.3	53.0±0.8
Oven - Sicomin	56.7±0.3	1.940±0.000	99.9±1.1	1.06±0.01	55.7±1.5	51.3±1.4
Oven - Araldite	56.2±0.1	7.142±0.047	224.9±2.5	1.01±0.01	42.4±1.8	53.4±1.4

strategy does not compromise the mechanical behaviour of its resulting FRPs. Further improvement of these properties, i.e. increasing the ILSS to match that of oven-cured Sicomin FRPs, could likely be achieved by further optimisation of the monomer composition while maintaining control over the front characteristics via extensive process control.

6.5 Conclusion

Manufacturing of FRPs by means of frontal polymerisation has the potential to bring large reductions in processing times and energy demand. The high V_fs typically sought for in the FRP industry presents a significant heat uptake, impeding current efforts to develop frontal polymerisation processing of FRPs. Using a model resin capable of RICFP, this chapter presents a novel self-catalysed frontal polymerisation manufacturing strategy that overcomes these limitations without requiring additional energy input. This method is based on the placement of a sacrificial resin in thermal contact the FRP part, allowing for effective preheating of high-V_f impregnated preforms and thereby lowering the activation energy threshold and hence enable frontal polymerisation at V_fs up to 60% range that would normally see fronts being quenched. The method was found compatible with both conductive and insulating fibre types at a wide range of FRP thicknesses while thermal analysis suggested the process to be self-adaptive based on the constituents and geometry. The presence of a filler material in the resin channel was found to be of large influence on the frontal polymerisation process, affecting the front characteristics while also inducing a consistent front morphology. A comparison with conventional oven-cured FRPs showed that the novel self-catalysed frontal polymerisation processing method gives comparable resulting mechanical properties while requiring only a fraction (a >99.5% reduction) of the total energy cost. Analysis of the T_gs moreover showed self-catalysed frontal polymerisation processing to be favourable over oven-curing of a frontal polymerisation resin. Future work comprises the optimisation of the process by increased control over the heat flow in combination with the adaptation of self-catalysed frontal polymerisation processing for implementation in other conventional FRP processing methods.

7 Modelling of Radical Induced Cationic Frontal Polymerisation

This chapter is based on the supervised master thesis work carried out by M. Lefort.

Modelling of frontal polymerisation is essential part to address the complex concurrent phenomena and reach an effective process design. As discussed in Section 2.5, models describing FROMP have already shown good potential to fulfil these roles while no efforts have been made on describing RICFP systems to-date. We present here the exploratory work that was conducted on the modelling of RICFP. A reaction-kinetics model is derived based on experimental DSC analysis for pure and composite RICFP systems followed by the estimation of temperature-dependent material parameters. The defined model is implemented in a finite difference method and calibrated and validated with experimental recordings. Finally, the developed model is applied to several case studies related to Sections 5 & 6 to further shine light on the reported experimental observations.

7.1 Kinetic modelling of RICFP

Dynamic DSC analysis carried out at various heating rates β allowed for the determination of the enthalpy of polymerisation H_r as well as the kinetic parameters of Equation 3.11. As shown in Table 7.1, the polymerisation enthalpy was consistent for all heating rates while the variability is attributed to inaccuracies during the weighing of the resin that were amplified by the low sample quantities (i.e. 2-3 mg) used for DSC analysis. The overall averaged heat output of the reduced resin equalled 568.6±18.2 J/g which was slightly lower than the enthalpy of the composite RICFP resin of 617.7±14.1 J/g. This difference was explained by potential differences in curing degrees following Section 5.2.

Two peaks were observed in all DSC recordings in Figure 7.1, i.e. a large initial exothermic heat output followed by a smaller peak that was attributed to post-curing of the formed polymer after overcoming its T_g, which directly translated to a dual-peak in conversion rates. The first peak appeared at a temperature of ~120°C while the second temperature peak had its maximum at ~170°C. Both peak temperatures increased with increasing heating rate and thus
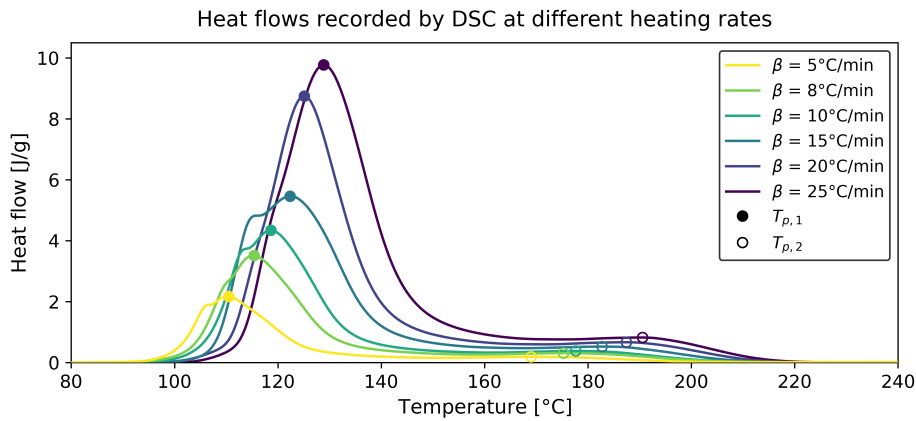
Figure 7.1: Exemplary heat flow curves recorded by DSC analysis at varying heating rates β, indicating the peak temperatures T_p of the first and second apparent heat flow peak.

Table 7.1: Overview of resin enthalpies H_r and peak temperatures T_p recorded in dynamic DSC analysis with varying heating rates β for reduced and composite RICFP resins.

β [°C/min]	5	8	10	15	20	25
			Reduced RICFP resin			
H_r [J/g]		546.4±9.5	571.9±6.8	583.5±20.2	574.4±32.0	
$T_{p,1}$ [°C]		121.4±0.5	122.9±1.4	129.0±1.0	135.1±5.7	
$T_{p,2}$ [°C]		173.2±0.3	176.9±1.5	181.4±0.4	185.5±0.5	
			Composite RICFP resin			
H_r [J/g]	621.4±27.6	620.4±24.6	624.7±16.7	616.7±5.8	608.6±10.7	622.9±43.3
$T_{p,1}$ [°C]	109.9±1.3	114.0±2.8	118.4±0.3	121.8±1.1	124.8±0.6	124.9±7.4
$T_{p,2}$ [°C]	169.5±1.0	175.4±0.2	177.9±0.4	183.3±1.0	187.2±0.7	189.4±2.3

fulfilled the requirement for the use of the Ozawa-Flynn-Wall method. Linear regression of the inverted peak temperature over the heating rate, shown in Figure 7.2, resulted in activation energies of 75.56 and 119.61 kJ/mol for $T_{p,1}$ and $T_{p,2}$ of the reduced RICFP system, respectively. The determined activation energies for the composite RICFP systems equalled 102.84 kJ/mol for $T_{p,1}$ and 124.74 kJ/mol for $T_{p,2}$. All the fitted activation energies showed R^2 values ranging between 90-100% from which the confidence in the regression procedure was concluded. The coefficient of determination of the regression on $T_{p,1}$ was lower for both resin systems compared to that on $T_{p,2}$, which was a result of inconsistencies in the curing behaviour, e.g. as observed at a heating rate of 15°C/min in Figure 7.1, at lower heating rates due to the fast initial curing rates and concurrent cooling by the DSC to maintain the set heating rate.

Fitting of of the dynamic DSC curves by Equation 3.11 led to the optimum model parameters listed in Table 7.2. Figure 7.3 shows that the model approximated the experimental curing behaviour with reasonable accuracy at the various heating rates, which supports the foreseen
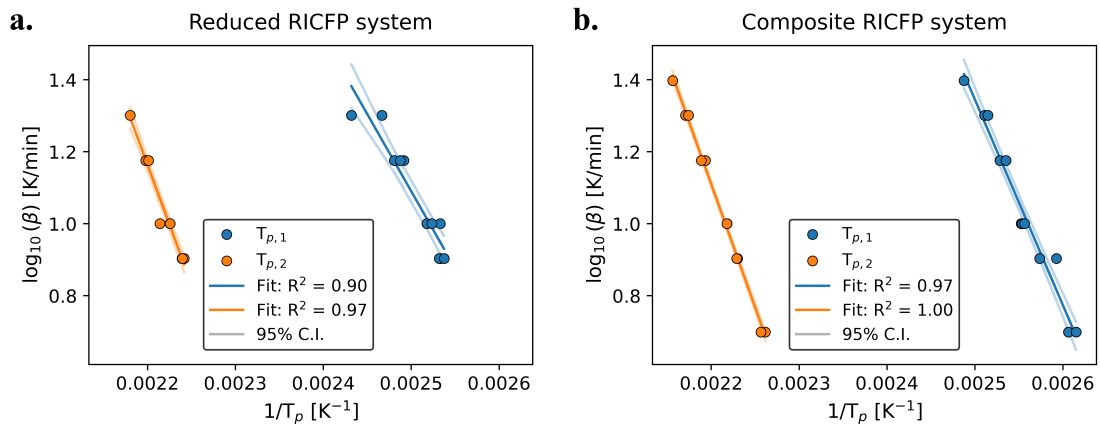
Figure 7.2: Derivation of activation energies by linear regression on peak temperatures for a) reduced and b) composite RICFP systems. The acronym C.I. denotes the confidence interval.

beneficial use of a model considering two curing reactions. The derived reaction-kinetics model was able to capture the curing behaviour of the reduced RICFP system as a function of temperature (Figure 7.3a) as well as its dependence on the overall conversion (Figure 7.3b). The highest fitting accuracy was achieved for intermediate heating rates, e.g. 10-15 °C/min, while variability in the recorded DSC signals, e.g. the appearance of a deviation for a β of 15°C/min at ~120°C, might have induced slight differences between the modelled and experimental heating rates. This was more apparent when considering the conversion rate as a function of conversion, depending largely on the shape of the DSC signal that resulted in increased differences. A similar observation was made for fitting of the composite RICFP system (Figure 7.3c & d) where heating rates of 10-15°C/min showed the best approximation by the fitted kinetic model while larger offsets were recorded for elevated heating rates.

The derived models for describing the reduced and composite RICFP systems were thus believed to provide a representative description of the RICFP systems for subsequent use in finite difference simulations. Further improvements on the model accuracy could be foreseen by expanding the dataset used for the CMA-ES fitting procedure so as to minimise the influence of experimental variability of the DSC recordings. Compared to the kinetics model reported for pDCPD systems [212], i.e. capable of undergoing FROMP, the most apparent difference can be seen in the frequency factor A_1 which was reported by Robertson et al. [20] to be in the order of 10^{15} s^{-1}, i.e. 7 and 3 orders of magnitude higher as compared to the assessed reduced and composite RICFP systems. This difference in frequency factor, largely determining the amplitude of the model, was in agreement with the reduced conversion rates that were about an order of magnitude lower for the RICFP systems [212].

The derived model moreover gave an insight on the relative dominance of the two peak signals. The first exothermic peak for the reduced RICFP system was found to make up 88.2±0.8% of the surface integral of the heat flow recorded in DSC analysis and hence the polymerisation enthalpy H_r.
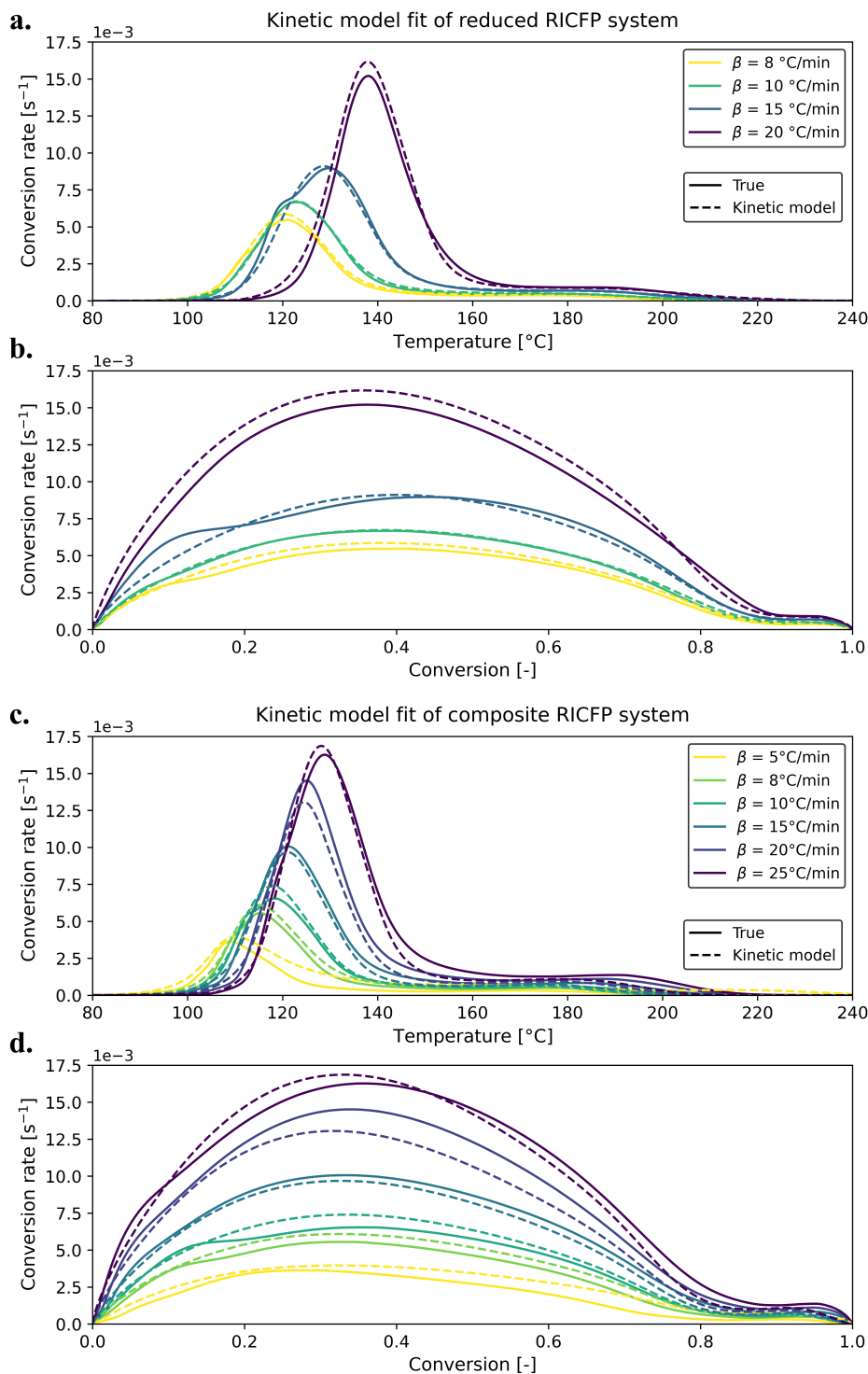
Figure 7.3: Overview of the reaction-kinetics fitting results of the conversion rates recorded by dynamic DSC analysis for the reduced RICFP system as a function of a) temperature and b) conversion and the composite RICFP system as a function of c) temperature and d) conversion.

Table 7.2: Model parameters derived of reduced and composite RICFP systems by DSC analysis with varying heating rates.

A_1 [s^{-1}]	$E_{a,1}$ [kJ/mol]	n_1 [-]	m [-]	c_d [-]	α_c [-]	A_2 [s^{-1}]	$E_{a,2}$ [kJ/mol]	n_2 [-]
$2.80 \cdot 10^8$	75.56	1.90	0.63	23.48	0.82	$1.09 \cdot 10^{12}$	119.61	1.15
$2.33 \cdot 10^{12}$	102.84	2.66	0.65	26.55	0.76	$2.68 \cdot 10^{13}$	124.74	1.88

Consequently, the second peak attributed to post-curing made up 11.8±0.8% of the heat flow. The composite RICFP system showed similar distributions with the first and second peaks making up 82.2±0.8 and 17.8±0.8% of the polymerisation enthalpy, respectively.

7.2   Heat capacity modelling

Experimental characterisation of the heat capacities of carbon fibre and PMI foam, shown in Figure 7.4a, showed consistently increasing trends with increasing temperatures. The heat capacity of carbon fibre was closely followed by the fitted linear trends, despite slight deviations at the extremities. The PMI foam on the other hand showed increased deviations, in particular at elevated temperatures, that were attributed to melting and degradation as the foam was subjected to temperatures above its service temperature of 180°C recommended by the supplier. Both of the constituents thus showed significant increases over the expected temperatures experienced during frontal polymerisation, i.e. 58.5% and 59.8% for carbon fibre and PMI foam, respectively. These strong increases support the hypothesised advantage of including temperature-dependent material properties to accurately model frontal polymerisation, in contrast to the constant heat capacities used by e.g. Refs. [20, 174, 176, 211, 222].
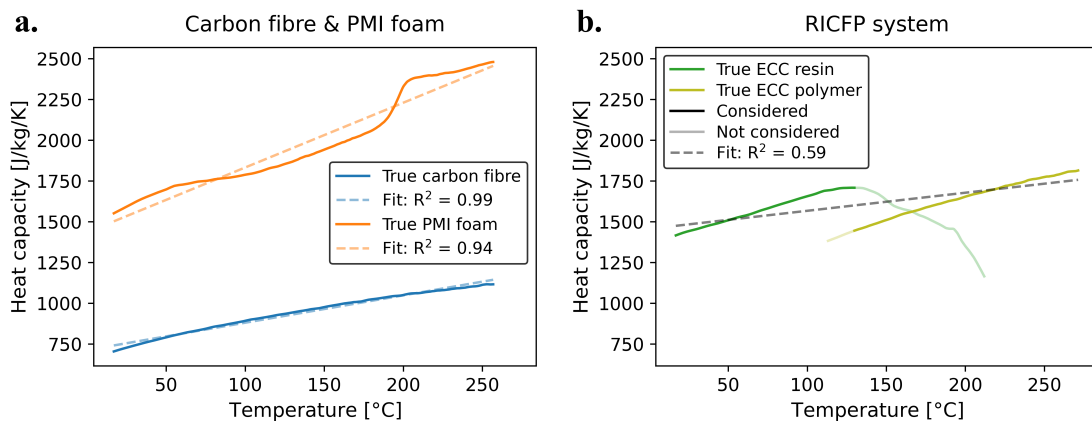
Figure 7.4: Experimental characterisation and fitting of heat capacities of different components for modelling of the RICFP process: a) carbon fibre and PMI foam and b) the RICFP systems composed of ECC monomer and polymer.

Table 7.3: Overview of temperature-dependent heat capacities for RICFP resin, carbon & glass fibre and PMI foam.

Material	Heat capacity [J/kg/K]	R^2
RICFP system	$1.11 \times T + 1153$	0.586
Carbon fibre	$1.68 \times T + 254.9$	0.988
Glass fibre	$1.24 \times T + 441.9$	-
PMI foam	$3.97 \times T + 350.4$	0.938

The recorded heat capacity of ECC monomer resin showed a steady increase followed by a sudden drop at ~135°C which was attributed to decomposition of the monomer in the absence of a curing reaction. Polymer produced with the same resin on the other hand possessed a gradually increasing heat capacity up to 270°C that was significantly lower than that of the monomer resin. The absence of an overlap between the two recorded curves in Figure 7.4b, combined with the inability to monitor the curing degree during the rapid RICFP, hampered the direct derivation of a combined description of the heat capacity of the RICFP system. Instead, an approach was followed where a cut-off between monomer and polymer was arbitrarily set to 130°C and fitting was carried out considering the heat capacity of monomer resin below the cut-off temperature and the heat capacity recorded for polymer above the cut-off. While Figure 7.4b and a coefficient of determination of 0.586 show that the linear description is of limited accuracy, this approach was believed to be preferential as it would avoid potential numerical errors induced by a step-change between the two phases. The resulting descriptions of all constituents used in the continuation of this work are listed in Table 7.3.

7.3 Numerical stability

Numerical stability of finite difference models describing frontal polymerisation is generally complicated by the highly localised reaction zones and consequently large thermal gradients [211, 220], imposing the need for highly refined meshes and time resolutions to avoid undesired numerical errors as described in Section 2.5.2.2. Refinement of the simulation domain however comes at the cost of the computational efficiency and hence an optimisation of the resolution was desired in order to accurately simulate the RICFP process at a minimum computation time. Given a set element size Δx and timestep Δt, four different cases could unfold that could be segregated in different domains as a function of Δx and timestep Δt. The various domains are indicated for the reduced RICFP resin in Figure 7.5a while exemplary temperature profiles corresponding to each of the domains are presented in Figure 7.5b. Simulations with relatively large timesteps combined with small mesh sizes were found to give significant instabilities with front temperatures periodically varying over several order of magnitude. The onset of unstable front behaviour correlated with deviations from the Neu-
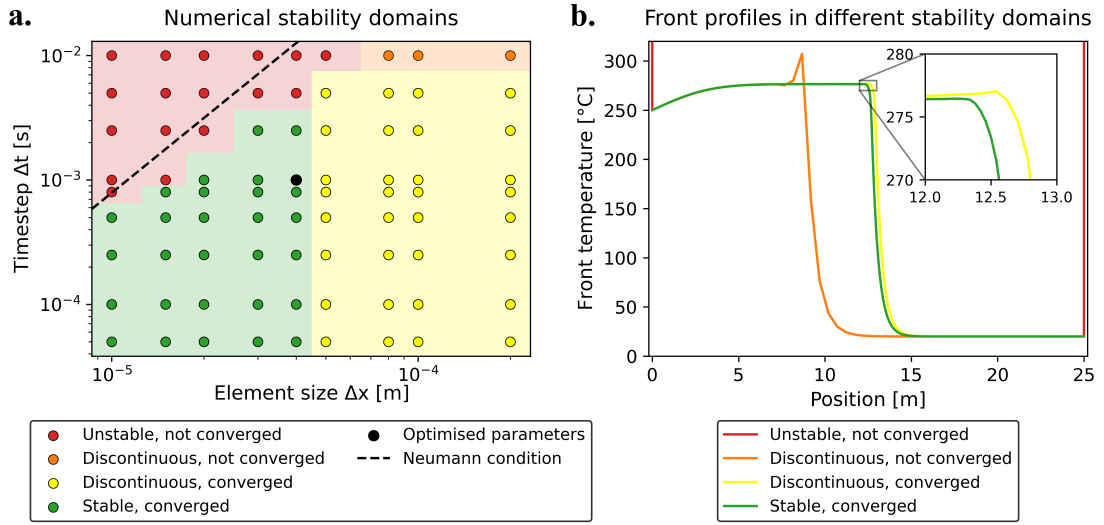
Figure 7.5: a) Numerical stability domains of the reduced RICFP model and b) exemplary front temperature profiles corresponding to the various domains.

mann condition, i.e. Equation 3.21. This correlation moreover supports the applicability of the Neumann conditions for thermal models with additional heat generation terms for gaining a first indication of the required timestep at a given spatial resolution, although offsets of ~30% were observed at some element sizes. Increasing the element size above $8 \cdot 10^{-5}$ metre with a timestep of 10^{-2} seconds, and hence being below the Neumann condition, largely removed the numerical instabilities with artificial peaks of ~30-50°C appearing irregularly at the front location. These instabilities however prevented the model from converging at timesteps above ~$8 \cdot 10^{-4}$ while the instabilities with timesteps below this threshold were significantly smaller and did not introduce any issues for the convergence of the model.

A domain size resulting in the absence of numerical instabilities was identified at element sizes below $5 \cdot 10^{-5}$ metre and timesteps in the order of 10^{-3} to 10^{-4} seconds, resulting in smooth temperature profiles and constant front temperatures during the complete steady-state phase of the RICFP process. An element size of $4 \cdot 10^{-5}$ metre and a timestep of 10^{-3} seconds were thus chosen as the optimal trade-off between the numerical accuracy and computational costs, while the timestep was believed to be sufficiently small to avoid the introduction of numerical instabilities at different simulation conditions, i.e. potentially inducing minor shifts in the domains of Figure 7.5a. Using these optimised settings, the computational time was decreased by 37% for one-dimensional and 85% two-dimensional simulations compared to, for example, an element size of $2 \cdot 10^{-5}$ metre without compromising for the numerical accuracy. Following the Neumann condition, the domains presented in Figure 7.5a were expected to shift due to the change in thermal conductivity in the presence of fibrous reinforcements. This change was limited for insulating glass reinforcement and the optimum element size and timestep was found to remain in the stable domain. These however had to be adjusted for highly conductive carbon fibre reinforcements, requiring a timestep of $2 \cdot 10^{-4}$ seconds at an element size of
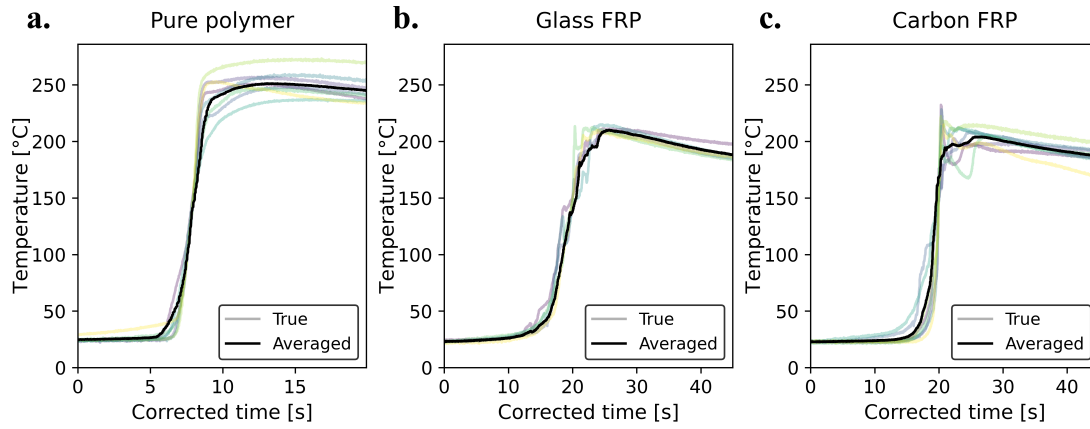
Figure 7.6: Experimental and averaged temperature profiles recorded during a) production of pure polymer using the reduced RICFP resin and b) glass and c) carbon FRPs using the composite RICFP system that were used for calibration of the developed models describing RICFP.

$4 \cdot 10^{-5}$ metre, increasing the computation time by a factor five.

7.4 Experimental validation

Calibration and validation of the developed model was done on a series of temperature recordings and derived front velocities as described in Section 3.4.6. Figure 7.6 shows that significant differences between thermocouple recordings were observed. These were largely attributed to experimental inaccuracies in the thermocouple positioning, e.g. away from the centreline of the mould cavity, for a pure polymer system in Figure 7.6a. The glass and carbon FRP systems in Figures 7.6b & c, respectively, showed inconsistencies during both the initial heating phase and the occurrence of a thermal peak. This behaviour is in line with prior experimental observations on composite systems presented in Sections 5 & 6 and is attributed to the inhomogeneous microstructure of the fabric architectures. To overcome this experimental variability, the model calibration was carried out on averaged front characteristics and temperature profiles. Figure 7.6 shows that the averaged temperature profiles were representative of the experimental behaviour for all of the considered systems.

The developed model for the reduced RICFP system, i.e. in the absence of fibrous reinforcements, yielded front temperatures as high as 335°C in a one-dimensional domain which was significantly higher than the experimentally recorded front temperature of 251.3°C. Similar differences were recorded between experimental and simulated temperatures for composite RICFP resin systems containing 40% V_f carbon and glass reinforcement. For that reason, several adaptations were made to the numerical implementation of the derived model. Two parameters were initially chosen for adaptation as they presented an experimental uncertainty. The thermal conductivity was fitted to account for the potential resin flow imposed by the

rapid thermal expansion of the resin upon frontal polymerisation, as was experimentally observed by an outgoing flow at the resin outlet, and the resulting mass transfer could induce differences in the front characteristics. The derived thermal conductivity κ_c can thus be understood as the sum of the intrinsic thermal conductivity (listed in Table 3.3) and the fitted part κ_{fit}. Secondly, a difference may be present between the heat output of a resin, i.e. H_r, recorded in the dynamic DSC analysis (Table 7.1) and heat released during frontal polymerisation, e.g. due to differences in the final curing degrees. A reduction factor was therefore introduced to define an effective polymerisation enthalpy being released during RICFP. In addition, lowering of the amplitude for the second term in the reaction-kinetics model (Equation 3.11) by a factor 0.1 and capping the maximum curing degree to 0.9 were empirically found to strongly enhance the model accuracy. Although these adjustments are not directly in relation to ongoing physical phenomena, their beneficial use was believed to relate to slower diffusion-controlled kinetics at elevated temperatures that is generally not well captured in phenomenological reaction-kinetics models, as discussed in Section 2.5.1.
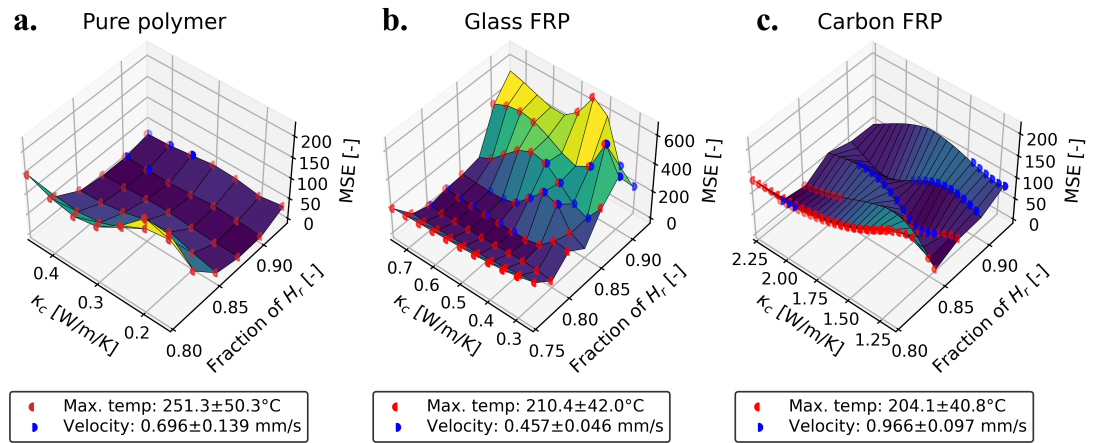
Figure 7.7: Gridsearch response surfaces describing the mean squared error between numerical and experimental temperature profiles with different parametric combinations for a) pure polymer, b) glass FRP and c) carbon FRP systems.

Gridsearch optimisation of the thermal conductivity and effective polymerisation enthalpy, assessed by a combination of the similarity between temperature profiles below 150°C, the front velocities and the peak temperatures, did not directly yield an optimum parametric combination. The resulting grids for the MSE in Figure 7.7 moreover showed significant variability, in particular for the composite systems, and the best fitting temperature profile, i.e. yielding the lowest MSE, did not necessarily correspond to close approximations of the front velocity and peak temperatures. The response surfaces for these two parameters can be found in Appendix A.2.1. A preliminary selection was therefore introduced where parametric combinations were first assessed on their approximation of the front characteristics after which the combination giving the lowest MSE of this selection was believed to be the optimum.

Pure polymer systems (Figure 7.7a) showed the largest offset between experimental and numerical front characteristics and for that reason parametric combinations were selected if they gave front velocities and temperatures within a ±20% range of those recorded experimentally. The origin of these difference may be found in ongoing phenomena that are currently not captured in the model, e.g. minor degradation of the polymer, which are more prominent in the absence of high fibre contents and at high front temperatures. Further investigation is however required to find the exact origin of these differences and to develop expressions to account for them in the numerical model. The optimum resin thermal conductivity and heat output for approximating the front temperature were found to be 0.4 W/m/K and $0.90 \times H_r$, i.e. 511.7 J/g, as listed in Table 7.4. Using these parameters, the front temperatures decreased to 280.7°C in a two-dimensional domain and hence reducing the offset between experimental and numerical temperatures from 33.5% to 11.7%. Figure 7.8a moreover shows that the experimental temperature profile was overall closely approximated by the developed model. Front velocities could only be captured with limited accuracy, resulting in underestimations of -17.4% and -28.7% in one- and two-dimensional domains and further work is to be carried out to elucidate the origin of these offsets.
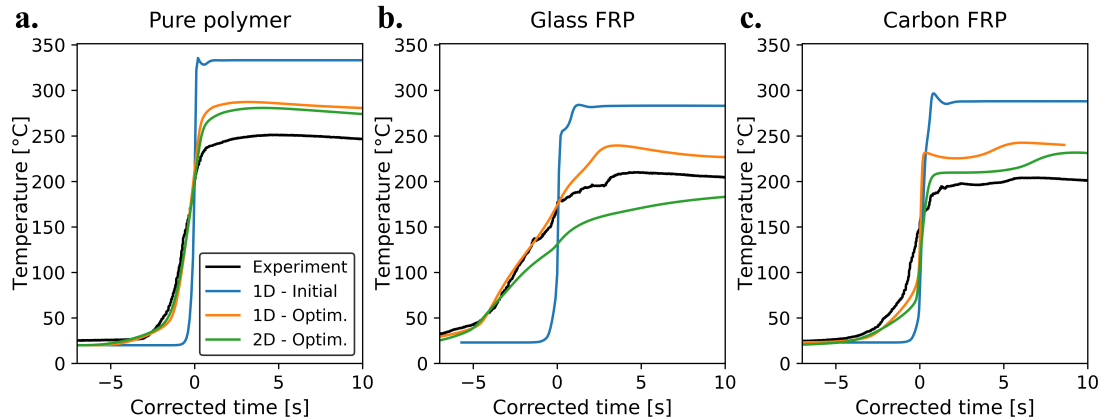
Figure 7.8: Comparison of experimental and numerical temperature profiles for a) pure polymer, b) glass FRP and c) carbon FRP systems in one- and two-dimensional domains. Initial temperature profiles are derived using the initial models while the acronym 'Optim.' denotes the optimised models after calibration with experimental data.

Application of the same fitting procedure on the composite RICFP resin gave a closer correlation between the simulation results and the experimental front characteristics derived for carbon and glass FRP systems. A selection was therefore made on parametric combinations giving front velocities that range within 10% of the experimental data while a range of 20% was used for the peak temperatures. The number of fitting parameters fulfilling these requirements was significantly higher as compared to the pure polymer system, as is illustrated in Figures 7.7b & c. This was attributed to the lower resin fraction in these systems hence making potential model inaccuracies less apparent. The optimised parametric combinations, giving the lowest MSE, are listed in Table 7.4. A negative value for κ_{fit} was found to be the optimum for

the carbon FRP system which, although contradicting the aforementioned reasoning for fitting of thermal conductivity, is explained by the interdependence of the simultaneously fitted H_r and κ_c parameters. The simulated temperature profiles for composite systems in Figures 7.8b & c showed increased deviations from the experimental temperature recordings. This is attributed to the increased complexity of FRP systems for describing transient phenomena, e.g. due to the absence of a dedicated description of the fabric microstructure, while the FRP systems were also significantly affected by thermal instabilities as is further discussed in Section 7.5. The steady-state front characteristics were on the other hand closely approximated resulting in limited underestimations of the front velocities of 4.6% and 8.3% for the respective glass and carbon FRP systems in a two-dimensional domain, while temperatures were overestimated by 9.8% and 13.4%, respectively. The accuracy of these estimations is comparable to that achieved by models describing FROMP discussed in Section 2.5.2.2.

Table 7.4: Overview of optimised fitting parameters and resulting front characteristics. Acronym Exp. denotes that values were recorded experimentally while the acronyms 1D and 2D indicate the use of one- and two-dimensional simulation domains.

Type	**Frac.** H_r	κ_c	κ_{fit}
	[-]	**[W/m/K]**	**[W/m/K]**
Pure polymer	0.900	0.40	0.23
Glass FRP	0.825	0.55	0.24
Carbon FRP	0.875	1.55	-0.06

	Front temperature			**Front velocity**		
	Exp.	**1D**	**2D**	**Exp.**	**1D**	**2D**
Pure polymer	251.3	287.3	280.7	0.696±0.013	0.575	0.496
Glass FRP	210.1	239.4	230.7	0.457±0.011	0.437	0.436
Carbon FRP	204.1	242.5	231.6	0.966±0.090	0.933	0.886

Optimisation of the model parameters thus allowed for an accurate description of the RICFP process in FRPs, capturing both the overall temperature profiles as well as the frontal polymerisation characteristics. It should be noted that the effective polymerisation enthalpies, i.e. the recorded enthalpy of Table 7.1 multiplied by the fitted fraction in Table 7.4, are for all of the considered systems comparable to the enthalpy of the first term in Equation 3.11 equalling, as previously discussed in Section 7.1, 88.2±0.8% of the total enthalpy for the reduced RICFP system and 82.2±0.8% for the composite RICFP system. Taking this second exothermic peak out of consideration, e.g. assuming that its reaction rate cannot follow the rapid conversion during RICFP, did however not result in an improved approximation of the front characteristics as it would result in a rapid spike in the released heat while the discussed introduction of a general reduction factor decreases the heat release rate over the complete temperature range. The latter would consequently reduce the heating rate upon frontal polymerisation hence increase the influence of competing thermal diffusion, resulting in reduced

front temperatures. The optimised reduction factor was therefore used in the continuation of this work and an overview of the model parameters and model conditions can be found in Appendix A.2.2. Further investigation is required to develop a descriptive model that captures all of the ongoing phenomena. Improvements of the model descriptions are foreseen by the development of a more accurate numerical description of the experimental configuration. A particular focus on an improved representation of the microstructure, i.e. compared to the current homogenised model, since the largely heterogeneous distribution of V_fs is believed to have a significant influence on the front propagation, in line with Sections 5 & 6.

7.5   Case studies

Supplementary recordings are provided for improved visualisation of the results presented in this chapter. The videos can be accessed by clicking the red fonts *throughout this chapter.*

7.5.1   Variation of the initial temperature

The influence of the initial resin temperature was investigated as a first case study using the developed models. Both the pure polymer reduced RICFP system in Figure 7.9a and the systems containing 40% V_f of glass and carbon reinforcement in Figures 7.9b and 7.9c, respectively, showed significant changes in the simulated temperature profiles with varying initial temperature. This is supported by the temperature profiles recorded over the mould length at specific instances that are shown in Appendix A.2.3. The numerical results suggest that RICFP could be successfully induced in the reduced resin system at initial temperatures as low as -5°C. Thermal instabilities were however predicted at this temperature that gradually decreased in amplitude until they completely disappeared at an initial temperature of 20°C initial temperature of 20°C. The dependence of the occurrence of thermal instability on the initial temperature in line with predictions using the Zeldovich number [192, 193]. The observed transition hence corresponds to a critical Zeldovich number $\beta_{z,c}$ of 7.86 for the reduced RICFP system. Stable fronts would thus be expected when $\beta_z \geq \beta_{z,c} = 7.86$ while unstable front propagation is predicted at $\beta_z < 7.86$. The observed $\beta_{z,c}$ value of 7.86 is comparable to those reported by Masere et al. [194] and Goli et al. [191] which supports the validity of the numerical findings.

The formation of thermal instabilities was predicted to be amplified in FRP systems, with sharp temperature peaks appearing periodically near the front at initial temperatures up to 40°C for the glass FRP system in Figure 7.9b. The critical Zeldovich number was therefore found to be significantly higher and equalled 54.4, which was believed to be a result of the reduced resin fraction, i.e. 60% of the total volume, and hence reduced heat release.
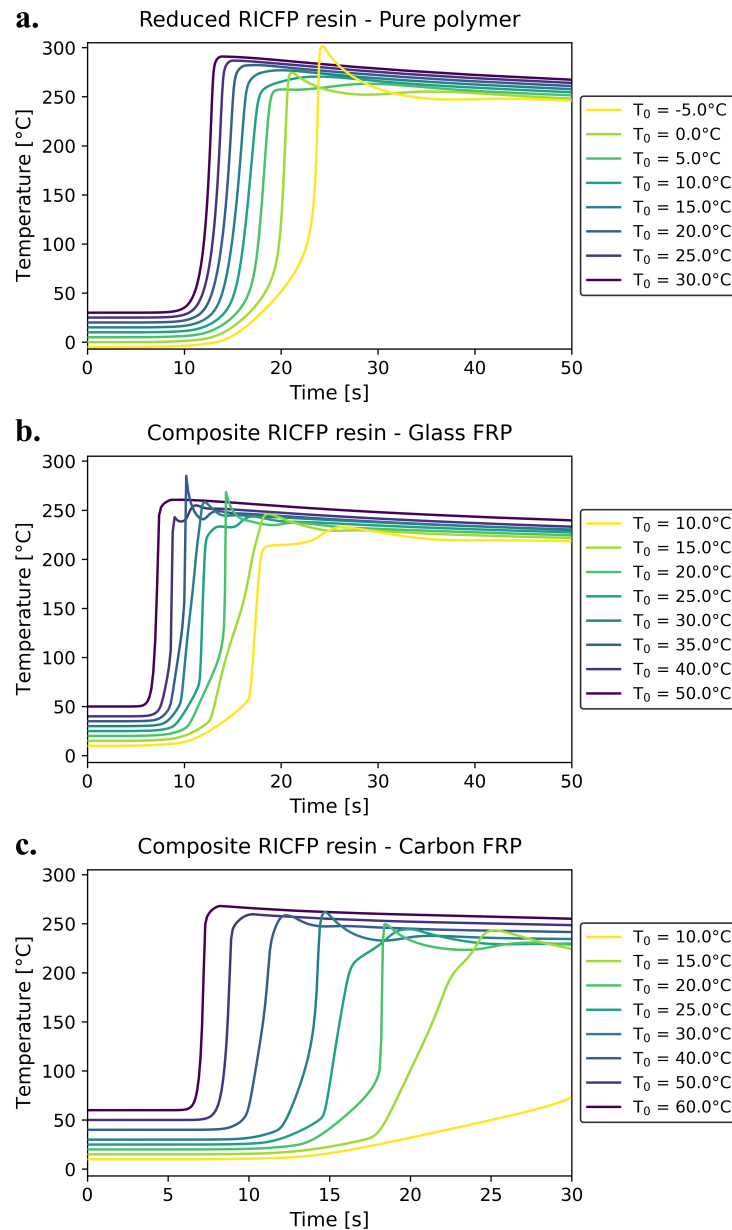
Figure 7.9: Simulated temperature profiles at a the centre of the mould at 15 mm from the initiation point of the a) reduced RICFP resin system and composite RICFP resin system with 40% V_f b) glass and c) carbon reinforcements.

Thermal instabilities in glass FRPs were evidenced experimentally by the formation of periodic patterns at the sample surface shown in Figure 7.10, where the darker sections are believed to correspond to lower front temperatures and sections with a yellow tone to the occurrence of thermal peaks. The critical Zeldovich number of the carbon FRPs system in Figure 7.9c was with 57.9 comparable to that recorded for glass FRPs while the thermal instabilities were recorded at temperatures up to 50°C. The resulting thermal peaks in unstable regimes
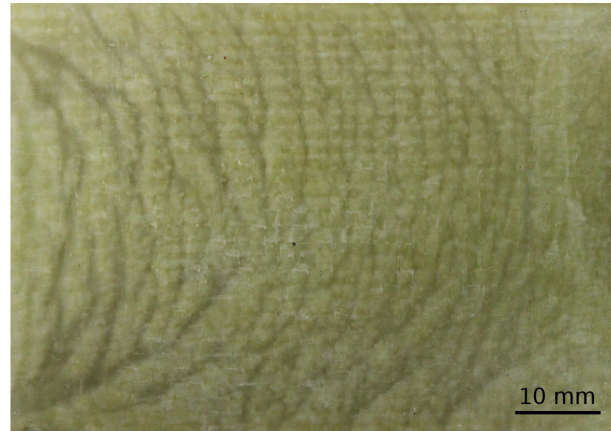
Figure 7.10: Optical image of a glass FRP sample showing patterns due to thermal instabilities.
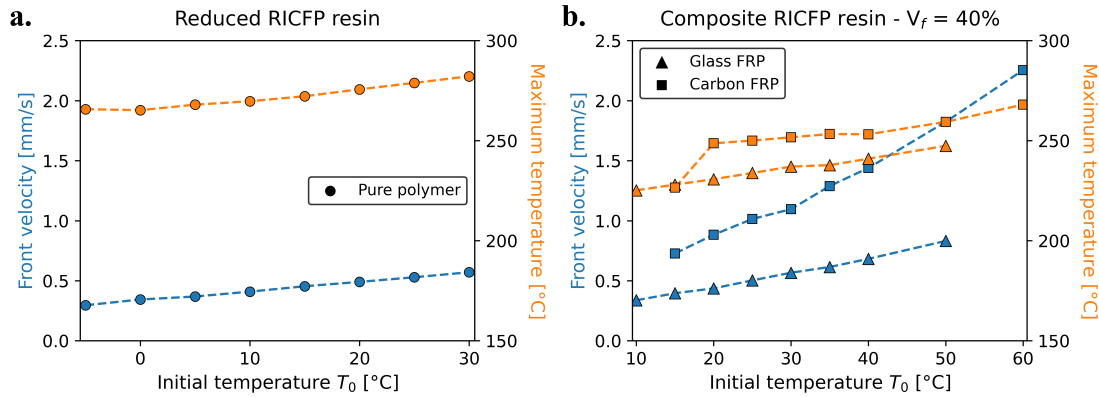
Figure 7.11: Overview of simulated front characteristics with varying initial temperatures of the a) reduced RICFP resin and b) composite RICFP resin in the presence of 40% V_f glass or carbon reinforcements.

appeared to be less sharp which is attributed to the conductive nature of carbon fibres, rapidly guiding the heat away from the front region.

The slopes of the temperature profiles were found to increase with increasing initial temperatures for all systems in Figure 7.9, which is explained by the reduced activation energy that has to be provided by thermal diffusion to enable the autocatalytic mechanism in a resin layer. This trend was also followed by the averaged front velocities in Figure 7.11 while the front temperatures increased only slowly after an initial stabilisation. The latter is explained by insulating mould configuration that ensured all the heat released by the resin to be maintained near the front region, resulting in similar temperature increases upon frontal polymerisation with offsets between trials correlating to the set offset in initial temperature. The extent of the front velocity increase depended on the resin type as well as the fibre type. Increasing the initial temperature of the reduced RICFP resin (Figure 7.11a) by 30°C translated to an increase of the front velocity of 66.1%. This was significantly lower than the increase recorded for the

composite RICFP system (Figure 7.11b), increasing 90.5% and 106.5% for glass and carbon FRPs, respectively. The numerical results thus support the hypothesis made in Section 6 that increasing the initial temperature, e.g. by preheating in self-catalysed frontal polymerisation, is beneficial for the RICFP process by reducing the influence of thermal instabilities and increasing the front characteristics.

7.5.2 Role of the trigger time

The initiation phase represents the only part of the frontal polymerisation process that requires external energy input. Minimisation of the initiation time to establish a self-sustaining polymerisation front is thus desired to minimise the energy demand of the process. A second case study was therefore carried out to numerically assess the influence of the trigger time, i.e. the time a thermal source is applied, on the propagation behaviour of the considered RICFP systems.
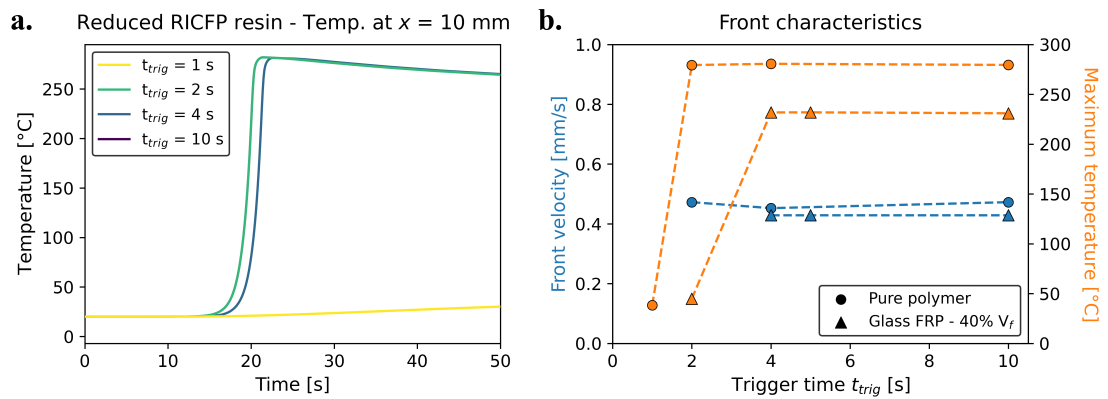
Figure 7.12: Overview of simulated front characteristics with varying trigger times: a) temperature profiles recorded for the reduced RICFP system and b) front characteristics of pure polymer and glass FRP systems.

Figure 7.12a shows that the application of a thermal source of 250°C was required for at least 2 seconds in order to successfully form a self-sustaining front. The front arrival taken at 10 mm from the initiation point was slightly delayed for a trigger time of 2 seconds, while further increase of the trigger time resulted in identical arrival times. This was attributed to lower temperature overshoot at the front initiation at a trigger time of 2 seconds due to the reduced energy input, in contrast to for example a trigger time of 4 seconds. The trigger time did not influence the steady-state front temperatures and velocities, shown in Figure 7.12b, which is line with the reasoning in Section 2.4.2 that the front characteristics in this regime are solely a result of the balance between the generation polymerisation enthalpy and potential heat losses. The same observation was made with glass FRPs (Figure 7.12b) although the heat losses induced by the presence of glass reinforcements increased the threshold trigger time for the successful formation of a self-sustaining front to 4 seconds.

a.

b.
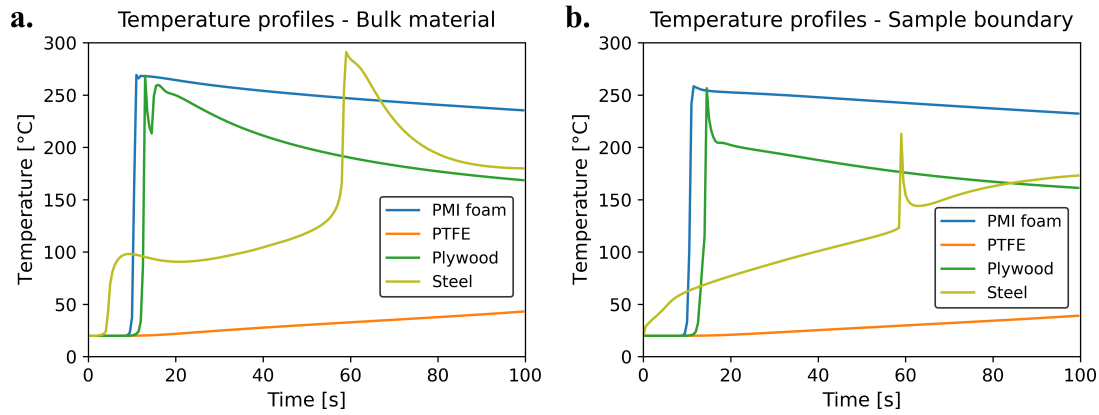
Figure 7.13: Simulated temperature profiles of a 20% glass FRP system with different mould materials of 5 mm thickness recorded at the a) bulk material and b) sample boundary.

7.5.3   Boundary conditions

The experimental observations presented in Section 5.2 suggested a significant influence of the choice of mould material on the resulting frontal polymerisation behaviour. A complementary numerical assessment was therefore made on the composite RICFP system with 20% V_f glass fibres. Mould materials were chosen to be comparable to those used in Section 5.2: PMI foam instead of the highly insulating Teflon-covered PVC foam core, PTFE to represent the silicone elastomer and steel. Simulations with plywood were moreover carried out as a further reference on the role of the mould properties. The thermal properties used for simulating plywood, PTFE and steel moulds are reported in Table 7.5.

Table 7.5: Overview of temperature-dependent heat capacities for RICFP resin, carbon & glass fibre and PMI foam derived by DSC analysis.

Material	Density [kg/m^3]	Thermal conductivity [W/m/K]	Specific heat [kJ/kg/K]	Thermal effusivity [kJ/m^2/K/s$^{0.5}$]
Plywood	500	0.13	2.50	40.3
PTFE	2200	0.25	1.30	84.6
Steel	7850	32.0	0.46	339.9

The numerical predictions supported the hypothesised relationship between the thermal effusivity and the front characteristics that was discussed in Section 5.2. The temperature profiles in Figure 7.13 showed comparable peak temperatures between PMI and plywood configurations both at the centre of the glass FRP domain (Figure 7.13a) as well as close to the mould interface (Figure 7.13b). The increased heat losses to the plywood mould type resulted in the higher cooling rates that were as expected more apparent at the sample boundary, indicating the formation of a thermal gradient behind the propagating front. Figure 7.14 shows
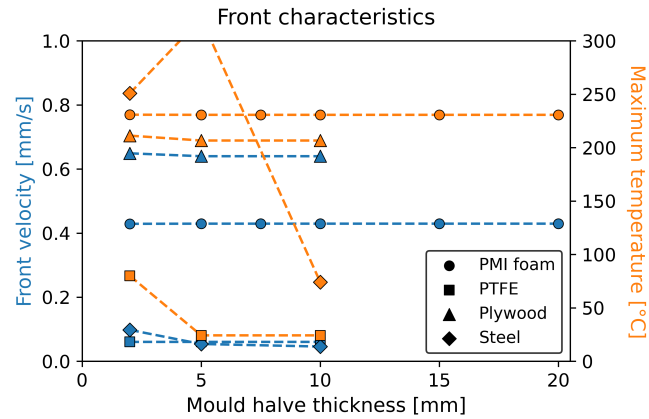
Figure 7.14: Simulated front characteristics with different mould materials and thicknesses.

that the simulated front velocities were the highest in the presence of the highly insulating PMI foam configuration, which agrees with the observations reported in Section 5.2. No influence of the mould thickness was observed from the current set of simulations. This is likely explained by the relatively low heat fluxes through the insulating mould halves as compared to the in-plane front propagation.

Despite the limited glass fibre V_f of 20%, simulations for systems with mould domains composed of PTFE did not show the self-sustaining frontal polymerisation and only gave minor temperature increase up to ~40°C due to thermal convection of the heat source. The absence of frontal polymerisation is related to the large heat uptake by the PTFE that was found to increase with the mould thickness, resulting in a decreased maximum temperature in Figure 7.14. Following Section 5.2, a further decrease of the temperature would be expected in the presence of a conductive steel mould. The simulated temperature profiles in Figure 7.13 showed an initial temperature increase up to ~80-100°C that was followed by an exothermic peak after ~60 seconds. This behaviour was a direct result of the small domain size where the recordings showed that the application of a thermal source resulted in the rapid heating of the mould domain that subsequently preheated the glass FRP domain. Frontal polymerisation of the sample domain took place once it was sufficiently preheated. Although this behaviour complicates a direct comparison with the experimental observations, the temperature profile in Figure 7.13a was highly similar to those recorded for the self-catalysed frontal polymerisation method in Section 6 and hence confirm capability of the model to capture the effects of transient preheating. The exothermic peak width was significantly smaller near the mould interface, which is explained by the increased heat flux upon the temperature increase induced by frontal polymerisation as was also observed experimentally during oven-cured RICFP processing in Section 6.4 and Appendix A.1.3. The developed model could thus be employed to gain further insights in the role of the boundary conditions on the RICFP process. Although the numerical observations were related to experimental observations reported in other sections, dedicated experimental validation is desired to increase the confidence in the numerical findings.

7.5.4 The influence of fibrous reinforcements

The extensive heat uptake by fibrous reinforcements has already been discussed to influence the frontal polymerisation in several instances of this thesis work. For that reason, a final case study was carried out to assess the capability of the model to describe the frontal polymerisation processing of FRPs. Glass FRP systems showed the expected decreasing trend of both the front temperature and velocity with increasing V_f as shown in Figure 7.15. Contrary to Refs. [174, 176, 177] and Figure 2.11, the carbon FRPs systems did not show an initial increase at low V_f. The numerical front velocities predicted for both composite systems closely approximated the experimentally recorded values, confirming the previously described accuracy of the derived model. Front temperatures were overestimated by ~15°C, which is in the same order as discussed in Section 7.4. It should be noted however that experimental validation was limited to a small range of V_fs due to the delicate balance between the quenching of the system at too high V_fs and degradation of the polymer, altering the front characteristics as discussed in Section 2.4 and 5.

The numerical simulations predicted the maximum V_f that could successfully be polymerised in a PMI foam mould configuration kept at room temperature to be 55% and 42.5% for glass and carbon FRP systems. The increased maximum V_f for insulating fibre types is in agreement with the work of Dung Tran et al. [22]. The maximum V_f of carbon FRP systems is in the same order as observed experimentally with the same resin system in Sections 5 & 6 while the minor differences are attributed to the inhomogeneous microstructure of experimental FRPs. Continued investigation combined with experimental validation is foreseen to elucidate the role of preheating, i.e. as done in self-catalysed frontal polymerisation, on the maximum V_f.
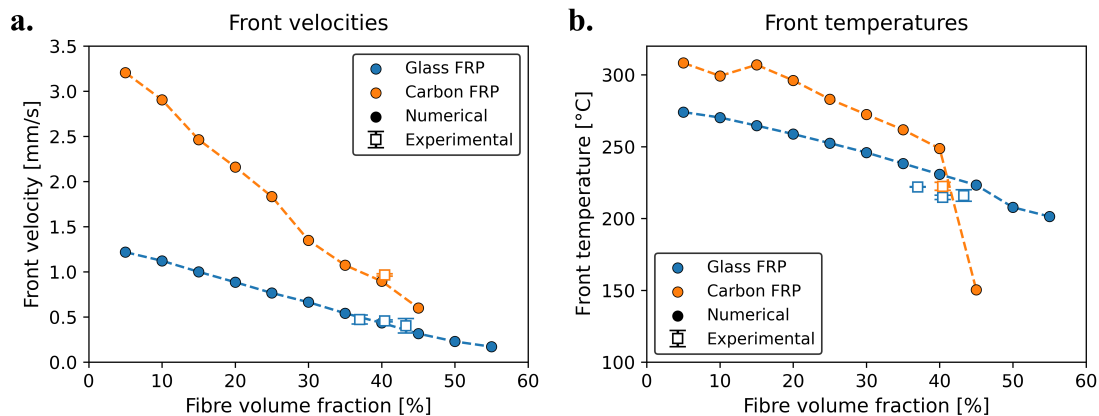
Figure 7.15: Simulated front characteristics with varying V_fs: a) front velocities and b) front temperatures.

7.6   Conclusion

The development of a model for describing of RICFP is presented in this chapter. Two resin systems were modelled: one for the production of pure polymer and one for the production of carbon and glass FRPs. A two-term reaction-kinetics model was found to give the best description of the curing kinetics for both resin systems while temperature-dependent heat capacities were characterised to enhance the potential model accuracy. The derived consitutive equations were subsequently implemented in a finite difference model of which the size of the elements and time steps were optimised to avoid the introduction of numerical errors. Calibration of the developed models was done on a series of experimentally derived temperature profiles and front velocities and resulted in strongly improved model accuracy. Front velocities were approximated with 4.6% and 8.3% accuracy for the glass and carbon FRP systems, while front temperatures were generally overestimated by 9.8-13.4%. The models were subsequently applied to a number of case studies to complement the experimental findings reported in Sections 5 & 6. Future work comprises the continued validation and optimisation of the numerical models, while its extension to describe more complex geometries is also highly desired.

8 Conclusion & Outlook

8.1 Conclusion

This thesis work aimed to develop methods for microstructural evaluation of dynamic flow behaviour and frontal polymerisation curing in the context of liquid composite moulding (LCM) processes for FRP processing with epoxy based matrices.

Characterisation of the dynamic flow behaviour of resins infiltrating fibrous reinforcements at a microstructural level is complicated by the required high spatial and time resolutions. UV-flow freezing has been proposed as a promising method to overcome these limitations by rapid UV-photopolymerisation of the infiltrating resin, allowing for characterisation of the characteristic flow patterns without restrictions on the time resolution. The resin composition was optimised to ensure fast curing upon UV-irradiation while a post-curing procedure was enabled by the addition of a free-radical thermal initiator to ensure that the maximum attainable conversion could be reached and hence to minimise the chance of distortions induced during post-processing. Suitable additives were identified to facilitate the variation of the capillary number by altering the resin viscosity and surface tension. The UV-flow freezing methodology was optimised by the use of UV-transparent PMMA mould halves to maximise the UV-transmittance while rapid relaxation of the resin pressure was found to minimise the front propagation during UV-irradiation. The optimised method was subsequently applied for the analysis of flow patterns corresponding to viscous-dominated, balanced and capillary-dominated flow regimes. μCT analysis allowed for a volumetric assessment of the flow front morphology at a microstructural level and was used for the derivation of saturation curves. The resolutions of the microstructural representations were in the order of those reported using synchrotron-μCT analysis while being compatible with a far greater range of processing conditions. The optimised UV-flow freezing methodology thus confirmed its foreseen potential as an accurate and versatile method.

Frontal polymerisation-assisted production of FRPs has the potential to bring unmatched reductions in curing time and energy demand. The use of frontal polymerisation for FRP processing is compromised by the excessive heat uptake of fibrous reinforcements at the high

V_fs sought for in industry (i.e. >55%), impeding autonomous front propagation. Enhanced thermal management of the local governing heat balance was thus investigated in order to overcome these limitations. Control of the heat generation of a model epoxide system capable of undergoing RICFP was possible by variation of the photo- and thermal initiating compounds. The mould configuration was found to exert a strong influence on both the front characteristics and the resulting curing degrees by the formation of strong thermal gradients over the sample thickness. Highly-insulating foam core mould configurations were beneficial for the RICFP process by reducing the heat losses to the environment and thereby inducing a shift in the local heat balance. A processing window was defined using the improved mould configuration that related the formation of a self-sustaining or supported front to the initiator content and V_f. It was moreover possible to produce carbon FRPs with maximum V_fs of 45.8% while frontal polymerisation supported by UV-irradiation could cure FRPs with V_fs up to 50%.

Although this confirms the need for controlling the governing heat balance to successfully produce FRPs with elevated V_fs, additional efforts were required to reach the V_fs of >55% that are sought for in the FRP industry. A novel self-catalysed frontal polymerisation processing method is therefore proposed where rapid RICFP of a sacrificial resin channel placed in thermal contact with the FRP results in efficient preheating of the fabric stack. This preheating reduces the energy needed to surpass the activation energy threshold for enabling of the auto-catalytic RICFP mechanism and thereby allowing for self-sustaining frontal polymerisation at V_fs that would normally see fronts being quenched. The method was validated on both conductive carbon and insulating glass FRP systems and was compatible with a wide range of FRP thicknesses. Placing filler materials in the sacrificial resin channel was suggested to have a strong influence on the frontal polymerisation behaviour and paves a way towards increased process control. Carbon FRPs were produced with V_fs up to 62.2%, i.e. 16.4% higher than what was achieved by conventional frontal polymerisation processing. The novel self-catalysed frontal polymerisation process reduced the energy demand by >99.5% compared to oven-curing procedures while yielding higher T_gs and comparable mechanical properties, confirming the potential of the novel method.

Finally, an exploratory numerical model is proposed to complement the experimental findings. Separate resin systems were modelled to describe RICFP of pure polymer and of FRP systems and a phenomenological two-term kinetic model was found give the best description for the complex cure kinetics of RICFP. Temperature-dependent material properties were characterised to improve the model accuracy. The frontal polymerisation process was simulated using a finite difference method and the model was further calibrated based on experimental recordings of the temperature profile, front velocity and front temperature. Both developed models provided good approximations approximations of the front velocity while front temperatures were generally overestimated by 10-20%. Application of the models in several case studies allowed for a further insight on the role of initial conditions, mould type and fibre contents, as well as the appearance of thermal instabilities.

8.2   Outlook

The efforts presented in this work are believed to offer a good potential for future implementation in the field of composite processing. The broader use of the UV-flow freezing methodology for the characterisation of dynamic flow behaviour in LCM processes would first of all require further validation at a microstructural level, which would be foreseen at different spatial levels. An assessment of the method accuracy, i.e. the similarity between dynamic and frozen flow front morphologies, similar to that presented in Section 4 for a wider range of flow conditions, i.e. values of the capillary number, would be desired to define the range of conditions on which UV-flow freezing can be applied. In a similar manner, an investigation on the flow front morphology at the intra-yarn scale would confirm the hypothesised applicability at scales beyond those presented in this work, e.g. to analyse dynamic contact angles. This would inherently require an in-situ comparison with dynamic flow behaviour at these scales and is envisioned to be achieved by synchrotron-μCT analysis at low flow velocities. A particular focus on the role of thermal effects and shrinkage during UV-photopolymerisation on the flow front morphology is desired during this characterisation. Extending the UV-flow freezing methodology to enable the analysis of flow behaviour of opaque, e.g. carbon, fibrous preforms is desired because of the wide industrial use of these fibre types. The use of frontal polymerisation was foreseen to enable this but was complicated by the observed extensive thermal expansion, resulting in severe distortions of the flow front morphologies. The development of frontal polymerisation-assisted UV-flow freezing thus requests the development of resin formulations that 1. show minimal thermal expansion, 2. can undergo rapid frontal polymerisation and 3. are representative commercial resin formulations. Once this has been achieved, the application of the UV-flow freezing is foreseen to bring a significant contribution to the understanding of dynamic flow behaviour on a microstructural level.

Future work on the use of frontal polymerisation for curing of FRPs would comprise a further optimisation and extension of the self-catalysed frontal polymerisation processing method. Investigations on improved channel geometries, fillers and optimised spacer materials, are desired to both provide a further understanding of the ongoing phenomena as well as to allow for enhanced process design. Extension of the methodology to make it compatible for implementation in other conventional FRP manufacturing methods, e.g. VARI, and at larger part sizes would increase its potential applicability. A more fundamental understanding on the use of different fabric architectures is desired as it was suggested to be of influence in several instances in this work while it has remained largely out of consideration by the field to-date. This would ideally be achieved by a combined experimental and numerical effort. Further investigations on the resulting FRP properties and e.g. the presence of residual stresses, would confirm findings presented in this work and hence the potential of frontal polymerisation as a tool for FRP production. Fine-tuning of the resin formulation considering both the resulting properties and the frontal polymerisation behaviour is envisaged to optimise the processing method.

The model presented in this work has shown the potential of simulating RICFP. A continued

investigation on reaction-kinetic models is envisioned to further improve the model accuracy while an extended experimental validation procedure, i.e. with different initial conditions or mould materials, would increase the confidence in the numerical findings. Extension of the model for efficient simulation of frontal polymerisation in versatile and more complex geometries is desired and could be achieved by its integration into commercial finite element method packages. Finally, strategies for reducing the computational cost are required to allow for efficient predictive modelling and process design. Achievement of these experimental and numerical improvements would pave the way for the use frontal polymerisation-assisted processing in the FRP industry.

A Appendix

A.1 Self-catalysed frontal polymerisation processing

A.1.1 Assessment of precuring

The proposed self-catalysed frontal polymerisation method allows for the successful polymerisation of FRPs with elevated V_fs by preheating the fabric stack ahead of the secondary front that passes through the fabric stack. While preheating was found to be an effective measure to reduce the required activation energy to surpass the threshold for the autocatalytic RICFP mechanism, extensive precuring could induce negative effects on the front characteristics as it reduces the available polymerisation enthalpy that can be released upon frontal polymerisation. An assessment of the polymerisation enthalpy and the role of precuring was made by dynamic DSC, following the procedure described in Section 3.2.4. Extrapolation of the maximum heat flow rate moreover gave an estimate of the onset temperature of autocatalytic curing mechanism that equalled 95.7°C as shown in Figure A.1.
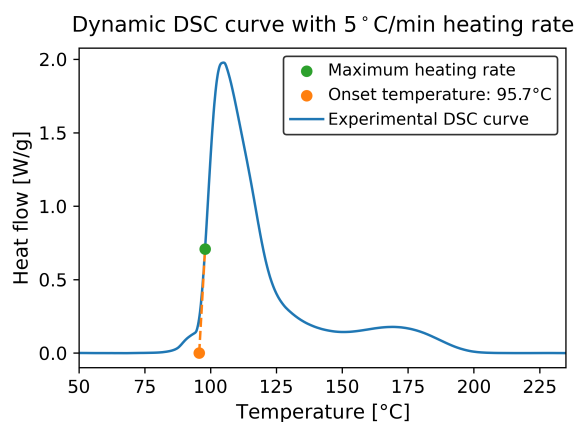
Figure A.1: Dynamic DSC curve of the ECC RICFP resin indicating the estimated onset temperature of the autocatalytic curing mechanism.

The influence of preheating was subsequently assessed by a combination of a quasi-isothermal procedure, described in Section 3.3.2, followed by a dynamic heat flow scan. Preheating temperatures up to ~60°C resulted in negligible heat flows during the isothermal procedure in Figure A.2a, while the polymerisation enthalpies (Figure A.2b) were in the same order as that of the pristine resin. On the contrary, preheating temperatures near the onset temperature, e.g. 90°C, reduced the available polymerisation enthalpy by over 35%.
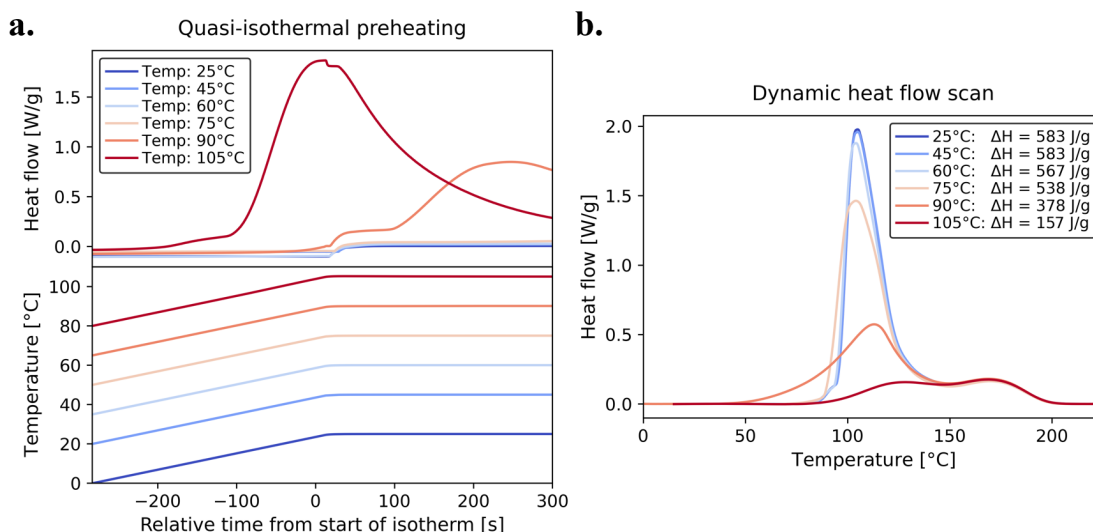
Figure A.2: Assessment of potential precuring by DSC simulating: a) preheating phase by a quasi-isothermal procedure, b) front propagation phase by a dynamic heat flow scan.

The results presented in Section 6.2 and Figure 6.5 however showed that, despite the suggested reduced enthalpy, high preheating temperatures did not inhibit frontal polymerisation to take place while front temperatures were only slightly lower in the presence of glass fibre reinforcements. This is partially explained by the reduced preheating times in self-catalysed frontal polymerisation compared to the preheating times in Figure A.2a, hence limiting the extent of enthalpy losses at high preheating temperatures, while the increased temperature and available thermal energy for activation of the RICFP mechanism are believed to largely compensate these losses. It can therefore be concluded that although precuring during the preheating period is likely taking place in the current configuration, it has a negligible influence on the overall process.

A.1.2 Temperature profiles in self-catalysed frontal polymerisation

The composition of the resin channel was found to be a part of the configuration with large influence on the resulting front characteristics. The difference between self-catalysed frontal polymerisation with an unfilled resin channel and with a resin channel filled with breather fabric has been explained in Section 6.3 and the described trends can be further understood from the temperature profiles in Figure A.3. Temperature profiles with a filled resin channel in

Figure A.3a showed an initial strong increase of the top thermocouples followed by a gradual temperature increase at locations further from the resin channel. Passing of the secondary front occurred after a relatively short delay time of ~50 seconds. As shown in Figure A.3a, the temperature peaks occurred almost simultaneously followed by a gradual decrease.
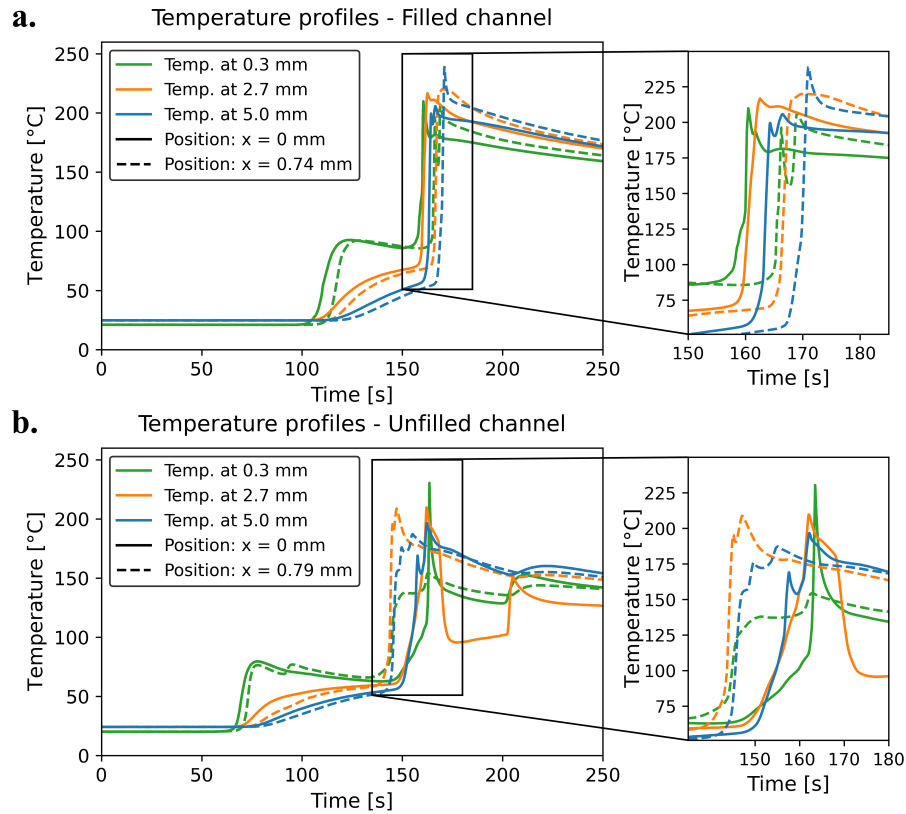
Figure A.3: Temperature profiles recorded in a) filled and b) unfilled self-catalysed frontal polymerisation configurations.

This is in contrast with the temperature profiles that were recorded for unfilled configurations shown in Figure A.3b. These configurations showed longer delay times that caused the temperature close to the resin channel to decrease after the expected initial spike, resulting in a more homogeneous preheating temperature. The temperature peaks upon passing of the front in Figure A.3b showed large variability, without an apparent sequence, between thermocouple position and appeared to be significantly less smooth compared to when a breather fabric was present. While this was understood as the absence of a continuously propagating secondary front which was hypothesised to be a result of the more homogeneous preheating temperatures and potentially increased precuring, the results in Figure A.3 emphasise the need for careful control of the heat flow in both the fabric stack and resin channel.

A.1.3   Temperature profiles for oven-cured FRP processing

A comparative assessment was made between carbon FRPs produced by the novel self-catalysed frontal polymerisation method and by an oven-curing procedure of 25 minutes at 150°C. Using identical resin compositions, several differences in the resulting mechanical properties were indicated in Section 6.4, which were partially attributed to the different curing conditions of the respective FRP types. The temperature profile recorded during the oven-curing cycle at the centre of an oven-cured RICFP FRP in Figure A.4a showed an initial gradual preheating phase of 21 minutes followed by the initiation of frontal polymerisation, resulting in a temperature peak that reached up to 219.9°C. The sample temperature subsequently rapidly decreased to ~110°C, while slowly decreasing after being removed from the oven.
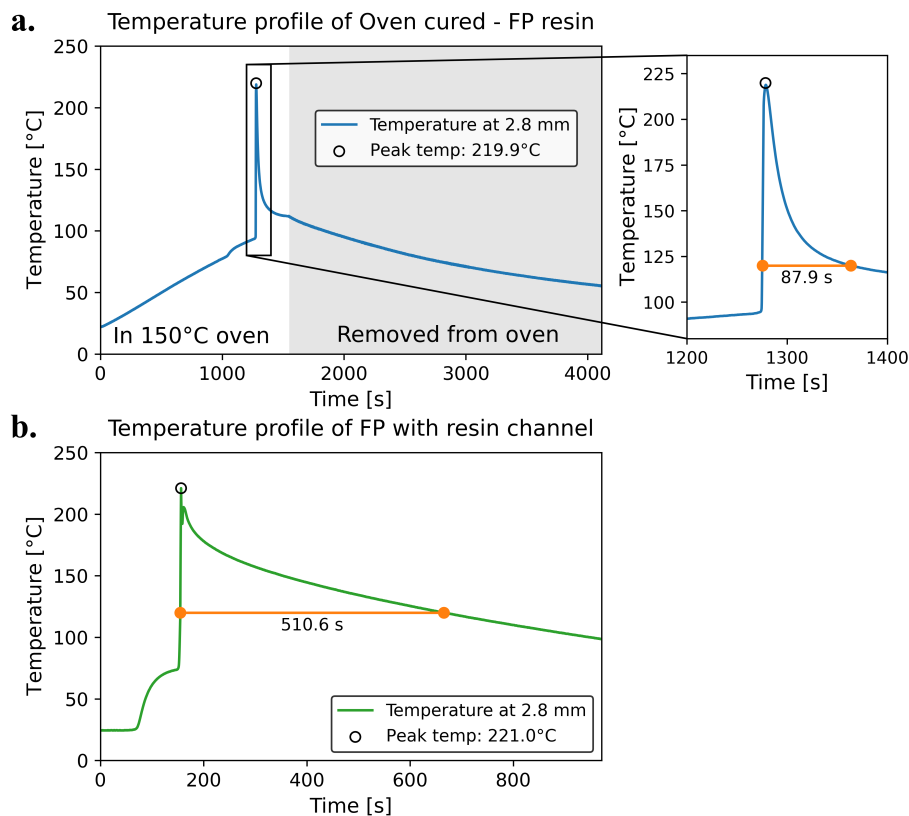
Figure A.4: Representative temperature profiles recorded during the production of a) oven-cured RICFP FRPs and b) self-catalysed frontal polymerisation FRPs. Thermocouples were integrated at the centre of the fabric stack.

This is in contrast with self-catalysed frontal polymerisation processing, showing a sharp temperature peak after the initial preheating phase, followed by a slow decrease. The cooling rate in self-catalysed frontal polymerisation processing was significantly lower than that during oven-cured RICFP FRP production, which is attributed to the difference in thermal properties between the highly-insulating Rohacell foam and conductive steel moulds, respectively. To

demonstrate the extent of these differences, Figure A.4 shows that self-catalysed frontal poly-merisation FRPs remained over 5.5 times longer above a temperature of 120°C. In Section 5 it was suggested the cooling phase can act as an intrinsic post-curing procedure, resulting in increased resulting monomer conversions. The shorter cooling phase, and hence the limited extent of intrinsic post-curing, is believed to have resulted in the inability of oven-cured RICFP FRPs to achieve their maximum attainable curing degrees, resulting in lower T_gs as observed in Figure 6.8b and larger scattering in resulting properties between samples as observed in Figures 6.8d & e. This hypothesis is supported by the possibility to increase the T_g in Figure 6.8c, confirming the benefit of FRP production using the novel self-catalysed frontal polymerisation method in combination with a highly insulating mould configuration.

A.2   RICFP modelling

A.2.1   Fitting of RICFP models

Gridsearch optimisation was used in Section 7.4 to determine the best parametric combinations for describing the respective systems considered in this work. The front characteristics of the assessed parametric combinations were used for a preliminary selection so as to ensure that the resulting model was capable to accurately approximate the steady-state front characteristics. The response surfaces for predictions of the front velocity are shown in Figure A.5 and the estimations on the maximum front temperature in Figure A.6. Accurate approximation of the front velocity appeared to be the bottleneck in this preliminary selection since the number of parametric compositions fulfilling the set condition, i.e. within ±20% for the reduced RICFP resin and ±10% for the FRP systems, was significantly lower than those fulfilling the temperature condition. The selected parametric conditions appeared as diagonal clusters in Figures A.5 & A.6 as a result of the interdependence of the fitted polymerisation enthalpy and thermal conductivity.
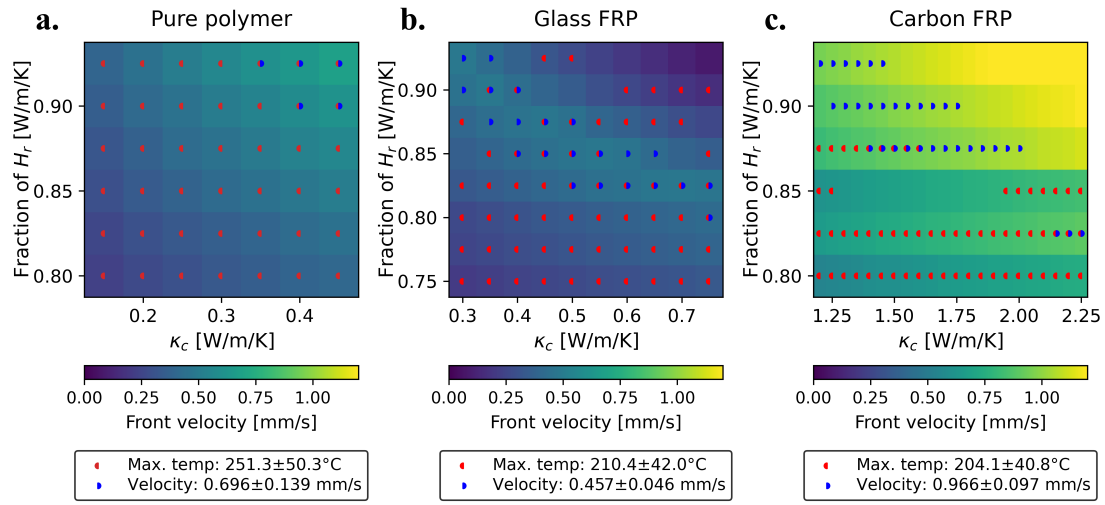
Figure A.5: Gridsearch response surfaces for front velocities predicted by for one-dimensional domains for a) pure polymer, b) glass FRP and c) carbon FRP systems.
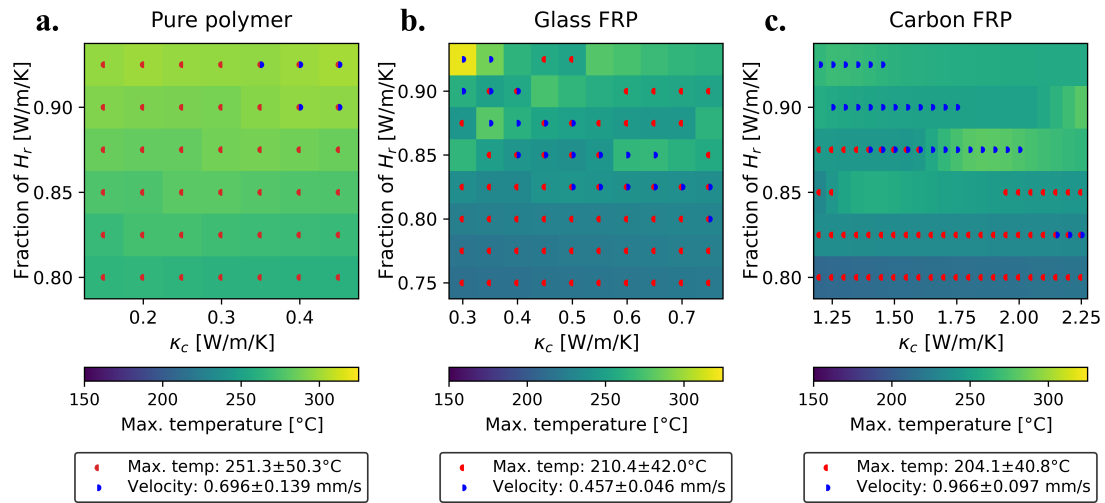
Figure A.6: Gridsearch response surfaces for maximum front temperatures predicted by for one-dimensional domains for a) pure polymer, b) glass FRP and c) carbon FRP systems.

A.2.2   Model parameters

The development of models describing RICFP processing of pure polymer and FRP systems has been extensively discussed in Section 7. A summary of the parameters used for modelling the different systems is presented in the Table A.1.

Table A.1: Summary of the model parameters used for simulating the different systems.

Type	Pure polymer	Glass FRP	Carbon FRP
α [-]	$0.05 \leq \alpha \leq 0.9$	$0.01 \leq \alpha \leq 0.9$	$0.01 \leq \alpha \leq 0.9$
$H_{r,eff}$ [J/g]	511.7	509.6	540.5
A_1 [s^{-1}]	$2.80 \cdot 10^8$	$2.33 \cdot 10^{12}$	$2.33 \cdot 10^{12}$
$E_{a,1}$ [kJ/mol]	75.56	102.84	102.84
n_1 [-]	1.90	2.66	2.66
m [-]	0.63	0.65	0.65
c_d [-]	23.48	23.48	23.48
α_c [-]	0.82	0.76	0.76
A_2 [s^{-1}]	$1.09 \cdot 10^{12}$	$2.68 \cdot 10^{13}$	$2.68 \cdot 10^{13}$
$E_{a,2}$ [kJ/mol]	119.61	124.74	124.74
n_2 [-]	1.15	1.88	1.88
κ [W/m/K]	0.40	0.55	1.55
Δx [m]	$5 \cdot 10^{-5}$	$5 \cdot 10^{-5}$	$5 \cdot 10^{-5}$
Δt [s]	$1 \cdot 10^{-3}$	$1 \cdot 10^{-3}$	$2 \cdot 10^{-4}$

Simulations were, unless specified otherwise, initialised under the following conditions:

- The initial temperature T_0 was set to 20°C.
- The simulation time was set to 60 seconds and the length of the simulation domain was fixed to 25 mm.
- The thermal trigger was applied during the whole simulation time and its temperature was set to 250°C for the reduced RICFP resin and 210°C for the composite RICFP resin.
- Mould domains had a thickness of 15 mm and were assumed to be made of PMI foam. A heat transfer coefficient h of 15 W/m^2/K was assumed at the domain boundaries to represent air in a steady condition.
- The fibre content V_f of FRP systems was fixed to 40 %.

A.2.3   Temperature profiles

Variation of the initial temperature of the developed models describing RICFP was related to the occurrence of thermal instabilities in Section 7.5. In addition to the data presented in Section 7.5, the spatial temperature distributions captured at a 20 seconds of simulation time for pure polymer and glass FRP systems and 10 seconds for carbon FRP systems is shown in

Figure A.7. These distributions support the observations in Section 7.5 while also confirming that the thermal instabilities are only present at the moment the front arrives since no residual oscillations over the sample length behind the front could be observed.
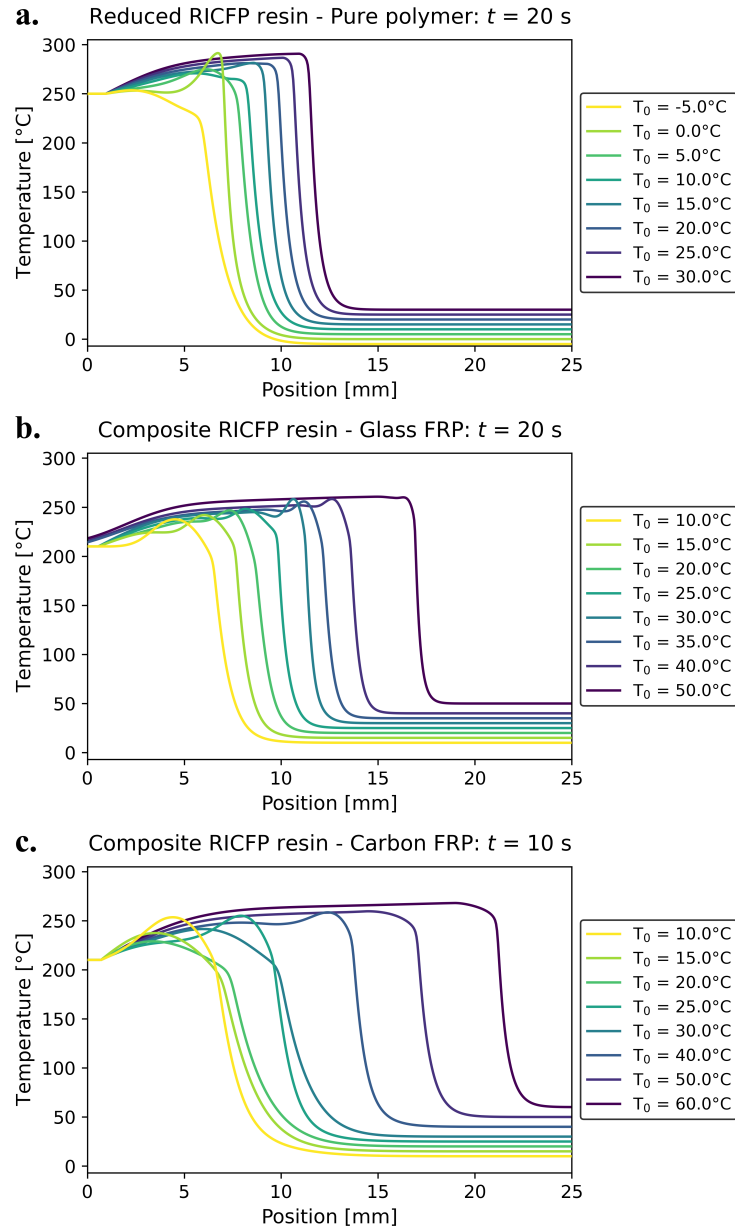
Figure A.7: Simulated spatial temperature distributions at a the centreline of the mould at a fixed time of the a) reduced RICFP resin system and composite RICFP resin system with 40% V_f b) glass and c) carbon reinforcements.

Bibliography

[1] JEC Observer: Current trends in the global composites industry 2021-2026 (2021).

[2] Sauer, M. & Schüppel, D. Market report 2021: The Global Market for Carbon Fibers and Carbon Composites (2022).

[3] Giurgiutiu, V. Introduction. In *Structural Health Monitoring of Aerospace Composites*, 1–23 (Academic Press, 2016). URL https://www.sciencedirect.com/science/article/pii/B9780124096059000015https://linkinghub.elsevier.com/retrieve/pii/B9780124096059000015.

[4] Friedrich, K. & Almajid, A. A. Manufacturing aspects of advanced polymer composites for automotive applications. *Applied Composite Materials* **20**, 107–128 (2013).

[5] Brøndsted, P., Lilholt, H. & Lystrup, A. Composite materials for wind power turbine blades. *Annual Review of Materials Research* **35**, 505–538 (2005).

[6] Mehdikhani, M., Gorbatikh, L., Verpoest, I. & Lomov, S. V. Voids in fiber-reinforced polymer composites: A review on their formation, characteristics, and effects on mechanical performance. *Journal of Composite Materials* **53**, 1579–1669 (2019).

[7] Zingraff, L., Michaud, V., Bourban, P. E. & Månson, J. A. Resin transfer moulding of anionically polymerised polyamide 12. *Composites Part A: Applied Science and Manufacturing* **36**, 1675–1686 (2005).

[8] Schell, J. S., Deleglise, M., Binetruy, C., Krawczak, P. & Ermanni, P. Numerical prediction and experimental characterisation of meso-scale-voids in liquid composite moulding. *Composites Part A: Applied Science and Manufacturing* **38**, 2460–2470 (2007).

[9] Michaud, V. A Review of Non-saturated Resin Flow in Liquid Composite Moulding processes. *Transport in Porous Media* **115**, 581–601 (2016).

[10] Vilà, J. *et al.* An in situ investigation of microscopic infusion and void transport during vacuum-assisted infiltration by means of X-ray computed tomography. *Composites Science and Technology* **119**, 12–19 (2015).

[11] Teixidó, H., Staal, J., Caglar, B. & Michaud, V. Capillary Effects in Fiber Reinforced Polymer Composite Processing: A Review. *Frontiers in Materials* **9**, 1–24 (2022).

Bibliography

[12] Abliz, D. *et al.* Curing methods for advanced polymer composites - A review. *Polymers and Polymer Composites* **21**, 341–348 (2013). URL https://doi.org/10.1177/096739111302100602.

[13] Collinson, M. G. *et al.* Novel composite curing methods for sustainable manufacture: A review. *Composites Part C: Open Access* **9** (2022).

[14] Timmis, A. J. *et al.* Environmental impact assessment of aviation emission reduction through the implementation of composite materials. *International Journal of Life Cycle Assessment* **20**, 233–243 (2015).

[15] EDA Präsenz Schweiz – PRS. Energie - Fakten und Zahlen (2023). URL https://www.eda.admin.ch/aboutswitzerland/de/home/wirtschaft/energie/energie---fakten-und-zahlen.html.

[16] BMW Group. Six years of BMW i3: Electric vehicle pioneers drive over 200,000 km in their BMW i3. (2020). URL https://www.press.bmwgroup.com/global/article/detail/T0303913EN/six-years-of-bmw-i3:-electric-vehicle-pioneers-drive-over-200-000-km-in-their-bmw-i3?language=en.

[17] Pojman, J. A. Cure-on-Demand Composites by Frontal Polymerization. *Encyclopedia of Materials: Plastics and Polymers* 85–100 (2022).

[18] Suslick, B. A. *et al.* Frontal Polymerizations : From Chemical Perspectives to Macroscopic Properties and Applications. *Materials Chemistry* (2023).

[19] Pojman, J. A. *Frontal Polymerization*, vol. 4 (Elsevier B.V., 2012). URL http://dx.doi.org/10.1016/B978-0-444-53349-4.00124-2.

[20] Robertson, I. D. *et al.* Rapid energy-efficient manufacturing of polymers and composites via frontal polymerization. *Nature* **557**, 223–234 (2018).

[21] Centellas, P. *et al.* Rapid multiple-front polymerization of fiber-reinforced polymer composites. *Composites Part A: Applied Science and Manufacturing* **158**, 106931 (2022). URL https://doi.org/10.1016/j.compositesa.2022.106931.

[22] Dung Tran, A., Koch, T., Knaack, P. & Liska, R. Radical induced cationic frontal polymerization for preparation of epoxy composites. *Composites Part A: Applied Science and Manufacturing* **132**, 105855 (2020). URL https://linkinghub.elsevier.com/retrieve/pii/S1359835X20300932.

[23] Ermanni, P., Di Fratta, C. & Trochu, F. Molding: Liquid Composite Molding (LCM). In *Wiley Encyclopedia of Composites* (Wiley-VCH, 2012).

[24] Henne, M. Optimizing RTM process with pressure sensors (2013). URL https://www.plastix-world.com/optimizing-rtm-process-with-pressure-sensors/.

144

[25] Michaud, V. Permeability properties of composite reinforcements. In Boisse, P. (ed.) *Composite reinforcements for optimum performance (Second Edition)*, 443–472 (Permeability properties of composite reinforcements, 2021).

[26] Gueroult, S. *et al.* Analytical modeling and in situ measurement of void formation in liquid composite molding processes. *Advanced Composite Materials* **23**, 31–42 (2014). URL http://dx.doi.org/10.1080/09243046.2013.862383.

[27] Ruiz, E., Achim, V., Soukane, S., Trochu, F. & Bréard, J. Optimization of injection flow rate to minimize micro/macro-voids formation in resin transfer molded composites. *Composites Science and Technology* **66**, 475–486 (2006).

[28] Patel, N. & Lee, L. J. Modeling of Void Formation and Removal in Liquid Composite Molding. Part I: Wettability Analysis. *Polymer Composites* **17**, 96–103 (1996).

[29] Nordlund, M. & Michaud, V. Dynamic saturation curve measurement for resin flow in glass fibre reinforcement. *Composites Part A: Applied Science and Manufacturing* **43**, 333–343 (2012).

[30] Bonnard, B., Causse, P. & Trochu, F. Experimental characterization of the pore size distribution in fibrous reinforcements of composite materials. *Journal of Composite Materials* **51**, 3807–3818 (2017).

[31] Binetruy, C., Hilaire, B. & Pabiot, J. Tow Impregnation Model and Void Formation Mechanisms during RTM. *Journal of Composite Materials* **32**, 223–245 (1998). URL https://doi.org/10.1177/002199839803200302.

[32] Lundström, T. S., Gebart, B. R. & Lundemo, C. Y. Void Formation in RTM. *Journal of Reinforced Plastics and Composites* **12**, 1339–1349 (1993).

[33] Schell, J. S., Renggli, M., van Lenthe, G. H., Müller, R. & Ermanni, P. Micro-computed tomography determination of glass fibre reinforced polymer meso-structure. *Composites Science and Technology* **66**, 2016–2022 (2006).

[34] Leclerc, J. S. & Ruiz, E. Porosity reduction using optimized flow velocity in Resin Transfer Molding. *Composites Part A: Applied Science and Manufacturing* **39**, 1859–1868 (2008). URL http://dx.doi.org/10.1016/j.compositesa.2008.09.008.

[35] Park, C. H. & Lee, W. Modeling void formation and unsaturated flow in liquid composite molding processes: A survey and review. *Journal of Reinforced Plastics and Composites* **30**, 957–977 (2011).

[36] Kang, K. & Koelling, K. Void transport in resin transfer molding. *Polymer Composites* **25**, 417–432 (2004).

[37] Matsuzaki, R., Naito, M., Seto, D., Todoroki, A. & Mizutani, Y. Analytical prediction of void distribution and a minimumvoid angle in anisotropic fabrics for radial injection resin transfer molding. *Express Polymer Letters* **10**, 860–872 (2016).

Bibliography

[38] Lundström, T. S. & Gebart, B. R. Influence from process parameters on void formation in resin transfer molding. *Polymer Composites* **15**, 25–33 (1994).

[39] Eom, Y., Boogh, L., Michaud, V. & Manson, J. A. A structure and property based process window for void free thermoset composites. *Polymer Composites* **22**, 22–31 (2001).

[40] Afendi, M., Banks, W. M. & Kirkwood, D. Bubble free resin for infusion process. *Composites Part A: Applied Science and Manufacturing* **36**, 739–746 (2005).

[41] Kang, M. K., Lee, W. I. & Hahn, H. T. Formation of microvoids during resin-transfer molding process. *Composites Science and Technology* **60**, 2427–2434 (2000).

[42] LeBel, F., Fanaei, A. E., Ruiz, E. & Trochu, F. Prediction of optimal flow front velocity to minimize void formation in dual scale fibrous reinforcements. *International Journal of Material Forming* **7**, 93–116 (2014).

[43] Rohatgi, V., Patel, N. & James Lee, L. Experimental investigation of flow-induced microvoids during impregnation of unidirectional stitched fiberglass mat. *Polymer Composites* **17**, 161–170 (1996).

[44] Bréard, J., Henzel, Y., Trochu, F. F. & Gauvin, R. Analysis of dynamic flows through porous media. Part I: Comparison between saturated and unsaturated flows in fibrous reinforcements. *Polymer Composites* **24**, 391–408 (2003).

[45] Devalve, C. & Pitchumani, R. Simulation of void formation in liquid composite molding processes. *Composites Part A: Applied Science and Manufacturing* **51**, 22–32 (2013). URL http://dx.doi.org/10.1016/j.compositesa.2013.03.016.

[46] Teixidó Pedarròs, H. *Visualization and modelling of dynamic flow in fibrous preforms for liquid composite molding*. Ph.D. thesis, Ecole Polytechnique Fédérale de Lausanne (2023).

[47] Caglar, B., Tekin, C., Karasu, F. & Michaud, V. Assessment of Capillary Phenomena in Liquid Composite Molding. *Composites Part A: Applied Science and Manufacturing* **120**, 73–83 (2019). URL https://linkinghub.elsevier.com/retrieve/pii/S1359835X19300594.

[48] LeBel, F., Ruiz, E. & Trochu, F. Void Content Analysis and Processing Issues to Minimize Defects in Liquid Composite Molding. *Polymer Composites* **40**, 109–120 (2017).

[49] Lystrup, C. *et al.* Optical measurement of voids in situ during infusion of carbon reinforcements. *Journal of Composite Materials* (2020).

[50] Ravey, C., Ruiz, E. & Trochu, F. Determination of the optimal impregnation velocity in Resin Transfer Molding by capillary rise experiments and infrared thermography. *Composites Science and Technology* **99**, 96–102 (2014). URL http://dx.doi.org/10.1016/j.compscitech.2014.05.019.

[51] LeBel, F., Ruiz, E. & Trochu, F. Experimental study of saturation by visible light transmission in dual-scale fibrous reinforcements during composite manufacturing. *Journal of Reinforced Plastics and Composites* **36**, 1693–1711 (2017).

[52] Kistler, S. Hydrodynamics of wetting. In Berg, J. (ed.) *Wettability*, 311–429 (Marcel Dekker Inc., New York, 1993), 1 edn.

[53] Qiu, S., Fuentes, C. A., Zhang, D., Vuure, A. W. v. & Seveno, D. Wettability of a Single Carbon Fiber. *Langmuir* **32**, 9697–9705 (2016).

[54] Wang, J. *et al.* Wettability of carbon fibres at micro- and mesoscales. *Carbon* **120**, 438–446 (2017). URL http://dx.doi.org/10.1016/j.carbon.2017.05.055.

[55] Facciotto, S., Simacek, P., Advani, S. G. & Middendorf, P. Modeling of anisotropic dual scale flow in RTM using the finite elements method. *Composites Part B: Engineering* **214**, 108735 (2021). URL https://doi.org/10.1016/j.compositesb.2021.108735.

[56] van Genuchten, M. A Closed-form Equation for Predicting the Hydraulic Conductivity of Unsaturated Soils. *Soil Science Society American Journal1* **44**, 892–898 (1980).

[57] Brooks, R. & Corey, A. *Hydraulic Properties of Porous Media* (Colorado State University, 1964).

[58] Patel, N. & Lee, L. J. Effects of fiber mat architecture on void formation and removal in liquid composite molding. *Polymer Composites* **16**, 386–399 (1995).

[59] Labat, L., Bréard, J., Pillut-Lesavre, S. & Bouquet, G. Void fraction prevision in LCM parts. *EPJ Applied Physics* **16**, 157–164 (2001).

[60] Little, J. E., Yuan, X. & Jones, M. I. Characterisation of voids in fibre reinforced composite materials. *NDT and E International* **46**, 122–127 (2012). URL http://dx.doi.org/10.1016/j.ndteint.2011.11.011.

[61] Kedari, V. R., Farah, B. I. & Hsiao, K. T. Effects of vacuum pressure, inlet pressure, and mold temperature on the void content, volume fraction of polyester/e-glass fiber composites manufactured with VARTM process. *Journal of Composite Materials* **45**, 2727–2742 (2011).

[62] Madra, A., Hajj, N. E. & Benzeggagh, M. X-ray microtomography applications for quantitative and qualitative analysis of porosity in woven glass fiber reinforced thermoplastic. *Composites Science and Technology* **95**, 50–58 (2014). URL http://dx.doi.org/10.1016/j.compscitech.2014.02.009.

[63] Sisodia, S. M. *et al.* High-resolution computed tomography in resin infused woven carbon fibre composites with voids. *Composites Science and Technology* **131**, 12–21 (2016). URL http://dx.doi.org/10.1016/j.compscitech.2016.05.010.

Bibliography

[64] Lawrence, J. M., Neacsu, V. & Advani, S. G. Modeling the impact of capillary pressure and air entrapment on fiber tow saturation during resin infusion in LCM. *Composites Part A: Applied Science and Manufacturing* **40**, 1053–1064 (2009). URL http://dx.doi.org/10.1016/j.compositesa.2009.04.013.

[65] Caglar, B., Salvatori, D., Sozer, E. M. & Michaud, V. In-plane permeability distribution mapping of isotropic mats using flow front detection. *Composites Part A: Applied Science and Manufacturing* **113**, 275–286 (2018). URL https://doi.org/10.1016/j.compositesa.2018.07.036.

[66] Salvatori, D., Caglar, B., Teixidó, H. & Michaud, V. Permeability and capillary effects in a channel-wise non-crimp fabric. *Composites: Part A* **108**, 41–52 (2018). URL https://doi.org/10.1016/j.compositesa.2018.02.015.

[67] Chen, B. & Chou, T. W. Compaction of woven-fabric preforms: Nesting and multi-layer deformation. *Composites Science and Technology* **60**, 2223–2231 (2000).

[68] Yousaf, Z., Potluri, P. & Withers, P. J. Influence of Tow Architecture on Compaction and Nesting in Textile Preforms. *Applied Composite Materials* **24**, 337–350 (2017).

[69] Yoshihara, K. *et al.* Effect of wettability on viscous fluid impregnation in single-layer woven-fibre bundles driven by pressure difference. *Composites Part A: Applied Science and Manufacturing* **138** (2020).

[70] Lebel, F., Fanaei, A. E., Ruiz, E. & Trochu, F. Experimental Characterization by Fluorescence of Capillary Flows in the Fiber Tows of Engineering Fabrics. *Open Journal of Inorganic Non-metallic Materials* **2**, 25–45 (2012).

[71] Zhao, C. *et al.* Three-Dimensional Numerical Simulation of Meso-Scale-Void Formation during the Mold-Filling Process of LCM. *Applied Composite Materials* **26**, 1121–1137 (2019).

[72] Matuzaki, R., Seto, D., Naito, M., Todoroki, A. & Mizutani, Y. Analytical prediction of void formation in geometrically anisotropic woven fabrics during resin transfer molding. *Composites Science and Technology* **107**, 154–161 (2015). URL http://dx.doi.org/10.1016/j.compscitech.2014.12.013.

[73] Neitzel, B. & Puch, F. Optical Detection of Void Formation Mechanisms during Impregnation of Composites by UV-Reactive Resin Systems. *Journal of Composites Science* **6**, 1–15 (2022).

[74] Konstantopoulos, S., Fauster, E. & Schledjewski, R. Monitoring the production of FRP composites: A review of in-line sensing methods. *Express Polymer Letters* **8**, 823–840 (2014).

[75] Labat, L., Grisel, M., Breard, J. & Bouquet, G. Original use of electrical conductivity for void detection due to injection conditions of composite materials. *Comptes Rendus de l'Academie de Sciences - Serie IIb: Mecanique* **329**, 529–534 (2001).

148

[76] Carlone, P. & Palazzo, G. S. Unsaturated and Saturated Flow Front Tracking in Liquid Composite Molding Processes using Dielectric Sensors. *Applied Composite Materials* **22**, 543–557 (2015).

[77] Carlone, P., Rubino, F., Paradiso, V. & Tucci, F. Multi-scale modeling and online monitoring of resin flow through dual-scale textiles in liquid composite molding processes. *International Journal of Advanced Manufacturing Technology* **96**, 2215–2230 (2018).

[78] Di Fratta, C., Klunker, F. & Ermanni, P. A methodology for flow-front estimation in LCM processes based on pressure sensors. *Composites Part A: Applied Science and Manufacturing* **47**, 1–11 (2013). URL http://dx.doi.org/10.1016/j.compositesa.2012.11.008.

[79] Chiu, T. H. *et al.* Estimation of local permeability/porosity ratio in resin transfer molding. *Journal of the Taiwan Institute of Chemical Engineers* **91**, 32–37 (2018).

[80] Pouchias, A., Cunningham, P. R., Stein, J. & Kazilas, M. Development of a flexible dielectric sensor for flow monitoring of the liquid resin infusion process. *Sensors* **19** (2019).

[81] Caglar, B. *et al.* Functionalized Fiber Reinforced Composites via Thermally Drawn Multifunctional Fiber Sensors. *Advanced Materials Technologies* **6**, 1–8 (2021).

[82] Villière, M. *et al.* Dynamic saturation curve measurement in liquid composite molding by heat transfer analysis. *Composites Part A: Applied Science and Manufacturing* **69**, 255–265 (2015).

[83] He, Y., Li, Y., Hao, X., zhou, J. & Liu, S. Micro-flow sensor for continuous resin fluidity monitoring between fibers. *Sensors and Actuators, B: Chemical* **282**, 177–186 (2019).

[84] Schmachtenberg, E., Schulte Zur Heide, J. & Töpker, J. Application of ultrasonics for the process control of Resin Transfer Moulding (RTM). *Polymer Testing* **24**, 330–338 (2005).

[85] Stöven, T., Weyrauch, F., Mitschang, P. & Neitzel, M. Continuous monitoring of three-dimensional resin flow through a fibre preform. *Composites Part A: Applied Science and Manufacturing* **34**, 475–480 (2003).

[86] Thomas, S., Bongiovanni, C. & Nutt, S. R. In situ estimation of through-thickness resin flow using ultrasound. *Composites Science and Technology* **68**, 3093–3098 (2008). URL http://dx.doi.org/10.1016/j.compscitech.2008.07.012.

[87] Konstantopoulos, S., Grössing, H., Hergan, P., Weninger, M. & Schledjewski, R. Determination of the Unsaturated Through-Thickness Permeability of Fibrous Preforms Based on Flow Front Detection by Ultrasound. *Polymer Composites* **39**, 360–357 (2018).

[88] Endruweit, A., Glover, P., Head, K. & Long, A. C. Mapping of the fluid distribution in impregnated reinforcement textiles using Magnetic Resonance Imaging: Application

and discussion. *Composites Part A: Applied Science and Manufacturing* **42**, 1369–1379 (2011). URL http://dx.doi.org/10.1016/j.compositesa.2011.05.020http://dx.doi.org/10.1016/j.compositesa.2010.11.012.

[89] Neacsu, V., Leisen, J., Beckham, H. W. & Advani, S. G. Use of magnetic resonance imaging to visualize impregnation across aligned cylinders due to capillary forces. *Experiments in Fluids* **42**, 425–440 (2007).

[90] Mantle, M. D., Bijeljic, B., Sederman, A. J. & Gladden, L. F. MRI velocimetry and lattice-Boltzmann simulations of viscous flow of a Newtonian liquid through a dual porosity fibre array. *Magnetic Resonance Imaging* **19**, 527–529 (2001).

[91] Bijeljic, B., Mantle, D. M., Sederman, A. J., Gladden, L. F. & Papathanasiou, T. D. Slow flow across macroscopically semi-circular fibre lattices and a free-flow region of variable width - Visualisation by magnetic resonance imaging. *Chemical Engineering Science* **59**, 2089–2103 (2004).

[92] Bencsik, M., Adriaensen, H., Brewer, S. A. & McHale, G. Quantitative NMR monitoring of liquid ingress into repellent heterogeneous layered fabrics. *Journal of Magnetic Resonance* **193**, 32–36 (2008).

[93] Leisen, J. & Beckham, H. W. Void structure in textiles by nuclear magnetic resonance, Part I. Imaging of imbibed fluids and image analysis by calculation of fluid density autocorrelation functions. *Journal of the Textile Institute* **99**, 243–251 (2008).

[94] Bréard, J., Saouab, A. & Bouquet, G. Dependence of the Reinforcement Anisotropy on a Three Dimensional Resin Flow Observed by X-Ray Radioscopy. *Journal of Reinforced Plastics and Composites* **18**, 814–826 (1999). URL https://doi.org/10.1177/073168449901800903.

[95] Teixidó, H., Caglar, B., Revol, V. & Michaud, V. In-operando dynamic visualization of flow through porous preforms based on X-ray phase contrast imaging. *Composites Part A: Applied Science and Manufacturing* **149** (2021).

[96] Gresil, M. *et al.* EVITA Project: Comparison Between Traditional Non-Destructive Techniques and Phase Contrast X-Ray Imaging Applied to Aerospace Carbon Fibre Reinforced Polymer. *Applied Composite Materials* **24**, 513–524 (2017).

[97] Teixidó, H., Broggi, G., Caglar, B. & Michaud, V. Measurement and modelling of dynamic fluid saturation in carbon reinforcements. *Composites: Part A* **169**, 107520 (2023).

[98] Withers, P. J. *et al.* X-ray computed tomography. *Nature Reviews Methods Primers* **1** (2021). URL http://dx.doi.org/10.1038/s43586-021-00015-4.

[99] Castro, J., Sket, F. & Helfen, L. In situ local imaging and analysis of impregnation during liquid moulding of composite materials using synchrotron radiation computed laminography. *Composites Science and Technology* **215** (2021).

[100] Hemmer, J. *et al.* Unloading during the infusion process: Direct measurement of the dual-scale fibrous microstructure evolution with X-ray computed tomography. *Composites Part A: Applied Science and Manufacturing* **115**, 147–156 (2018). URL https://doi.org/10.1016/j.compositesa.2018.09.013.

[101] Ali, M. A., Umer, R., Khan, K. A. & Cantwell, W. J. In-plane virtual permeability characterization of 3D woven fabrics using a hybrid experimental and numerical approach. *Composites Science and Technology* **173**, 99–109 (2019). URL https://doi.org/10.1016/j.compscitech.2019.01.030.

[102] Larson, N. M. & Zok, F. W. Insights from in-situ X-ray computed tomography during axial impregnation of unidirectional fiber beds. *Composites Part A: Applied Science and Manufacturing* **107**, 124–134 (2018). URL https://doi.org/10.1016/j.compositesa.2017.12.024.

[103] Larson, N. M., Cuellar, C. & Zok, F. W. X-ray computed tomography of microstructure evolution during matrix impregnation and curing in unidirectional fiber beds. *Composites Part A: Applied Science and Manufacturing* **117**, 243–259 (2019). URL https://doi.org/10.1016/j.compositesa.2018.11.021.

[104] Castro, J., Sket, F. & González, C. S-XCT experimental determination of local contact angle and meniscus shape in liquid moulding of composites. *Composites Science and Technology* **199** (2020).

[105] Helfen, L. *et al.* On the implementation of computed laminography using synchrotron radiation. *Review of Scientific Instruments* **82** (2011).

[106] Bull, D. J., Spearing, S. M., Sinclair, I. & Helfen, L. Three-dimensional assessment of low velocity impact damage in particle toughened composite laminates using micro-focus X-ray computed tomography and synchrotron radiation laminography. *Composites Part A: Applied Science and Manufacturing* **52**, 62–69 (2013). URL http://dx.doi.org/10.1016/j.compositesa.2013.05.003.

[107] Fisher, S. L. *et al.* Laminography in the lab: Imaging planar objects using a conventional x-ray CT scanner. *Measurement Science and Technology* **30** (2019).

[108] Bomze, D., Knaack, P., Koch, T., Jin, H. & Liska, R. Radical induced cationic frontal polymerization as a versatile tool for epoxy curing and composite production. *Journal of Polymer Science, Part A: Polymer Chemistry* **54**, 3751–3759 (2016).

[109] Fortenberry, D. I. & Pojman, J. A. Solvent-Free Synthesis of Polyacrylamide by Frontal Polymerization. *Journal of Polymer Science, Part A: Polymer Chemistry* **38**, 1129–1135 (2000).

[110] Chechilo, N., Khvilivitskii, E. & Enikolopyan, N. On the Phenomenon of Polymerization Reaction Spreading. *Doklady Akademii Nauk SSSR* **204**, 1180–1181 (1972).

Bibliography

[111] Chechilo, N. & Enikolopyan, N. Effect of the concentration and nature of the initiatiors on the propagation process in polymerization. *Doklady Physical Chemistry* **221**, 391–394 (1975).

[112] Ritter, L. R., Volpert, V. A. & Olmstead, W. E. Initiation of Free-Radical Polymerization Waves. *SIAM Journal on Applied Mathematics* **63**, 1831–1848 (2003).

[113] Novozhilov, B. V. Propagation Rate of the Front of an Exothermic Reaction in Condensed Phase. *Doklady Akademii Nauk SSSR* **141**, 151–153 (1961).

[114] Liu, H., Wei, H. & Moore, J. S. Frontal Ring-Opening Metathesis Copolymerization: Deviation of Front Velocity from Mixing Rules. *ACS Macro Letters* **8**, 846–851 (2019).

[115] Mariani, A., Fiori, S., Chekanov, Y. & Pojman, J. A. Frontal ring-opening metathesis polymerization of dicyclopentadiene [5]. *Macromolecules* **34**, 6539–6541 (2001).

[116] Lloyd, E. M. *et al.* Efficient Manufacture, Deconstruction, and Upcycling of High-Performance Thermosets and Composites. *ACS Applied Engineering Materials* (2022). URL https://chemrxiv.org/engage/chemrxiv/article-details/6304e0710187d973829e5394.

[117] Schwab, P., France, M. B., Ziller, J. W. & Grubbs, R. H. A Series of Well-Defined Metathesis Catalysts- Synthesis of [RuCI2(=CHR')(PR3)2] and Its Reactions. *Angewandte Chemie - International Edition* **34**, 2039–2041 (1995).

[118] Schwab, P., Grubbs, R. H. & Ziller, J. W. Synthesis and applications of RuCl2(=CHR')(PR3)2: The influence of the alkylidene moiety on metathesis activity. *Journal of the American Chemical Society* **118**, 100–108 (1996).

[119] Robertson, I. D. *et al.* Alkyl Phosphite Inhibitors for Frontal Ring-Opening Metathesis Polymerization Greatly Increase Pot Life. *ACS Macro Letters* 609–612 (2017).

[120] Dean, L. M., Ravindra, A., Guo, A. X., Yourdkhani, M. & Sottos, N. R. Photothermal Initiation of Frontal Polymerization Using Carbon Nanoparticles. *ACS Applied Polymer Materials* (2020).

[121] Stawiasz, K. J., Paul, J. E., Schwarz, K. J., Sottos, N. R. & Moore, J. S. Photoexcitation of Grubbs' Second-Generation Catalyst Initiates Frontal Ring-Opening Metathesis Polymerization. *ACS Macro Letters* **9**, 1563–1568 (2020).

[122] Stawiasz, K. J., Wendell, C. I., Suslick, B. A. & Moore, S. Photoredox-Initiated Frontal Ring-Opening Metathesis Polymerization. *ACS Macro Letters* **11**, 780–784 (2022).

[123] Ivanoff, D. G., Sung, J., Butikofer, S. M., Moore, J. S. & Sottos, N. R. Cross-Linking Agents for Enhanced Performance of Thermosets Prepared via Frontal Ring-Opening Metathesis Polymerization. *Macromolecules* (2020).

[124] Davydovich, O. *et al.* Frontal Polymerization of Dihydrofuran Comonomer Facilitates Thermoset Deconstruction. *Chemistry of Materials* (2022).

[125] Dean, L. M., Wu, Q., Alshangiti, O., Moore, J. S. & Sottos, N. R. Rapid Synthesis of Elastomers and Thermosets with Tunable Thermomechanical Properties. *ACS Macro Letters* **9**, 819–824 (2020).

[126] An, Y., Jang, J. H., Youk, J. H. & Yu, W. R. Frontally polymerizable shape memory polymer for 3D printing of free-standing structures. *Smart Materials and Structures* **31** (2022).

[127] Aw, J. E. *et al.* Self-Regulative Direct Ink Writing of Frontally Polymerizing Thermoset Polymers. *Advanced Materials Technologies* **2200230** (2022).

[128] Wang, B. *et al.* 3D printing of in-situ curing thermally insulated thermosets. *Manufacturing Letters* **21**, 1–6 (2019). URL https://doi.org/10.1016/j.mfglet.2019.06.001.

[129] Garg, M. *et al.* Rapid synchronized fabrication of vascularized thermosets and composites. *Nature Communications* **12**, 1–9 (2021). URL http://dx.doi.org/10.1038/s41467-021-23054-7.

[130] Centellas, P. *et al.* Energy-efficient manufacturing of multifunctional vascularized composites. *Journal of Composite Materials* **0**, 1–12 (2022). URL https://doi.org/10.1177/00219983221142353.

[131] Gao, Y. *et al.* Controllable Frontal Polymerization and Spontaneous Patterning Enabled by Phase-Changing Particles. *Small* **17**, 1–9 (2021).

[132] Golaz, B., Michaud, V., Leterrier, Y. & Mnson, J. A. UV intensity, temperature and dark-curing effects in cationic photo-polymerization of a cycloaliphatic epoxy resin. *Polymer* **53**, 2038–2048 (2012). URL http://dx.doi.org/10.1016/j.polymer.2012.03.025.

[133] Sangermano, M. Advances in cationic photopolymerization. *Pure and Applied Chemistry* **84**, 2089–2101 (2012).

[134] Sangermano, M., Razza, N. & Crivello, J. V. Cationic UV-curing: Technology and applications. *Macromolecular Materials and Engineering* **299**, 775–793 (2014).

[135] Sangermano, M. *et al.* Synthesis of an epoxy functionalized spiroorthocarbonate used as low shrinkage additive in cationic UV curing of an epoxy resin. *European Polymer Journal* **44**, 1046–1052 (2008).

[136] Khoun, L. & Hubert, P. Cure Shrinkage Characterization of an Epoxy Resin System by Two in Situ Measurement Methods. *Polymer Compositesm* **31**, 1603–1610 (2010).

[137] Baikerikar, K. K. & Scranton, A. B. Photopolymerizable liquid encapsulants for microelectronic devices: Thermal and mechanical properties of systems with reduced in-mold cure times. *Journal of Applied Polymer Science* **81**, 3449–3461 (2001).

Bibliography

[138] Baikerikar, K. K. & Scranton, A. B. Photopolymerizable liquid encapsulants for micro-electronic devices. *Polymer* **42**, 431–441 (2001).

[139] Crivello, J. V., Falk, B. & Zonca, M. R. Photoinduced Cationic Ring-Opening Frontal Polymerizations of Oxetanes and Oxiranes. *Journal of Polymer Science, Part A: Polymer Chemistry* **42**, 1630–1646 (2004).

[140] Crivello, J. V. Investigation of the photoactivated frontal polymerization of oxetanes using optical pyrometry. *Polymer* **46**, 12109–12117 (2005).

[141] Bulut, U. & Crivello, J. V. Investigation of the reactivity of epoxide monomers in photoinitiated cationic polymerization. *Macromolecules* **38**, 3584–3595 (2005).

[142] Mariani, A. *et al.* UV-ignited frontal polymerization of an epoxy resin. *Journal of Polymer Science, Part A: Polymer Chemistry* **42**, 2066–2072 (2004).

[143] Crivello, J. V. & Liu, S. Free Radical Induced Acceleration of Cationic Photopolymerization. *Chemistry of Materials* **10**, 3724–3731 (1998).

[144] Sangermano, M., D'Anna, A., Marro, C., Klikovits, N. & Liska, R. UV-activated frontal polymerization of glass fibre reinforced epoxy composites. *Composites Part B* **143**, 168–171 (2018). URL https://doi.org/10.1016/j.compositesb.2018.02.014.

[145] Knaack, P, Klikovits, N., Tran, A. D., Bomze, D. & Liska, R. Radical induced cationic frontal polymerization in thin layers. *Journal of Polymer Science, Part A: Polymer Chemistry* **57**, 1155–1159 (2019).

[146] Bomze, D., Knaack, P. & Liska, R. Successful radical induced cationic frontal polymerization of epoxy-based monomers by C-C labile compounds. *Polymer Chemistry* **6**, 8161–8167 (2015).

[147] Malik, M. S., Schlögl, S., Wolfahrt, M. & Sangermano, M. Review on UV-Induced Cationic Frontal Polymerization of Epoxy Monomers. *Polymers* **12**, 2146 (2020).

[148] Crivello, J. V. The Discovery and Development of Onium Salt Cationic Photoinitiators. *Journal of Polymer Science Part A: Polymer Chemistry* **37**, 4241–4254 (1999).

[149] Fouassier, J. P. & Lalevée, J. *Photoinitiators for Polymer Synthesis: Scope, Reactivity and Efficiency* (Wiley-VCH Verlag GmbH, 2012).

[150] Crivello, J. V. Cationic polymerization — Iodonium and sulfonium salt photoinitiators. In *Initiators — Poly-Reactions — Optical Activity*, 1–48 (Springer Berlin Heidelberg, Berlin, Heidelberg, 1984).

[151] Crivello, J. V. & Lam, J. H. Diaryliodonium Salts. A New Class of Photoinitiators for Cationic Polymerization. *Macromolecules* **10**, 1307–1315 (1977).

[152] Crivello, J. V. & Lee, J. L. Alkoxy-substituted diaryliodonium salt cationic photoinitiators. *Journal of Polymer Science Part A: Polymer Chemistry* **27**, 3951–3968 (1989).

[153] Klikovits, N., Knaack, P., Bomze, D., Krossing, I. & Liska, R. Novel photoacid generators for cationic photopolymerization. *Polymer Chemistry* **8**, 4414–4421 (2017).

[154] Taschner, R., Liska, R. & Knaack, P. Iodonium Borate Initiators for Cationic Photopolymerization and Their Application in Radical-Induced Cationic Frontal Polymerization. *ACS Applied Polymer Materials* (2022).

[155] Manivannan, G. & Fouassier, J. P. Primary processes in the photosensitized polymerization of cationic monomers. *Journal of Polymer Science Part A: Polymer Chemistry* **29**, 1113–1124 (1991).

[156] Klikovits, N., Liska, R., D'Anna, A. & Sangermano, M. Successful UV-Induced RICFP of Epoxy-Composites. *Macromolecular Chemistry and Physics* **218**, 5–8 (2017).

[157] Sangermano, M., Antonazzo, I., Sisca, L. & Carello, M. Photoinduced cationic frontal polymerization of epoxy–carbon fibre composites. *Polymer International* **68**, 1662–1665 (2019).

[158] Groce, B. R., Gary, D. P., Cantrell, J. K. & Pojman, J. A. Front velocity dependence on vinyl ether and initiator concentration in radical-induced cationic frontal polymerization of epoxies. *Journal of Polymer Science* 1–8 (2021).

[159] Gachet, B. *et al.* Highly reactive photothermal initiating system based on sulfonium salts for the photoinduced thermal frontal cationic polymerization of epoxides: A way to create carbon-fiber reinforced polymers. *RSC Advances* **10**, 41915–41920 (2020).

[160] Taschner, R., Knaack, P. & Liska, R. Bismuthonium- and pyrylium-based radical induced cationic frontal polymerization of epoxides. *Journal of Polymer Science* 1–14 (2021).

[161] Liska, R., Bomze, D., Kern, W. & Knaack, P. Verfahren zur Frontalpolymerisatin kationisch polymerisierbarer Monomere (2015). URL http://xlink.rsc.org/?DOI=C5PY01451D.

[162] Malik, M. S., Wolfahrt, M., Sangermano, M. & Schlögl, S. Effect of a Dicycloaliphatic Epoxide on the Thermo-mechanical Properties of Alkyl, Aryl Epoxide Monomers Cured via UV-induced Cationic Frontal Polymerization. *Macromolecular Materials and Engineering* **2100976**, 2100976 (2022).

[163] Scognamillo, S., Bounds, C., Luger, M., Mariani, A. & Pojman, J. A. Frontal cationic curing of epoxy resins. *Journal of Polymer Science, Part A: Polymer Chemistry* **48**, 2000–2005 (2010).

[164] Scognamillo, S. *et al.* Frontal cationic curing of epoxy resins in the presence of defoaming or expanding compounds. *Journal of Applied Polymer Science* **131**, 1–11 (2014).

Bibliography

[165] Zhou, J., Jia, S., Fu, W., Liu, Z. & Tan, Z. Fast curing of thick components of epoxy via modified UV-triggered frontal polymerization propagating horizontally. *Materials Letters* **176**, 228–231 (2016). URL http://dx.doi.org/10.1016/j.matlet.2016.04.103.

[166] Maugeri, D., Sangermano, M. & Leterrier, Y. Radical photoinduced cationic frontal polymerization in porous media. *Polymer International* **70**, 269–276 (2021).

[167] Liu, Z. *et al.* Excessive radical induced cationic frontal polymerization lead to a decline of material properties. *Authorea* 1–11 (2022).

[168] Švajdlenková, H. *et al.* Microstructural study of epoxy-based thermosets prepared by "classical" and cationic frontal polymerization. *RSC Advances* **10**, 41098–41109 (2020).

[169] Datta, P., Efimenko, K. & Genzer, J. The effect of confinement on thermal frontal polymerization. *Polymer Chemistry* **3**, 3243–3246 (2012).

[170] Tiani, R., Pojman, J. A. & Rongy, L. Critical Role of Layer Thickness in Frontal Polymerization. *Journal of Physical Chemistry B* (2022).

[171] Gao, Y. *et al.* Frontal Polymerization of Thin Layers on a Thermally Insulating Substrate. *ACS Applied Polymer Materials* **4**, 4919–4927 (2022).

[172] Goli, E., Gai, T. & Geubelle, P. H. Impact of Boundary Heat Losses on Frontal Polymerization. *Journal of Physical Chemistry B* **124**, 6404–6411 (2020).

[173] Naseri, I. & Yourdkhani, M. Rapid and Energy-Efficient Frontal Curing of Multifunctional Composites Using Integrated Nanostructured Heaters. *ACS Applied Materials and Interfaces* **14**, 50215–50224 (2022).

[174] Vyas, S., Goli, E., Zhang, X. & Geubelle, P. H. Manufacturing of unidirectional glass-fiber-reinforced composites via frontal polymerization: A numerical study. *Composites Science and Technology* **184**, 107832 (2019). URL https://doi.org/10.1016/j.compscitech.2019.107832.

[175] Goli, E. *et al.* Frontal polymerization accelerated by continuous conductive elements. *Journal of Applied Polymer Science* **47418**, 1–9 (2018).

[176] Goli, E. *et al.* Frontal polymerization of unidirectional carbon-fiber-reinforced composites. *Composites Part A: Applied Science and Manufacturing* **130**, 105689 (2020). URL https://doi.org/10.1016/j.compositesa.2019.105689.

[177] Gao, Y. *et al.* Rapid frontal polymerization achieved with thermally conductive metal strips. *Chaos* **31**, 21–24 (2021).

[178] Gao, Y. *et al.* Anisotropic frontal polymerization in a model resin-copper composite. *Chaos* **32** (2022).

[179] Robertson, I. D., Moore, J. S., Sottos, N. R. & White, S. R. Frontal Polymerization for Fiber-Reinforced Composites (2018).

[180] Robert, L. & Dusserrea, G. Assessment of thermoset cure-induced strains by fiber Bragg grating sensor. *Polymer Engineering and Science* 1585–1594 (2014).

[181] Noè, C. *et al.* Frontal-Photopolymerization of Fully Biobased Epoxy Composites. *Macromolecular Materials and Engineering* **2100864**, 1–11 (2022).

[182] Parikh, N. A., Vyas, S. K., Ivanoff, D. G., Geubelle, P. H. & Sottos, N. R. Rapid-cure of Fiber-Reinforced Composites by Frontal Polymerization. In *Composites Meet Sustainability – Proceedings of the 20th European Conference on Composite Materials* (2022).

[183] Malik, M. S., Grasser, V., Wolfahrt, M. & Schlögl, S. ADDRESSING THE CHALLENGES IN FRONTAL CURING OF HIGH- PERFORMANCE CARBON FIBER REINFORCED COMPOSITES. In *20th European Conference on Composite Materials*, 1–7 (2022).

[184] Solovyov, S. E., Llyashenko, V. M. & Pojman, J. A. Numerical modeling of self-propagating polymerization fronts: The role of kinetics on front stability. *Chaos* **7**, 331–340 (1997).

[185] Goldfeder, P. M. *et al.* Mathematical Modeling of Free-Radical Polymerization Fronts. *The Journal of Physical Chemistry B* **101**, 3474–3482 (1997).

[186] Inamdar, S. R. *et al.* Spinning wave motion in frontal polymerization. *Chemical Engineering Science* **62**, 1448–1455 (2007).

[187] Urdiales, E. & Volpert, V. A. Linear stability analysis of spherically propagating thermal frontal polymerization waves. *Journal of Engineering Mathematics* **71**, 279–290 (2011).

[188] Bowden, G. *et al.* Effect of convection on a propagating front with a solid product: Comparison of theory and experiments. *Journal of Physical Chemistry B* **101**, 678–686 (1997).

[189] Bazile, M., Nichols, H. A., Pojman, J. A. & Volpert, V. Effect of Orientation on Thermoset Frontal Polymerization. *Journal of Polymer Science Part A: Polymer Chemistry* **40W**, 3504–3508 (2002).

[190] Lloyd, E. M. *et al.* Spontaneous Patterning during Frontal Polymerization. *ACS Central Science* **7**, 603–612 (2021).

[191] Goli, E., Peterson, S. R. & Geubelle, P. H. Instabilities driven by frontal polymerization in thermosetting polymers and composites. *Composites Part B: Engineering* **199**, 1–17 (2020).

[192] Kumar, A. *et al.* Surface pattern formation induced by oscillatory loading of frontally polymerized gels. *Journal of the Mechanics and Physics of Solids* **168**, 105055 (2022). URL https://doi.org/10.1016/j.jmps.2022.105055.

Bibliography

[193] Pojman, J. A. Mathematical Modeling of Frontal Polymerization. *Mathematical Modelling of Natural Phenomena* **14**, 604 (2019).

[194] Masere, J., Stewart, F., Meehan, T. & Pojman, J. A. Period-doubling behavior in frontal polymerization of multifunctional acrylates. *Chaos* **9**, 315–322 (1999).

[195] Lang, M., Hirner, S., Wiesbrock, F. & Fuchs, P. A Review on Modeling Cure Kinetics and Mechanisms of Photopolymerization. *Polymers* **14**, 1–58 (2022).

[196] Matias, J. M., Bartolo, P. J. & Pontes, A. V. Modeling and Simulation of Photofabrication Processes Using Unsaturated Polyester Resins. *Journal of Applied Polymer Science* **114**, 3673–3685 (2009).

[197] Da Silva Bartolo, P. J. Photo-curing modelling: Direct irradiation. *International Journal of Advanced Manufacturing Technology* **32**, 480–491 (2007).

[198] Ozawa, T. Kinetic analysis of derivative curves in thermal analysis. *Journal of Thermal Analysis* **2**, 301–324 (1970).

[199] Kissinger, H. E. Variation of Peak Temperature With Heating Rate In Differential Thermal Analysis. *Journal 0f Research of the National Bureau of Standards* **57**, 217–221 (1956).

[200] Kissinger, H. E. Reaction Kinetics in Differential Thermal Analysis. *Analytical Chemistry* **29**, 1702–1706 (1957).

[201] Bernath, A., Kärger, L. & Henning, F. Accurate cure modeling for isothermal processing of fast curing epoxy resins. *Polymers* **8**, 1–19 (2016).

[202] Henne, M., Breyer, C., Niedermeier, M. & Ermanni, P. A new kinetic and viscosity model for liquid composite molding simulations in an industrial environment. *Polymer Composites* **25**, 255–269 (2004).

[203] Keller, A., Masania, K., Taylor, A. C. & Dransfeld, C. Fast-curing epoxy polymers with silica nanoparticles: properties and rheo-kinetic modelling. *Journal of Materials Science* **51**, 236–251 (2015).

[204] Martin, J. Kinetic Analysis of Two DSC Peaks in the Curing of an Unsaturated Polyester Resin Catalyzed With Methylethylketone Peroxide and Cobalt Octoate. *Polymer Engineering and Science* **47**, 62–70 (2007).

[205] Hsieh, T. H. & Su, A. C. Cure behavior of an epoxy–novolac molding compound. *Journal of Applied Polymer Science* **44**, 165–172 (1992).

[206] Spoelstra, A. B., Peters, G. W. & Meijer, H. E. Chemorheology of a highly filled epoxy compound. *Polymer Engineering and Science* **36**, 2153–2162 (1996).

[207] González-Romero, V. M. & Casillas, N. Isothermal and temperature programmed kinetic studies of thermosets. *Polymer Engineering & Science* **29**, 295–301 (1989).

[208] Mathew, G., Rhee, J. M., Lee, Y. S., Park, D. H. & Nah, C. Cure kinetics of ethylene acrylate rubber/clay nanocomposites. *Journal of Industrial and Engineering Chemistry* **14**, 60–65 (2008).

[209] Wang, J.-F., Lin, M.-T., Wang, C.-P. & Fu-Xiang, C. Study on the Synthesis, Characterization, and Kinetic of Bulk Polymerization of Disproportionated Rosin (β-Acryloxyl Ethyl) Ester. *Journal of Applied Polymer Science* **113**, 3757–3765 (2009).

[210] Kessler, M. R. & White, S. R. Cure kinetics of the ring-opening metathesis polymerization of dicyclopentadiene. *Journal of Polymer Science, Part A: Polymer Chemistry* **40**, 2373–2383 (2002).

[211] Goli, E., Robertson, I. D., Geubelle, P. H. & Moore, J. S. Frontal Polymerization of Dicyclopentadiene: A Numerical Study. *Journal of Physical Chemistry B* **122**, 4583–4591 (2018).

[212] Yang, G. & Lee, J. K. Curing kinetics and mechanical properties of endo-dicyclopentadiene synthesized using different Grubbs' catalysts. *Industrial and Engineering Chemistry Research* **53**, 3001–3011 (2014).

[213] Kamal, M., Sourour, S. & Ryan, M. Integrated thermo-rheological analysis of the cure of thermosets. *SPE Tech. Pap.* **19**, 187–191 (1973).

[214] Grindling, J. *Simulation zur Verarbeitung von reaktiven Non-Post-Cure-Epoxidharz-Systemen im Druckgelieren und konventionellen Vergiessen.* Ph.D. thesis, Universität Paderborn (2006).

[215] Bailleul, J. L., Delaunay, D. & Jarny, Y. Determination of temperature variable properties of composite materials: Methodology and experimental results. *Journal of Reinforced Plastics and Composites* **15**, 479–496 (1996).

[216] Ruiz, E. & Trochu, F. Thermomechanical properties during cure of glass-polyester RTM composites: Elastic and viscoelastic modeling. *Journal of Composite Materials* **39**, 881–916 (2005).

[217] Spade, C. A. & Volpert, V. A. On the steady-state approximation in thermal free radical frontal polymerization. *Chemical Engineering Science* **55**, 641–654 (2000).

[218] Apostolo, M., Tredici, A., Morbidelli, M. & Varma, A. Propagation velocity of the reaction front in addition polymerization systems. *Journal of Polymer Science, Part A: Polymer Chemistry* **35**, 1047–1059 (1997).

[219] Volpert, V. A. Dynamics of Thermal Polymerization Wave. In *Self-Assembly, Pattern Formation and Growth Phenomena in Nano-Systems* (Springer, 2006).

[220] Wang, Y. Modeling the through-thickness frontal polymerization of unidirectional carbon fiber thermoset composites: Effect of microstructures. *Journal of Applied Polymer Science* **139**, 1–13 (2022).

Bibliography

[221] Gaston, D., Newman, C., Hansen, G. & Lebrun-Grandié, D. MOOSE: A parallel computational framework for coupled systems of nonlinear equations. *Nuclear Engineering and Design* **239**, 1768–1778 (2009).

[222] Vyas, S., Zhang, X., Goli, E. & Geubelle, P. H. Frontal vs. bulk polymerization of fiber-reinforced polymer-matrix composites. *Composites Science and Technology* **198**, 108303 (2020). URL https://doi.org/10.1016/j.compscitech.2020.108303.

[223] Kumar, A., Gao, Y. & Geubelle, P. H. Analytical estimates of front velocity in the frontal polymerization of thermoset polymers and composites. *Journal of Polymer Science* **59**, 1109–1118 (2021).

[224] El-Hage, Y., Hind, S. & Robitaille, F. Thermal conductivity of textile reinforcements for composites. *Journal of Textiles and Fibrous Materials* **1**, 251522111775115 (2018).

[225] Pietrak, K. & Wiśniewski, T. S. A review of models for effective thermal conductivity of composite materials. *Journal of Power Technologies* **95**, 14–24 (2015). URL http://papers.itc.pw.edu.pl/index.php/JPT/article/view/463.

[226] Frulloni, E., Salinas, M. M., Torre, L., Mariani, A. & Kenny, J. M. Numerical modeling and experimental study of the frontal polymerization of the diglycidyl ether of bisphenol a/diethylenetriamine epoxy system. *Journal of Applied Polymer Science* **96**, 1756–1766 (2005).

[227] Staal, J. *et al.* In-series sample methodology for permeability characterization demonstrated on carbon nanotube-grafted alumina textiles. *Composites Part A: Applied Science and Manufacturing* **150**, 106631 (2021).

[228] Sket, F. *et al.* Automatic quantification of matrix cracking and fiber rotation by X-ray computed tomography in shear-deformed carbon fiber-reinforced laminates. *Composites Science and Technology* **90**, 129–138 (2014). URL http://dx.doi.org/10.1016/j.compscitech.2013.10.022.

[229] Tan, U., Rabaste, O., Adnet, C. & Ovarlez, J. P. On the Eclipsing Phenomenon with Phase Codes. In *2019 International Radar Conference, RADAR 2019* (2019).

[230] Hansen, N. *The CMA Evolution Strategy: A Tutorial* (ArXiv e-prints, 2016). URL http://arxiv.org/abs/1604.00772.

[231] Chinkanjanarot, S. *et al.* Multiscale thermal modeling of cured cycloaliphatic epoxy/-carbon fiber composites. *Journal of Applied Polymer Science* **135**, 1–10 (2018).

[232] Clayton, W. Constituent and Composite Thermal Conductivities of Phenolic-Carbon and Phenolic-Graphite Ablators. In *Proceedings of the AIAA/ASME 12th Structures, Structural Dynamics and Materials Conference*, 1–17 (1971).

[233] Rohsenow, W. M., Hartnett, J. P. & Cho, Y. I. *Handbook of Heat Transfer* (McGraw-Hill, New York, 1998).

[234] Isaacson, E. & Keller, H. B. *Analysis of Numerical Methods* (Dover Publications, 1967).

[235] Green, W. *Industrial Photoinitiators: A Technical Guide* (Taylor & Francis, 2010).

[236] Lau, K. T. *et al.* Thermal and mechanical properties of single-walled carbon nanotube bundle-reinforced epoxy nanocomposites: The role of solvent for nanotube dispersion. *Composites Science and Technology* **65**, 719–725 (2005).

[237] Tang, L.-G. & Kardos, J. L. A Review of Methods for Improving the Interfacial Adhesion Between Carbon Fiber and Polymer Matrix. *Polymer Composites* **18**, 100–113 (1997).

[238] Salvatori, D. & Michaud, V. Strategies for in-Plane Thermoplastic Melt Impregnation of Glass-Fabrics. In *The 14th International Conference on Flow Processes in Composite Materials*, July, 1–2 (2018).

[239] Salvatori, D., Caglar, B. & Michaud, V. 3D spacers enhance flow kinetics in resin transfer molding with woven fabrics. *Composites Part A: Applied Science and Manufacturing* **119**, 206–216 (2019).

[240] Kessels, J. F., Jonker, A. S. & Akkerman, R. Optimising the flow pipe arrangement for resin infusion under flexible tooling. *Composites Part A: Applied Science and Manufacturing* **38**, 2076–2085 (2007).

[241] Wang, J., Simacek, P. & Advani, S. G. Use of medial axis to find optimal channel designs to reduce mold filling time in resin transfer molding. *Composites Part A: Applied Science and Manufacturing* **95**, 161–172 (2017).

[242] Montés, N. & Sánchez, F. A new computational tool for liquid composite moulding process design based on configuration spaces. *Composites Part A: Applied Science and Manufacturing* **41**, 58–77 (2010).

[243] Staal, J., Smit, E., Caglar, B. & Michaud, V. Thermal management in radical induced cationic frontal polymerisation for optimised processing of fibre reinforced polymers. *Composites Science and Technology* **237**, 110009 (2023).

Jeroen Staal
PhD candidate

Lausanne, Switzerland
Dutch nationality
(+31)611221570
jacobus.staal@epfl.ch

EXPERTISES

- Materials Science
- Data analysis
- Polymer science
- Fibre reinforced composites
- Photopolymerisation
- Frontal polymerisation
- Composite processing
- Material characterization
- Finite element analysis
- Additive manufacturing

TECHNICAL SKILLS

Materials characterisation
- DSC
- DMA
- Rheology
- FTIR
- TGA
- Mechanical testing

Software
Experienced:
- Python
- Matlab
- Office
- OriginPro
- Autodesk
- Photoshop

Basic:
- Abaqus
- Tensorflow
- Labview
- Solidworks
- LaTeX

LANGUAGES

Dutch
English
French
German
Chinese

ACTIVITIES

WORK EXPERIENCE

Ecole Polytechnique Fédérale de Lausanne | Lausanne, Switzerland
Laboratory for Processing of Advanced Composites - LPAC

2019-2023
(4.2 years)

Doctoral assistant

Objective: Develop novel strategies for microstructural evaluation and fast & energy-efficient frontal polymerisation processing of fibre reinforced composites
under supervision of prof. V. Michaud

Main tasks:
- Experimental research, project management, data analysis & visualisation and communication of results
- Teaching exercise sessions (in French) and lab courses
- Supervision of 4 master theses & 5 semester projects
- Responsible for characterization equipment, training of new users

Achievements: 1 patent, 3 publications, 3 presentations, 1 award

2018-2019
(4 months)

Visiting research student

Objective: Study the permeability of carbon nanotube-grafted alumina fabrics for composites as part of master thesis

Achievements: 1 publication

Katholieke Universiteit Leuven | Leuven, Belgium
Additive Manufacturing group - prof. B. Van Hooreweder

2017
(2 months)

Student assistant

Role: Summer internship, main tasks include experimental preparation and analysis and improvement of course material

Dutch National Badminton Organisation | the Netherlands

2009-2016
(7 years)

Licensed badminton teacher

Role: Teaching badminton at various organisations in the region of Helmond. Age groups ranged anywhere between 6-67 years old

EDUCATION

Katholieke Universiteit Leuven | Leuven, Belgium

2016-2019
(2.5 years)

Master in Materials Engineering (Cum Laude)

Tracks: Polymers & Composites, Nanomaterials

Thesis: 'Permeability and wetting behaviour of carbon nanotube-grafted alumina fabrics for composites'
under supervision of prof. S.V. Lomov, prof. D. Seveno, dr. L. Gorbatikh

Extracurricular: Representing member for the international students in the Permanent Education Committee and Department Council of the Materials Engineering department

Technische Universiteit Eindhoven | Eindhoven, the Netherlands

2013-2016
(3 years)

Bachelor in Chemical Engineering & Chemistry 163

Tracks: Chemistry, Chem. Engineering, Technology Entrepreneurship

Thesis: 'Light-responsive piezoelectric actuators'
under supervision of prof. A. Schenning, dr. M. Debije

PUBLICATIONS

2023 — **Self-catalysed frontal polymerisation towards low energy rapid processing of structural fibre reinforced epoxide composites**
in preparation
J.Staal, B. Caglar, V. Michaud

2023 — **Thermal management in radical induced cationic frontal polymerisation for optimised processing of fibre reinforced polymers**
Composites Science & Technology 237 (2023) | 10.1016/j.compscitech.2023.110009
J. Staal, E. Smit, B. Caglar, V. Michaud

2022 — **Capillary effects in fibre reinforced polymer composite processing: A review**
Frontiers in Materials 9 (2022) | 10.3389/fmats.2022.809226
H. Teixidó*, J. Staal*, B. Caglar, V. Michaud (*equal contribution)

2021 — **In-series sample methodology for permeability characterization demonstrated on carbon nanotube-grafted alumina textiles**
Composites Part A: Science & Technology 150 (2021) | 10.1016/j.compositesa.2021.106631
J. Staal, B. Caglar, T. Hank, B.L. Wardle, L. Gorbatikh, S.V. Lomov, V. Michaud

PATENTS

2023 — **Method for the Manufacture of Fiber-Reinforced Polymer Composites | Filed**

CONFERENCES

2022 — **37th Annual technical conference of the American Society for Composites | Tucson, USA**
Oral presentation

2022 — **20th European Conference on Composite Materials | Lausanne, Switzerland**
Oral presentation

2021 — **Virtual European Symposium of Photopolymer Sciences | Virtual**
Oral presentation

2019 — **SAMPE Europe 2019 | Nantes, France**
Poster

AWARDS

2022 — **Winner of the 2022 4-minute doctoral research impact competition**
American Society for Composites